Investigating Suitable Geochemical Tracers for Monitoring CO_2 Sequestration in Offshore Deep-Sea Basalt in the Cascadia Basin

by

Emma Louis

B.Sc., Frostburg State University, 2018

A Thesis Submitted in Partial Fulfillment of the Requirements for the Degree of

MASTER OF SCIENCE

in the School of Earth and Ocean Sciences

Investigating Suitable Geochemical Tracers for Monitoring CO_2 Sequestration in Offshore Deep-Sea Basalt in the Cascadia Basin

by

Emma Louis

B.Sc., Frostburg State University, 2018

Supervisory Committee

Dr. Kate Moran, Co-supervisor
School of Earth and Ocean Sciences

Dr. Laurence Coogan, Co-supervisor
School of Earth and Ocean Sciences

Dr. Martin Scherwath, Additional Member
School of Earth and Ocean Sciences

Abstract

Carbon dioxide concentrations in the atmosphere have drastically increased due to human activities, causing accelerating climate change. Carbon dioxide (CO_2) removal technologies are now deemed essential to aid in reaching international climate goals to limit further global surface temperature increase. As deep-sea basalt has significant potential to permanently sequester enormous quantities of CO_2 but has never been tested, an investigation into monitoring this process was carried out with an emphasis on the use of geochemical tracers to verify the success of CO_2 sequestration into deep-sea basalt as part of the Solid Carbon feasibility study. In basalt, CO_2 that would otherwise be released into the atmosphere is sequestered through chemically binding the injected CO_2 to form carbonate minerals in the pore spaces of the basalt. This research investigates geochemical tracers typically used in hydrogeologic and carbon capture and storage studies to determine their suitability at the temperature and pressure conditions within the basaltic crust in the Cascadia Basin. The most suitable conservative tracer for the planned CO_2 injection experiment is SF_5CF_3, for verifying CO_2-rich fluid breakthrough and determining fluid velocities and rates of dilution. The most suitable reactive tracer is concluded to be stable carbon isotopes, for confirming carbon has been removed from formation fluids through precipitation of carbonate minerals. Fluid samples collected before, during, and after injection with long-term osmotically pumped fluid sampling systems and mobile pumping systems could be used to analyze tracer concentrations, in addition to analyzing alkalinity, pH, dissolved inorganic carbon, and major ion and trace element concentrations to inform geochemical changes occurring *in-situ* in the deep-sea basaltic aquifer. A variety of measurements from sensors connected to the NEPTUNE cabled observatory were also evaluated to collect geochemical data in real time. Finding suitable tracers and geochemical monitoring parameters for the *in-situ* conditions in deep-sea basaltic crust is necessary for interpreting geochemical changes due to CO_2 injection. The monitoring parameters outlined in this research may be useful in future offshore deep-sea basalt CO_2 injection scenarios with more understanding of tracer behavior in supercritical CO_2/water systems under high pressures and temperatures.

Table of Contents

List of Figures

List of Tables

Acknowledgements

I want to take a moment to thank those who have helped me on this journey.
First, to my supervisory committee, Kate, Martin, and Laurence, thank you for your consistent guidance and support, and for giving me this opportunity to immerse myself in a topic that is so relevant for the future. I admire all of you as scientists and leaders.
To the entire Solid Carbon team, I feel grateful to have learned from and engaged with such amazing scientists and engineers and I will forever be inspired by their innovative minds.
To my undergraduate supervisor, Dr. Philip Allen, who saw something in me I did not see in myself, thank you for telling me I am capable of academic research and that perseverance will get me through.
To my family, thank you for whole-heartedly supporting me, especially during challenging times. I would have not been able to achieve this without you.
To my partner Nate, thank you for being a source of love, even from afar.
And last, thank you to my cat Penny, who truly is the best emotional support and office partner.

Dedication

I dedicate this work to my father Glenn,
for instilling in me a passion for science,
and to my grandfather Fred,
whose love of the natural world continues to inspire me to this day.

"Transformation is not accomplished by tentative wading at the edge."
– Robin Kimmerer

Chapter One: Introduction

1.0 Atmospheric CO_2 Pollution

The observed rise in atmospheric CO_2 concentrations contributing to increased warming of the planet is indisputable. Between 1850 and 2019, 2400 ± 240 $GtCO_2$ were emitted into the atmosphere, with more than half (58%) of the emissions occurring between 1850-1989 (139 years) and the remaining 42% between 1990 and 2019 (29 years) (IPCC, 2023). Between 1850-2019, global surface temperature has increased by ~1.1ºC (Figure 1.1a) (IPCC, 2023). In 2019, global anthropogenically produced greenhouse gas emissions (i.e., CO_2, methane, nitrous oxides, and fluorinated gases) were estimated to be 59 ± 6.6 Gt which is 54% higher than what was observed in 1990 (~21 Gt) (Figure 1.1b) (IPCC, 2023). Carbon dioxide is by far the largest greenhouse gas contributor, mainly from fossil fuel combustion and industrial processes like cement production (Figure 1.1b) (IPCC, 2023; NASEM, 2019). Importantly, there is high confidence that the observed increase in atmospheric CO_2 concentrations during these time periods have exceeded reconstructed CO_2 levels from the past two million years, and the observed temperatures during the most recent decade coincide with levels of warming reconstructed from ~125,000 years ago (Figure 1.1a) (IPCC, 2023).

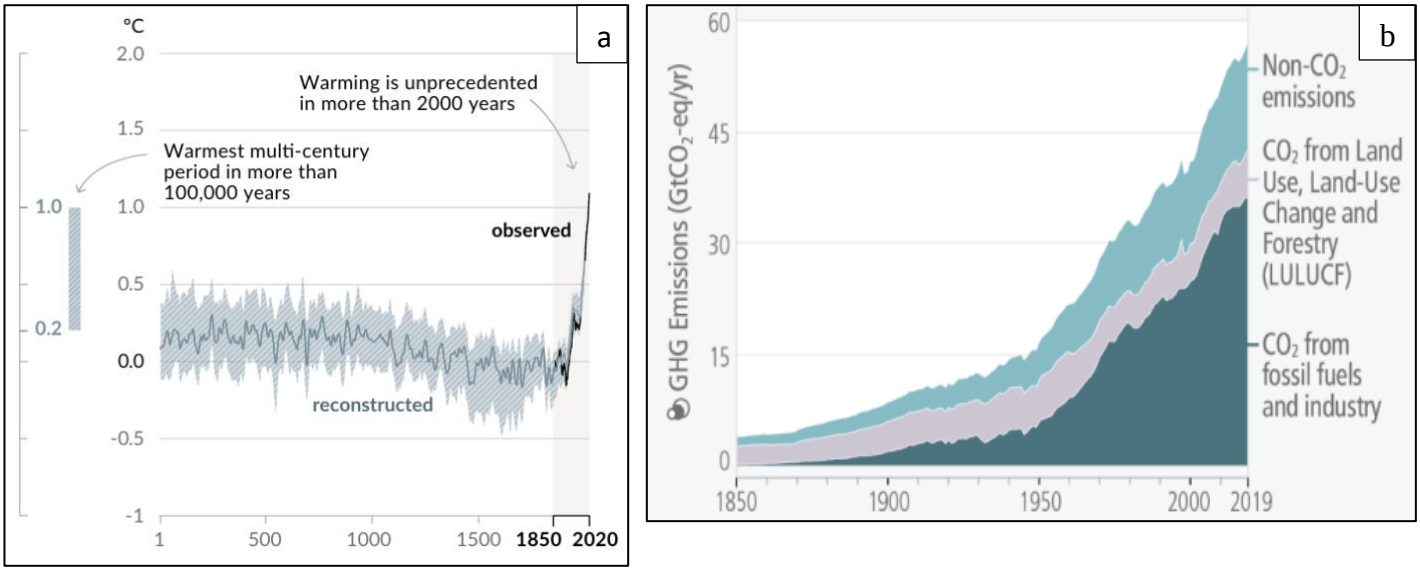

Figure 1.1: *Observed changes in global surface temperatures in the last 2,000 years and greenhouse gas emissions between 1850-2019.* ***a)*** *Graph showing change in average global surface temperatures (per decade) from 1-2,000 years (reconstructed from climate models) and 1850-2020 (observed). Y-axis shows the estimated temperature range during the Holocene epoch (~6,500 years ago), or the warmest period observed in the last 100,000 years. Observed temperatures in the most recent decade coincide with levels of warming reconstructed from ~125,000 years ago (or the last interglacial period of warming prior to the Holocene epoch). These past periods of global warming reconstructed from climate models indicate that the warming observed between 1850-1900 and 2010-2019 is human driven. Average global surface temperatures have increase by ~1.1ºC between 2011-2020 compared to 1850-1900 and coincide with increasing greenhouse gas emissions.* ***b)*** *Graph showing greenhouse gas emissions from human activities between 1850-2019 in $GtCO_2$/year. Global anthropogenic greenhouse gas emissions from CO_2 produced*

from fossil fuel combustion and industrial processes (shown in the dark green); CO_2 emissions from land-use change and forestry (shown in grey); emissions of methane (CH_4), nitrous oxides (N_2O), and fluorinated gases (PFCs, HFCs, SF_6) in units of CO_2 equivalent/year (i.e., emissions of these gases have been converted to represent the equivalent amount of CO_2 with the same global warming potential) (shown in light blue). Greenhouse gas emissions have caused increasing concentrations of several greenhouse gases in the atmosphere, in particular CO_2 from fossil fuel combustion and industry. Source: IPCC (2023).

To address this climate crisis, a legally binding international treaty, the Paris Agreement, was signed by 196 countries at the United Nations Conference of the Parties (COP21), for which the COP serves as the Conference that is the Meeting of the Parties to the Kyoto Protocol (CMP) in 2015. COP21 addressed climate change by setting emission targets for all countries (Delbeke et al., 2019). This treaty builds upon the Kyoto Protocol which was adopted in 1997 and focused on reducing greenhouse gas emissions in developed countries (Delbeke et al., 2019; Reilly et al., 2002). The emissions targets specified in the Paris Agreement focus on limiting global temperature increase to 1.5ºC above pre-industrial levels, and well below 2ºC, as conveyed by integrated assessment models presented from the Intergovernmental Panel on Climate Change (IPCC) (UNEP, 2019). In 2022, global energy related CO_2 emissions reached ~36.8 $GtCO_2$ (International Energy Agency, 2022).

1.1 Motivation of Study

The Solid Carbon feasibility study is planning to conduct a carbon dioxide (CO_2) injection experiment in the offshore deep-sea basaltic aquifer in the Cascadia Basin. The experiment will inject ~10,000 tons of CO_2 into a crustal aquifer and use existing boreholes as monitoring wells with a suite of sensors and fluid samplers to monitor the process where carbon will be secured in mineral form (i.e., carbonate mineralization) (Figure 1.1). A year or two following the injection, a ship-based expedition would collect basalt cores and *in-situ* fluid samples to validate CO_2 has formed minerals in the pore spaces of the basalt. Of the monitoring methods planning to be used, geochemical tracers are of interest due to their success in carbon sequestration studies in validating the geochemical changes occurring to carbon injected into geologic formations. This research investigates various tracers listed in the published literature on carbon sequestration, hydrogeology, and ocean drilling and their potential to be used to monitor CO_2 injection at the *in-situ* conditions in the basaltic crust at the Cascadia Basin site.

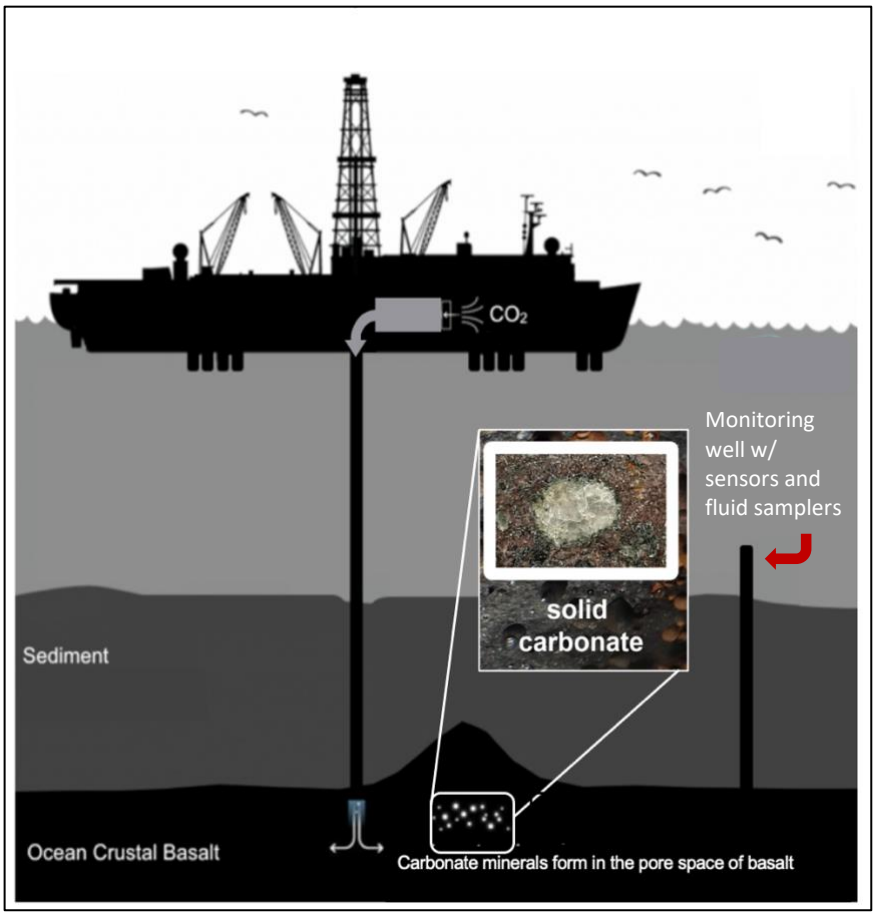

Figure 1.2: *Schematic of Solid Carbon CO_2 injection experiment in offshore deep-sea basalt in the Cascadia Basin. CO_2 injection into the ocean crust is expected to form carbonate minerals in the pore spaces of the basalt rock, known as carbonate mineralization. Monitoring will take place using fluid samplers, real-time measurements made by sensors in-situ, and geochemical tracers, which is the motivation for this research.*

1.1.1 Negative Emissions Technologies and Carbon Capture and Storage

To keep global temperatures from rising past 2ºC, some form of carbon dioxide removal, in addition to conventional mitigation techniques (e.g., decarbonization of the economy through renewable energy, low-carbon fuels, nuclear power, sustainable agriculture), is required to remove ~10 $GtCO_2$/year by 2050 and ~20 $GtCO_2$/year by 2100 (NASEM, 2021) with a goal to reduce emissions from the energy sector by 80-100% (NASEM, 2019). Deploying technologies to reduce and remove CO_2 being emitted into the atmosphere must be achieved between now and 2050, according to climate and integrated assessment models from IPCC (Energy Futures Initiative, 2022; IPCC, 2021). Negative emissions technologies, also known as carbon dioxide removal, have been proposed as solution technologies. Negative emissions technologies (NETs) are technologies that remove CO_2 from the environment, where it is locked away for decades or centuries (McLaren, 2012). These technologies are projected to be less disruptive and expensive than reducing emissions in some sectors, such as transportation, land-use, and agriculture

(NASEM, 2019). Therefore, NETs can facilitate an accelerated removal of emissions over the long term that can offset emissions from those sectors which are hard to decarbonize (Figure 1.3) (Fawzy et al., 2020; NASEM, 2019). Examples of existing NETs include bioenergy with carbon capture and storage (BECCS), direct air capture and carbon storage (DACCS), carbon mineralization via enhanced rock weathering, ocean fertilization, biochar, soil carbon sequestration, afforestation, and reforestation (McLaren et al., 2012, Fuss et al., 2018). Carbon sequestration in deep-sea basalt has been cited as a NET in the literature (Campbell et al., 2022; NASEM, 2019; Haszeldine et al., 2018) and has the potential to play a key role in reaching net zero emissions if scaled globally.

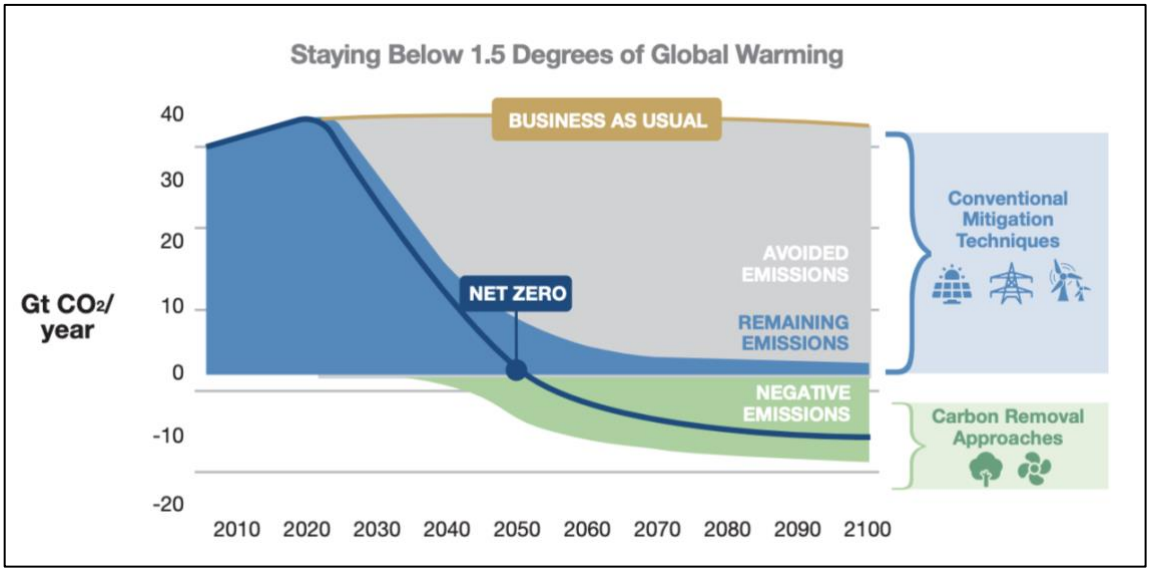

Figure 1.3: *The role of negative emissions technologies for achieving net-zero. Current global energy related annual CO_2 emissions are ~36.8 $GtCO_2$/year (International Energy Agency, 2022). Gigaton-scale carbon dioxide removal approaches are needed to avoid the business-as-usual case and stay within the targeted temperature range of <2ºC above pre-industrial levels. Conventional mitigation techniques such as renewable energy and nuclear power help reduce emissions, while carbon dioxide removal approaches can offset any remaining emissions from sectors which are challenging to decarbonize. Source: Energy Future Initiative (2022), originally adapted from IPCC (2018).*

Carbon capture and storage (CCS) involves the separation, capture, transport, and sequestration of CO_2 into subsurface geologic formations. CCS projects can serve as a NET by either removing CO_2 directly from the atmosphere (e.g., DACCS) or helping to limit emissions from existing industry processes (e.g., cement production, iron and steel manufacturing, natural gas treatment), by separating and capturing the CO_2 produced and storing it in subsurface geologic formations (Boot-Handford et al., 2014). Carbon dioxide is typically pressurized before being transported by rail, ship, or pipeline to a storage site (Boot-Handford et al., 2014; White et al., 2003), where it is injected into a geologic formation capable of trapping the CO_2 for hundreds to thousands of years. CCS projects have been demonstrated both onshore and offshore at the commercial scale (Clark et al., 2020; Duong et al., 2019; Furre et al., 2017; Wildgust et al., 2013) and have adopted knowledge and experience of CO_2 injection from mainly the oil

industry, where CO_2 injection is routine for enhanced oil recovery (Boot-Handford et al., 2014), except the goal for CCS projects is to durably store CO_2 to limit emissions of CO_2 into the atmosphere. CCS projects are mentioned in this research, mainly serving as examples for monitoring that pilot projects, such as Solid Carbon, that can see benefit.

1.1.2 Advantages of Offshore Basalt Reservoirs for Carbon Sequestration

1.1.2.1 Introduction

Subseafloor basalts offer several unique advantages for long-term sequestration of CO_2 such as global abundance (Goldberg and Slagle, 2009), very large reservoir capacities for many years' worth current annual CO_2 emissions, a highly durable form of storage (Snæbjörnsdóttir et al., 2020), *in-situ* availability of hydrothermally circulated seawater allowing for long fluid retention times (> 500 years) (Elderfield et al., 1999), and a low risk of leakage due to low permeability sediment blankets in some regions.

The sections that follow provide an overview of the global potential of basalt for carbon sequestration, storage mechanisms that exist which will ensure the injected CO_2 stays in the formation, and two terrestrially based pilot projects that have successfully injected CO_2 into basalt where it formed carbonate minerals within a few years. The need for monitoring the CO_2 sequestration process in the offshore environment is also introduced.

1.1.2.2 Global Potential of Basaltic Reservoirs for CO_2 Sequestration

The global distribution of basaltic reservoirs provides ample opportunities to store CO_2 in basalt at a global scale. Basalt is the most abundant mafic rock, making up >5% of continents and ~70% of the Earth's surface, mostly the upper portion of the ocean crust (Raza et al., 2022; Snæbjörnsdóttir et al., 2020). Large areas of continental flood basalts exist in the continental U.S, China, central India, Siberia, and Yemen (Figure 1.4) (Snæbjörnsdóttir et al., 2020; McGrail et al., 2003, 2006). Oceanic plateaus also exist across the globe (Kerr, 2015). Iceland is unique as it is a basaltic land mass that exists on the mid-Atlantic spreading ridge and has ample amounts of accessible basalt for storage that is not technically offshore (Callow et al., 2018). Storage estimates of deep-sea basalts, along mid-ocean spreading ridges and oceanic plateaus, are enormously large (29-150 Tt CO_2) (Figure 1.4) (Goldberg and Slagle, 2009) with storage capacity for millennia worth of current CO_2 emissions (~36.8 $GtCO_2$ per year) (International Energy Agency, 2022).

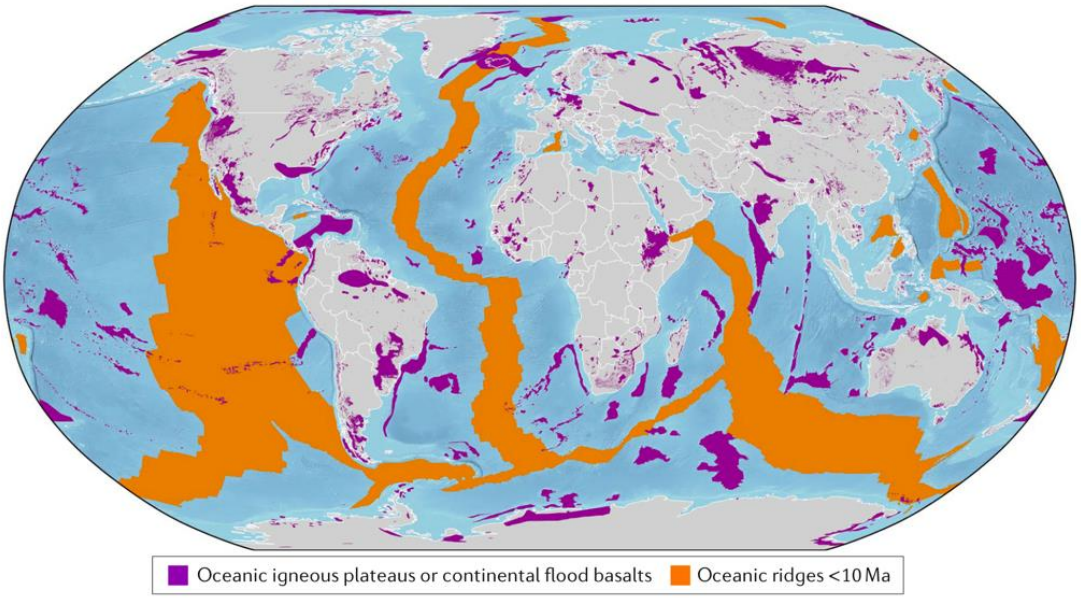

Figure 1.4: *Viable basaltic formations for in-situ carbon mineralization and storage. Oceanic ridges younger than 10 Ma are shown in orange, and oceanic igneous plateaus and continental flood basalts are shown in purple. Source: Snæbjörnsdóttir et al. (2020).*

A global assessment of deep-sea basaltic aquifers was conducted by Goldberg and Slagle (2009) to estimate total volumes available for CO_2 sequestration in basalt at a global scale. They chose to only investigate aseismic ridges and seafloor spreading ridges due to being the most globally significant and determined their findings based on the following criteria:

- the presence of seafloor spreading ridges (crustal age <15 Ma) or aseismic ridges,
- average porosity in basalt of 10% and within interflow zones for aseismic ridges,
- sediment thickness of >200m overlying basaltic crust,
- the area is at least 20 km away from a plate boundary,
- and water depth of ≥2700m at the seafloor.

Basaltic crustal age of <15Ma is significant because according to seismic evidence, it is estimated that half of the initial porosity of ocean crust is retained after 15Ma years (Jarrard et al., 2003).

Sediment thickness data was from the National Geophysical Data Center, which includes data from ocean drilling results, seismic reflection profiles, and maps. Ocean bathymetric data was obtained through the Marine Geoscience Data System, which integrates multibeam bathymetry data with regional low-resolution data. A Geographic Information System (GIS) was used to analyze the data from global databases and isolate the regions that meet the desired criteria. Eleven seafloor spreading ridge sites were selected (Figure 1.5) in addition to seven areas of deep-sea basalt that form because of intraplate volcanism (i.e., aseismic ridges).

Based on these criteria, the total potential volume for global seismic ridge deep-sea basalts ranges from 8-42 Tt CO_2, and aseismic ridges from 22-109 Tt CO_2 (Figure 1.5), although there is greater uncertainty in the range for aseismic ridges due to less historical data (Goldberg and Slagle, 2009). The total volume for all deep-sea basalt considered is estimated between 29-150 Tt CO_2 (Figure 1.5). The Juan de Fuca ridge estimates considered both the east and west flanks with the same crustal age and combined have capacity to sequester 506-2,452 Gt CO_2 (Goldberg and Slagle, 2009).

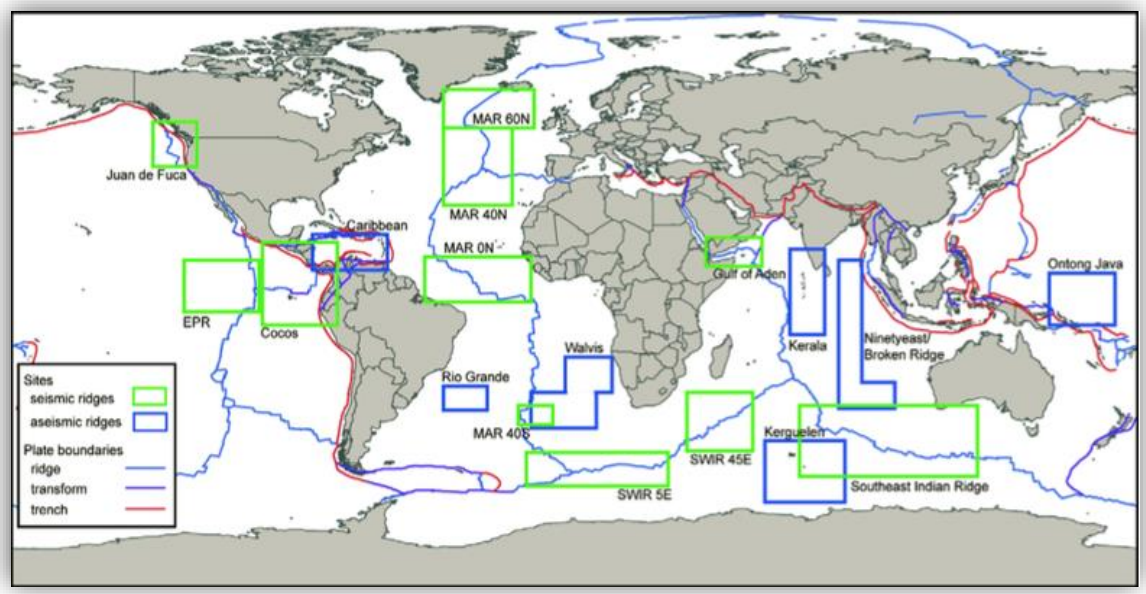

Region[a]	Area (km²)[b]	20 m net thickness[c]	100 m net thickness[c]	Carbon (Gt)
Juan de Fuca	244,963	490	2,450	134 – 668
East Pacific Rise	491,561	983	4,916	268 – 1,340
Cocos Ridge	891,510	1,783	8,915	486 – 2,431
Mid-Atlantic Ridge 60N	52,734	105	527	29 – 144
Mid-Atlantic Ridge 40N	139,141	278	1,391	76 – 379
Mid-Atlantic Ridge 0	220,842	442	2,208	120 – 602
Mid-Atlantic Ridge 40S	3,778	8	38	2 – 10
Southwest Indian Ridge 5E	81,329	163	813	44 – 222
Southwest Indian Ridge 45E	15,757	32	158	9 – 43
Gulf of Aden	30,763	62	308	17 – 84
Southeast Indian Ridge	2,068,304	4,137	20,683	1,128 – 5,640
Caribbean flood basalt	541,611	1,083	5,416	295 – 1,477
Rio Grande Rise	831,818*	1,664	8,318	454 – 2,268
Walvis Ridge	1,933,711*	3,867	19,337	1,055 – 5,273
Kerala Basin	952,761	1,906	9,528	520 – 2,598
Ninetyeast Ridge/Broken Ridge	2,198,757	4,398	21,988	1,199 – 5,996
Kerguelen Plateau	1,788,834*	3,578	17,888	976 – 4,878
Ontong Java Plateau	2,616,646*	5,233	26,166	1,427 – 7,136
			Total Seismic Sites	**2,313 – 11,564 Gt**
			Total Aseismic Sites	**5,925 – 29,627 Gt**
			Total for All Sites	**8,238 – 41,191 Gt**

[a] Above the line are seismic ridges; below are aseismic ridges (see Fig. 2).
[b] Asterisks indicate uncertain regional boundaries.
[c] These calculations assume 10% average aquifer porosity.

Figure 1.5: *Results from a global assessment of volume estimates for carbon sequestration potential in deep-sea basalt. All sites listed in the table are included on the map. The top portion of sites in the table*

are seismic ridges (green box on map), and the bottom portion is aseismic ridges (blue box on map). Note the Juan de Fuca spreading ridge (including both east and west flanks) has an estimated carbon storage capacity of 138-668 Gt of carbon (506-2,452 Gt CO_2). Assumptions for the assessment included aquifer porosity of 10%, at least 2,700 m water depth, <15 Ma crustal age, located 20 km away from a plate boundary, and sediment thickness of more than 200 m. Source: Goldberg and Slagle (2009).

1.1.2.3 Storage Mechanisms

Storage mechanisms naturally exist in various types of geologic formations based on rock type, depth, porosity, and permeability (Gunter et al., 1993, 1997). Four storage mechanisms exist for CO_2 storage in geologic formations: 1) physical trapping, 2) residual trapping of the free-phase CO_2, 3) solubility trapping where the CO_2 dissolves into aquifer fluids, and 4) mineralization of carbonate minerals through CO_2-fluid-rock interactions (Pollyea et al., 2014; Matter and Kelemen, 2009). Secondary storage mechanisms include gravitational trapping and CO_2 hydrate formation, which occurs when the physical properties of the CO_2 change due to changing temperature and pressure (Marieni et al., 2013; House et al., 2006). These can ensure additional storage security for CO_2. Each storage mechanism comes into effect during different periods of the sequestration process and contributes to a certain percentage of overall CO_2 storage security (Figure 1.6). Each mechanism is described in detail below in the context of CO_2 injection into a deep-sea basaltic aquifer.

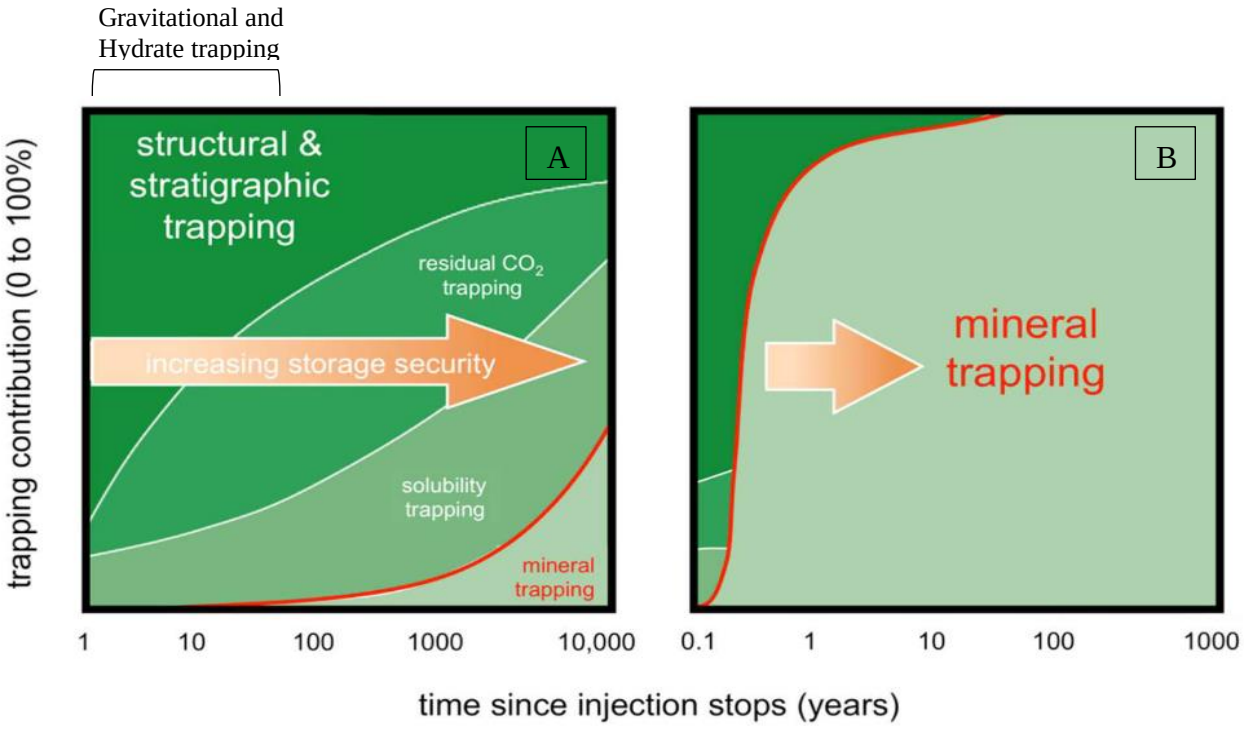

Figure 1.6: *Geologic storage mechanisms for CO_2 and percent contribution to CO_2 trapping on various time scales.* ***A)*** *In sedimentary formations; physical trapping contributes to a large percentage of*

trapping less than 100 years after injection, while solubility and geochemical trapping have a larger contribution to trapping after 100 years. There is uncertainty around time scales for gravitational and hydrate trapping. ***B)*** *In mafic and ultramafic formations including deep-sea basaltic aquifers; These formations can react much faster (within a few years) with CO_2 to form carbonate minerals. Source: Kelemen et al. (2019); Snæbjörnsdóttir et al. (2017); NASEM (2019), originally modified from Benson et al. (2005).*

Physical trapping involves an impermeable caprock (i.e., less permeable zone above a higher permeable zone) which stratigraphically seals and prevents vertical migration of CO_2 out of the intended storage reservoir (Figure 1.7a) (Zhao et al., 2014). For the basalt in Cascadia Basin, the impermeable cap consists of very low permeability sediments which lies above a more permeable basaltic crustal aquifer. This physical trapping mechanism can also represent very slow CO_2 migration over long distances in open systems, known as hydrodynamic trapping (Schaffer et al., 2013). The injected CO_2 will initially be in a buoyant, supercritical phase, or a phase where the CO_2 gas cannot be liquified regardless of more pressure applied (White et al., 2003), so it is essential the sediments are thick enough to act as a physical barrier to keep the CO_2 in place for enough time to allow for CO_2-fluid-rock reactions to take place. Oil and gas fields have naturally trapped hydrocarbon fluids that are buoyant for millions of years with the help of caprocks that are impermeable (i.e., clays or shales) (Holland and Gilfillan, 2013).

Basaltic crust is highly porous (10-15%) (Davis and Becker, 1998) so once injected, the supercritical CO_2 will enter the pore spaces and displace the fluids already present in the aquifer. As reservoir fluids permeate back into the pore space in accordance with the CO_2 plume, small droplets of supercritical phase CO_2 will be trapped by capillary forces (Holland and Gilfillan, 2013) and left behind as residual (Zhao et al., 2014) (Figure 1.7b). The supercritical phase CO_2 droplets are disconnected from the plume and surrounded by the formation fluids (Krevor et al., 2015). This is known as residual or capillary trapping and is controlled by interfacial fluid dynamics at the pore scale (Schaffer et al., 2013).

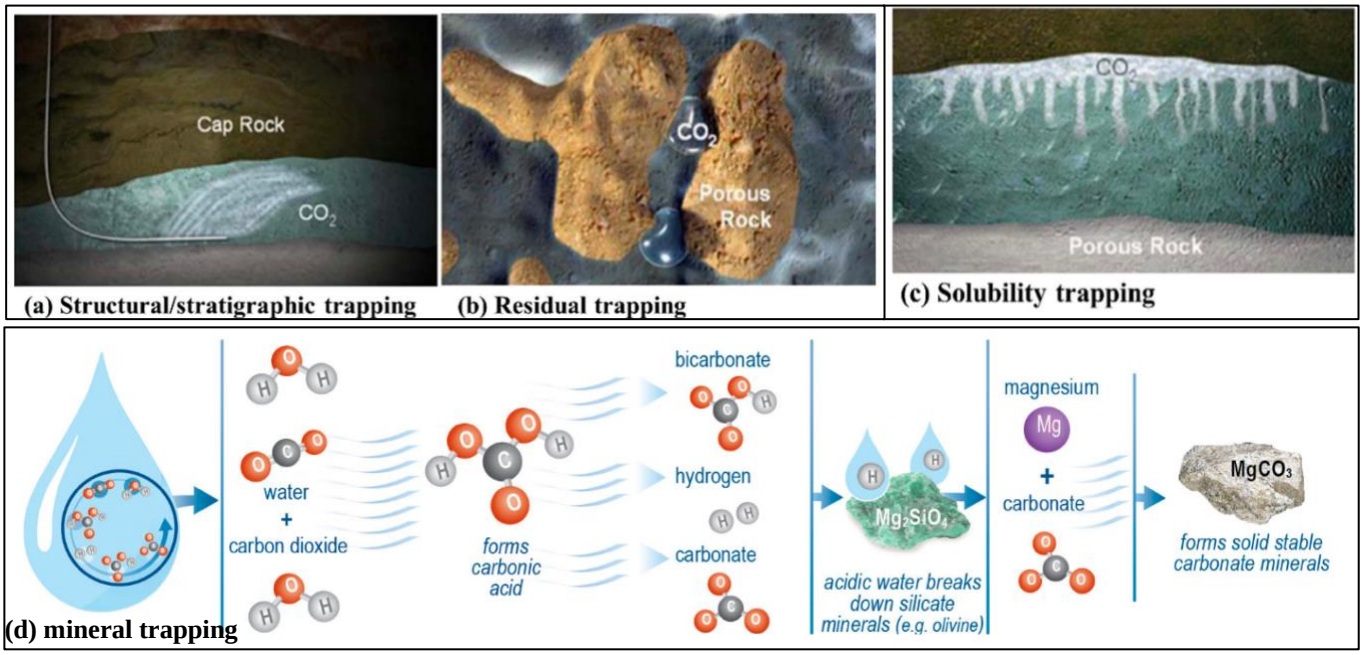

Figure 1.7: *Graphical depictions of storage mechanisms for CO_2. (a) physical/structural trapping of CO_2 with an impermeable caprock or overlying geologic layer that is less permeable and keeps the injected CO_2 in the aquifer; (b) residual trapping of the supercritical CO_2 phase in the pore spaces of the basalt through capillary forces; (c) solubility trapping through CO_2 dissolution into formation fluids. The supercritical CO_2 plume is expected to rise to the top of the aquifer before dissolving into formation fluids. (d) geochemical trapping at the molecular scale after dissolution of CO_2 into formation fluids. Carbonate minerals can form magnesium carbonate, calcite, dolomite, and ankerite, dependent on primary mineral availability. Sources: (a), (b), (c) from Zhao et al. (2014); (d) from Sandalow et al. (2021).*

CO_2 is soluble in water so the injected CO_2 will eventually dissolve into the formation fluids in the pore spaces of the basalt (Holland and Gilfillan, 2013) This is known as solubility trapping since the CO_2 is no longer a buoyant separate phase (Figure 1.7c) (Gislason et al., 2014; Matter and Kelemen, 2009). CO_2 dissolves into water and forms carbonic acid (H_2CO_3) which dissociates into bicarbonate (HCO_3^-) and carbonate (CO_3^{2-}) ions through (Matter et al., 2011):

$$CO_{2(aq)} + H_2O = H_2CO_{3(l)} = HCO_3^- + H^+ = CO_3^{2-} + 2H^+ \quad \text{Eq (1)}$$

The release of the H+ ions in Equation 1 causes the pH of the water to decrease which causes dissolution of the primary silicate minerals found in basalt such as olivine, plagioclase, and pyroxenes (Giacomel et al., 2018; Earle, 2019):

$$(Ca, Mg, Fe)_2SiO_{3(s)} + 2H^+ = 2(Ca, Mg, Fe)^{2+} + SiO_{2\,(aq)} + H_2O_{(l)} \quad \text{Eq (2)}$$

Divalent cations (Ca^{2+}, Mg^{2+}, Fe^{2+}) are released into solution from dissolution of primary silicate minerals (Equation 2). The divalent cations react with the dissolved CO_2 to precipitate stable carbonate minerals such as calcite ($CaCO_3$), ankerite ($CaMg(CO_3)^2$), or dolomite (Ca(Fe, Mg, Mn)$(CO_3)^2$) (Tutolo et al., 2021; Matter et al., 2011):

$$(Ca, Mg, Fe)^{2+} + CO_{2(aq)} + H_2O_{(l)} = (Fe, Ca, Mg)CO_{3(s)} + 2H^+ \quad \text{Eq (3)}$$

The H^+ ions released from the reaction given in Equation 3 are consumed by further dissolution reactions of other primary minerals (forsterite, Ca-plagioclase), which provide additional cations to promote more precipitation (Giacomel et al., 2018; Matter et al., 2011). This process is known as mineral trapping, or chemically binding CO_2 to form stable carbonate minerals and is the most secure form of carbon storage.

Figure 1.7 graphically portrays the geochemical trapping mechanism sequence. This process mimics the carbonate-silicate geochemical cycle that controls the evolution of Earth's climate over geologic timescales where atmospheric CO_2 levels are regulated through weathering of silicate rocks followed by deposition of carbonate minerals in sedimentary rocks (Urey, 1956; Walker et al., 1981). Weathering of silicate rocks releases divalent cations (Ca^{2+}, Mg^{2+}) which react with carbonate ions (CO_3^{2-}) to precipitate as carbonate minerals deposited on the ocean floor (Walker et al., 1981). This process is known to draw down 0.5 billion tons of atmospheric CO_2 per year (Liu et al., 2011), although there are uncertainties around this number due to the sensitivity of weathering rates to changes in climate and the partial pressure of CO_2 in the atmosphere (Penman et al., 2020). Human-induced carbon storage in basalt is accelerating this process to draw more atmospheric CO_2 down on shorter timescales to meet climate targets (Sandalow et al., 2021).

The rate and extent of carbonate mineral formation under human-induced conditions depends on the composition of the injected CO_2, *in-situ* temperature, the surface area of the basalt, chemical composition and mineralogy, and the rate of release of ions from of the primary minerals (Raza et al., 2022; Marieni et al., 2013). The rate of reaction between the dissolved CO_2 and basalts depends on pH, temperature, availability of cations, and partial pressure of CO_2 affecting the rate of carbonate mineral formation (Basava-Reddi, 2011; Sandalow et al., 2021). Basalt dissolution rates increase with increasing temperature so the basalt donates divalent cations to solution faster than it would at lower temperatures (25°C) (Gysi and Stefansson, 2012; Van Pham et al., 2012). If the structural trapping mechanism is in place, CO_2-fluid-rock geochemical reactions will continue, affecting the overall porosity and permeability of the reservoir (Goldberg and Slagle, 2009).

Gravitational trapping of CO_2 may occur in deep ocean environments with high pressures (>25 MPa) and low temperatures (0-30°C) with injection of liquid CO_2 (Marieni et al., 2013; Goldberg and Slagle, 2009). This is because liquid CO_2 is denser than seawater under these conditions and therefore can be trapped gravitationally (Levine et al., 2009). Marieni et al. (2013) assessed suitable deep-sea environments where gravitational trapping in sediments would occur and found the Juan de Fuca region to be unsuitable for gravitational trapping because the sediment cover above the basaltic basement results in high temperatures (>30°C) in the sediments making the CO_2 less dense than the seawater. The high pressure and low temperature

requirement for gravitational trapping is more easily met in locations where older basaltic crust and thinner sediments exist (Marieni et al., 2013).

If the CO_2 leaks into the pore fluids of the sediments where cooler temperatures exist, CO_2 hydrate formation may occur (Goldberg and Slagle, 2009). A CO_2 hydrate is a crystalline lattice of water that surrounds a bubble of liquid CO_2 and is highly stable in deep-ocean sediments where pressure is high enough and the temperature low enough as is the case in the Cascadia Basin (Goldberg and Slagle, 2009; Goldberg et al., 2008). For the Cascadia Basin site (~2,700 m water depth and 2ºC at the seafloor), there is a short interval (the top 50 m) below the seafloor where hydrate formation could occur and is dependent on sediment thickness which is variable across existing borehole sites; the thicker the sediment, the smaller the temperature gradient and therefore the thicker the hydrate stability zone (House et al., 2006).

1.1.2.4 Pilot Projects

Consideration of utilizing deep ocean basalt for accelerated CO_2 disposal was originally introduced in the early 1990's (Seifritz, 1990; Lackner et al., 1995). Between the 1990's and present, there has been focus on CO_2 sequestration in depleted oil and gas reservoirs (Gyore et al. 2015, 2017; Wildgust et al., 2013; Underschultz et al., 2011; Vandeweijer et al., 2011) and sedimentary formations (Rock et al., 2017; Johnson et al., 2009; Arts et al., 2008; Kharaka et al., 2006).

The basaltic lava flows in southwest Iceland (Snæbjörnsdóttir et al., 2016, 2020), the Columbia River flood basalts in Washington, USA (McGrail et al., 2011, 2014), coastal marine basalts in Hawaii (De Paolo et al., 2021), and the basaltic crust in the Juan de Fuca region (Goldberg et al., 2008, 2018) have been the focus for conceptual studies of using basalt for carbon capture and storage. At the time of this research, only two pilot projects in Iceland and Washington, USA have successfully injected CO_2 into basalt and observed mineralization within a few years (McGrail et al., 2017b; Matter et al., 2016). The following sections describe those two pilot projects and their methodology for monitoring CO_2 sequestration.

1.1.2.4.1 The CarbFix Pilot Project

Introduction

The CarbFix pilot project was a highly successful carbon storage project that has laid a foundation for CO_2 injection and storage in basalt. The project stemmed from re-using CO_2 produced as a by-product of geothermal energy production (Gislason et al., 2010) and re-injecting the produced CO_2 into the basaltic rock as a pilot investigation for CO_2 sequestration by way of *in-situ* carbon mineralization. Located in southwest Iceland, the Hellisheidi geothermal power plant currently produces ~40,000 tons of CO_2 per year (Sigfusson et al., 2018). Pure CO_2 is separated from other gases (primary constituents are H_2S, H_2, and secondary constituents are N_2, CH_4, Ar) produced as a by-product of geothermal energy production (Snæbjörnsdóttir et al., 2020; Aradottir et al., 2011). The CO_2 is then transported 3 km via pipeline from the power plant to the CarbFix CO_2 injection site (Figure 1.8a) (IEAGHG, 2017). Carbfix currently captures 12,000 tons of CO_2/year, about 33% of the current CO_2 emissions from the Hellisheidi power plant (Snæbjörnsdóttir et al., 2020).

The pilot phase of the project consisted of two injection tests during 2012. The results of the injection tests were so successful that CarbFix moved forward with industrial scale operations in 2014, known as CarbFix 2. CarbFix 2 injected twice the amount of CO_2 compared to the pilot phase (23,200 MT CO_2), at deeper injection depths (>700 m), and higher *in-situ* temperatures (>250°C). In 2017, a direct air capture (DAC) unit was added to the site in collaboration with Climeworks, a Swiss direct air capture company (Gislason et al., 2018; Ratouis et al., 2022). Since September 2021, the DAC unit captures ~4,000 tons of CO_2/year. CarbFix is planning to install more DAC units at a new plant called Mammoth to reach ~40,000 tons/year by 2024 (https://www.carbfix.com/the-new-plant-called-mammoth-increases-the-direct, accessed on June 26, 2023). CarbFix 2 observed that over 60% of the injected CO_2 had mineralized within 4-9 months (Clark et al., 2020). Since the pilot project was completed, CarbFix has advanced to a commercial scale operation. Given that this thesis is focused on pilot projects, the industrial scale injections in 2014 and 2017 will not be discussed but more information can be found in Clark et al. (2020).

Site Characterization

The bedrock in this region is 90% basaltic (Saemundsson et al., 2020) and the target injection formation at the depth interval 400-800 m below the surface consists of basaltic lava flows and lies below hyaloclastite formations which separates the injection interval from a shallow near-surface basaltic aquifer at ~200 m below sea level (Figure 1.8b) (Matter et al., 2011). The hyaloclastites have a much lower permeability than the target injection formation (Gislason et al., 2010). Permeability in the injection interval is highest between 400-500 m and greatly decreases below 800 m (Aradottir et al., 2011). A single deep injection well (HN-02; 2,000 m depth) and eight monitoring wells (150-1,300 m depth) were used (Figure 1.8b) (Snæbjörnsdóttir et al., 2017). The pre-injection pH of the closest monitoring well (HN-04) was 9.5-9.6, DIC was 1.3-1.4 mmol/l, and temperature between 400-800 m injection depth ranged between 30-55°C (Gislason et al., 2010).

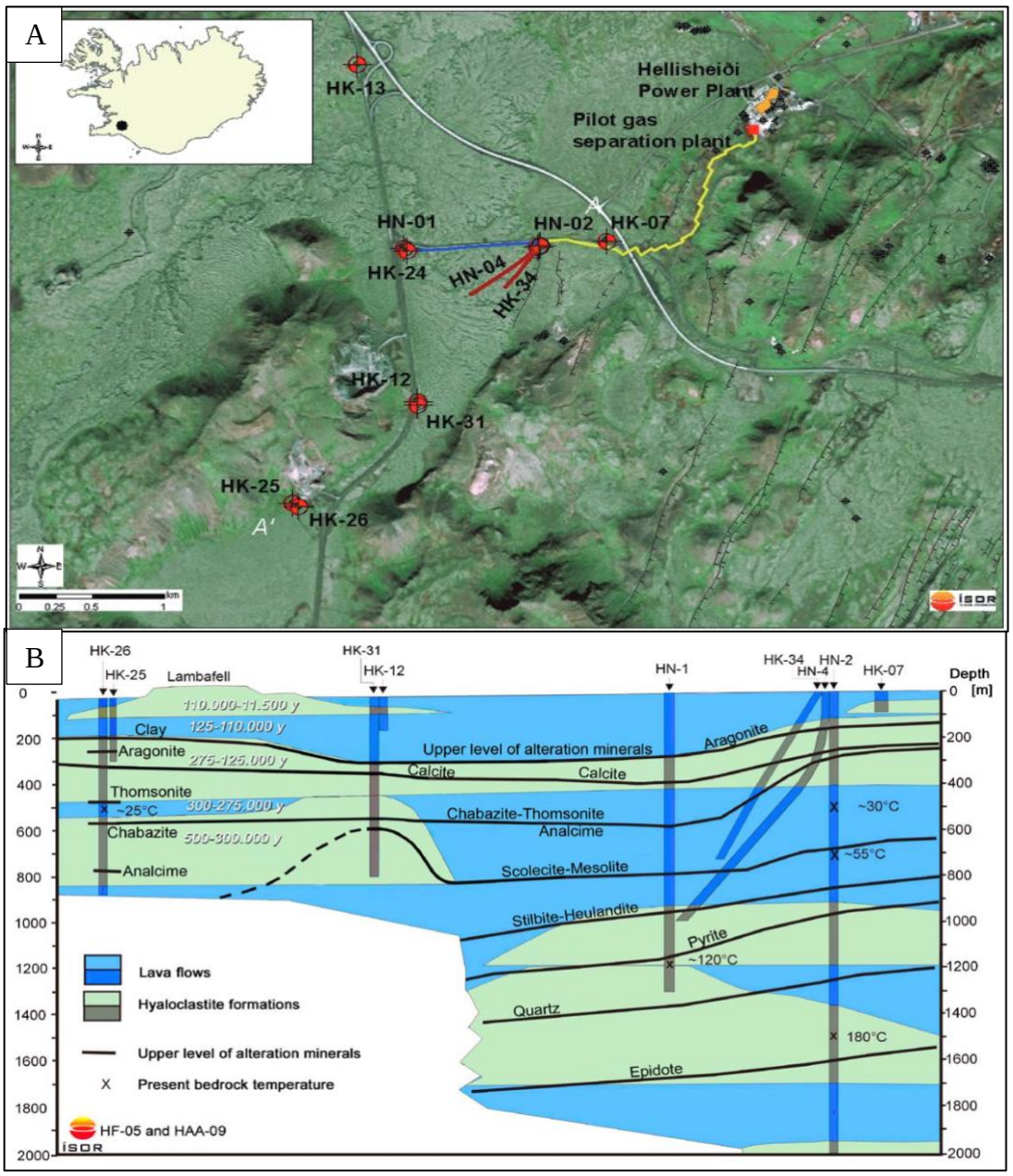

Figure 1.8: *Site location of CarbFix pilot project.* ***A)*** *Aerial map of CarbFix pilot phase CO_2 injection site showing Hellisheidi power plant, CO_2 separation plant, and wells (HN-XX) used for injection and monitoring in southwest Iceland, as depicted from the inset map (top left). Locally sourced groundwater is pumped from well HN-01 and transported via pipeline (blue line) to the injection well (HN-02). The gas mixture produced as a by-product of geothermal energy production is captured at the Hellisheidi power plant and CO_2 and H_2S are separated at the pilot gas separation plant. CO_2 is then transported to the injection well via pipeline (yellow line) where it is injected with the groundwater simultaneously and is fully dissolved at depth. The A-A' transect (white lettering) represents the cross section depicted in B.* ***B)*** *Lithological cross-section of the CarbFix CO_2 injection site with NE-SW orientation. Boreholes are represented as columns. HN-2 is the injection well, extending to 2,000 m depth. The target injection formation for the pilot project is 400-800 m depth, consisting of basaltic lava flows (blue areas) and hyaloclastite formations (light green areas). Temperatures in the injection zone range between 35-50ºC.*

Tracers have been detected in the nearest monitoring well (HN-4), 9 m away from the injection well at the surface with distance increasing with depth due to deviation of the well. Sources: A) Aradottir et al. (2011); B) Gislason et al. (2010).

Pre-injection site characterization was conducted to understand hydrogeology and geology of the reservoir and surrounding formations. Methodologies included monitoring of groundwater chemistry and geophysical measurements in wells (e.g., resistivity, natural gamma, flowmeter) (Matter et al., 2009). In addition, a short duration tracer test was conducted in 2007 (Khalilabad et al., 2008) using a fluorescent dye (Na-Fluorescein) to characterize the hydrology and build reactive transport models prior to initiating CO_2 injection (Aradottir et al., 2012; Gislason et al., 2010; Khalilabad et al., 2008).

The tracer test was conducted between December 2007 and May 2008. Wells HN-02 (injection) and HN-04 (monitoring) were primarily used, with a distance between them of 9 m at the surface and increases to 60 m at 400 m depth (see deviation of well HN-4 with depth in Figure 1.8b) (Khalilabad et al., 2008). The test was conducted using forced-gradient conditions, whereby water is pumped into the injection well (5 kg/s) and water was pumped out of the monitoring well (10 kg/s), to create a flow field between the two wells (Khalilabad, 2008; Matter et al. 2009). 500 g of Na-Fluorescein was diluted with 100 l of water and injected as a tracer solution into the injection well (HN-02) (Khalilabad, 2008). Samples were collected from both wells four times a day for two weeks, then reduced to once per day for 125 days, then once per week for three weeks. Fluid samples were also collected in other nearby wells to monitor any lateral flow (Khalilabad, 2008).

No tracer was detected in any well other than the nearest monitoring well, HN-04. The observed tracer recovery curve (Figure 1.9) shows a small peak immediately after injection, which was interpreted to represent a low volume fracture or channel. A second, much larger, peak is interpreted to be caused by a much larger, more preferential, flow path containing the bulk of the fluid (Khalilabad, 2008). Tracer recovery curves were also simulated using a computer model (Khalilabad, 2008). The model simulated the measured concentrations assuming three different flow channels (Figure 1.9) to create a detailed interpretation of fluid transport in the injection formation prior to CO_2 injection. The interpretation of this tracer test becomes important for interpreting the tracer data in the pilot phases of CO_2 injection.

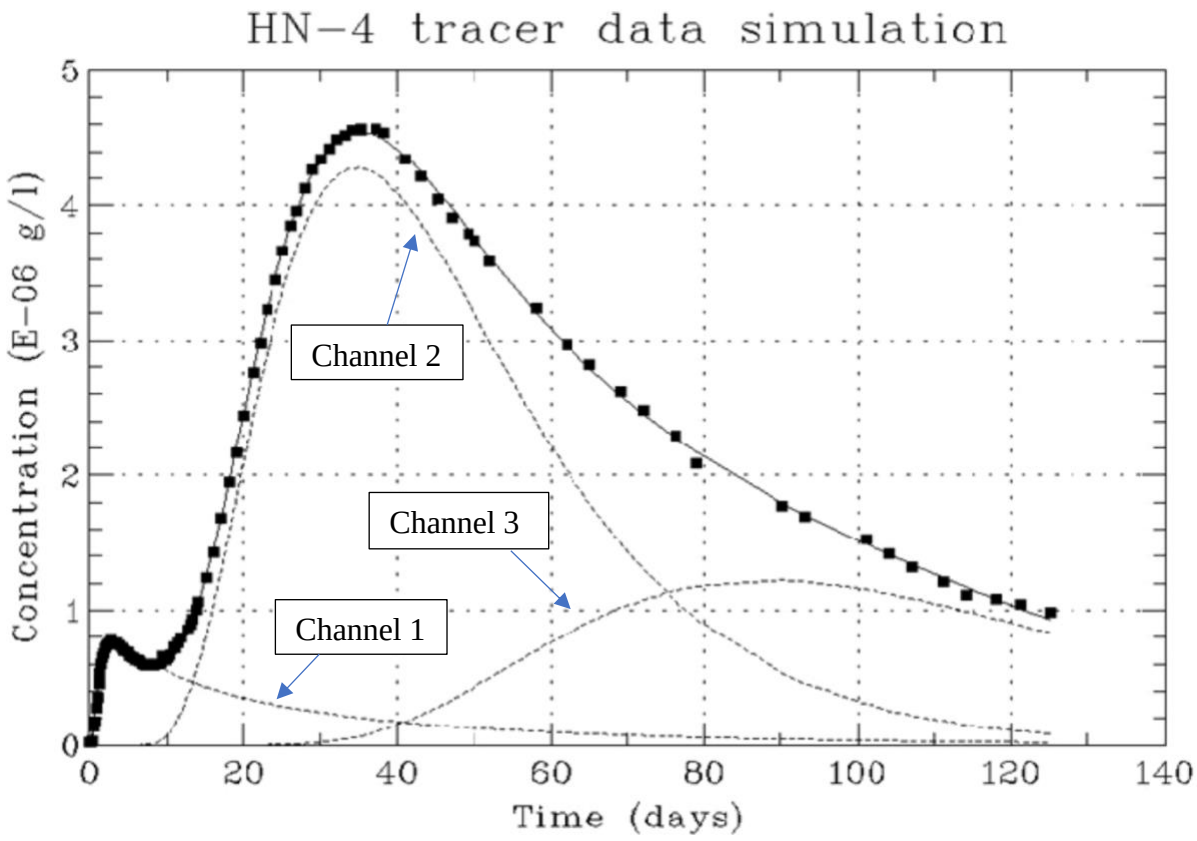

Figure 1.9: *Na-Fluorescein tracer recovery curve from short duration tracer test. Filled squares show measured tracer concentrations (in g/l) from samples taken from well HN-04. Dashed lines represent simulated tracer recovery curves from computer model TRINV, which included inputs such as well logging data, temperature profiles, and lithological stratigraphy. The model simulated the measured concentrations using three flow channels. Each channel's depth was determined based on lithology, well logging data, and temperature profiles. Each channels distance from the injection well was calculated based on known deviation of well HN-04 with depth (Figure 1.8). Each dashed curve represents a channel and its associated contribution to the total measured concentration of tracer. Channel 1 represents an aquifer at 400 m depth and 60 m distance between wells. This channel has fast tracer arrival with the smallest pore volume and was interpreted to be a fracture that provided a small volume of the total tracer concentrations (~3.2%). Channel 2 represents an aquifer at 550 depth and 150 m distance between wells. This channel had the highest tracer mass recovery (~35%) and was interpreted to represent a much larger aquifer such as within a high permeability lava flow. Channel 3 represents an aquifer at 850 m depth and distance of 350 m between wells. It had a much slower response, likely because of the distance and depth between wells delaying transport. Channel 3 was simulated to contribute ~12% of the total measured concentrations. This channel is inferred to be highly porous with higher flow velocity, and despite its depth, it made a considerable contribution to the total measured concentration. Modified from Khalilabad et al. (2008).*

CO_2 Injection and Monitoring

The injection strategy used at CarbFix involved pre-dissolving CO_2 into locally sourced groundwater (HN-1 in Figure 1.8b) during injection, producing a single aqueous phase injection (Snæbjörnsdóttir et al., 2017). This technique allows geochemical reactions in the reservoir to happen quickly since the CO_2 is pre-dissolved. The CO_2-rich water (at 25 bar, ~35°C) is injected to a depth of ~500 m (Figure 1.8b) and reacts with the surrounding basalt (Matter et al., 2011).

Geochemical monitoring methods were relied upon to verify CO_2 movement in the subsurface, as geophysical monitoring techniques cannot be applied for CO_2 pre-dissolved into water (Matter et al., 2011). Chemical tracers were co-dissolved into the injected CO_2-rich water (Matter et al., 2016; Snæbjörnsdóttir et al., 2017). Sulfur hexafluoride (SF_6) gas and Trifluoromethyl sulfur pentafluoride (SF_5CF_3) gas were used as conservative tracers to monitor physical transport processes such as advection and dispersion of the fluid injected (Matter et al., 2011). CarbFix also obtained a license to use up to 20 millicurie (mCi) of radiocarbon (^{14}C) over 12 months (Matter et al., 2011). Radiocarbon was chosen as a reactive tracer to monitor the amount of CO_2 precipitated into carbonate minerals (Matter et al., 2015). The reservoir had an initial ^{14}C concentration of 0.0006 Bq/L (^{14}C:^{12}C ratio of 1.68×10^{-13}) (Matter et al., 2015). Radiocarbon was added to the groundwater injection stream as an aqueous $H^{14}CO_3^-$ solution, which was created by adding 10 mCi of a ^{14}C-tagged sodium bicarbonate solution to 100 L of groundwater from well HN-01 (Matter et al., 2016).

In phase I of the pilot phase, 175 tons of pure CO_2 was injected and tagged with SF_6 and ^{14}C tracers (Table 1.1). In phase II, 73 tons of CO_2-H_2S gas mixture (75 mol% CO_2, 24 mol% H_2S, 1 mol% H_2) was injected and tagged with SF_5CF_3 and ^{14}C. The purpose of injecting the CO_2-H_2S gas mixture was to test the feasibility of injecting a mixture of gas compared to pure CO_2 (Matter et al., 2016). Table 1.1 summarizes each phase of CO_2 injection and the associated added tracers (Snæbjörnsdóttir et al., 2017).

Table 1.1: *Summary of chemical tracers used in Phase I and Phase II CO_2 injections during the pilot phase of CarbFix.*

Phase I: Pure CO_2 Injection		
Tracers Used	**Concentration**	**^{14}C: ^{12}C ratio**
^{14}C	40.0 Bq/L	2.16×10^{-11}
SF_6	2.33×10^{-8} ccSTP/cc	
Phase II: Injection of CO_2 mixture (75% CO_2, 24% H_2S, 1% H_2)		
Tracers Used	**Concentration**	**^{14}C: ^{12}C ratio**
^{14}C	6.0 Bq/L	6.5×10^{-12}
SF_5CF_3	2.24×10^{-8} ccSTP/cc	

Sources: Matter et al. (2016) and Snæbjörnsdóttir et al. (2017).

Fluid samples were collected twice weekly at *in-situ* reservoir conditions using a high-pressure bailer system in the injection well and submersible pumps in the monitoring wells (Snæbjörnsdóttir et al., 2017; Matter et al., 2011). Samples for SF_6 and SF_5CF_3 were collected in 100 ml glass bottles (Matter et al., 2016). Samples for ^{14}C analysis were collected in 125 ml glass bottles (Matter et al., 2016). Fluid samples were also collected to analyze for pH, alkalinity, and total dissolved element concentrations to monitor geochemical changes because of CO_2-fluid-

rock reactions. SF_6 and SF_5CF_3 were analyzed by gas chromatography (Matter et al., 2011, 2016). For ^{14}C analysis, fluid samples were acidified to release the DIC as CO_2 (Matter et al., 2016). The ^{14}C concentration was measured with Accelerator Mass Spectrometry at two separate laboratories (Matter et al., 2016). Results of ^{14}C analysis are reported as fractions of the Modern Standard $\Delta^{14}C$ (Matter et al., 2016). Major elements (Si, Ca, K, Mg, Na, S) were analyzed using an inductively coupled plasma optical emission spectrometry (ICP-OES) with an uncertainty of ± 5% (Snæbjörnsdóttir et al., 2017). Dissolved inorganic carbon was calculated from measured pH, alkalinity, *in-situ* temperature, and total dissolved element concentrations (Snæbjörnsdóttir et al., 2017).

Results

All of the monitoring wells were sampled during the experiment, but injected tracers have only been detected in the closest monitoring well (HN-04) (Snæbjörnsdóttir et al., 2017). Both SF_6 and SF_5CF_3 behaved similarly in the subsurface (Matter et al., 2015). Breakthrough of the CO_2 fluid at well HN-04 was confirmed by an initial peak of SF_6 concentrations at 56 days after injection during phase I (Figure 1.10). The SF_6 decreased slightly before increasing again with a peak concentration at 406 days since injection started. The SF_5CF_3 detected breakthrough of the CO_2+H_2S fluid after 58 days during phase II (200 days after phase I injection started), followed by a temporary decrease in concentration (Figure 1.10). At 350 days, the SF_5CF_3 concentrations started increasing, similar to the SF_6 time series. The double peaks in both SF_6 and SF_5CF_3 are consistent with observations made during the short duration tracer test, where the initial smaller peaks represent the fast-flowing fracture or channel and much of the injected fluid arriving later suggesting a slower pathway (Figure 1.9). This was interpreted as the formation being a homogenous porous media intersected by a low volume flow path that channels ~3% of the total flow between the two wells (Matter et al., 2016).

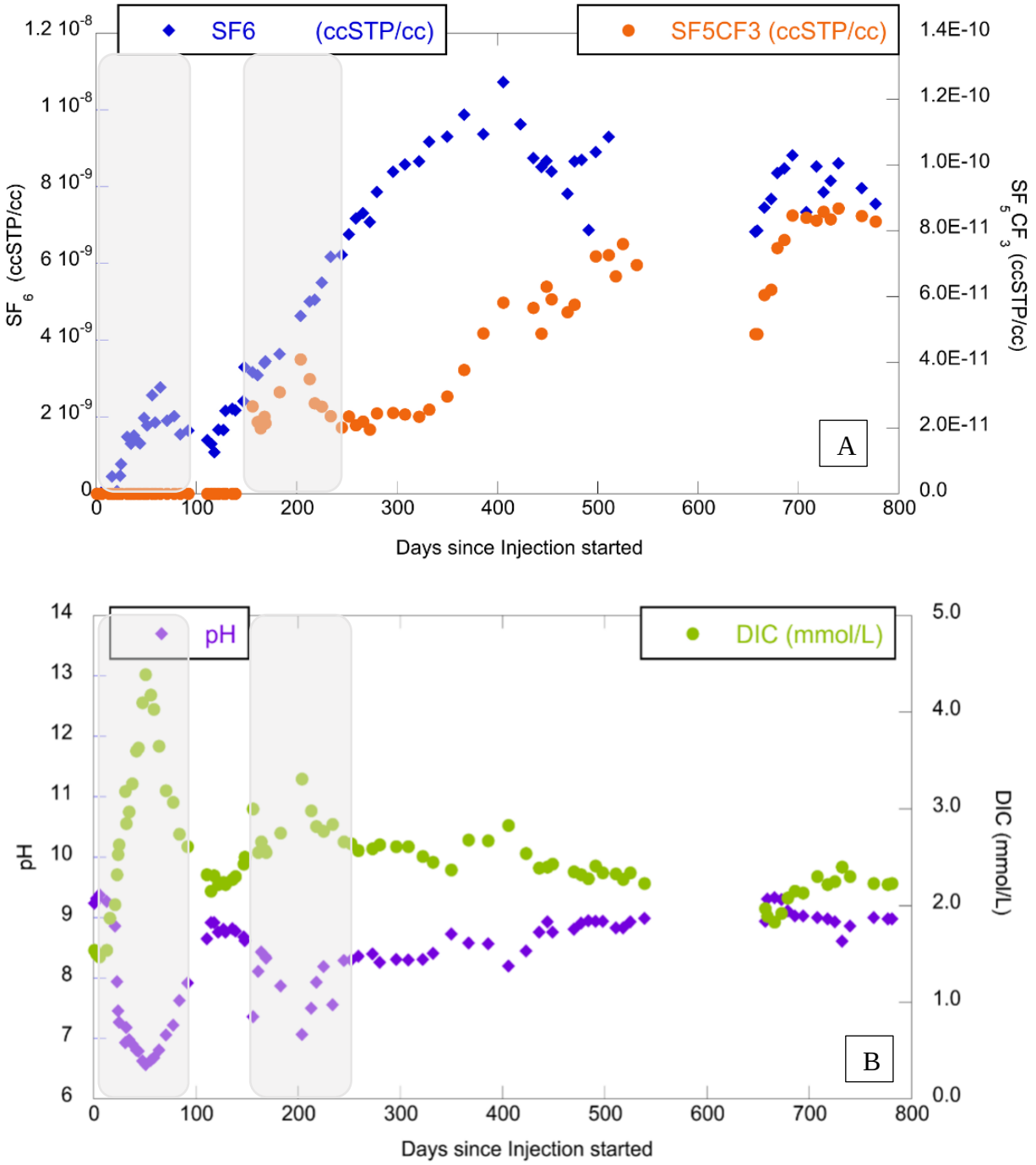

Figure 1.10: *Time series of conservative tracers (A) and DIC and pH (B) during phases I and II of the CarbFix pilot project and collected from monitoring well HN-04. Each phase of injection is shown with a grey column. The gap in data between 550 and 650 days since injection started was due to failure and subsequent replacement of a submersible pump. (A) Time series of conservative tracer SF_6 (injected during phase I), and SF_5CF_3 (injection during phase II). Concentrations are shown per cm^3 at standard temperature and pressure (ccSTP/cc). (B) Time series of pH and total dissolved inorganic carbon (DIC)*

in mmol/l for both phases. Phase II started ~200 days after injection which is represented by a small increase in DIC and decrease in pH around this time. Modified from Matter et al. (2015).

Matter et al. (2015) reported the ^{14}C tracer results in comparison to the SF_6 and SF_5CF_3 tracer results. The timeseries of ^{14}C (Figure 1.11) and DIC concentrations (Figure 1.10) from well HN-04 initially show the same pattern as SF_6/SF_5CF_3 time series (Figure 1.10), with peak concentrations of ^{14}C and DIC at ~56 days (for phase I) and ~200 days (for phase II). Their concentrations decreased after the initial peak and stayed about constant for the remaining sampling period (Matter et al., 2015). During phase I, pH drops to ~6.6 while DIC peaks to 4.4 mmol/L, 50 days after injection started and 10 days before a peak in ^{14}C concentrations. The same pattern occurred in phase II, but pH dropped to 7.1 and DIC peaked to 3.3 mmol/L, concurrent with the initial peak of SF_5CF_3. Concentrations of Ca, Mg, and Fe from fluid samples collected post-injection show an increase during both phases of injection and a slow decline for a few months. The increases in Ca, Mg, and Fe concentrations peaked ~56 days, the same time as both conservative tracers (Snæbjörnsdóttir et al., 2017).

The similarity between the concentration data for both conservative and reactive tracers suggest very similar transport of carbon and tracers in the reservoir (Matter et al., 2016). Although, ^{14}C and DIC concentrations continue to decline even when a large portion of the conservative tracers arrived at ~400 days, which suggests some of the injected CO_2 was mineralized (Snæbjörnsdóttir et al., 2017; Matter et al., 2015).

Based on mass-balance calculations conducted by Matter et al. (2016), differences between the calculated and measured values for DIC and ^{14}C confirm that more than 95% of the injected carbon precipitated into carbonate minerals in the pore spaces of the basalt between the injection and monitoring wells within the two-year monitoring period (Figure 1.11) (Snæbjörnsdóttir et al., 2017; Matter et al., 2016). In addition, the H_2S injected during phase II was mineralized to pyrite (Clark et al., 2020). The rapid mineralization time is likely due to the CO_2 being pre-dissolved into water before injection and the dissolution rate of the basalt (Matter et al., 2016). The submersible pump that failed during the monitoring period was recovered with precipitates consisting of >94% calcium, and <3% iron, <2% silica, and <1% magnesium (Snæbjörnsdóttir et al., 2017). The dominant mineral phase was determined as calcite by x-ray diffraction (XRD) analysis, and no other crystalline phases were identified (Snæbjörnsdóttir et al., 2017). Carbon-14 analysis of the carbon in the calcite precipitates confirms that it formed from the injected ^{14}C-labeled CO_2 (Matter et al., 2016). The ^{14}C concentration of the injected CO_2 was 7.48 ± 0.8 fraction modern and the ^{14}C concentration in the precipitated calcite was 7.82 ± 0.05 fraction modern. Average ^{14}C concentration of the DIC in the monitoring borehole during injection phases was 7.93 ± 0.05 fraction modern (Matter et al., 2015, 2016). The similarity between the ^{14}C of the injected CO_2 and the ^{14}C in the precipitated calcite suggests the precipitated calcite formed from the injected ^{14}C-labelled CO_2 (Matter et al., 2016). The loss in DIC and ^{14}C is consistent with carbonate precipitation, while dissolution would increase DIC values and decrease ^{14}C in the remaining fluid (Figure 1.11) (Matter et al., 2015).

The results of this experiment demonstrate the ability for tracers to accurately monitor CO_2 injected into a basaltic aquifer and show evidence of the tracers used (SF_6 and SF_5CF_3) behaving

similarly during transport at the *in-situ* conditions of the site. It also demonstrates how the various monitoring parameters complement one another in the interpretation of the data.

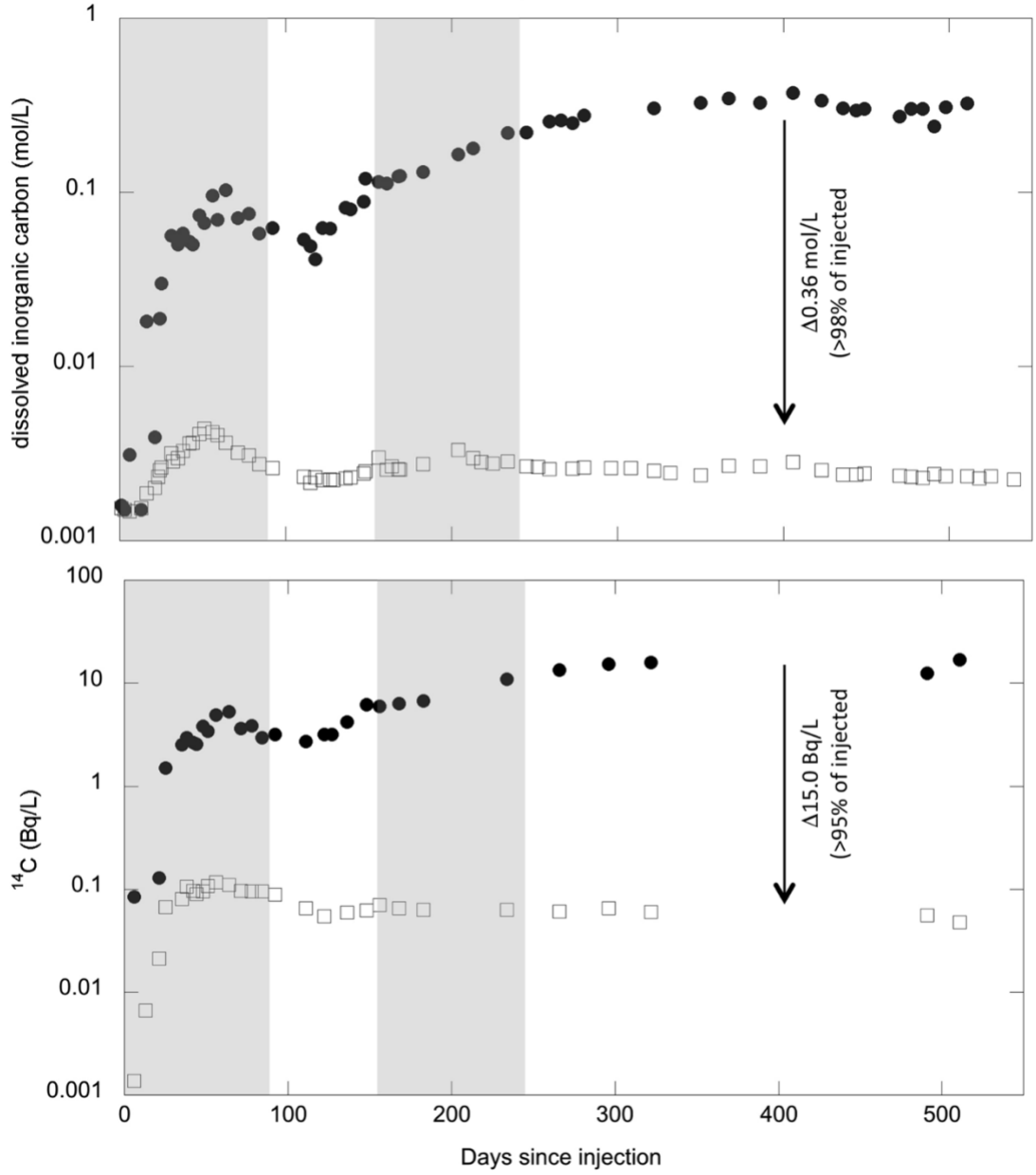

***Figure 1.11**: Expected versus measured DIC and ^{14}C concentrations from fluids collected in the target depth interval from monitoring well HN-04. Expected concentrations are shown as solid circles, and measured concentrations are shown as open squares. Shaded areas represent phase I and II injection periods. (A) Time series of DIC (mol/l) showing >98% of the injected CO_2 was converted to carbonate minerals. (B) Time series of ^{14}C (Bq/l) showing >95% of the injected ^{14}C-labeled CO_2 precipitated into carbonate minerals. The DIC of the injected fluid during phase I was 0.82 mol/l and was 0.43 mol/l for phase II. ^{14}C concentration of the injected fluid for phase I was 40.0 Bq/l, and 6.0 Bq/l for phase II. Source: Matter et al. (2016).*

1.1.2.4.2 The Wallula Basalt Pilot Project

Introduction

The U.S. Department of Energy's Big Sky Carbon Sequestration Partnership conducted a field pilot study for CO_2 storage in continental flood basalts near the town of Wallula in southeastern Washington, USA. The Columbia River flood basalts, known as the Columbia River Basalt Group (CRBG), are continental-based large igneous provinces that formed when basaltic lava erupted onto the continental crust (Reidel et al., 2013). The CRBG formed from eruptions between 16.7 Ma and 5.5 Ma (Barry et al., 2013) forming a basin that covers large portions of Washington, Oregon, and Idaho with a thickness of >4 km at the center of the basin (Reidel et al., 1989). CO_2 was injected into the Grande Ronde Basalt formation (Figure 1.12) (Reidel et al., 2013). The Columbia River basin contains more than 200,000 km^3 of flood basalt (Reidel et al., 2002) and its estimated storage capacity is greater than 100 Gigatons CO_2 (McGrail et al., 2006; Gislason et al., 2010).

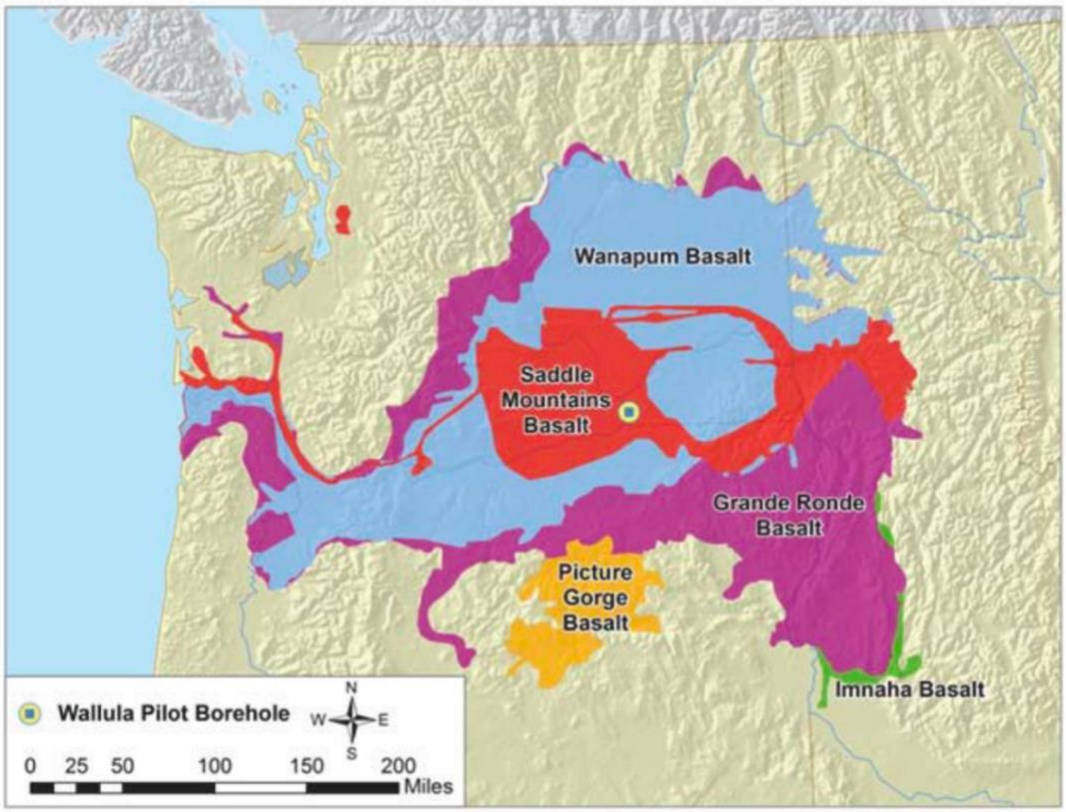

***Figure 1.12**: Map showing extent of the Columbia River Basalt Group (CRBG) through eastern Washington, northeastern Oregon, and western Idaho. The CRBG is divided into six formations and has an estimated storage capacity of >100 $GtCO_2$ (McGrail et al., 2006). Carbon dioxide in a supercritical phase was injected into the Grande Ronde Basalt, which lies beneath both Saddle Mountains Basalt and Wanapum Basalt flows (Reidel et al., 2013). The Wallula pilot well location is shown with a green square inside of a circle in southeastern Washington. Source: McGrail et al. (2014).*

Site Characterization

After site selection was completed, extensive characterization of the site followed prior to initiating CO_2 injection. Prior to this project, there was limited information about the subsurface in the area, and the nearest well was within a six-mile radius with a comparatively shallow depth of 279 m (McGrail et al., 2011). The site was characterized in the following ways:

- soil gas monitoring for surface leakage pathways,
- seismic surveys to characterize the subsurface stratigraphy and detect any faults,
- and borehole drilling to create the injection well in addition to hydrogeologic characterization.

A "drill-and-test" strategy was used which obtains hydrogeologic information simultaneously with drilling and creation of a borehole (McGrail et al., 2011). A target injection zone was identified between 828-887 m, which lies below a massive Umtanum Member of the Grande Ronde Basalt that is characterized as low-permeability (9.87×10^{-19} m^2) basalt-brecciated interflow zones and served as caprocks in their sequestration strategy (Spane et al. 2012; McGrail et al., 2009). The pilot well was drilled to a total depth of 1252.7 m and was cemented back to the target injection zone depth of 887 m (injection zone is between 827 and 887 m) (McGrail et al., 2011). After the injection well was completed, wireline logging, sampling for rock cuttings and sidewall cores, and sampling of groundwater with geochemical analysis were conducted to establish baseline conditions prior to CO_2 injection (McGrail et al., 2011). No major faults were identified in the borehole from geophysical characterization (McGrail et al., 2011). The rock cuttings were examined using x-ray fluorescence (XRF) to determine rock geochemistry of the injection well (McGrail et al., 2011). The mineral structure of the sidewall cores extracted pre-injection were identified with XRD as calcite (McGrail et al., 2017a). Groundwater samples collected pre-injection were analyzed for major ions and trace metals (McGrail et al., 2011). Prior to injection, the *in-situ* temperature was ~36°C and pressure of ~77 bar (McGrail et al., 2017b) which caused the CO_2 to be supercritical at depth. The injection zone had an initial pH of 9.68 and measured porosity and permeability in the target injection zone were estimated to be 15-25% and between 44-90 mD, respectively (McGrail et al., 2011). Simulations of CO_2 injection using the STOMP-H2O-CO2-NaCl model were also performed to model injection of 1000 MT CO_2 over 14 and 30 days (McGrail et al., 2011).

CO_2 Injection and Monitoring

The project was authorized to inject 1000 tons of food grade CO_2 from refineries in the state of Washington and California (IEAGHG, 2017). The CO_2 was provided in four 60-ton skid tanks and re-filled with CO_2 delivered in 20-ton delivery tanker trucks (McGrail et al., 2014). The CO_2 stream was heated to 44°C, 8 degrees greater than the *in-situ* reservoir temperature (McGrail et al., 2014) which introduced a thermal anomaly (McGrail et al., 2017b). For 25 days in July-August 2013, a total of 977 metric tons (MT) of CO_2 was injected into the basaltic formation from the pilot well, at a rate of 40 MT/day (McGrail et al., 2014, 2017a). There was no monitoring well used in this experiment.

Monitoring leakage consisted of injecting a perfluorocarbon (PFC) tracer, perfluorodimethylcyclobutane (PDCB), into the CO_2 stream for the first 48 hours and collecting soil-gas PDCB measurements. There was an accidental spill of the PDCB tracer at the surface

which compromised the viability for using the tracer for detection of leakage at the site (McGrail et al., 2014). The spike from the spill was documented to decrease over time and soil-gas samples portrayed no evidence of CO_2 leakage at the surface (McGrail et al., 2014).

Post-injection monitoring downhole consisted of fluid sampling, logging surveys, and hydrological testing for determination of characteristics and changes in permeability within the reservoir (McGrail et al., 2017b). Well logging confirmed CO_2 presence in the injection zone with no evidence of vertical movement surrounding the borehole casing (McGrail et al., 2014). Fluid samples were collected at *in-situ* conditions using a Kuster downhole fluid sampler at 3-month intervals post-injection (McGrail et al., 2014). The samples were analyzed for stable carbon and oxygen isotope content, tritium, pH, electrical potential (Eh), and electrical conductivity (McGrail et al., 2014).

Results

Isotopic analysis of collected fluid samples and groundwater chemistry data together show evidence of successful mineralization of the supercritical CO_2 within 24 months of injection (McGrail et al., 2017b). Fifty side-wall cores were extracted from the injection zone post-injection. These cores were analyzed using XRD (McGrail et al., 2016) and identified as Ankerite ($Ca[Fe,Mg,Mn](CO_3)_2$), a carbonate mineral and was the sole crystalline component within the nodule (McGrail et al., 2017a). The carbonate nodule was chemically characterized using scanning electron microscopy (SEM) and energy dispersive x-ray spectroscopy (EDXS) (McGrail et al., 2017b). The EDXS analysis identified a Ca-rich phase near the center of the nodule ($Ca_{0.75},Mn_{0.13}$, $Fe_{0.11}(CO_3)_2$) which transitions to an Fe-rich phase near the surface of the ankerite nodule ($Ca_{0.41},Mn_{0.01},Fe_{0.57}(CO_3)_2$) (McGrail et al. 2017b). Trace amounts of Mn was also found present in the nodule. For reference, the calcite vein collected pre-injection showed pure Ca composition with no measurable Fe or Mn (McGrail et al., 2017b).

This project did not inject any tracers or tag the CO_2 prior to or during injection. Instead, the research group analyzed the isotopic composition of carbon and oxygen in i) drill cuttings and sidewall basalt cores recovered pre-injection, ii) injected CO_2, iii) groundwater samples post-injection (McGrail et al., 2014), and iv) three individual nodules recovered post-injection in 2015 (McGrail et al., 2017b). Carbon and oxygen isotopic ratios are reported relative to the Vienna Pee Dee Belemnite standard (McGrail et al., 2017a). Isotopic shifts were observed for all samples confirming that ankerite minerals formed from the injected CO_2 (Figure 1.13). The Ankerite nodules recovered post-injection had an average $\delta^{18}O$ value of -22.47 ± 2.32‰ (1σ; n = 21), the average $\delta^{13}C$ value was -37.72 ± 2.11‰ with an internal precision of 0.7‰ (n = 9) (McGrail et al., 2017b). The $\delta^{18}O$ average value for the pre-injection calcite vein (-21.1 ± 0.58‰) was like the $\delta^{18}O$ average value for the Ankerite nodules, but the $\delta^{13}C$ average for the calcite vein (+15.8 ± 0.99‰) was enriched with $\delta^{13}C$ in comparison (McGrail et al., 2017a). Put simply, the pre-injection drill cuttings and calcite vein are enriched with $\delta^{13}C$, while the post-injection Ankerite nodules, CO_2 source, and post-injection formation waters are all depleted in $\delta^{13}C$ (Figure 1.13).

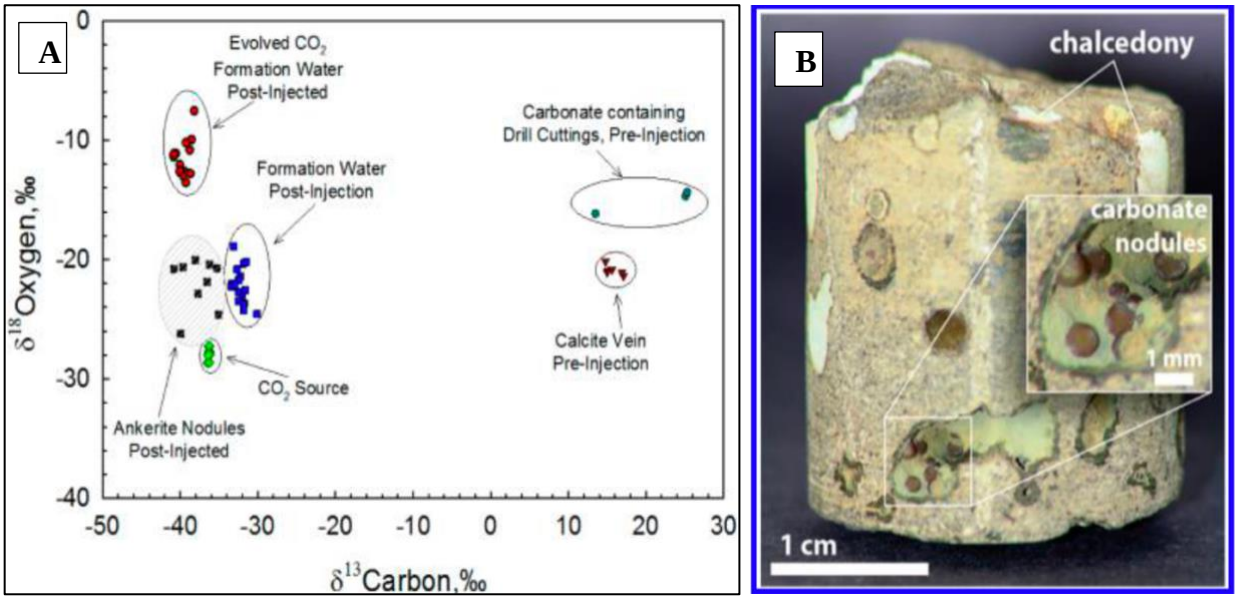

Figure 1.13: *Results from the Wallula Basalt Pilot Project. A) $\delta^{13}C$ and $\delta^{18}O$ ratios for: 1) a pre-CO_2 injection calcite vein from a sidewall core (856.7 m), 2) post-injection carbonate nodules from sidewall core (857.1 m) recovered 24 months after CO_2 injection, 3) pre-injection rock cuttings, 4) post-injection formation water from samples, 5) evolved formation water post-injection, and 6) the CO_2 source. Average $\delta^{13}C$ values for the pre-injection calcite vein are enriched with $\delta^{13}C$, while the post-injection nodules were depleted, like the average $\delta^{13}C$ value for the CO_2 source. B) Image of sidewall core recovered from within the injection zone (856.5 m) of the pilot well 24 months after CO_2 injection showing post-injection ankerite nodules. Source: McGrail et al. (2017b).*

Downhole fluid samples collected post-injection showed alkalinity and concentrations of Ca, Mg, Fe, and Mn were 1.5-3 orders of magnitude higher compared to the pre-injection fluid samples (Figure 1.14) (McGrail et al., 2014, 2017b). Measurements for total dissolved solids were 40 times higher than pre-injection levels (McGrail et al., 2017a). This is consistent with basalt dissolution in contact with the injected CO_2.

White et al. (2020) attempted to quantify the amount of CO_2 that had mineralized by developing a conceptual basalt layer model that was representative of the reservoir properties and applying a numerical model to analyze the pre- and post-injection hydrologic test results to characterize the spatial distribution of the free-phase CO_2 plume. It was concluded that up to 60% of the injected CO_2 was mineralized within two years and took up ~4% of the available pore space in the reservoir (White et al., 2020).

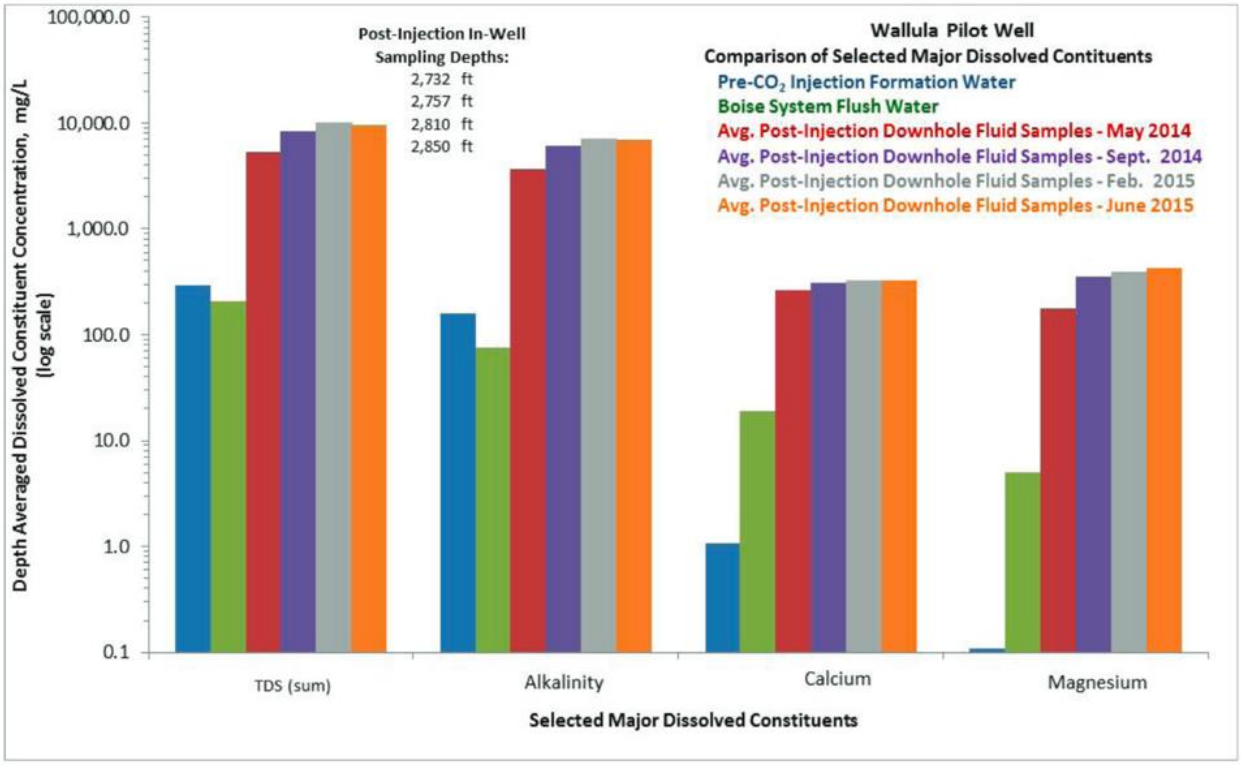

Figure 1.14*: Comparison of total dissolved solids (TDS), alkalinity, calcium, and magnesium concentrations in pre- and post-injection downhole fluid samples collected from the Wallula pilot well. Post-injection samples were collected in 2014 and 2015 and show concentrations ~1.5-3 orders of magnitude greater compared to pre-injection samples. Alkalinity expressed as mg/l of $CaCO_3$. Source: McGrail et al. (2017a).*

1.1.2.4.3 Comparison of Injection Methods

CarbFix and Wallula pilot projects chose very different injection methodologies (Figure 1.15), and the advantages and disadvantages of each warrant a brief discussion. CarbFix chose to inject CO_2 and water as an aqueous solution, letting the CO_2 dissolve into water as it descends into the formation, to avoid logistical challenges of the buoyancy of liquid CO_2 at shallow depths (Sigfusson et al., 2015; Burton and Bryant, 2009). An advantage of this is that it removes the requirement for a caprock seal, removing the risk of CO_2 leaking back to the atmosphere and introduces a solution that can react with the basalt rock immediately after being injected. A single-phase solution eliminates complications related to two-phase flow and saturation fronts when using pure CO_2 (Burton and Bryant, 2009). The downside to this CO_2 injection method is the large amount of water required to dissolve CO_2 gas, which is ~27 tons of water per ton of CO_2 injected at 2.5 MPa and 25°C (Raza et al. 2022; IEAGHG, 2017). Conducting this in an offshore setting would likely be very energy intensive (Raza et al., 2022) and costly (Burton and Bryant, 2009), but there would be no difficulty in finding available water. Additionally, injection of large amounts of fluid into the aquifer can increase pressures in the target formation (Sigfusson et al., 2015). CarbFix used extraction wells to make sure enough water was being pumped out so there were no major pressure changes (Snaebjornsdottir et al., 2020; Burton and

Bryant, 2009), but is something CCS projects should consider. Furthermore, the cost associated with injection of larger fluid volumes is also much higher than injecting pure CO_2 (Burton and Bryant, 2009). Moreover, CO_2 dissolved in water is acidic and corrosive to drilling equipment, in particular carbon steel, which is typically used for transporting CO_2 (Pearce et al., 2022; Gunnarsson et al., 2018). Injecting CO_2 in a pressurized state eliminates the risk of corrosion since it acidifies the fluids after it enters the formation.

There is a potential for mineral precipitates to build up on the equipment in the borehole. This was observed at CarbFix when the submersible pump failed due to the pump being clogged by precipitated carbonate minerals (Snaebjornsdottir et al., 2017). This also happened at Wallula since carbonate mineral precipitate was recovered at the injection site given there was no monitoring conducted away from the injection hole.

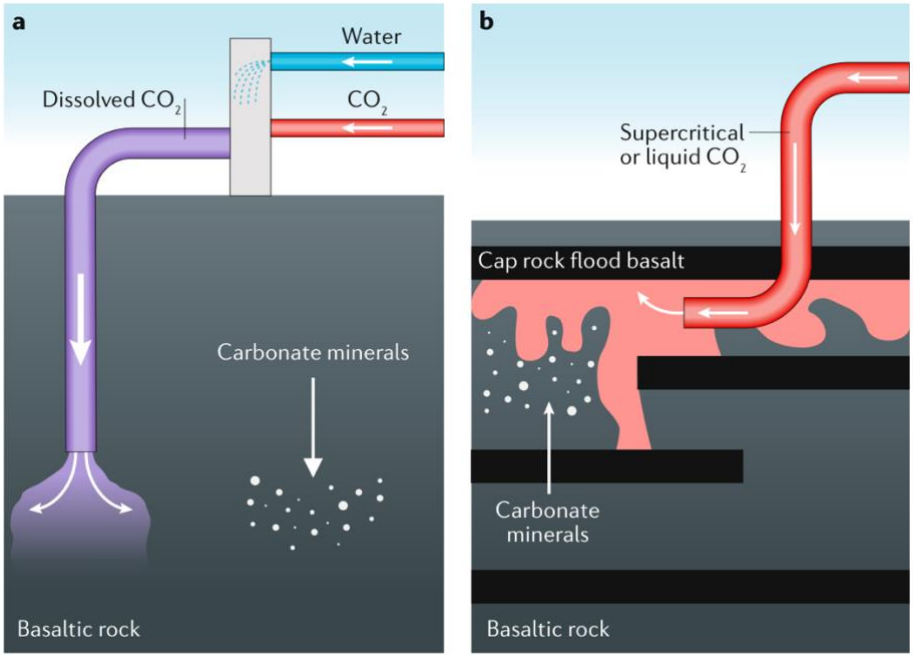

***Figure 1.15**: Visual comparison of injection methods. a) CarbFix method: CO_2 is co-injected with locally sourced groundwater and fully dissolved once in the storage reservoir. b) Conventional method used at the Wallula Basalt pilot project: pressurized CO_2 in a supercritical phase was injected into continental flood basalts and dissolves into formation fluids after entering the storage reservoir. Figure is not to scale. Source: Snaebjornsdottir et al. (2020).*

Postma et al. (2022) created field-scale simulations using a vertically integrated reactive transport model (VIRTra) to compare both injection methods and mineralization rates during large scale CO_2 injections (Figure 1.16). The model combines vertically integrated descriptions of two-phase flow in porous media with a customizable geochemistry solver (Postma et al. 2022). The simulations are concordant with the rates reported from CarbFix and Wallula with

more moderate estimations of mineralization rates (e.g., 100% of the injected CO_2 mineralized in 60 years in the case for pre-dissolving CO_2). Although pre-dissolving CO_2 into water increases rates of mineralization, the rates of injection of CO_2 are stunted (i.e., the amount of CO_2 injected with CarbFix's method is 30 times less than what it would be if supercritical CO_2 was used) (Figure 1.16) (Postma et al., 2022). At larger scales, injecting CO_2 in a supercritical phase is more advantageous regarding rates of injection and likely logistically simpler. It does take more time for supercritical CO_2 to mineralize in the subsurface (i.e., why caprocks seals are essential for this type of injection), but more can be injected at once which is helpful in an offshore scenario where ship time is limited and costly.

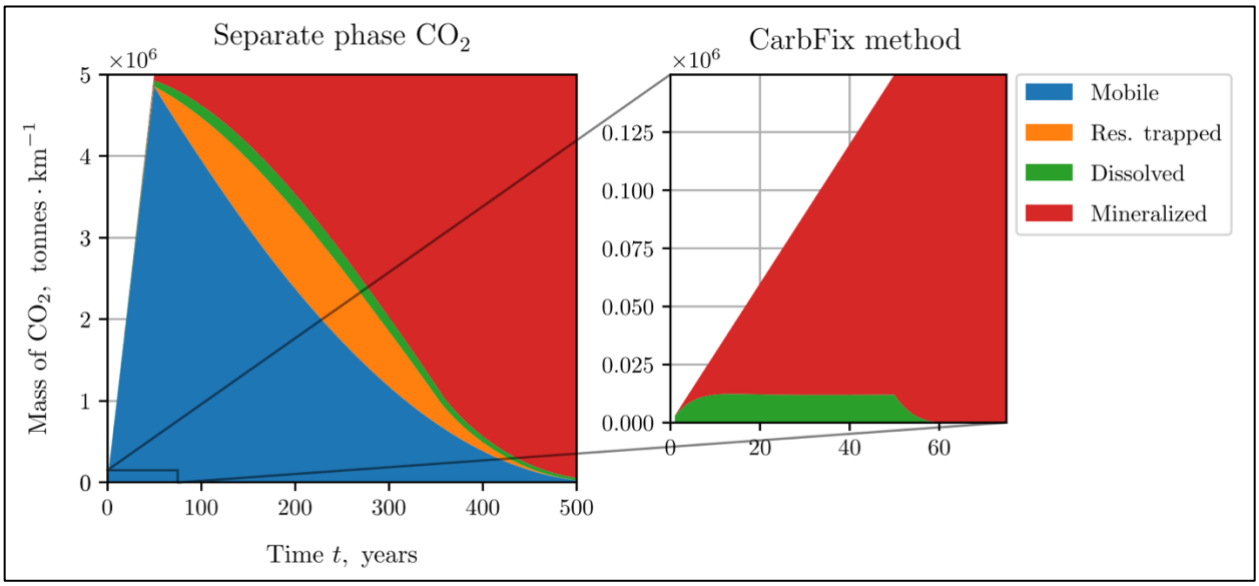

***Figure 1.16**: Plots from reactive transport model (VIRTra) comparing CO_2 distribution in a porous media aquifer system for injection of CO_2 as a separate phase and for injection of CO_2 pre-dissolved in water (CarbFix's method) with the same injection volumes and rates for each plot. The model included a constant aquifer thickness of 30 m and a temperature of 30ºC. Simulations considered varying permeability (10-1000 mD) and initial porosities (0.10, 0.15, 0.20). The CO_2 is shown in tons of CO_2 per kilometer of the model array for injection and distributed across four different states (mobile, residually trapped, dissolved, and mineralized). This shows that injecting CO_2 pre-dissolved into water substantially decreases the total volume of CO_2 that can be injected compared to separate phase CO_2 injection, although the time it takes for mineralization to occur with separate phase CO_2 is much longer (see difference in scale for axes). Source: Postma et al. (2022).*

1.1.3 The Need for Monitoring

Monitoring CO_2 sequestration in offshore deep-sea basalt is not only applicable for basalt along the eastern flank of the Juan de Fuca ridge but also in locations around the world where basalt is accessible (Figure 1.4) and meets the criteria determined by Goldberg and Slagle (2009) (Figure 1.5). Monitoring needs differ between approaches (e.g., aqueous CO_2 injection, supercritical CO_2 injection). For example, an aqueous CO_2 injection removes the requirement for monitoring CO_2 dissolution into the existing aquifer fluids. If the monitoring approach includes a supercritical CO_2 phase, monitoring the state and movement of the supercritical CO_2 plume as it slowly dissolves into the aquifer fluids is necessary. Geochemical tracers can aid in detection of key processes for each monitoring approach such as identification of the injected CO_2 plume for supercritical CO_2 injection, CO_2 dissolution, the extent of mineralization, and the physical transport processes affecting fluid transport in the basaltic crustal aquifer. The Cascadia Basin is one example for how tracer monitoring plans will need to be developed but the pros and cons of various methods will apply more broadly to other locations feasible for CO_2 sequestration offshore deep-sea basalt.

1.1.3.1 CO_2 Phases During Transport

Carbon dioxide pressure is controlled by compressing it to reach a supercritical state. If CO_2 is pressurized to a supercritical state for transport and the pressure is maintained during injection, it is important to know how changes in temperature and/or pressure affect the CO_2 while it is transported to the deep sea. At low pressures and temperatures such as the sea surface (0.1 MPa, 14.85°C), CO_2 exists as a gas. At the seafloor, pressure is higher (~27 MPa) and temperature is lower (1.85°C), so the CO_2 will exist as a dense phase liquid (Figure 1.17). The critical temperature and pressure for pure CO_2 are 31.1°C and 7.38 MPa (Figure 1.17) (Budisa et al., 2014). Above this temperature and pressure, CO_2 exists as a supercritical phase, or a phase where the CO_2 gas cannot be liquified regardless of more pressure applied (White et al., 2003). The pressure (~30 MPa) and temperature (~65°C) conditions in the basaltic aquifer are above the

critical temperature and pressure for CO_2, meaning the CO_2 will exist as a supercritical phase (Figure 1.17).

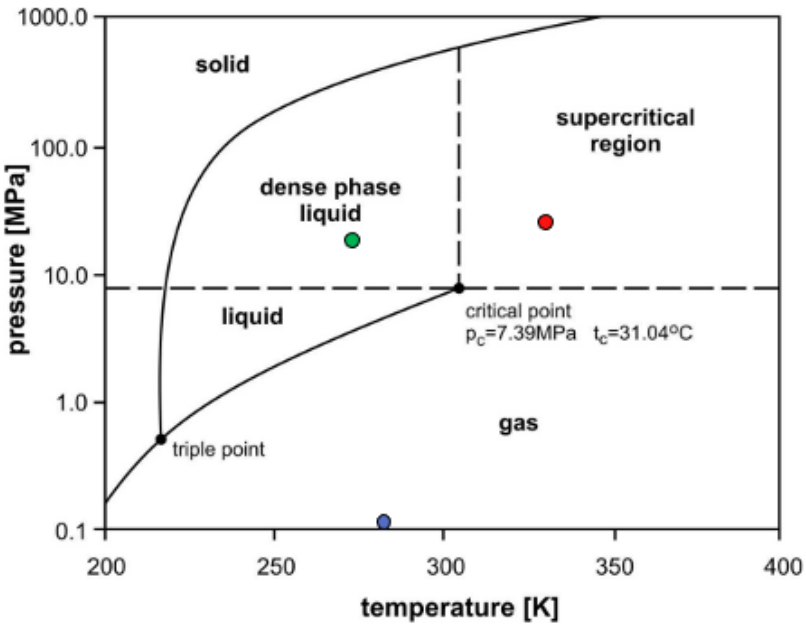

***Figure 1.17**: Pressure-temperature phase diagram of CO_2. Carbon dioxide exists in solid, liquid, and gas phases, and can also exist as a supercritical fluid, which is a state above its critical temperature (t_c; 31.1°C) and critical pressure (p_c; 7.38 MPa). The blue circle represents the pressure and temperature (P-T) conditions for the CO_2 at the sea surface in a gas phase (0.1 MPa; 288 K). The green circle represents the P-T conditions for CO_2 at the seafloor (~27 MPa; 275 K). The red circle represents the P-T conditions for CO_2 in the basaltic crustal aquifer (~30 MPa; 338 K). Modified from Witkowski et al. (2014).*

1.1.3.2 Evolution of Injected CO_2 in the Basaltic Crust

Injection of CO_2 in a supercritical phase into an aqueous environment will lead to multi-phase flow conditions and is more complicated than tracing single phase fluid flow. CO_2 in a supercritical phase will displace the reservoir fluid and initially remain a buoyant separate phase. This is because increases in temperature (i.e., when the CO_2 enters the basaltic aquifer) at a constant pressure will reduce the density of the supercritical CO_2 in relation to the surrounding seawater (Uwineza and Waskiewicz, 2020). The supercritical CO_2 plume is expected to rise to the top of the permeable portion of the crustal aquifer and move laterally in response to pressure gradients (Awolayo et al., 2022; Krevor et al., 2015; Schaef et al., 2011). This advective transport of fluids will occur to both the existing aquifer fluids and CO_2 until the added pressure from injection dissipates.

The CO_2 is expected to remain in a supercritical phase with dissolution and precipitation reactions occurring only at the junction between the CO_2 plume and aquifer fluids (Awolayo et

al., 2022; Schaffer et al., 2013). Dissolution of the CO_2 into an aqueous phase is limited by the reactive surface between the CO_2 and formation fluids (Awolayo et al., 2022). Alternating injection of CO_2 and water (section 4.5.1), known as water-alternating-gas (WAG) injection in the hydrocarbon industry, is an approach that could be used to increase the rates of CO_2 dissolution into the aqueous phase (Goldberg et al., 2018a).

The introduction of CO_2 into the aquifer will affect the local carbonate system, which controls the acidity of the aquifer fluids and determines the reactivity of dissolved inorganic carbon species which make up the carbonate system (Emerson and Hedges, 2008). Dissolved inorganic carbon (DIC) is present in seawater as carbon dioxide, carbonic acid (H_2CO_3), bicarbonate (HCO_3^-), and carbonate (CO_3^{2-}) ions (Park and Weyl, 1964). As CO_2 dissolves into the aquifer fluids, it will increase the acidity of the solution and the partial pressure of CO_2 (pCO_2). The increased acidity increases the reactivity of the basalt leading to dissolution of primary basalt minerals and release of divalent cations, which react with the injected CO_2 (i.e., CO_3^{2-}) to form carbonate minerals. This chain of reactions is highly dependent on changes in pH, with low pH promoting basalt dissolution and high pH for carbonate precipitation (Wu et al., 2021; Holford et al., 2021; Gislason and Oelkers, 2014). This is due to the relationship between pH and the carbonate species that together make up DIC. Once carbonate mineralization starts to take place, permeability and porosity of the basalt will be altered which may impact transport processes through the aquifer (Luhmann et al., 2017). In areas that are dominated by diffusion (e.g., the bulk rock matrix), precipitation of carbonate minerals has been found to also decrease porosity (Andreani et al., 2009).

Storage mechanisms (section 1.1.3.2) play a major role in both keeping the carbon physically trapped and chemically altering the carbon to be permanently sequestered into newly formed carbonate minerals (Schaffer et al., 2013). For example, when the supercritical CO_2 plume migrates away from the injection hole, some of the CO_2 will enter the pore spaces of the basalt and may be left behind as isolated residual CO_2 droplets which will eventually dissolve into formation fluids (Krevor et al., 2015).

Based on numerical model simulations shown in Figure 1.18, a 10,000-ton CO_2 injection over 35 days does not create a significant supercritical CO_2 plume extension away from the injection hole before dissolving into formation fluids. Six months to one year after injection (Figure 1.18b), the CO_2 plume is simulated to fully extend from the bottom to the top of the permeable portion of the aquifer (uppermost 300 m) and throughout that time extends a radius of <50 m from the injection hole. At three years post injection (Figure 1.18c), the bottom of the plume in the simulation has fully dissolved, with supercritical CO_2 remaining only towards the top of the aquifer. After 5 years in the simulation, the supercritical CO_2 plume is expected to have dissolved almost completely into the existing fluids (Figure 1.18d). At larger injection volumes (50 MT), simulations depict the supercritical CO_2 plume extends to a maximum radius of 700 m within the most permeable portion of the aquifer (Awolayo et al., 2022). It is important to note that models cannot inform exactly what will happen in the actual CO_2 injection experiment but can make predictions based on the model assumptions and how well it was parameterized to the conditions at the site.

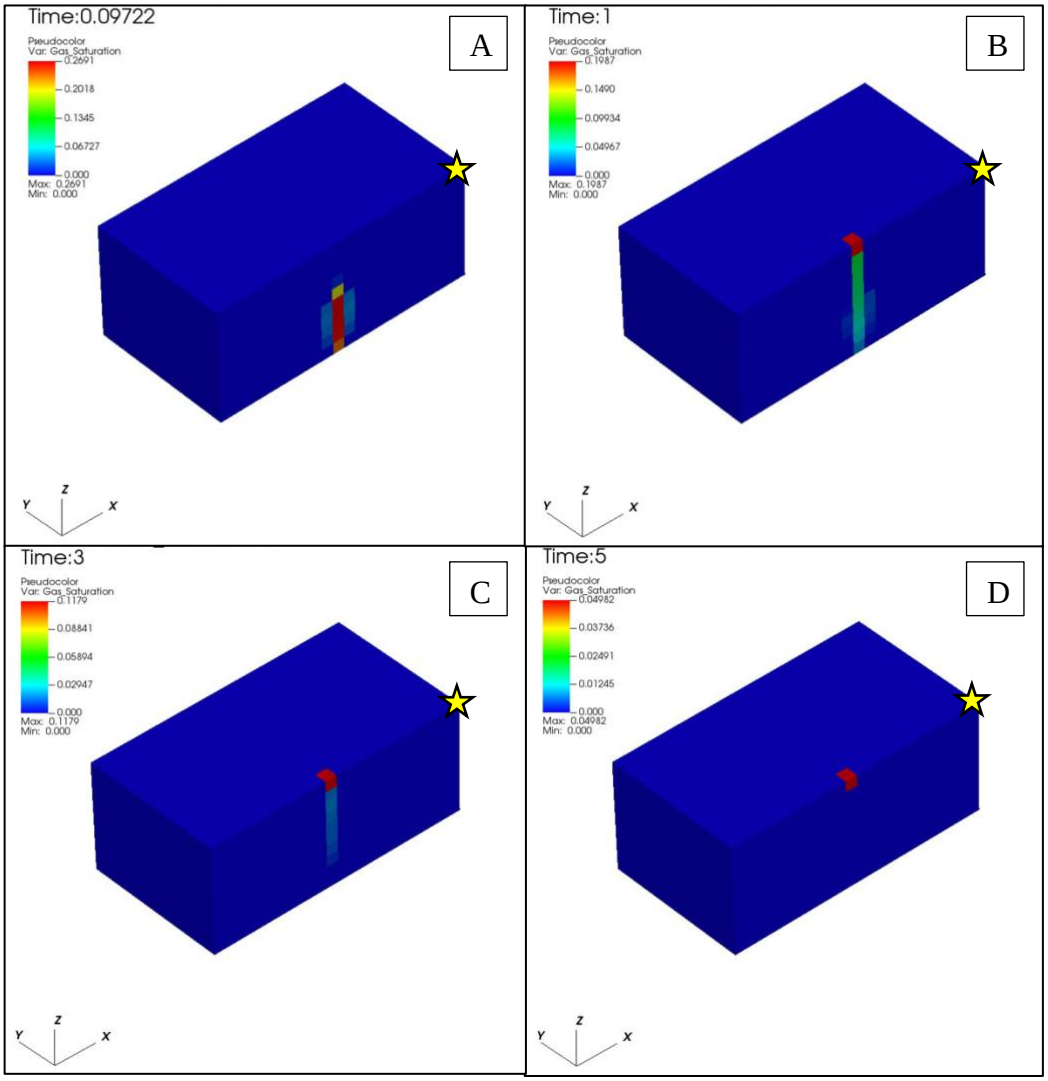

***Figure 1.18**: Reactive transport model estimations of supercritical CO_2 plume extent and gas saturation in the permeable portion of the basaltic aquifer (uppermost 300 m). The model was extracted from the crustal-scale model developed by Winslow and Fisher (2015) in the Cascadia Basin. The area shown here is a zoomed-in version of the large-scale (50 MT) model developed by Awolayo et al. (2022). The injection well is positioned at the center of each aquifer grid, with 300 m distance on each side of the injection hole (600 m length). For the existing monitoring wells, the closest distance between them is ~300 m, which is represented by the yellow star. Simulations have the datum set at the bottom of the injection well with an initial temperature of 67.5°C and depth-dependent hydrostatic pressure of 34.1 MPa. The simulation injected 10,000 tons (at 3.307 kg/s) of CO_2 over ~35 days at 20°C. Time is listed in years. The model does not include mineralization, only CO_2 dissolution into aquifer fluids. **(A)** Plume extent at 0.09722 years (35 days) after injection. Most of the plume remains in the injection hole towards the bottom portion of the aquifer extending a <50 m radius around the injection hole. **(B)** Plume extent 1 year after injection. The plume expands to the top of the permeable portion of the aquifer and does not extend further than 50 m on each side of the injection hole. **(C)** Plume extent 3 years after injection. The bottom of the supercritical plume has started to dissolve, leaving the remaining at the top of the aquifer where there are lower temperatures. **(D)** Plume extent 5 years after injection. Most of the supercritical*

CO2 has dissolved into the aquifer fluids. Based on the modeled results, the supercritical CO_2 plume associated from a 10,000-ton CO_2 injection is not expected to extend more than 50 m on each side of the injection hole before dissolving into the aquifer fluids. Original format is a short video from the time of injection to seven years post-injection. Sourced from Adedapo N. Awolayo.

Chapter Two: Background and Study Area

2.1 Study Area Location

The study area is in the Cascadia Basin at roughly 48°N 127°W, in ~2,700 m of water, along the eastern flank of the Endeavour segment of the Juan de Fuca spreading ridge (Figure 2.1). The Juan de Fuca ridge forms a divergent plate boundary between the Pacific plate, to the west, and the Juan de Fuca plate, to the east. At the spreading ridge, oceanic basement is exposed at the seafloor where the ridge is topographically high. The Endeavour segment of the Juan de Fuca ridge is located ~300 km offshore west of Vancouver Island and creates new oceanic lithosphere at a rate of roughly 6 cm/year full rate (Kelley et al., 2012; Fisher et al., 2005a; Davis et al., 1996). The Cascadia Subduction Zone, where the Juan de Fuca plate subducts under the North American plate, runs along the west coast of North America from Northern Vancouver Island to Northern California (Figure 2.1). During the Pleistocene epoch of the Quaternary period, glacial melt episodes caused high deposition rates of terrigenous sediments (~170 cm/kyr during the Pleistocene epoch versus ~10 cm/kyr during the Holocene epoch) from along the North American continental margin primarily at the Juan de Fuca Strait, Queen Charlotte Sound, and the Grays Harbor and Columbia River estuaries (Underwood and Hoke, 2000; Davis et al., 1996). This heavily sedimented region found between the Juan de Fuca spreading ridge and the Cascadia Subduction Zone is known as the Cascadia Basin.

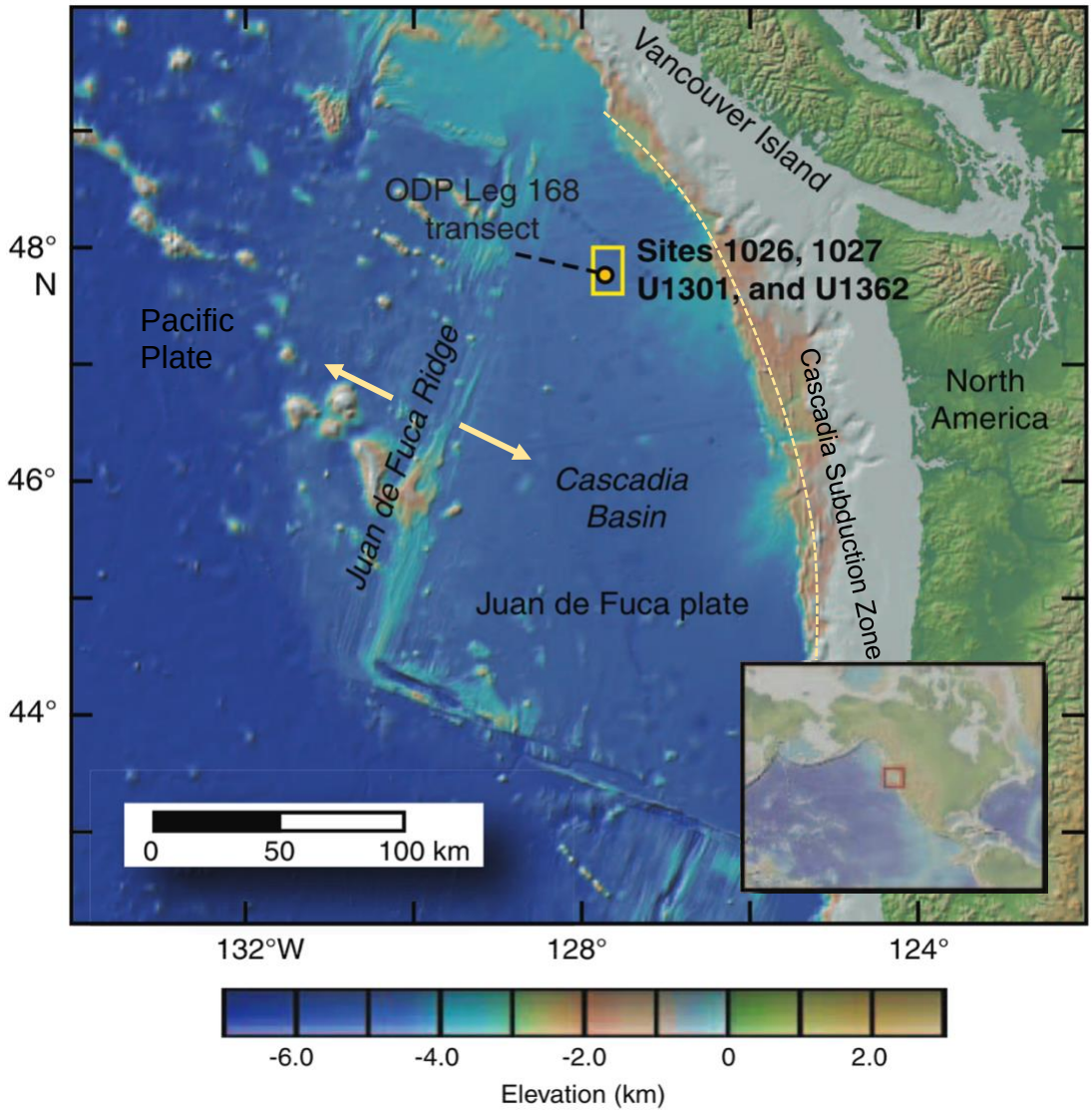

Figure 2.1*: Regional Setting of Cascadia Basin. The Cascadia Basin is the sedimented basin located between the Juan de Fuca spreading ridge and North American Plate. Due to its water depth and flat bathymetry, the basin is characterized as an abyssal plain. The Cascadia Subduction Zone is where accretion of sediment at the continental margin begins due to subduction of the Juan de Fuca plate beneath the North American plate. The Juan de Fuca plate and Pacific plate are diverging at the spreading ridge. The orange dot inside the yellow box is the proposed site for a CO_2 injection demonstration where relevant sites with existing boreholes are located. ODP Leg 168 is a scientific drilling expedition which drilled sites along the dashed line representing the transect, discussed in this section. Modified from Fisher et al. (2011a,e).*

2.1.1 Geologic Setting

The northeast Pacific Ocean geology offshore the coasts of southwestern Canada and northwestern United States is a convergent margin, driven by the tectonic spreading of the Juan

de Fuca ridge. This seafloor spreading pushes the adjacent Juan de Fuca plate eastward, driving it beneath the North American plate. This geologic process has resulted in the formation of a classic subduction zone, named the Cascadia Subduction Zone (Figure 2.2). As the Juan de Fuca plate subducts, the terrigenously derived sediment deposited on top of the plate prior to it subducting gets scraped off and left behind and accreted to the continental slope (Carlson and Nelson, 1987). The deeper layers of the Juan de Fuca plate are fully subducted, while a small fraction of the top portion of the plate is scraped off along with the sediment layers (Davis and Hyndman, 1989). This process forms an accretionary wedge (Figure 2.2), which is a wedge-shaped mass of rock fragments and sediments that have accumulated along the Cascadia Subduction Zone (Guillot et al., 2009).

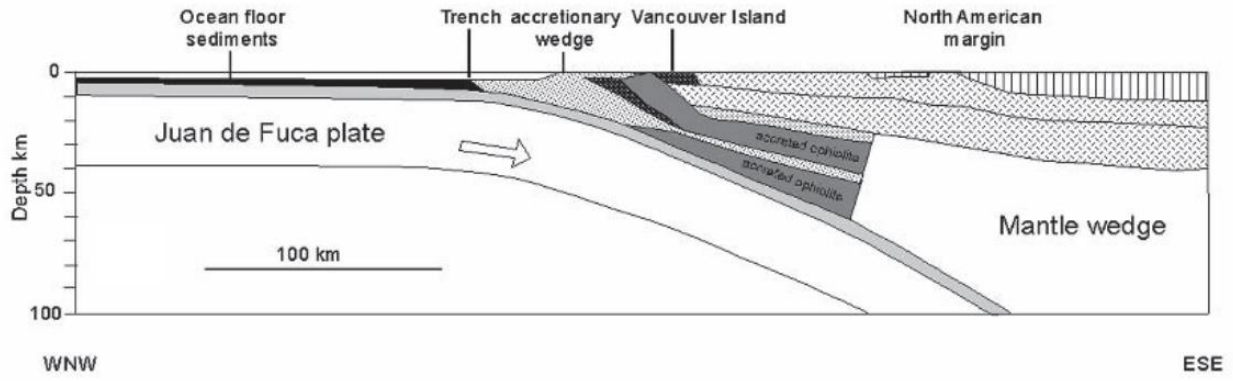

Figure 2.2*: Schematic of cross-section of the Cascadia Subduction Zone showing subduction of the Juan de Fuca plate underneath the North American plate. An accretionary wedge forms at the front of the overlying North American plate. Source: Guillot et al. (2009).*

The basaltic crust along the eastern flank of the Juan de Fuca spreading ridge is dominated by elongated troughs and abyssal hills that are separated by normal faults found parallel to the spreading ridge (Fisher et al. 2011a). In addition to faulting, these features are produced from variations in magma supply from the ridge (Expedition 327 Scientists, 2010). Basement relief along the ridge-flank ranges from 300 to 700 m high and 3 to 7 km separating the ridges towards the east. Closer to the spreading ridge, basement relief ranges from 100 to 200 m (Davis et al. 1992, 1996). The average depth to sediment-basement interface near the proposed area for injection is ~250 meters below the seafloor (mbsf) based on seismic surveys and recovered core data from previous drilling expeditions (Figure 2.3) (Davis et al., 1992). Estimated basement ages range between 0 Ma at Juan de Fuca spreading ridge to 7 Ma at the deformation front of the Cascadia Subduction Zone (Stanislowski et al., 2022; Johnson et al., 2012). The basement age at the proposed site for this experiment is roughly 3.5 Ma (Figure 2.3), based on lithostratigraphy previously determined from drilling experiments (Fisher et al. 2011a).

Based on the recovered core data, the basalt in the region is made up of highly fractured, porous (10-15% porosity), basaltic basement (Davis and Becker, 1998). Pillow lavas and massive basalt flows make up most of the basalt previously recovered (Fisher et al., 2005c). Two sites with boreholes (Integrated Ocean Drilling Program Sites 1301 & 1362) near the proposed site for CO_2

injection had 30% core recovery of basement rock and pillow basalts were the most abundant (Fisher et al., 2005a, 2011a, 2014). Pillow basalts are identified by the presence of chilled margins and radial cooling cracks (Fisher et al., 2011a; Fisher et al. 2005a). Sheet flows and less porous massive basalts were also identified from the recovered cores, with some massive flows >10 m thick (Fisher et al., 2014). Geophysical logs and recovered cores show the presence of high angle fractures and void spaces within the pillow basalts and fractured zones alternated with massive basalt (Goldberg et al., 2008; Fisher et al., 1997, 1998).

Plagioclase (~55%), olivine (~5%), and clinopyroxene (~40%) are the primary minerals found in the recovered pillow basalts, with 5-25% consisting of secondary minerals found in the veins and/or fractures, which are evidence of hydrothermal alteration (Marieni et al., 2020; Fisher et al. 2014 & 2011a). Clay minerals were the most abundant secondary mineral, followed by celadonite, pyrite, and calcite from the recovered cores (Fisher et al. 2011a & 2005a). Additionally, geochemical analysis confirms the basalt at all sites is normal depleted mid-ocean ridge basalt (N-MORB), with evidence that the basalt from each site came from a single magmatic source (Fisher et al., 2011a; Fisher et al., 2005a).

Sediment thickness in the Cascadia Basin ranges from ~2 km at the eastern edge of the Cascadia Basin to between 200-600 m in the basin's flat abyssal plain, apart from seamounts and smaller outcrops, located both north and south of the proposed site for CO_2 injection (Johnson et al. 2012; Fisher et al., 2011a & 2005a). Average rates of sediment deposition in the Cascadia Basin are between 4 and 6 cm/kyr (Davis et al., 1997). Sedimentary units generally consist of fine to coarse-grained sandy and silty turbidites, which overlie larger intervals of silt turbidites and hemipelagic mud (Fisher et al., 2005a). Sedimentary depositional regimes in the region are impacted by variations in basement relief along the Juan de Fuca ridge flank, with observed differences in hemipelagic mud thickness between drilling sites located ~1.07 km apart (i.e., Sites 1026 and 1301) (Fisher et al., 2005a). Bulk density values for the hemipelagic sediment layers increases with depth below the seafloor to 100 mbsf, corresponding with a decrease in porosity of 30% within this interval (Fisher et al., 2005a). These sediments act as a relatively impermeable layer, providing a seal between the sediment-basement interface, which means that basement fluids remain within the crust at an elevated temperature (~62-65°C) (Wheat et al., 2003). The thickness of the sediments in the region and continuity of sediment between seafloor basement outcrops provide necessary trapping mechanisms that have the potential to prevent CO_2 injected into the basaltic basement from migrating upward through the sediments to the seafloor (Goldberg et al., 2008).

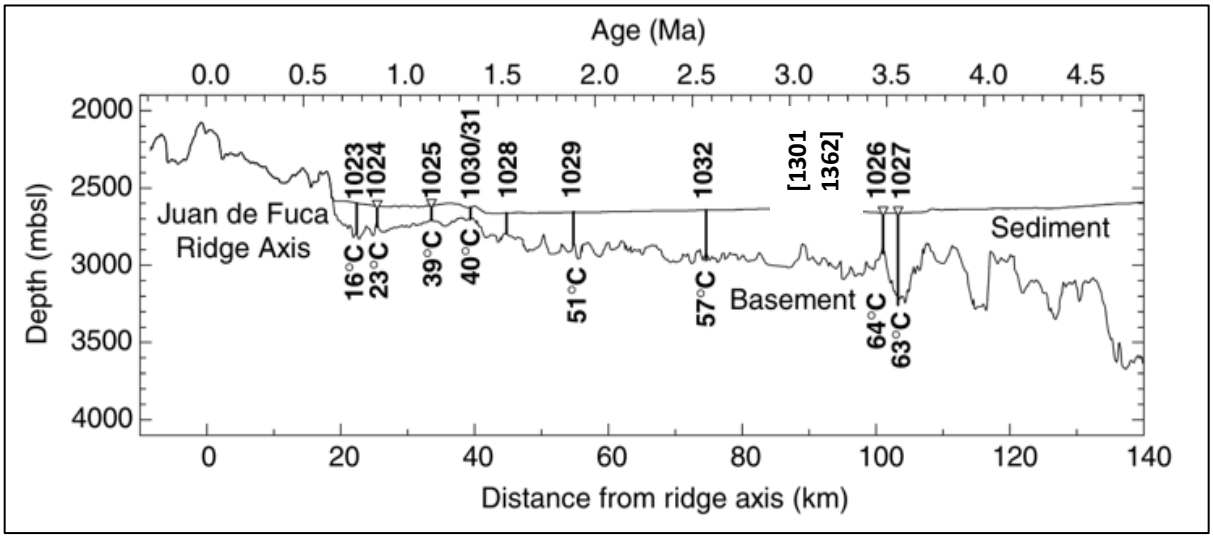

Figure 2.3*: Profile of Ocean Drilling Program Leg 168 drilling transect oriented perpendicular from the Juan de Fuca spreading ridge along the eastern flank of the ridge. Profile derived from seismic reflection data, the profile shows distance from the ridge axis, seafloor topography, and crustal age along the transect. Recorded basement temperatures are listed below each site. The proposed site location for CO_2 injection using existing borehole sites (1026, 1027, 1301 and 1362, which were drilled later) is located where the crustal age is ~3.5 Ma and the sediment-basement interface is ~250 meters below the seafloor. Modified from Fisher et al. (2000).*

2.2 Previous Work at Proposed Site

2.2.1 Drilling, Downhole Measurements, & CORKs

2.2.1.1 Introduction

For over three decades, scientific ocean drilling has been conducted along the eastern flank of the Juan de Fuca ridge using a unique scientific ocean drilling vessel. The Joint Oceanographic Institutions for Deep Earth Sampling (JOIDES) is a partnership of universities in 27 countries committed to exploring subseafloor geology (Exon and Malone, 2015). Named after this collective partnership, the *JOIDES* Resolution (JR) (Figure 2.4a) is a conventional (riserless) scientific research vessel that drills and recovers core samples, collects subseafloor measurements, and was used to drill boreholes and emplace sealed subseafloor observatories (CORKs) during previous scientific expeditions relevant to this study (discussed in Section 2.2.2) (Exon and Malone, 2015; Delaney and Higgins, 2009). The vessel is owned by Overseas Drilling Limited but operated by the JOIDES Resolution Science Operator (JRSO) at Texas A&M University, funded by the U.S. National Science Foundation (Exon and Malone, 2015). Data from previous scientific expeditions in the Cascadia Basin can be accessed through the Gulf Coast Repository (GCR) at Texas A&M University. The JR has gone through a series of upgrades in tandem with the progression of scientific drilling expeditions in the Cascadia Basin region (Exon and Malone, 2015). Equipped with research laboratories on board, the *JOIDES* Resolution can analyze recovered cores and the borehole data obtained during drilling operations and short-term hydrologic experiments (Delaney and Higgins, 2009). Additional sensors and fluid samplers can be installed within the subseafloor observatories for collection of additional

data over longer time periods. This section includes details of standard drilling operations conducted by the *JOIDES* Resolution in the region and the purpose and use of long-term subseafloor boreholes observatories.

2.2.1.2 Drilling Operations and Downhole Measurements

The *JOIDES* Resolution conducts riserless drilling, where the drill pipe is run through the open water towards the seafloor and seawater is used as the drilling fluid (Figure 2.4a). The bottom hole assembly at the end of the drill pipe contains the drill bit which drills through the sediments and ocean crust. Cores are recovered during this process and brought back to the drill ship (Manley et al., 2004). This process allows multiple boreholes to be drilled in a short period of time compared to other methods of ocean drilling. Samples of ocean crust are collected as cores, or intervals designated by distance from the top of section to the top and bottom of the core sample removed. Coring tools conventionally used are rotary core barrel (RCB), extended core barrel (XCB), and advanced piston corer (APC). RCB and XCB are typically used to core hard sediments and igneous basement, while APC can recover undisturbed soft sediments (Figure 18a) (Exon and Malone, 2015; Huey and Storms, 1985). The core barrels collect and store core material and are brought up to the drill ship. Full core recovery from the basaltic basement is difficult because of the fractured nature of the rock. Core samples brought to the surface are not in their original temperature and pressure conditions. Observations from recovered core samples are complemented by downhole measurements, which have the added benefit of recording the physical property *in-situ*.

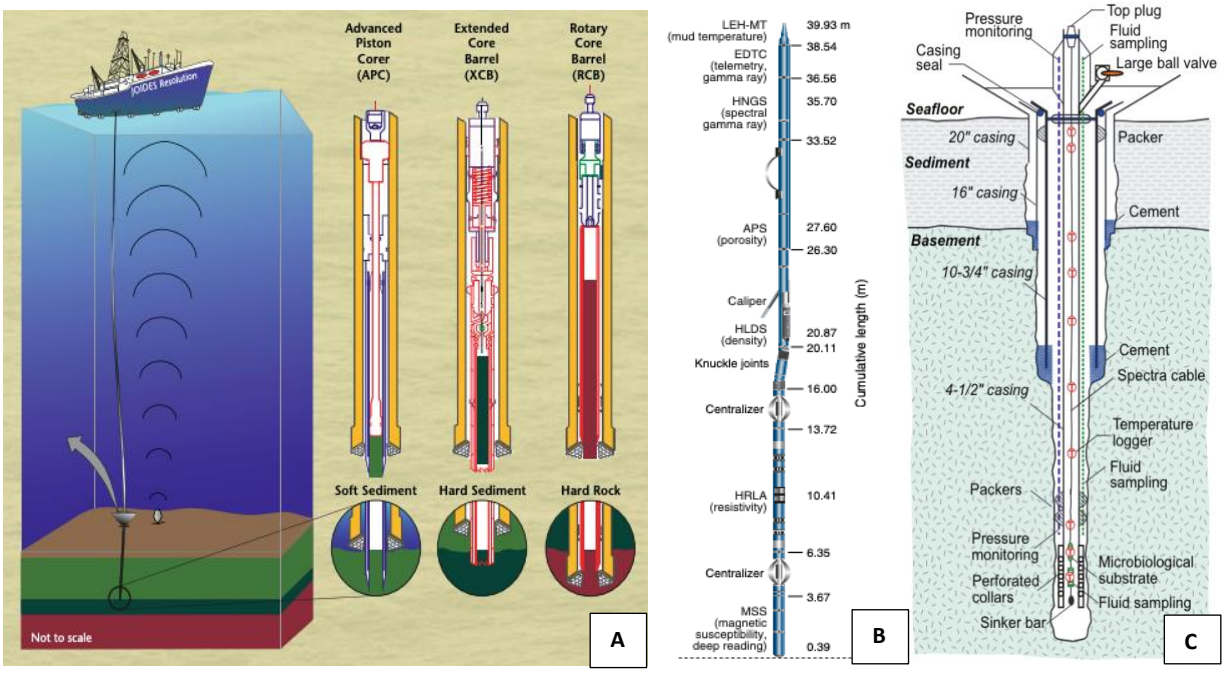

Figure 2.4*: Ocean drilling and coring tools used to drill boreholes in ocean crust. A) Schematic showing riserless drilling vessel JOIDES Resolution positioned above borehole location and the drill pipe and coring tools used to drill a borehole. Three types of coring tools are used depending on the type of material being cored. The bottom hole assembly retrieves and stores the core material cut by the drill bit at the end of the drill string. The core material is brought back to the rig floor of the drill ship where they*

are recovered. (IODP JRSO, 2014). B) Schematic of triple combo tool which acquires geophysical measurements during wireline logging after a borehole is drilled to gain information about the physical properties of the formation (IODP JRSO, 2014). C) Diagram showing features of CORK systems deployed during IODP Expedition 327 (Holes 1362A and 1362B) showing hole completion and design. Pressure monitoring (purple dashed line); fluid sampling line (green dotted line) collects basement fluids from depth. Source: Fisher et al. (2014).

After drilling is complete, geophysical measurements can be made in the open hole using wireline logging, or continuously recording physical properties (lithology, rock alteration) of the formation with depth (Fisher et al., 2014). A common wireline logging tool is a triple combo tool string (Figure 2.4b) that acquires logs of caliper (hole diameter), porosity, resistivity, bulk density, seismic velocity, and borehole temperature (Fisher et al., 2014). After wireline logging, hydrologic testing can be conducted in the borehole using a drill string packer system to test the permeability of the formation (Becker and Fisher, 2000). A packer is a rubber balloon tool that is intentionally inflatable, sealing and isolating the space between the drill string and the inner borehole wall (Manley et al., 2004). The pressure and the formations response to being perturbed is recorded. The combined analysis of the recovered cores, geophysical measurements, and hydrologic testing help determine the physical and chemical states that make up of the formation within and surrounding the borehole.

2.2.1.3 Purpose and Description of CORKs

To conduct long term scientific experiments in ocean crust, crustal boreholes are outfitted with Circulation Obviation Retrofit Kits, or CORKs (Figure 2.4c). CORKs are installed with the intention to be revisited and serve as long-term, sealed, subseafloor observatories. These operate in a way analogous to a cork sealing a bottle, except the bottle is the subseafloor ocean crust. They are designed to operate under various conditions in ocean crust including immediately following drilling and instrumenting a borehole. CORKs are typically built around concentric casings which are metal pipes that stabilize the hole and isolates the basement from the ocean bottom water (Fisher et al., 2014; Neira et al., 2016). The concentric casings prevent collapse of the hole (Figure 2.4c) (Manley et al., 2004). If the formation is stable, a smaller hole is cored below the casing to have access to the zone of experimental interest. If the formation is unstable, the entire hole is cased, and the zone of interest is accessed through a screen or perforated casing (Wheat et al., 2011).

CORKs isolate depth intervals that instruments can be deployed in to monitor temperature and pressure *in-situ*, and to collect fluids for long periods of time (Dalit, 2004). Submersibles and remoted operated vehicles (ROV) can retrieve the data from the top of the CORK exposed at the seafloor using an ROV platform (Figure 2.4c) or can be attached to a subsea cable where it can be downloaded in real time (Fisher et al., 2014). Adding cables and valves to the CORK allows for temperature measurements throughout the hole and fluid sampling (Figure 2.4c). The valves control flow of fluids from depth, while a cable can be used to hang temperature sensors, or osmotically pumped fluid sampling systems for collecting basement fluids (section 2.3). The autonomous temperature loggers and fluid samplers must be recovered to obtain the data (Fisher et al., 2014). A caveat for deploying additional loggers and samplers is that they must be smaller than the diameter of the casing, since they are deployed through the drill string (Fisher et al., 2014).

2.2.2 Scientific Expeditions

Several offshore expeditions completed in the early 1990's established the eastern flank of the Juan de Fuca spreading ridge as one of the most studied ridge flanks across the globe (Davis et al. 1996), with seismic surveys first conducted in the region in the 1950s and 1960s (Fisher et al. 2005a). Geophysical surveys followed in the mid-1990s, with a focus on hydrothermal circulation along the ridge flank using heat flow measurements, pore water analysis from sediment cores, and correlation of heat flow measurements with changes in seismic velocities in the upper crust (Davis et al., 1989, 1992; Wheat and Mottl, 1994; Rohr, 1994). Additionally, Davis et al. (1997) compiled heat flow data in the region between 1978-1995. The data collected from these surveys led to scientific drilling operations conducted in the region by an international partnership of scientists and research institutions known as the Ocean Drilling Program (ODP). ODP Leg 168 investigated various aspects of hydrothermal circulation throughout the eastern flank of the JDF spreading ridge, including alteration of sediments and the upper igneous crust (Davis et al., 1997).

The International Ocean Drilling Program (IODP), which later transitioned to the International Ocean Discovery Program (IODP), built upon the scientific success of previous drilling and coring operations conducted by ODP, by establishing multiple drilling platforms through various expeditions that were used to reach new areas of the subseafloor that remained unexplored (Koppers et al., 2019; Manley et al., 2004). IODP Expeditions 301 and 327 continued investigating the magnitude and distribution of hydrogeologic properties along the eastern flank of the Juan de Fuca ridge, the extent of fluid circulation between boreholes, and how hydrological pathways are connected in this area through establishing a close network of boreholes and a successful 24-hour pumping and tracer injection experiment (Fisher et al., 2011a). An overview of the objectives from each scientific expedition conducted near the proposed site for CO_2 injection and existing boreholes in the region are described in the following sections. These expeditions contributed to our current understanding of the potential for the basaltic crust in the Cascadia Basin to permanently sequester carbon.

2.2.2.1 Ocean Drilling Program Leg 168

Ocean Drilling Program Leg 168 explored how ridge-flank hydrothermal circulation affects basaltic basement fluid composition by drilling along an 80-km transect (Figure 2.5) of eight shallow basement penetrating (upper tens of meters of ocean crust) boreholes with a crustal age range of 0.9 to 3.6 Myr (Davis et al., 1997). Four of the eight boreholes included subseafloor borehole observatories for long-term monitoring. These borehole observatories were used to observe lateral gradients in the conditions within the basement (i.e., temperature, pressure, physical and chemical alteration to basement rock, and fluid composition), including investigating how heat is transported through the upper ocean crust from downhole temperature and pressure measurements, sample collection (sediments, rock, fluids), and observations post-drilling (Davis et al., 1996b). Out of the eight boreholes drilled during ODP Leg 168, Holes 1026B and 1027C, along the eastern end of the transect, are available for monitoring the CO_2 injection experiment (Figure 2.5).

Holes 1026B and 1027C are located at ODP Sites 1026 and 1027, 100 km east of the spreading ridge, with more rugged basement compared to other sites along the transect (Figure 2.5) (Davis

et al., 1997). Both holes were drilled using RCB and XCB coring tools and contain a single depth level CORK (Shipboard Scientific Party, 1997a). Hole 1027C lies over a basement trough, while Hole 1026B is positioned over a basement ridge. The holes are separated by 2.2 km. Hole 1027C was drilled ~400 m deeper into the basement than Hole 1026B. The original CORK installed in Hole 1027C remains in place, is still fully sealed, and is recording formation pressure (Fisher et al., 2011c). Pressure and temperature loggers in both are currently connected to the NEPTUNE subsea cabled observatory (Fisher et al., 2014) operated by Ocean Networks Canada, with data downloaded in real time, accessible through the Oceans 3.0 data portal (Owens et al., 2022; https://data.oceannetworks.ca/home).

Temperature measurements were made at Sites 1026 and 1027 (Shipboard Scientific Party, 1997b). The recorded temperatures at 247.1 mbsf at Site 1026 ranged between 61-64°C while Site 1027 recorded a temperature of ~63°C measured at 613.7 mbsf (Shipboard Scientific Party, 1997a, b). A water sampling temperature probe was used to collect fluids discharging from Hole 1026B and was the first successful basement fluid sampling conducted by ODP. The fluid sample was used to determine the age of the formation fluids using Carbon-14 dating and was determined to be <10,000 years old at velocities of 1-3 m/year (Elderfield et al., 1999; Shipboard Scientific Party, 1997b). Even with variable sediment cover (~250 m at Site 1026 vs ~600 m at Site 1027) both sites had similar sediment-pore water compositions (Davis et al., 1996b). Drill-string packer experiments and slug tests (to estimate the hydraulic conductivity of the aquifer) conducted in both holes indicated relatively high permeabilities (10^{-12} to 10^{-14} m^2) at the scale measured with short-term single hole testing (Becker and Fisher, 2000).

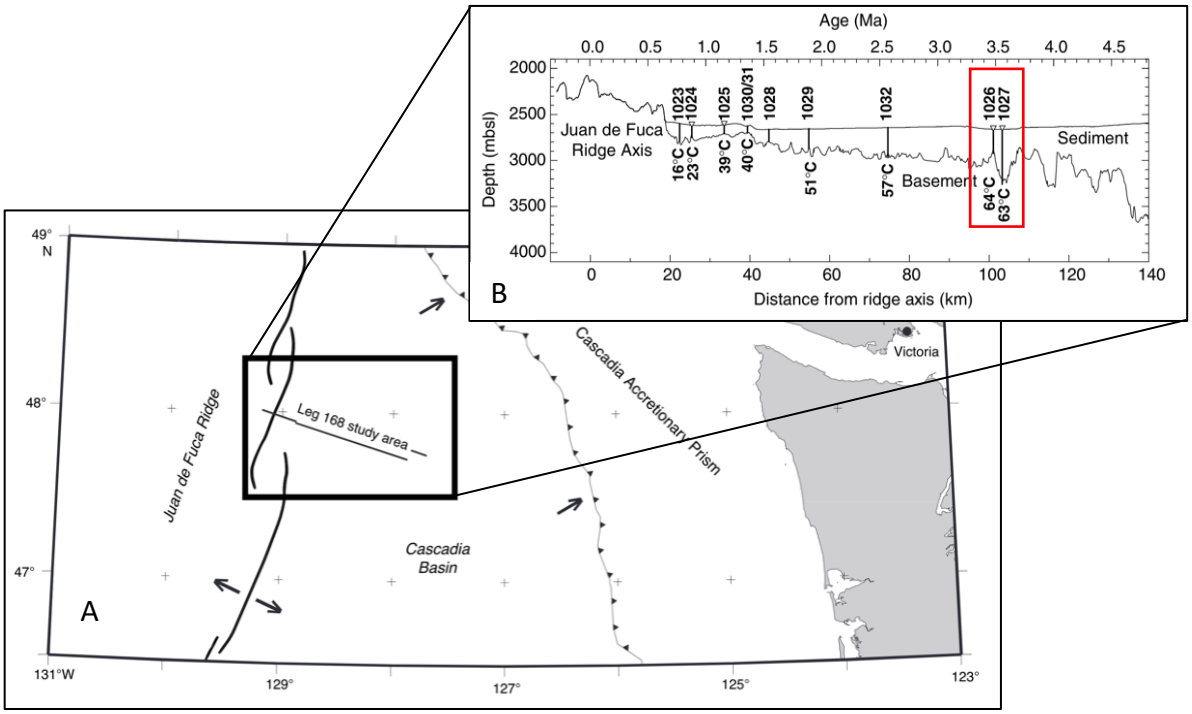

***Figure 2.5**: Location of ODP Leg 168 Drilling Transect showing axis of the Juan de Fuca Ridge. Inset of drilling transect shows cross-section of ODP Leg 168 drilling sites showing seafloor and basement topography and crustal age. ODP Sites 1026 and 1027 are possible sites for monitoring the CO_2 injection experiment, outlined in the red box. Open triangles shown in the inset indicate locations of borehole observatories, with associated borehole temperatures measured at the sediment-basement interface. Sources: Shipboard Scientific Party (1997b), Fisher et al. (2000).*

2.2.2.2 International Ocean Drilling Program Expeditions 301 and 327

With the intention to build upon the outcomes of the experiments conducted during ODP Leg 168, the International Ocean Drilling Program (IODP) performed two separate drilling expeditions, Expedition 301 (June 2004) and Expedition 327 (July 2010). These Expeditions were designed to evaluate the distribution of fluid pathways in an active hydrothermal system and integrate stratigraphic, alteration characteristics, microbiological, and seismic data collected to form a picture of formation-scale hydrogeologic processes for the Juan de Fuca ridge flank (Fisher et al., 2005a). Drilling was intentionally split between Expeditions 301 and 327, with the overall goal of establishing a cabled network of subseafloor observatories throughout the Juan de Fuca plate, to be able to monitor scientific experiments actively and passively in the ocean crust for years to come (Fisher et al., 2005a).

IODP Expedition 301 benefited from the successful operations and scientific achievements of ODP Leg 168 (Fisher et al., 2005a). It was the first IODP expedition with a cross-hole hydrogeologic experiment as a primary goal. Formation disturbances that resulted from drilling required the cross-hole tracer experiment to start during Expedition 327 so that small changes could be observed after the borehole had equilibrated to its pre-drilling state (Fisher et al., 2005a). The cross-hole tracer experiment was performed using a dissolved gas tracer (SF_6), rare earth element salts, and fluorescent microspheres to test the rates and direction of fluid transport in the crust and permeability, including anisotropy, using a network of sealed CORK borehole observatories instrumented with fluid samplers (Figure 20) (Neira et al., 2016; Fisher et al., 2011a). The CORKs installed during IODP Expeditions 301 and 327 were designed to be cabled observatories compatible for future monitoring experiments to download data in real time (Fisher et al., 2011e).

Expedition 301 focused on the eastern end of the ODP Leg 168 drilling transect and drilled two new boreholes, Holes 1301A and 1301B, at Site U1301 (Figure 2.6) (Fisher et al., 2005a). IODP Expedition 301 expanded the results of ODP Leg 168 in the following ways: 1) drilled and cored deeper into the basement with additional measurements, 2) applied microbiological and biogeochemical analyses to collected samples, and 3) established a network of borehole observatories to be used for long-term crustal-scale experiments (Fisher et al., 2005a). Holes 1301A and 1301B penetrated 108 and 320 m into the basaltic basement respectively, and are located 36 m apart (Fisher et al., 2005a). Sediment thickness is approximately the same at both holes (263-265 m) (Neira et al., 2016). Once the boreholes were drilled and cased, both holes were hydrologically tested and fitted with CORKs. Hole 1301A contains a single depth below seafloor CORK while the deeper Hole 1301B was fitted with a multi-depth CORK. Additionally, only Hole 1301B was cored and geophysically logged to obtain more information about the physical properties of the formation in this location (Fisher et al., 2005a). Drill string packer

experiments at Site 1301 suggest permeabilities of 10^{-12} to 10^{-11} m^2 (Becker and Fisher, 2008; Fisher et al., 2011a). The CORK in Hole 1026B was replaced during this expedition.

IODP Expedition 327 returned to the same area where work was completed for Expedition 301. Primary objectives included drilling two new basement boreholes, Holes 1362A and 1362B, at Site U1362 along the same buried basement ridge as Site U1301 and ODP Site 1026 (Figure 2.6) and carrying out a 24-hour tracer injection and pumping test which initiated a long-term cross-hole experiment. Holes 1362A and 1362B were drilled using an RCB coring tool to 528 and 359 mbsf, respectively, and are located 311 m apart (Fisher et al. 2011a). Sediment thickness is relatively uniform between holes; Hole 1362A has ~236 m and Hole 1362B has ~242 m sediment thickness (Neira et al., 2016). Hole 1362A was cored, geophysically logged, hydrologically tested, and fitted with a multi-level CORK. Hole 1362B was fitted with a single-level CORK and used as the injection hole for the 24-hour pumping test and tracer injection experiment (section 2.2.2.3) and was not cored or geophysically logged for this reason. Both CORKs included a large-diameter ball valve at the wellhead that can be opened to allow fluids to flow up or down within each borehole (Fisher et al., 2011a). These valves were used during the cross-hole tracer experiment (section 2.4) where flow of the injected tracer was monitored using the borehole observatories from ODP Leg 168 and IODP Expeditions 301 and 327.

The results of the drill string packer experiments in Hole 1362A were consistent with permeability measurements recorded in Hole 1301B (Becker and Fisher, 2008). Furthermore, thermal conductivity values tested from recovered pillow basalts from Hole 1362A (average of 1.67 W/(m·K)) at various depths were similar to those collected at equivalent depth intervals in Hole 1301B (1.70 W/(m·K)) (Fisher et al., 2011a). Moreover, penetration rates and caliper logs in Holes 1301B, 1362A, 1362B suggest along-strike, lateral continuity in the main basement units between these holes (Fisher et al., 2011a). In total, there are six CORK observatories operating within an area of 2.5 km^2 near the proposed sites, with CORKs in Holes 1301B and 1362A isolated across multiple basement depths (Fisher et al., 2011g; Fisher et al., 2014).

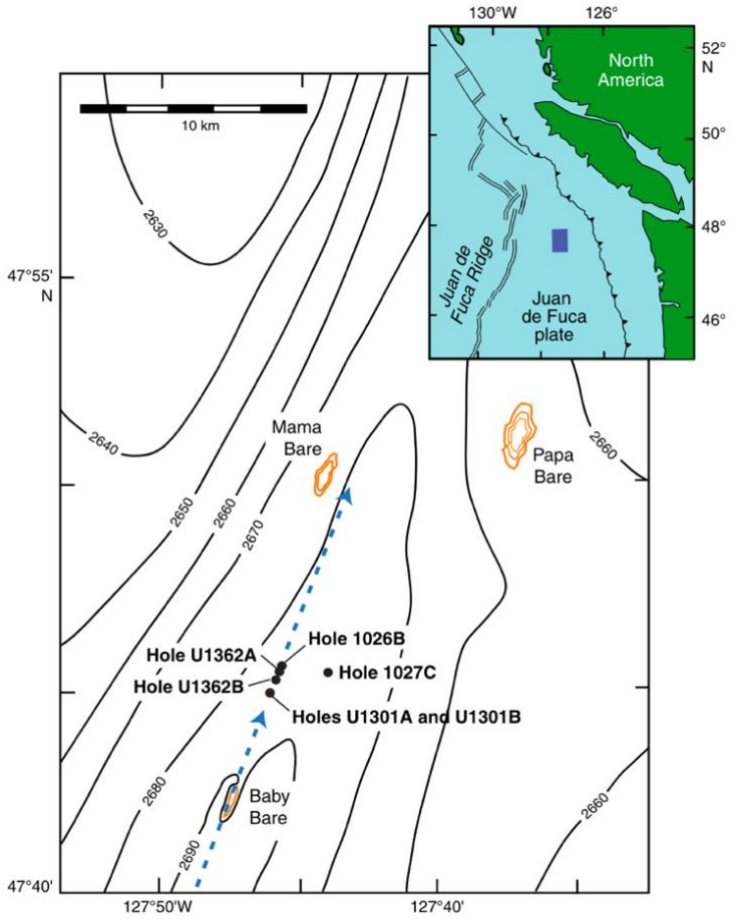

Figure 2.6*: Site map of existing boreholes near the proposed site for CO_2 injection. Shown is the location of Holes 1301A and 1301B drilled during IODP Expedition 301, and Holes 1362A and 1362B drilled during IODP Expedition 327 along the eastern end of ODP Leg 168 drilling transect. Hole 1362B was used as the injection hole for the cross-hole hydrologic experiment. Holes 1026B and 1027C were drilled during ODP Leg 168, shown for spatial reference. Gold contours show the location of basement exposure of outcrops in the area (Baby Bare, Mama Bare, Papa Bare). Small inset shows work area. Blue arrow indicates inferred dominant fluid flow direction in the crust for tracer injection experiment (Fisher et al., 2011f).*

2.2.2.3 Tracer Injection Experiment

As part of IODP Expedition 327, a 24-hour pumping and tracer injection test was conducted to assess transport rates and direction of the pathways of lateral fluid transport through the crust in this region. Hole 1362B was used as the injection hole and sulfur hexafluoride (SF_6) served as the main conservative tracer to track fluid flow between the boreholes used in the experiment (Figure 2.7) (Fisher et al., 2011b). Additional tracers injected included trace element salts Cesium Chloride (CsCl), Erbium Chloride Hexahydrate ($ErCl_3 \cdot 6H_2O$), and Holmium Chloride Hexahydrate ($HoCl_3 \cdot 6H_2O$), as well as fluorescent particle tracers consisting of stained bacteria extracted from surface seawater and microspheres ranging between 0.49-1.1 µm diameter (Table 2.1). The trace element salts were not expected to behave completely conservatively in the subsurface (De Jong, 2020; Fisher et al., 2011f).

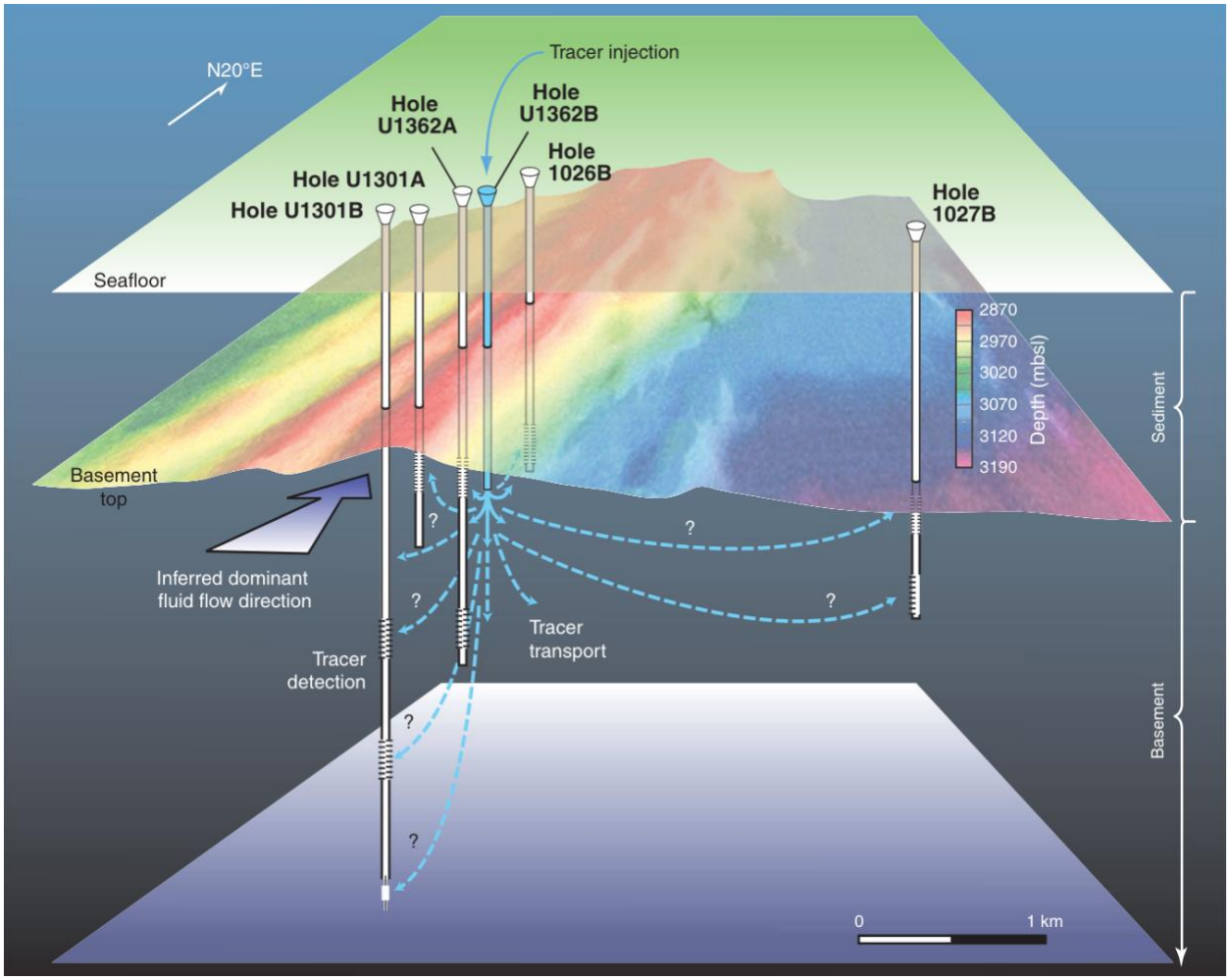

Figure 2.7*: Illustration of tracer injection experiment conducted during IODP Expedition 327. All boreholes are equipped with CORKs that sample borehole fluids and are oriented parallel to structural strike in this area. Inferred dominant flow direction is shown with purple arrow. Not to scale. Source: Fisher et al. (2011f).*

Prior to the experiment, SF_6 gas was held under pressure in compressed gas bottles to avoid loss to the atmosphere before introducing it to the injection stream. Trace element salt tracers were dissolved into seawater in a 5-gallon container and later added to seawater in a mixing tank (cement additive tank) and circulated until fluid was introduced into the formation through a delivery pump and injected in two batches (Figure 2.8). Fluorescent particle tracers were made of polystyrene tagged with bright blue (BB) Coumarin and yellow green (YG) Fluorescein dyes were added to the mixing tank and continually circulated in freshwater prior to injection (Figure 2.8) (Fisher et al., 2011f).

Using the tracer injection system illustrated in Figure 2.8, the solute and particle tracers were injected in pulses to maximize concentrations entering the formation, while the SF_6 was injected continuously throughout the experiment (Fisher et al., 2011f). Injection of seawater at a rate of 20 strokes per minute (SPM) (6.7 l/sec) initiated the experiment. After 80 minutes, freshwater was injected for 1 hour (Fisher et al., 2011a). A pumping rate of 20 SPM (6.7 l/sec) was used throughout most of the 24-hour injection and created a pressure response in the other boreholes used for monitoring. Higher pumping rates were intentionally avoided to limit tracer dilution (Fisher et al., 2011f). SF_6 was pumped into a back-pressured standpipe which delivered surface seawater to the mud pump (Figure 2.8). From there, the fluid mixture was sent to the rig floor through a drill pipe and into the volcanic crust at a constant rate throughout the 24-hour injection period using a manifold developed for tracer testing in a terrestrial aquifer (Fisher et al., 2011f; Clark et al., 2005).

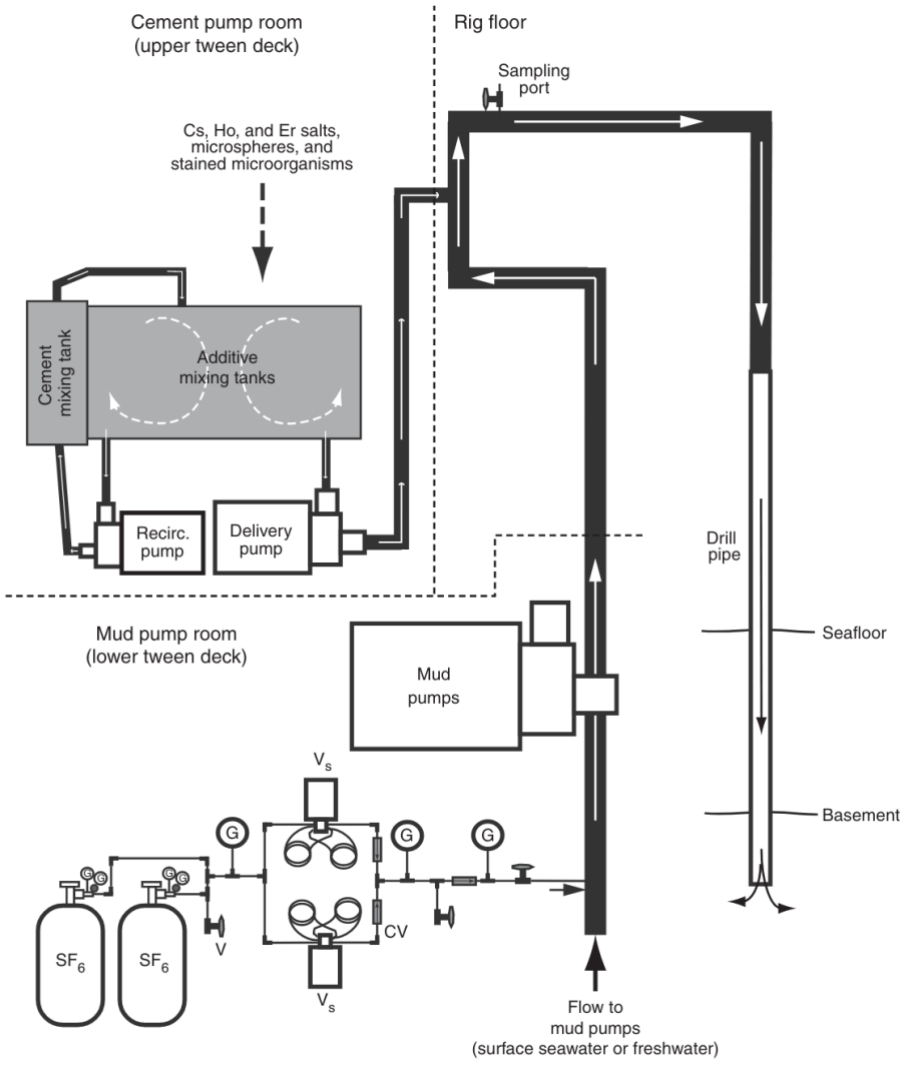

Figure 2.8*: Schematic of tracer injection system used shipboard during Expedition 327 showing pumps, manifolds, areas of mixing. Mud pumps were used to inject fluid into the formation during the 24-hour experiment.* SF_6 *gas introduced upstream from the mud pumps using an injection manifold to control the*

concentration of gas. Fluid from the mud pumps was directed into the drill pipe at the rig floor. For brief periods during injection, metal salt tracers and particle tracers were added to the flow stream using a cement pump system. Seawater was mixed with metal salt tracers, and seawater or freshwater was mixed with solutions of particle tracers, then added to the flow generated by the mud pump system. The sampling port at the rig floor was used to collect injectate samples before they were pumped into the drill pipe. V = sampling valve. Vs = switching valve, CV = check value, G = pressure gauge. Not to scale. Source: Fisher et al. (2011f).

Continuous injection of SF_6 initiated after 20 minutes and continued until all SF_6 gas was injected after 20.5 hours, with a mean injection rate of 0.0192 mol/min (Table 2.1) (Fisher et al., 2011f). Pressure was recorded at the inlet of the gas injection manifold every 15 minutes throughout injection. The total amount of SF_6 injected was 23.3 moles (injected concentration of 47.6 µM and a mean pumping rate of 6.7 l/sec). It was observed during injection that the SF_6 formed small bubbles, but these were assumed to dissolve once the fluid was transported below 200 m of water depth (>2 MPa). The rapid flow of fluid delivered to depth through the pipe combined with high pressures at the seafloor (~27 MPa) and low temperatures of bottom seawater (2°C) further suggest dissolution of SF_6 into solution before being introduced to the crustal aquifer.

The first batch of trace element salt tracers contained CsCl (89.1 mol of Cs) and $ErCl_3$ (60.3 mol of Er) and was introduced for 7.5 minutes during the 3rd hour of the test at 4.3 l/sec, while the second batch contained CsCl (89.1 mol of Cs) and $HoCl_3$ (60.6 mol of Ho) and was introduced for 8 minutes during the 19th hour of the test at 5.3 l/sec (Table 2.1) (Fisher et al., 2011f). Concentrations of each trace metal were ~10-18 µM during injection and based on the pumping rate and quantity of each metal salt (Fisher et al., 2011f).

The fluorescent stained bacteria and microspheres were injected separately since the stained bacteria was mixed with surface seawater, while the microspheres were mixed with freshwater to minimize clumping while suspended. Microspheres in fluid were injected for 6 minutes at 20 hours and 13 minutes of pumping, with a total concentration of 2×10^7 microspheres/ml injected (Table 2.1) (Fisher et al., 2011f). Fluorescent stained bacteria were introduced to the injectate stream generated by the mud pumps (Figure 2.8) and injected into the formation for 8 minutes at 21 hours 15 minutes at a rate of 3.4 l/sec and a mean concentration of ~10^4 cells/ml (Fisher et al., 2011f). The last hour of the experiment served to let the borehole equilibrate without pumping (Fisher et al., 2011b).

Table 2.1: *Characteristics of tracers injected during the 24-hour pumping and tracer injection during Expedition 327.*

Tracer	Quantity	Injection duration	Mean injectate concentration	Concentration in bottom seawater*	Detection limit	Dilution factor
SF_6	3.40 kg 23.3 mol	20.22 h	47.6 µM	ND	0.07 pM	~7×10^8
Cs (as CsCl)	2 × 15 kg 2 × 89.1 mol	7.5 min 8 min	18.0 mM 15.6 mM	2.2 nM	0.1 nM	~8×10^6 ~7×10^6
Er (as $ErCl_3 \cdot 6H_2O$)	23 kg 60.3 mol	7.5 min	12.2 mM	9.6 pM	0.1 nM	~1×10^9
Ho (as $HoCl_3 \cdot 6H_2O$)	23 kg 60.6 mol	8 min	10.6 mM	2.7 pM	0.02 pM	~3×10^9
BB Coumarin, 1.0 µm†	4.5×10^{12} spheres	6 min	2×10^6 spheres/mL	ND	1/mL	~2×10^6
YG Fluorescein, 1.1 µm†	2.3×10^{13} spheres	6 min	1×10^7 spheres/mL	ND	1/mL	~1×10^7
BB Coumarin, 0.49 µm†	3.6×10^{13} spheres	6 min	2×10^7 spheres/mL	ND	1/mL	~2×10^7
DAPI-stained cells	10^{11} cells	8 min	~10^4 cells/mL	ND	1/mL	~10^4
Freshwater (chlorinity)	48,000 L total	2 h	0 mmol/kg	542 mmol/kg	1 mmol/kg	~5×10^2

Table Footnotes: * = SF_6, fluorescent microspheres, and fluorescent-stained microbes are anthropogenic and would not be detected in ocean water in this region unless artificially introduced. Bottom water concentrations for trace metals are from Hulme et al., (2008) and Wheat et al., (2010). Detection limit for SF_6 is from Clark et al., (2005) and trace metals from Hulme et al., (2008). †= trade name of fluorescent dye and mean sphere diameter. Mean injectate concentrations are estimated from known quantities added and total rates of injectate pumping with mud pumps and cement pumps. Actual injectate concentrations are determined through post-expedition analyses of samples collected. Dilution factors are calculated as (mean injectate concentration)/(detection limit) for SF_6, fluorescent particles, and freshwater. Dilution is calculated as (mean injectate concentration)/(concentration in bottom seawater) for trace metals. DAPI-stained cell numbers are based on regional surveys of bacterial concentrations in surface seawater (Sherr et al., 2001). ND = not detected. Source: Fisher et al. (2011f).

Formation fluids were collected for several years using long-term osmotically pumped fluid samplers installed in the four surrounding boreholes shown in Figure 2.7. The results from the fluid analysis and interpretation of tracer transport are discussed in Section 2.4.

2.2.3 Heat and Fluid Flow in the Region

2.2.3.1 Overview

Thermal gradients in ocean crust are primarily controlled by the plate tectonic cycle through interaction of the ocean and the underlying solid earth (Stein and Stein, 1992). Newly formed crust at spreading ridges have the highest documented seafloor heat flow values and these values decrease as the plate moves away from the spreading ridge due to seafloor spreading. Thermal models of the lithosphere crust are based on the fact that the seafloor crust cools as it moves away from the spreading center. Thus, crustal heat flow is estimated from its age and depth (Stein and Stein, 1992). Measured heat flow at the seafloor for crust younger than 65 Myr is substantially less than what is predicted by these thermal models that simplify all heat transfer as only controlled by the upward movement of heat, or conduction of heat through the crust (Figure 2.9) (Stein and Stein, 1992). The discrepancy between predicted and observed values reflects the actual complexity of the system which includes the transport of heat through circulation of water through the crust, known as hydrothermal circulation (Stein et al., 1995). A considerable amount of this hydrothermal circulation occurs not only near the spreading ridge, but also in areas that are distal, such as along ocean ridge-flanks (Figure 2.9) (Fisher, 2005d).

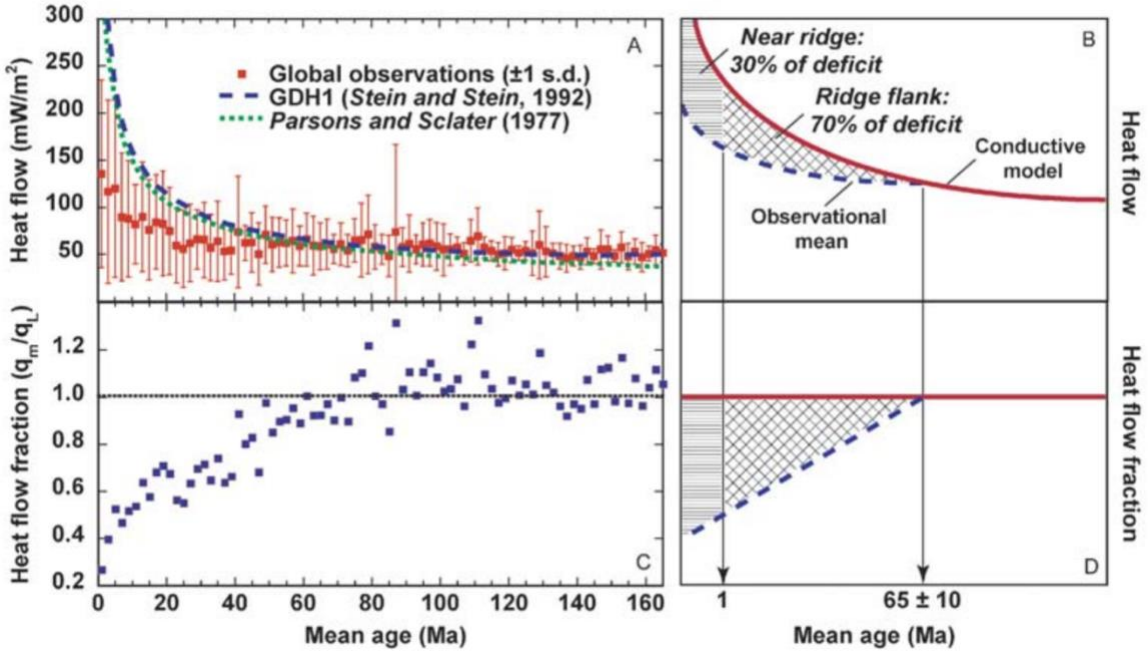

Figure 2.9*: Hydrothermal circulation along ridge-flanks compared to observed global seafloor heat flow values. A) Global seafloor heat flow data at 1-m-year intervals. Vertical bars indicate ± 1 standard deviation, squares are mean values. Dotted and dashed curves represent models of conductive lithospheric cooling that are widely recognized. A discrepancy exists between observed values and lithospheric cooling models. B) Illustration of the heat flow discrepancy, which varies with seafloor age. Along the seafloor, ~30% of heat from the lithosphere is unaccounted for in (A), and this heat is removed from the crust through advection by flow of water. In ocean crust older than 1 Myr, most of this advection (70%) is observed along ridge flanks. C) Heat flow fraction versus mean age of crust. Heat flow observations are below the mean until crustal age reaches 65 Myr. D) Illustration of relationship between mean observational measurements and conductive cooling predictions shown in (C). Source: Fisher (2005d).*

Along the eastern flank of the Juan de Fuca ridge, the upper basement becomes more isolated from the overlying ocean due to increasing sediment thickness. This influences the conductive seafloor heat flux, with basement temperatures increasing and heat flux more suppressed to the east (Davis et al., 1992). Observed seafloor heat flow values in the region along the ridge flank are lower than what is predicted by lithospheric cooling models by 15-20% (Winslow et al., 2016; Hutnak et al., 2006), suggesting that heat is being removed through other processes such as advection of heat from the crust by flow of water which is common for ridge flanks older than 1 Myr (Figure 2.9) (Fisher, 2005). Interpretations about fluid transport in the region are based on seismic reflection surveys (Zühlsdorff et al., 2005), geochemical analysis of formation fluids from boreholes and local outcrops (Hulme and Wheat, 2019; Wheat et al., 2000, 2003; Elderfield et al., 1999), heat flux measurements (Davis et al., 1999; Mottl and Wheat, 1994), and mathematical modeling (Winslow et al., 2016; Hutnak et al., 2006). Together, the data and models provide evidence of substantial hydrothermal circulation in the upper crust (basement) between highly permeable outcrops and influenced by faults and fractures parallel to the spreading ridge (Hutnak et al., 2006; Spinelli and Fisher, 2004; Fisher et al., 2003; Mottl and

Wheat, 1994). Further, basement fluid chemistry in the region is consistent with these heat flow measurements (Hulme and Wheat, 2019).

2.2.3.2 Fluid Transport in the Region

Hydrothermal circulation in the region includes outcrop-to-outcrop flow and local convection (i.e., mixing) (Winslow and Fisher, 2015; Hutnak et al., 2006; Fisher et al., 2003; Davis et al., 1989,1992). Fluid flow has been observed to be driven by circulation of fluids between nearby outcrops, which act as localized areas of recharge and discharge. Basaltic seafloor outcrops, Grizzly Bare and Baby Bare, were identified through bathymetric and multibeam mapping, seismic and geochemical surveys, and heat flow measurements (Davis et al., 1989; Fisher et al., 2003; Hutnak et al., 2006; Zühlsdorff et al., 2005; Wheat et al., 2000). These outcrops are located south of the proposed site for CO_2 injection (Figure 2.10) and are exposed at the seafloor above the nearly continuous sediment layers, acting as high permeability vents for basaltic basement fluids (Mottl et al., 1998). Fluid flow between them is driven by differences in fluid pressure between descending (cool) and ascending (warm) columns of formation fluids (Lauer et al., 2018). Unaltered (cold) bottom seawater is recharged at the Grizzly Bare outcrop where it enters the crust and migrates ~52 km north-east to the Baby Bare outcrop where this warmed, altered seawater is discharged, forming a hydrothermal siphon between the outcrops (Figure 2.10) (Wheat et al., 2010; Fisher et al., 2003).

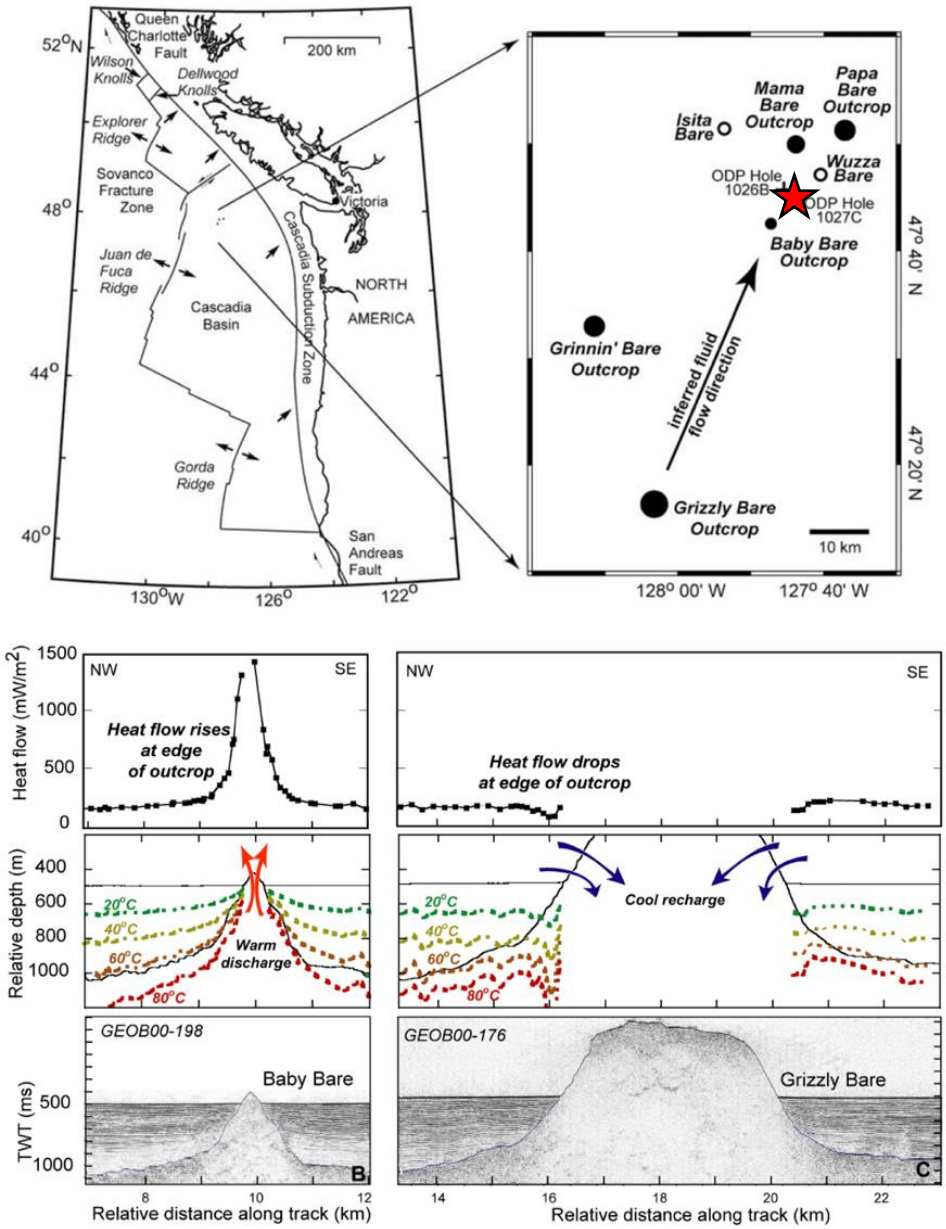

***Figure 2.10**: Fluid flow in the upper basement along the eastern flank of the Juan de Fuca spreading ridge. (**Top**) Regional map with inset depicting the general path of formation fluid flow within the basement between Grizzly Bare and Baby Bare outcrops (black arrow). Basaltic outcrops in the region are shown as solid circles. The red star is the proposed location of CO_2 injection where ODP sites 1026, 1027, and IODP Sites 1301 and 1362 are located. Source: Wheat et al. (2004). (**Bottom**) Heat flow values across Baby Bare and Grizzly Bare outcrops. Cold bottom seawater enters the crust at Grizzly Bare (recharge) and warm, altered formation fluids are discharged at Baby Bare outcrop ~52 km north-east. Baby Bare stands 65 m above the sediments while Grizzly Bare stands 450 m above sediments. Source: Zühlsdorff et al. (2005).*

Permeability of the crust influences the vigor of the convectively driven fluid flow, with the most permeable crust in the basaltic basement estimated to be in the upper 300-500 m of pillow basalts (Fisher et al., 1998). Permeability in heterogenous (fractured rock) systems can produce different values depending on the scale of measurement. For example, core-scale measurements result in the lowest permeabilities, single-hole tests yield intermediate values, and large-scale modeling studies produce the highest permeabilities (Spinelli and Fisher, 2004). Single-hole estimates of permeability from packer testing were found to be 2×10^{-11} m^2 from a 30-m interval between 442-472 mbsf from Hole 1301B (Becker and Fisher, 2008). Based on modeled results, hydrothermal circulation between these outcrops is found to be sustained when permeability in the basement is $\geq 10^{-12}$ m^2 (Fisher et al., 2011a). For reference, when permeability is too high (10^{-10} to 10^{-9} m^2), numerical models predict basement temperatures would lower to between 20-50°C due to rapid fluid circulation between outcrops, and if permeability is too low, fluid circulation cannot be naturally sustained as too much energy is found to be lost (Fisher et al., 2011a). Upper basement (~320 m) permeabilities in this location range between 10^{-12} to 10^{-11} m^2 (Fisher et al., 2011a; Wright and Rothery, 1998; Davis et al., 1992; Becker and Fisher, 2008) allowing water to travel 52 km north-eastward towards Baby Bare outcrop. Hutnak et al. (2006) used numerical and analytical calculations of coupled fluid-heat flow to constrain the nature of hydrothermal circulation guided by Grizzly Bare and Baby Bare outcrops and found that local convection alone cannot explain heat flux observations near the outcrops but with sustained recharge and discharge between outcrops when permeability is high enough, seafloor heat flux observations can be explained. Winslow et al., (2016) presented 3-D simulations with the addition of crustal permeability and basement aquifer thickness. Simulations that set the as aquifer >300 m thick and permeability $>10^{-12}$ m^2 were found to result in lower heat flux than has been observed. Simulations that set the aquifers ≤300 m thick are a better match to field observations (Winslow et al., 2016).

2.2.3.3 Chemical Observations

Ridge-flanks play an important role in hosting large seawater fluxes that influence the chemistry of the ocean and atmosphere (Stein et al., 1995). As seawater is circulated through the crust along the ridge-flank, it reacts with the surrounding rock and sediments, warms, and ages (a microbe-driven process), resulting in geochemical compositions distinct from bottom seawater (Table 2.2) (Wheat et al., 2003, 2010). The composition of altered crustal fluid in this region is known based on samples collected from IODP Site 1301, ODP Sites 1026 and 1027, and nearby outcrops (Wheat et al., 2000, 2003, 2010; Elderfield et al., 1999).

Table 2.2: *Basic chemistry (DIC, pH, alkalinity) of bottom seawater and basement fluids along the eastern flank of the Juan de Fuca Ridge. Major ion concentrations are listed in Table 4.6.*

Measurement	Basement Fluids	Bottom Seawater
pH	7.30	7.9
Alkalinity	0.43 mmol/kg	2.5 mmol/kg
Dissolved inorganic carbon (DIC)	0.55 mmol/kg	2.6 mmol/kg

Table Footnotes: pH measurements in bottom seawater taken from Wheat and Mottl (2000); pH in basement fluids collected from ODP Site 1026 taken from Elderfield et al. (1999); Alkalinity in bottom seawater from Wheat et al. (2003) and Wheat and Mottl (2000); Alkalinity in basement fluids from Elderfield et al. (1999). DIC in bottom

seawater from Walker et al. (2008); DIC in basement fluids is an average of two measurements collected from ODP Site 1026 and taken from Walker et al. (2008).

Wheat et al. (2000, 2022) and Wheat and Mottl (2000) found geochemical evidence for fluid transport along a south-north transect, parallel to the spreading ridge, based on fluid samples collected from Baby Bare and Mama Bare outcrops, and ODP Site 1026 (Figure 2.10). There is a clear pattern of increasing alteration of fluids due to hydrothermal reactions from south to north along this transect where certain constituents are removed, and others leached from the ocean crust (Wheat and Mottl, 2000). A similar pattern was observed along the ODP Leg 168 transect perpendicular to the ridge with alteration of fluids increasing from west to east (Elderfield et al., 1999). Fluid compositions furthest away from the ridge (ODP Sites 1026 and 1027) were younger (<10,000 yrs.) and more similar to springs discharging at Baby Bare outcrop, mixing in the upper basement at temperatures near 65°C (Elderfield et al., 1999; Fisher et al., 2005a). Wheat et al., (2000) suggests these two flow systems are distinct from each other due to lack of exchange of fluids from the south-north transect with basement fluids from closer to the ridge to the west. Fisher et al., (2003) used thermal data and calculations from measured hydrogeologic properties of recovered basement cores to suggest that recharge of fluids found at Baby Bare outcrop and ODP Site 1026 occur at Grizzly Bare outcrop. Understanding the dominant direction of fluid transport and the chemical changes that occur as the fluids move through the upper crust towards the proposed site for CO_2 injection is important for choosing where to monitor the injected fluid and for interpreting concentration data obtained prior to injection.

2.3 Fluid Sampling Capabilities

2.3.1 Introduction

The remote location of the subseafloor presents many challenges for collection of fluid samples. The evolution of CORK borehole observatories has allowed improvement of how fluids are collected in ocean crust using fluid-sampling systems (Jannasch et al., 2004). The functionality of fluid sampling in the offshore deep-sea environment requires a custom-fit approach for the needs of each experiment, such as the length and scale of the experiment, and the analytical needs of the fluid samples. The fluid sampling systems described below can serve as monitoring stations for observing hydrogeological properties in ocean crust on a large scale, resulting in significant reduction in cost of sampling (Fisher et al., 2010). For the purposes of monitoring a CO_2 injection experiment, observing changes to the injected fluid overtime requires collection of fluid samples at the *in-situ* temperature and pressure conditions over the course of the experiment and is vital for successfully verifying the CO_2 is chemically progressing towards mineralization as expected.

2.3.2 Osmosamplers

2.3.2.1 Purpose and Description of Osmosamplers

CORKs can isolate and seal depth intervals within the borehole to prevent fluid exchange between the formation fluids and bottom seawater and pore water in sediments. This allows for deployment of fluid samplers to collect formation fluids *in-situ* and undisturbed for long periods of time (e.g., days to several years) (Dalit, 2004). Originally developed by Hans Jannasch and his team at the Monterey Bay Aquarium Research Institute (MBARI), Osmosamplers were developed for continuous collection of long-term data in remote environments, such as the

subseafloor, without the need for software, batteries, or any moving parts (Dalit, 2004). In the context of subseafloor boreholes, an Osmosampler can be deployed either at the CORK wellhead at the seafloor (Figure 2.11) or downhole along an instrument string. These samplers are customizable, self-contained, osmotically pumped fluid samplers that can preserve collected fluid samples with high temporal resolution at timed intervals where temperature is reasonably stable (Jannasch et al., 2004). Furthermore, Osmosamplers are designed specific to the desired length of deployment and the analytical needs of the fluid samples (Neira et al., 2016), which can determine the length of sample tubing or coils required and the total number of samplers for each experiment.

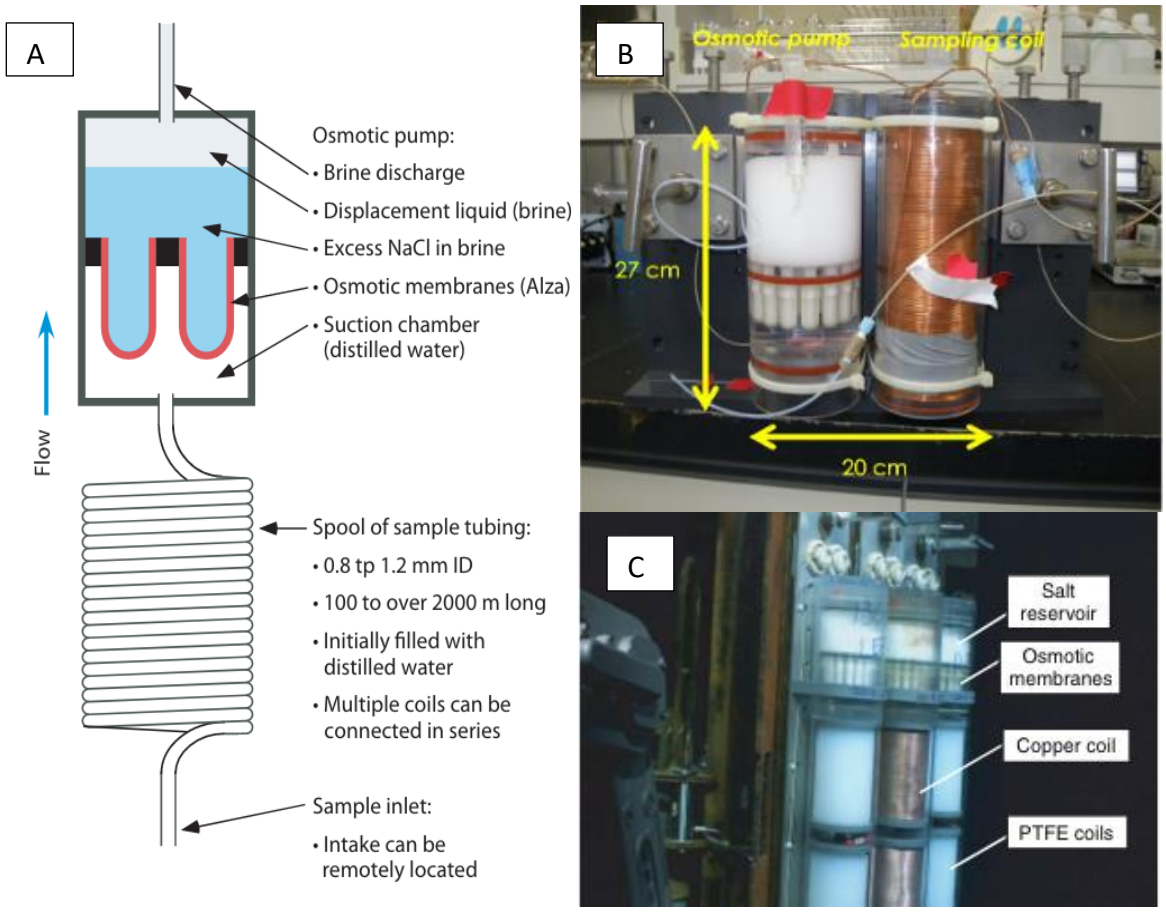

Figure 2.11*: Osmosampler components.* ***A****) Schematic of Osmosampler. Formation fluids are drawn through the sample inlet into the spool of small diameter sample tubing using the osmotic pump, which operates through osmosis. Within the pump there is a suction chamber filled with distilled water, a separate discharge chamber filled with a brine with excess salt, and semi-permeable osmotic membranes separating the two chambers. The osmotic pressure difference between the excess salt and the distilled water drives the distilled water across the membrane towards the brine chamber, indicated by the blue flow direction arrow. The pumping rate is determined during development of the sampler and is dependent on the salt gradient, number/size/type of membranes, and operating temperature. The brine is typically discharged through small inner diameter tubing (to avoid loss of salt) above the pump to the surrounding environment. Source: Kastner et al. (2006).* ***B****) Close up showing the size of osmotic pump*

containing 12 semi-permeable membranes and one spool of 1.1-mm-inner diameter copper sampling coil 322 m in length prior to deployment. The type, size, and length of sample tubing is dependent on the length of deployment and analytical needs of the fluid samples. Source: Owari et al. (2019). ***C****) Arrangement of three Osmosamplers deployed at the seafloor in geochemical sampling bay at the CORK wellhead in Hole 1301B during R/V Atlantis Expedition AT15-66. When deployed on the seafloor, the osmotic pump sits above the sample tubing, like in A. Polytetrafluoroethylene (PTFE) and copper coils are used for the Osmosamplers shown in the image obtained from ROV Jason. Source: Fisher et al. (2011f).*

2.3.2.2 Osmosampler Components

Osmosamplers allow formation fluids to be collected at depth with osmotic pumps which pull the fluid into very long small-diameter sample tubing or coils. The osmotic pumps are autonomous and fluid flow through the tubing is driven by the osmotic pressure difference across a rigid semi-permeable membrane which separates two chambers containing solutions with different salinities (Kastner et al., 2006). On one side of the semi-permeable membrane, there is a chamber with an excess supply of salt (NaCl) in a saturated brine. The other side of the membrane contains a solution of distilled water (suction chamber) (Figure 2.11). Osmosis is a form of diffusion which is governed by the concentration gradient present. The effect of osmotic flow will cause the solution chamber with a lower solute concentration (i.e., lower osmotic pressure) to flow across the membrane towards the solution with a higher solute concentration (i.e., higher osmotic pressure). Therefore, the freshwater is attracted to the excess salt in the brine because of lower initial osmotic pressure of the freshwater compared to the brine. The sample tubing is pre-filled with distilled water and terminates at the suction chamber in front of the set of osmotic membranes (Figure 2.11). The outflow from the saturated brine chamber is typically released to the surrounding environment through small-diameter tubing (0.8 mm-inner diameter) to avoid loss of salt, although additional sample coils can be attached to the outflow of the pump, as part of an Osmosampler tracer package for using added injected tracers (Wheat et al., 2011; Jannasch et al., 2004).

The flow rate generated by the osmotic pump is calibrated during development of each sampler and is determined by the type of membranes used, the magnitude of the salt gradient across the membranes, the surface area and thickness of the membranes, and the operating temperature (Jannasch et al., 2004). In past lab and field experiments, pumps made with commercially available membranes (Alza, Inc., Alzet) were successful in continuously collecting fluids for more than three years and can function between a temperature range of 4°C-70°C (Jannasch et al., 2004). If there is a difference in salinity across the membrane, fluids will be naturally drawn into the tubing (Dalit, 2004). In this way, fluids are pumped at a slow, steady rate. Each Osmosampler system includes space for a self-recording temperature sensor, since changes in temperature affect flow rate (Wheat et al., 2011; Wheat et al., 2003; Jannasch et al., 2004). Figure 2.12 shows the nonlinear relationship between temperature and flow rates of the osmotic pumps where, as temperature increases, the flow rate across the membranes also increase. This is because the most important factor controlling flow rate into the tubing is the rate of diffusion of water across the membrane, which increases with increasing temperature (Jannasch et al., 2004).

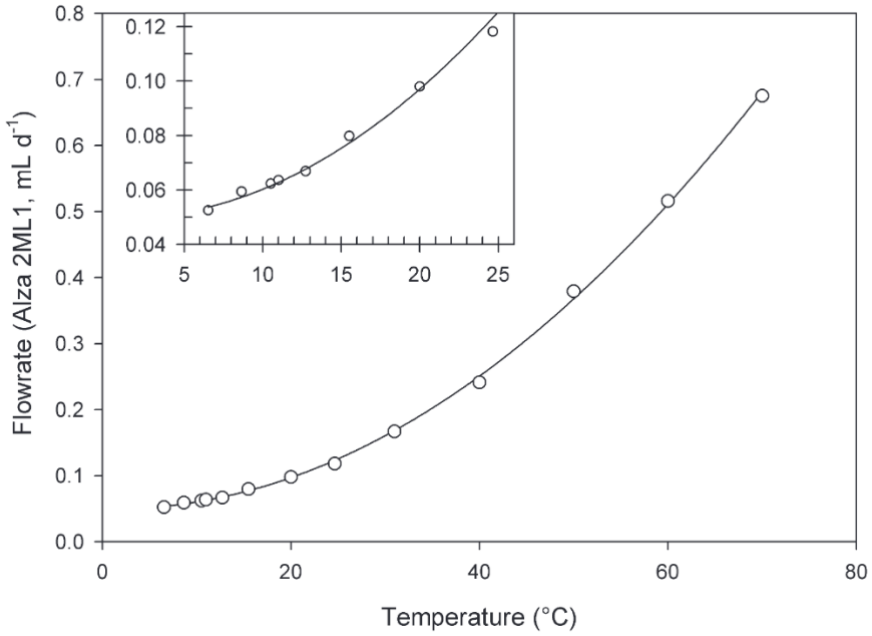

Figure 2.12: *Relationship between temperature and flow rates of osmotic pumps with Alza model 2ML1 membranes. Flow rates are normalized to a single membrane separating fresh water from a saturated brine. Inset shows a closer look at 5℃-25℃ temperatures (Jannasch et., 2004).*

2.3.2.3 Logistics of Deployment

The length of sample tubing or coils required and the total number of samplers for each experiment depends on the desired length of deployment and the analytical needs of the fluid samples (Neira et al., 2016). A single downhole package is typically 3-6 m long and includes both the osmotic pump and sample coils (Wheat et al., 2011). Depending on the duration of deployment, the Osmosamplers can have additional spools of tubing attached in a series ranging from 100 to 2400 m in length (Figure 2.11) (Jannasch et al., 2004). A typical sampler is designed to draw in 0.5 ml of sample per day over several years, which allows changes in fluid composition over days to weeks to be observed (Wheat et al., 2011). For different sampling requirements, sample tubing can be made of Polytetrafluoroethylene (PTFE), Teflon, copper coils, stainless steel, or Teflon-lined stainless steel, depending on the analytical needs of samples. Teflon and PTFE have high gas permeability and so cannot be used for dissolved gas analyses (Jannasch et al., 2004). Less permeable tubing can be made from copper, stainless steel, or Teflon-lined stainless steel, although stainless steel has a potential to corrode and be a source for contamination if analyzing trace metals. Samples have been successfully analyzed for SF_6 (Neira et al., 2016) and cesium chloride (De Jong, 2020) which were both collected with 1.1-mm-inner diameter (ID) copper coils. Major ions have also been analyzed from fluids collected in Osmosamplers using 1.0-mm-ID Teflon tubing (Wheat et al., 2003). The size of tubing used determines the volume of fluid collected. The diameter of the tubing can range from 0.5-mm-ID to 1.19-mm-ID (Wheat et al., 2011; Kastner et al., 2006; Jannasch et al., 2004). The larger diameter (1.19 mm) is more common since it holds more water per unit length of tubing (Wheat et al., 2011).

2.3.2.4 Types of Osmosampler Packages

The evolution of designing Osmosampler systems has evolved in direct connection with the evolution of the CORK system and were designed to be compatible together. Various types of Osmosampler configurations have been successfully used for both the seafloor and downhole based on the demands of a given experiment. Each Osmosampler package is designed specific to the sampling requirements of the experiment.

A standard Osmosampler package contains a single pump and multiple PTFE coils which are ideal for ship and shore-based analysis of ions in seawater and microbiological characteristics (Wheat et al., 2011). A gas Osmosampler package is best suited for measuring dissolved gas concentrations, and copper tubing replaces the PTFE tubing. The acid-addition package contains two pumps (lower and upper), a series of sample coils, and a T-connector, which connects the two pumps to the coil. The added acid serves as a fixing agent, preventing precipitation or adsorption, preserving the fluids collected for later trace metal analysis (Jannasch et al., 2004). The tracer package is designed for introduction of a chemical tracer into the borehole at a constant rate to quantify mixing of fluids within the borehole. It consists of a standard package with additional coils attached to the saturated brine outflow of the pump and comprises a single pump and two sets of sample coils (Wheat et al., 2011). A flowmeter package documents the speed and direction of fluid flow within a borehole and consists of three standard Osmosampler packages and one tracer package (Solomon et al., 2009). When using a tracer package, it is vital the injected tracer solution has concentration many orders of magnitude higher than concentrations naturally occurring, or remaining, in the formation (Wheat et al., 2011). For CO_2 injection, a tracer package should be used for the Osmosamplers deployed in the injection hole.

2.3.2.5 Fluid Analysis

After the duration of deployment, when the sample tubing is filled with formation fluid of different ages, the Osmosampler is recovered by ROV or drillship. The water-filled tubing is cut into short segments (typically 1 m), and each segment contains fluid collected during a specified period of time. These time periods are determined by identifying the interface between the distilled water and collected formation fluids, assuming collection occurred at a constant rate (Jannasch et al., 2004). If collection does not occur at a constant rate for any reason, the average flow rate can be determined from the temperature sensor records. The formation fluids from each segment of tubing are expelled into vials and sealed to preserve the water and gases inside (Dalit, 2004). Each 1-m section provides between 0.5-1.11 ml of sample, for 0.8-mm-ID and 1.19-mm-ID tubing, respectively (Wheat et al., 2011; Jannasch et al., 2004).

Although only milliliter sized, the fluid samples are sufficient to complete the following analyses: chlorinity measurements (~0.05 ml), major ions (~0.05 ml), minor ions (~0.25 ml), and trace elements in seawater (~0.1 ml) (Wheat et al., 2011). Cesium, Rubidium, Rare Earth Elements, SF_6, labeled isotopes, and fluorescent microspheres have been used in past experiments using an Osmosampler tracer package with copper sampling coils (Wheat et al., 2011; Fisher et al., 2005b).

The analysis of the fluids generates a time series of geochemical or particle concentration data showing concentration changes in the fluids on week timescales (Neira et al., 2016; Wheat et al.,

2011). If fluid analysis requires larger volumes (e.g., several milliliters), it is possible to combine samples although this would lower the temporal resolution of the time series of data (Wheat et al., 2011; Jannasch et al., 2004).

2.3.2.6 Dispersion and Temporal Resolution

Osmosamplers have shown to have difficulty preserving temporal variations in the chemical composition of the fluid samples continuously drawn into the sample coils before being recovered. These changes over time are likely caused by 1) molecular diffusion due to concentration gradients and 2) gradient dispersion from interactions within the tubing walls which both contribute to a smearing effect, or broadening of the analytical data, and a decreased temporal resolution depending on the length of the experiment (De Jong, 2020; Wheat et al., 2011; Jannasch et al., 2004).

Jannasch et al. (2004) calculated the amount of molecular diffusion within a concentration gradient over time at 25°C for a theoretical interface between distilled water and saline solution using an analytical solution derived from Fick's second law (Crank, 1975) and a molecular diffusion coefficient of 1.5 x 10^{-5} cm^{-2} s^{-1} (for NH_3) from Yuan and Gregory (1974). Fick's second law describes how diffusion within a tube leads to changes in concentration with respect to time. A step change in concentration represents the change in a concentration gradient due to an injected tracer entering the sample coil which is initially free of any concentration of tracer. This is described by:

$$C(x,t) = \frac{C_0}{2} erf/(2\sqrt{Dt})$$

Where C(x,t) is the tracer concentration at distance x from the initial boundary at time t, C_0 is the initial concentration at $x < 0$ ($C = 0$ for $x > 0$ at $t = 0$), and D is the molecular diffusion coefficient for ions in solution (Jannasch et al., 2004). Figure 2.13 illustrates concentration gradient spreading due to molecular diffusion with time, as calculated by Jannasch et al. (2004). Distances greater than zero along the length of tube represent fluids collected into the tubing before an injected tracer arrives. Negative distances represent how much tracer has been lost or diffused into another section of tubing and the amount lost depends on how quickly diffusion takes place and the amount of time the tracer remains in the tubing. For the theoretical case at 25°C, 0.8-mm-ID tubing, and a molecular diffusion coefficient of 1.5 10^{-5} cm^{-2} s^{-1} (Figure 2.13), over 99.9% of the maximum change in concentration at the interface of the distilled and saline solution due to molecular diffusion will be contained within 1 m of tubing after one year, with 2 m of temporal resolution (De Jong, 2020; Jannasch et al., 2004). However, the molecular diffusion coefficient of a given tracer may be higher with the high *in-situ* temperature in Cascadia Basin compared to the model presented by Jannasch et al. (2004).

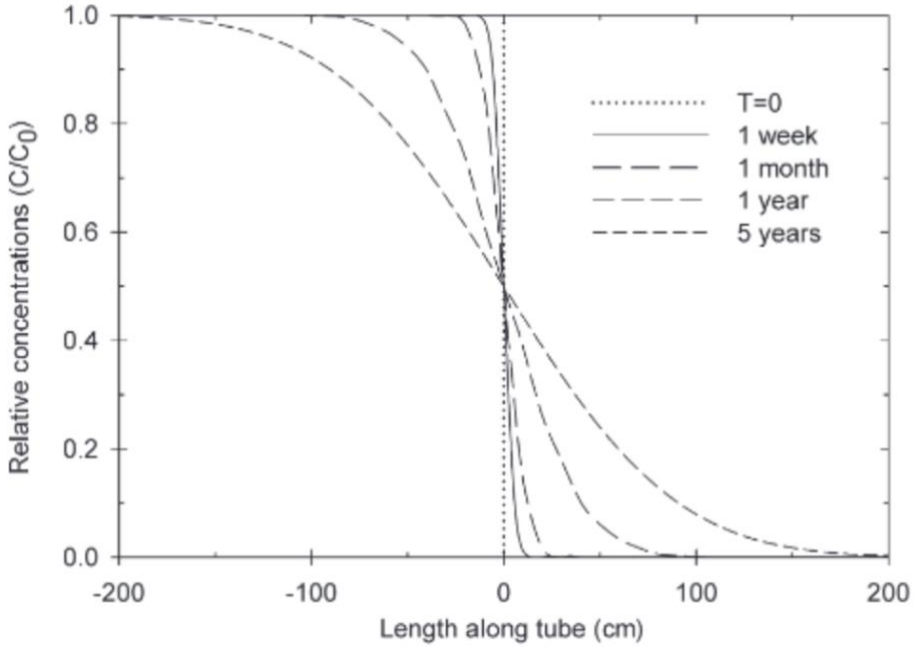

***Figure 2.13**: Example of concentration gradient spreading due to molecular diffusion within Osmosampler sample tubing (0.8-mm-ID) using a molecular diffusion coefficient of 1.5 x 10^{-5} cm^{-2} s^{-1} at 25℃ (Yuan and Gregory, 1974) and a theoretical pumping rate of 1 m/day. Each line represents the spreading distance of a step change in concentration for a given time within the tubing due to molecular diffusion alone. Negative distances represent how much tracer has been lost and depends on how quickly it diffuses and the amount of time it remains in the tube. Molecular diffusion coefficients are a function of temperature and may be higher in the Cascadia Basin where in-situ temperatures are ~65℃, much higher than the temperature used to create this model (25℃). Source: Jannasch et al. (2004).*

Dispersion of chemical gradients is a result of fluids traveling at different rates inside of the sample tubing, which may cause a portion of the injected tracer to be retained within the tubing leading to a smearing of the concentration of tracer into other parts of the sample coil due to interaction within the tubing walls (Li et al., 1974; Johnson, 2021; Jannasch et al., 2004). Taylor (1953) modeled concentration gradients in small bore tubing (mm-sized) and showed that these gradients disperse evenly around a centre plane that moves with an average fluid flow rate (i.e., advective transport) (Figure 2.14). Jannasch et al. (2004) also conducted lab experiments to test the effect of smearing caused by advection. The Osmosampler tubing (0.8-mm-ID) was alternated between seawater and altered seawater at 20ºC for a period of 3 months. The maximum change in concentration was observed to remain within 1-m of tubing after 3 months, which agrees with the theoretical calculations and confirms that at 20ºC and 1 atm, dispersion of dissolved solutes from diffusion and smearing is not more than what is expected from molecular diffusion at flow rates of less than 1 ml/day and sample tubing diameter >0.5 mm-ID (Jannasch et al., 2004; Wheat et al., 2000). It is important to note that increases in dispersion do occur if Osmosamplers are calibrated to pump fluids at faster rates (Jannasch et al., 2004).

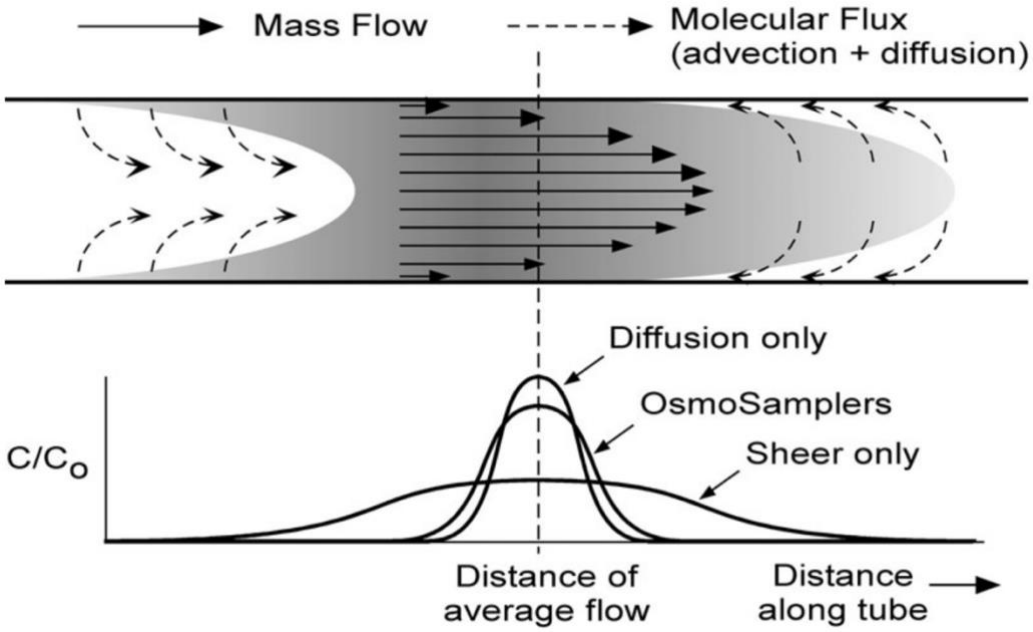

Figure 2.14*: Illustration showing dispersion of collected fluids within an Osmosampler tube. Dispersion of concentration gradients is caused by advection and molecular diffusion (dashed arrow). Larger diffusion coefficients (typical for gases) are expected to result in less smearing of the concentration data at 20ºC and 1 atm. Smearing due to advection in the sample tubing should not affect molecular diffusion when flow rates across the membrane are <1 ml/day and tubing diameter is >0.5 mm-ID. Source: Jannasch et al. (2004).*

The flow rate across the membrane is highly temperature sensitive: an increase of 1 °C will increase the flow rate up to 5% at ∼20 °C at a water depth of 940 m (Wheat et al., 2000). The *in-situ* temperature and pressure at Cascadia Basin (65ºC, 30 MPa) are higher than what was used in the laboratory (20-25ºC, 0.1 MPa) by Jannasch et al. (2004). If the operating temperature is 65°C for a downhole sampler, with a 0.5 m/day pumping rate, the length of tube containing 99.9% of the original fluid composition decreases to ± 1.5 m, indicating a resolution of 3 m after one year of deployment (De Jong, 2020). The resolution is further reduced to 4.6 m with a pumping rate of 1 m/day because there would be more fluid entering the tube per day, which would lead to more diffusion in the tube and potential smearing of the data which may be greater than the theoretical case presented by Jannasch et al (2004). The downhole Osmosamplers used for the cross-hole tracer study operated for four years with a theoretical resolution of 6 m at 0.5 m/day pumping rate. Including one year of diffusion during storage of samples prior to analysis, the resolution decreases to 6.2 m, which is equivalent to smearing over 12.4 days at the oldest end of the coil (De Jong, 2020). Preserved fluid samples should be sub-sampled soon (ideally < 1 year) after recovery to avoid additional diffusion within the tubing that decreases the temporal resolution further.

2.3.2.7 Seafloor vs Downhole Systems

Osmosampler systems can either sit on the CORK wellhead at the seafloor or be hung at depth inside the borehole along an instrument string. Osmosampler systems attached to the CORK

wellhead don't have as many concerns as ones deployed downhole and rely on umbilical and valve systems to allow fluids to be transported from the subseafloor to the seafloor without coming in contact with the steel casing (Wheat et al., 2011). They can also be recovered and replaced by using an ROV and do not require a drill ship. Since the tubing is suspended at depth, the fluids must rise through the tubing before being collected and the *in-situ* temperature and pressure are therefore not maintained, potentially producing lower quality data than would be collected downhole (Wheat et al., 2011). The formation is known to be slightly over pressured relative to hydrostatic pressure, so a pump may not be needed to pull fluids towards the seafloor when the valves are opened (Shipboard Scientific Party, 1997a). Changes in formations pressures expected during injection of CO_2 would lead to changes in flow rate of the basement fluids. It is likely injection would increase the flow rate of the fluids up to the seafloor, confirming the idea of a pump not being necessary for using wellhead Osmosamplers. Since the osmotic pumping rate is heavily dependent on temperature, it is likely an advantage to keep the Osmosampler at the wellhead where the temperature is more stable, keeping the pump rate stable compared to downhole systems that may encounter more temperature fluctuations.

For downhole fluid samplers, there is a size restriction due to the confined space inside the borehole casing but are positioned at the *in-situ* temperature and pressures and will likely have better quality fluid samples for this reason (Fisher et al., 2012; Wheat et al., 2011). The use of milk crates tied to the CORK wellhead (Figure 2.15) can serve as a sampling bay to hold additional Osmosampler tubing and overcome the limited tubing that can be deployed downhole, if needed (Orcutt et al., 2021). If downhole OS systems are installed after recent drilling, the sampler should stay in place for at least three years, since it takes at least two to four weeks for the borehole to return to its natural state post-drilling (Wheat et al., 2003, 2011). Recovery and replacement of downhole Osmosamplers is more difficult than for wellhead samplers and a drill ship may be required. This requires planning for a drill ship to be available, which is challenging.

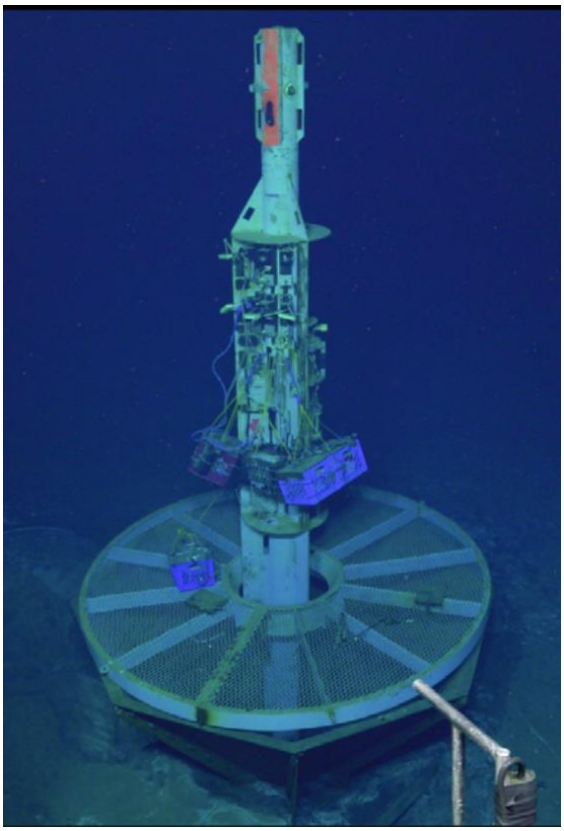

Figure 2.15*: CORK wellhead exposed at the seafloor at the North Pond site. Milk crates can be secured to the side of the CORK wellhead, which can serve as a sampling bay to extend the amount of Osmosampler tubing that can be deployed for monitoring. Source: Orcutt et al. (2021).*

The decision for whether to use wellhead, downhole, or both, will rely on cost and logistics of the experiment. The wellhead Osmosamplers are more cost effective as they do not rely on a seal and spectra line, since only the sample tubing is hung at depth. If more fluid samplers are required, then it may be wise to use wellhead samplers where more of them can be designed at a lower cost. For reference, a single downhole fluid sampler instrument string can cost up to $400,000 USD (E. Solomon, pers. comm, 2021). Although, once the instrument package is built, the cost of re-deploying is much less (E. Solomon, pers. comm., 2021). Logistics are dependent on available ship time and good weather for recovering any downhole samplers.

2.3.2.8 Caveats and Limitations

Osmosampler systems are limited by the inability to monitor data collected in real time. They also have caveats such as the harshness of the *in-situ* environment on the components of the sampler, and the presence of pipe grease from previously recovered downhole samplers.

Osmosamplers need to be physically recovered to analyze the samples collected while deployed. The effect of this limitation impacted the cross-hole tracer experiment conducted previously at this site (section 2.4). Unforeseen circumstances caused a one-year delay of recovery of the samplers, resulting in three of fourteen sample coils over pumping and losing the initial fluid samples which indicated tracer arrival at some boreholes. In addition, any delay in analysis of

samples due to remote collection can compromise the original concentrations of the preserved samples.

The small sample volumes collected during deployment of an Osmosampler is a limitation for the overall analytical program for an experiment (Wheat et al., 2000). Additionally, the sampling rate cannot be changed once the sampler is deployed so it is essential sample volumes for fluid analysis of specific tracers are constrained prior to development so there is enough sample volume for required analyses (e.g., sufficient tubing to collect fluids for one year longer than what is aimed for) (Wheat et al., 2011; Jannasch et al., 2004).

An issue with downhole samplers is that pipe grease infiltrates open cavities of the sampler (Orcutt et al., 2011), although no Osmosamplers have ever been clogged with particles or grease (Wheat et al., 2011). Additionally, the elevated temperatures and anoxic conditions in the downhole environment can be harsh on the components of the Osmosampler systems when deployed for extended periods of time. This was observed during recovery of a downhole Osmosampler deployed in Hole 1027C for a total of three years, where the protective polycarbonate outer tubing surrounding the sampler became brittle in the downhole environment overtime (Wheat et al., 2003). The temperature change between the basement (~64°C) and bottom seawater (~2°C) caused the outer tubing to shatter during recovery (Wheat et al., 2003).

2.3.2.9 Previous Use of Osmosamplers and Implications for CO_2 Injection

During IODP Expedition 301, Osmosamplers were deployed to monitor the effects of drilling, seawater-basalt interactions, and rates of fluid flow for years after the boreholes were drilled (Wheat et al., 2010). A cross-hole tracer experiment conducted as part of IODP Expedition 327 used a suite of Osmosamplers to monitor tracer transport for a total of nine years in the region planned for CO_2 injection (De Jong, 2020; Neira et al., 2016) in the region planned for CO_2 injection. Section 2.4 of this thesis includes discussion of recovery and analysis of fluid samples for this experiment.

Osmosamplers were used in a second cross-hole tracer experiment conducted in 8 Myr old basaltic crust west of the Mid-Atlantic spreading ridge at North Pond (Wheat et al., 2020). The basaltic crustal aquifer in this region is slower spreading, having a lower *in-situ* fluid temperature (<10°C) and more discontinuous sediments compared to the Cascadia Basin region. CORK borehole observatories installed during IODP Expedition 336 were used as monitoring wells with downhole OS and discrete fluid samples collected at the wellhead (Wheat et al., 2020). A cesium salt solution and bottom seawater were used as tracers. The downhole Osmosamplers consisted of standard and acid-addition packages and were deployed in the monitoring well in 2011, and the injection well in 2012 (Wheat et al., 2020, Suppl. pp. 5-7). The tracer solution was injected in 2017 using an ROV. Osmosamplers were recovered from the monitoring hole 11 days after tracer injection, and from the injection hole 6 days after tracer injection. Once recovered, the sample coils were cut into 1.2 m sections and the fluid was expelled into hot acid washed microcentrifuge tubes (Wheat et al., 2020, Suppl. pp. 5-7). The downhole Osmosamplers successfully captured cesium changes associated with tracer injection (Wheat et al., 2020, Suppl. pp. 5-7).

Osmosamplers were also used at the hydrothermal vent sites on Loihi Seamount in Hawaii to document chemical and thermal changes in hydrothermal fluid after a tectonic-volcanic event (Wheat et al., 2000). *In-situ* temperatures were 53-77ºC at one of the selected vent sites for sampling (Lohiau Vent). Osmosamplers were deployed for ~1 year (1996-1997) with 200 m of 0.8-mm-ID Teflon tubing. An additional 2 m section of tubing separating the sample intake and the osmotic pump to ensure the pump was not in contact with any venting hydrothermal fluid since the pump rate is dependent on temperature. The Osmosamplers deployed only worked for a short time before bacterial growth near the intake prevented continuous sample collection (Wheat et al., 2000). The acid-addition Osmosampler packages that are currently used prevent biological contamination (Wheat et al., 2011) and did not exist when this research was conducted. Recovered fluid samples were analyzed for all major ions and minor ions including Fe and Mn (Wheat et al., 2000).

Osmosamplers have also been used in the shallow sedimentary environment on the eastern margin of the Japan Sea, where active gas venting and gas hydrates were previously identified (Owari et al., 2019). The fluid samplers were used to record geochemical changes to sulfate (SO_4^{2-}), chloride (Cl^-), methane (CH_4), and ethane (C_2H_6) dissolved in sediment pore fluids (30 cm below seafloor) over the course of one year. This experiment monitored for dissolved gases, so copper tubing was used. The copper tubing was 322.27 m long with 1.1-mm-ID tubing which was deployed for 374 days (equivalent to 187.02 m of tubing). The sample tubing was cut every 50 cm, which corresponds to one sampling volume (length) per day (Owari et al., 2019). Each 50-cm piece was divided into sections: 30 cm (equivalent to 300 μl) for gas analyses and 20 cm (equivalent to 200 μl) for ion analyses (Owari et al., 2019). The documented flow rate was 0.475 ml/day at an *in-situ* temperature of 0.22-0.34°C, a lower rate than expected. The expected flow rate was 0.6 ml/day which was based on the diffusion model presented by Jannasch et al. (2004) of NaCl in a distilled water-filled coil (Owari et al., 2019). The difference between expected and observed flow rates can be explained by the differences in adsorption rates of individual membranes (Owari et al., 2019). Temperature fluctuations throughout the experiment were a maximum change of 0.026°C, so the sampling rate was considered constant (Owari et al., 2019).

More recently, IODP Expedition 375 used Osmosamplers and an Osmo-flowmeter (Solomon et al., 2009) to monitor the temporal variations in fluid geochemistry, temperature, pore fluid pressure, and flow rate in a shallow fault zone interval at the Hikurangi Subduction Margin in New Zealand (Saffer et al., 2018). An Osmo-flowmeter includes four Osmosamplers around a central tracer port which simultaneously sample fluids in all four directions to determine relative fluid direction and rates of fluids moving past the borehole (Solomon et al., 2009). CORK-II borehole observatories were installed and a 22 m long Osmosampler package with a Teflon coil was installed at ~315 mbsf in the monitoring well (Saffer et al., 2018).

Solid Carbon is planning to use injected tracers to track the injected fluid in the crust during a CO_2 injection experiment and estimate the extent of CO_2 dissolution and carbonate mineral formation. Monitoring wells surrounding the injection hole will host Osmosamplers to collect fluid samples both at the wellhead and downhole. Important parameters to consider for deciding on the length of the Osmosampler tubing include:

- flow rate across the membrane (which is affected by the *in-situ* temperature and diameter of tubing chosen);

- tube diameter (the smaller the tube, the less dispersion and slower flow rate);
- selection of seafloor (wellhead) or downhole system;
- analytical needs of fluid samples (i.e., sample size);
- duration of deployment; and
- back-up time in case of delay in recovery.

In case of delays in recovery, it might be helpful to include length of tubing for two years, even if the Osmosamplers are deployed for one year and recovered. A standard Osmosampler consists of four 305 m long 1.2-mm-ID sample tubing, which can sample 0.5 ml/day at the *in-situ* temperature in the basaltic basement in Cascadia basin (Fisher et al., 2011e). For a two-year deployment at 65ºC and 30 MPa, ~6 spools of 300 m 1.2-mm-ID tubing could be used. This is estimated to collect ~1300 ml of sample within 1.8 km of tubing (Wheat et al., 2003). These estimates are based on deployment of Osmosamplers for two years in the CORK at ODP Site 1027 in the Cascadia basin (Wheat et al., 2003), where the observed interface between distilled water and basement fluids spread less than 3.5 m into the tubing over two years, collecting ~1.0 ml/day. A one-year deployment would then require ~3 spools of 300 m tubing, with fluids being collected at ~0.5 ml/day.

2.3.3 Mobile Pumping Systems

In addition to fluid sampling using Osmosamplers, mobile pumping systems can also be deployed for collection of formation fluids at a CORK wellhead and may be useful for measurements that require a volume of sample larger than the Osmosamplers. Mobile pumping systems are pumping systems that were modified from the GeoMICROBE sled (Cowen et al., 2012), which is an autonomous system that is connected to the CORK fluid delivery lines (Figure 30) and can collect formation fluid samples at timed intervals for up to one year. Mobile pumping systems are not autonomous but are operated by ROVs or human-operated vehicles (HOVs) and are used for short-term sampling of large volumes of basement fluids in real time (Cowen et al., 2012). A pump, electronics including a microcontroller, flow sensor, and other sensors (temperature, O_2) are their main components (Cowen et al., 2012). The components are held in a milk crate that is secured to the side of the ROV basket and can collect many litres of basement fluids from the CORK fluid delivery lines (Figure 30) and directed into medium or large volume bag samplers (Cowen et al., 2012). The fluid delivery lines should be flushed with three times their volume prior to sampling (Lin et al., 2012). The ROV and collected samples are brought back up to the ship at sea and analyzed or preserved and brought back to a lab onshore.

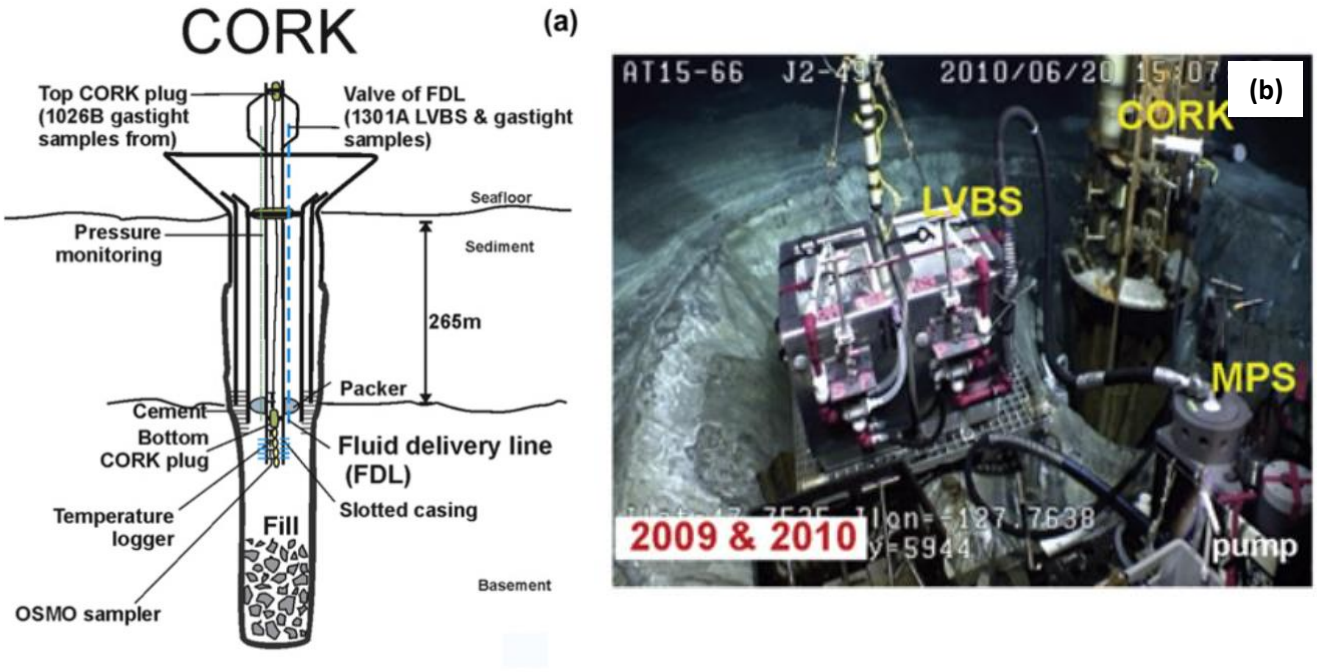

Figure 2.16*: Sampling methods for collection of basement fluids using a mobile pumping system (MPS) connected to the CORK wellhead in Cascadia Basin. (a) Not-to-scale diagram of CORK showing location of fluid delivery line (FDL) (blue dotted line), which are stainless steel for both CORKs in Hole 1301A and Hole 1026B; (b) Image of CORK wellhead at Hole 1301A showing MPS and Large Volume Bag Sampler (LVBS) used to collect large volumes of pristine basement fluids in real time from the CORK FDLs. The LVBS includes a custom-made 60 L Tedlar bag housed in a Nalgene high density polyethylene box. Source: Lin et al. (2012).*

This system has been used to collect formation fluids from a CORK wellhead in IODP Hole 1301A in the Cascadia Basin (Figure 2.16) (Lin et al., 2012). The fluids were collected at a sampling rate of 200-600 ml/min from CORKs that have 1/8" inside diameter fluid delivery lines (Lin et al., 2012). The newer CORKs with 1/2" inside diameter fluid delivery lines have sampling rates of >500 ml/min (Cowen et al., 2012). A temperature sensor was used to monitor the temperature of the fluids during flushing of the fluid delivery lines and subsequent sampling (Lin et al., 2012). After recovery to the ship, fluids from the sample bags were transferred to sample vials and analyzed for alkalinity, pH, major ions, total organic carbon, total dissolved iron, nitrate, phosphate, and total dissolved nitrogen (Lin et al., 2012). This study helped improve the technique for sampling crustal fluids from CORKs. The mobile pumping system was also deployed in 2011 at CORKs in Holes 1362A and 1362B (Cowen et al., 2012) and used to collect basement fluid samples from CORKs at North Pond (western flank of Mid-Atlantic ridge) in addition to utilizing Osmosamplers (section 4.6.1.6) (Wheat et al., 2020).

The mobile pumping sampling method could benefit the monitoring program for Solid Carbon by increasing the volume of fluids that can be sampled in real time to observe changes in the formation fluids after CO_2 injection. Although a ship is required to deploy the ROV, the mobile pumping system could be deployed for a short time when Osmosamplers are being recovered from the CORKs. Formation fluids collected in sampler bags could be analyzed for dissolved inorganic carbon, alkalinity, and major and minor ions and trace elements. The fluids collected *in-situ* with the Osmosamplers can then be used for analysis of added tracers, or vice versa, depending on the tracers chosen and the volumes required for analysis.

2.4 Cross-Hole Tracer Experiment

2.4.1 Overview

During IODP Expedition 327 (Fisher et al., 2011f), a 24-hour cross-hole tracer injection experiment (Section 2.2.1.3) was conducted using Hole 1362B as the injection well and utilizing four borehole observatories equipped with CORKs instrumented with Osmosamplers to collect fluid samples for analyses (Figure 2.17). The tracer injection into Hole 1362B was conducted before a CORK was deployed in that hole. The cross-hole nature of monitoring the injected tracer plume from multiple boreholes after injection and collecting fluid samples with temporal resolution assessed transport rates, direction, and pathways of lateral fluid transport through oceanic crust in this location (Figure 2.17). This was the first cross-hole tracer experiment completed in ocean crust using multiple borehole observatories with isolated depth intervals and autonomous fluid samplers deployed over a total of nine years (De Jong, 2020; Neira et al., 2016). The results of this experiment provide a backbone for the possibility of using tracers for the CO_2 demonstration. Osmosamplers collected fluids from both the wellhead and downhole at two boreholes in the direction of natural fluid flow towards the north (1026B, 1362A) and one hole located in the direction opposite to natural fluid flow (1301A) and the injection hole (1362B) (Figure 2.17). These samplers were retrieved, replaced, and data was downloaded from temperature and pressure loggers during multiple site visits throughout the experiment.

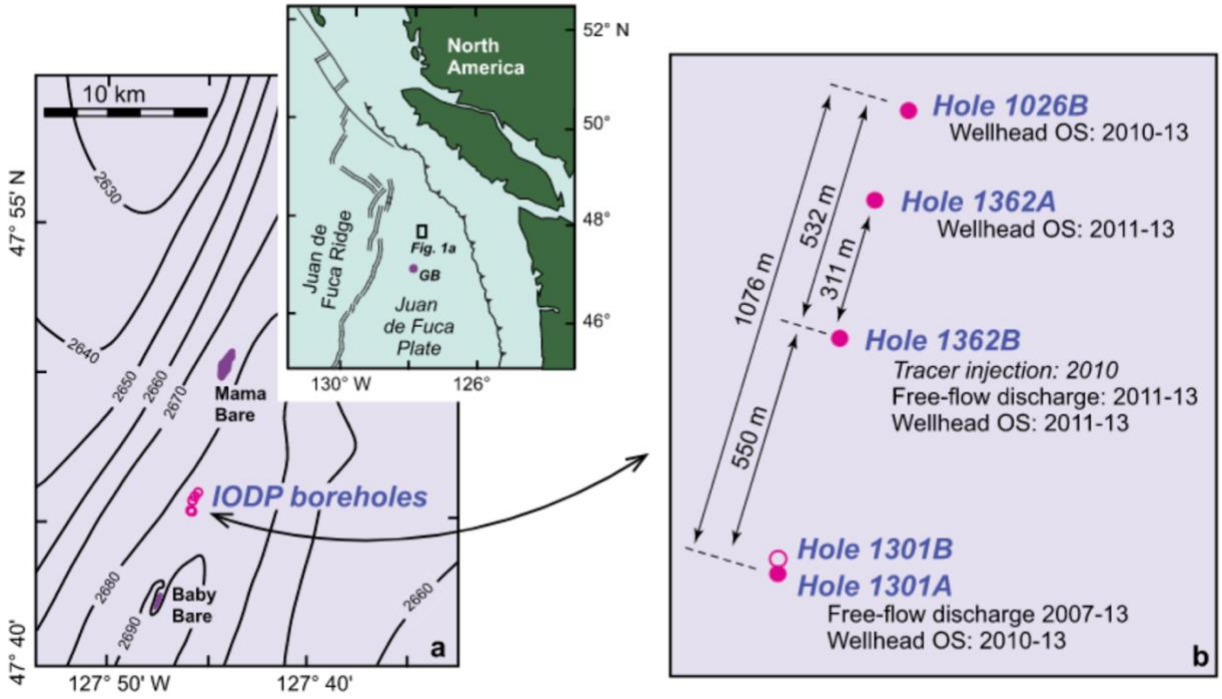

Figure 2.17*: Boreholes used for 24-hour cross-hole tracer experiment. a) Map of region showing experimental boreholes along the eastern flank of the Juan de Fuca ridge. b) Detailed map showing distances between boreholes used for cross-hole tracer experiment. Source: Neira et al. (2016).*

2.4.2 Recovery of Fluid Samplers

The Osmosamplers that operated at the wellhead in Holes 1026B and 1301A were installed during Expedition 301 and allowed formation fluid to flow up the boreholes at a rate of ~1ml/sec through 3-mm outside diameter (OD) tubing and the Osmosamplers drew in fluid at a rate of ~0.8 ml/day (Neira et al., 2016). Holes 1362A and 1362B contained downhole Osmosamplers installed prior to the 24-hour tracer injection during Expedition 327 (Fisher et al., 2011b). Both Holes 1362A and 1362B did not have wellhead Osmosamplers installed during the first year post injection to allow equilibration of pressure, thermal, and geochemical conditions after drilling as part of Expedition 327 (Neira et al., 2016; Fisher et al., 2011b). Table 2.3 provides a summary of when the fluid samplers were deployed and recovered, depths of downhole fluid sampling packages, and rapid fluid flow (entering/discharging) recorded in boreholes.

During a servicing cruise, one year after injection, a new generation (section 2.3.2.7) of wellhead Osmosamplers and fittings were instrumented to the wellheads on the CORKs in Holes 1362A and 1362B at 313- and 316-days post injection, respectively (Neira et al., 2016). These Osmosamplers had a larger diameter tubing that permitted more rapid flow (~20-50 ml/sec) of fluids from depth in these holes (Neira et al., 2016). On the same cruise, a flowmeter was installed, and the ball valve opened on the wellhead in Hole 1362B (injection hole) to allow discharge of overpressured formation fluid to flow at a rate of 4 ± 1 l/sec (Fisher et al., 2011f). This was an intentional attempt to draw tracer fluid to flow back to the injection hole that may have migrated away (Fisher et al., 2011f) and to induce pumping conditions (De Jong, 2020).

Two years later, the ball valve for Hole 1362B was closed and Hole 1362A borehole was opened, discharging fluids at a similar rate to Hole 1362B (De Jong, 2020).

Downhole Osmosamplers were recovered from Holes 1362A, 1362B, and 1026B in 2014, along with wellhead Osmosamplers from all holes. New wellhead Osmosamplers were installed for operation in Holes 1362A and 1362B until retrieved in 2019 (De Jong, 2020). At present, there are no Osmosamplers installed at the site (De Jong, 2020).

Table 2.3*: Summary of boreholes and fluid samplers used for the tracer injection experiment. Adapted from Neira et al. (2016), De Jong (2020), Fisher et al. (2011e).*

Hole	Seafloor Fluid Samplers Deployed[a]	Downhole Fluid Samplers Deployed[b]	Depth of Sampler Package (mbsf)[c]	Tracer[d]	Rapid Fluid Flow[e]
1301A	2010-2014	2009-2019	276-290	M	2004-2007 (down) 2007-2014 (up)
1301B	2010-2014	No sampler installed	-	M	2004-2008 (down)
1362A	2011-2014 & 2019	2010-2014	438-466	M	-
1362B	2011-2014 & 2019	2011-2014	279-310	I/M	2011-2014 (up)
1026B	2010-2014	2010-2014	200-213	M	Slow leak since install (up)

Table Footnotes:

Hole 1027C did not serve as a monitoring well for the tracer injection experiment.

[a] Years of recording data from seafloor (wellhead) fluid samplers. Seafloor systems were installed before tracer injection for Holes 1026B, 1301A, and 1301B, but installed one year after tracer injection for Holes 1362A and 1362B. Some of the wellhead samplers from 1362A and 1362B were recovered in 2014, and remaining wellhead samplers recovered in 2019. No samples were recovered from Hole 1301B from sampling line clogged.

[b] Years of recording data from downhole fluid samplers. Downhole systems were installed before tracer injection for Holes 1026B, 1301A, 1362A, 1362B. Sampler installed downhole in Hole 1301A by submersible *Alvin* but was not recovered from the hole in 2014. Acid addition fluid sampling package (see Section 2.3.5) installed downhole in Hole 1362A but malfunctioned resulting in no data. No downhole sampler was installed in Hole 1301B.

[c] Depth range for downhole fluid sampling includes the entire fluid sampling package and temperature loggers along the spectra line

[d] I = injection hole; M= tracer monitoring location (wellhead and/or downhole)

[e] Cold water pumped into all holes during drilling. Hole 1026B has leaked formation fluid at a slow rate since installation in 2004. Holes 1301A and 1301B were not properly sealed during installation with cold bottom water entering these holes for several years. The flow direction in Hole 1301A spontaneously reversed to discharge formation fluids in 2007 (~5 +/- 2 l/sec). Hole 1301A and 1301B were cemented to stop flow in 2008. Hole 1301B was sealed but Hole 1301A continued to discharge fluids. Flow from Hole 1362B (~4 +/- 1 l/sec) was initiated in 2011 by ball-valve until 2013, when Flow from Hole 1362A was initiated as part of the cross-hole tracer experiment.

2.4.3 Analysis of Fluid Samples

Post-recovery, the sample coils were extracted from the samplers, unspooled, and cut into 0.1-1 m length sections and sealed with noble gas clamps. Every 10 m of coil, three 1-m sections were chosen for SF_6 analysis, and the remaining coil was archived for future analysis. Each 1-m

section produced ~1.1 ml of fluid (Neira et al., 2016). The University of California Santa Barbara (UCSB) completed the analysis of the SF_6 samples using a gas chromatography (GC) instrument and the trace metal samples were prepared at MBARI and analyzed at the University of California Santa Cruz (UCSC) using inductively coupled plasma mass spectrometry (ICP-MS) (De Jong, 2020).

Neira et al. (2016) calculated pumping rates for each Osmosampler deployed which differed for each system based on the duration of deployment and the length of coil that contained collected formation fluids. If a sample coil was entirely filled with borehole fluid, the total amount of water pulled into the front-end fluid reservoir was calculated based on dilution. The typical pumping rate found for all wellhead Osmosamplers was ~0.8 ml/day which is equivalent to ~0.75 m/day of sample coil (Neira et al., 2016). This pumping rate is higher than was calibrated (0.5 ml/day) indicating *in-situ* temperatures almost 10°C higher than predicted (De Jong, 2020). A tubing length of 300 m (0.8 ml/day pump-rate, 1.1-mm-ID tube diameter, four years deployed) was used for this experiment (De Jong, 2020). The planned CO_2 injection experiment for Solid Carbon may need more than 300 m of sample tubing to account for potential differences in pumping rates during deployment of the Osmosamplers (De Jong, 2020).

Even with sample loss and a decrease in temporal resolution, the raw data from connecting series of four sample coils from a single Osmosampler is shown to preserve the natural variability of the data (Figure 2.18). This is likely due to the formation being heterogeneous, as a decrease in temporal resolution of the data in a homogenous system could smooth the data further (De Jong, 2020).

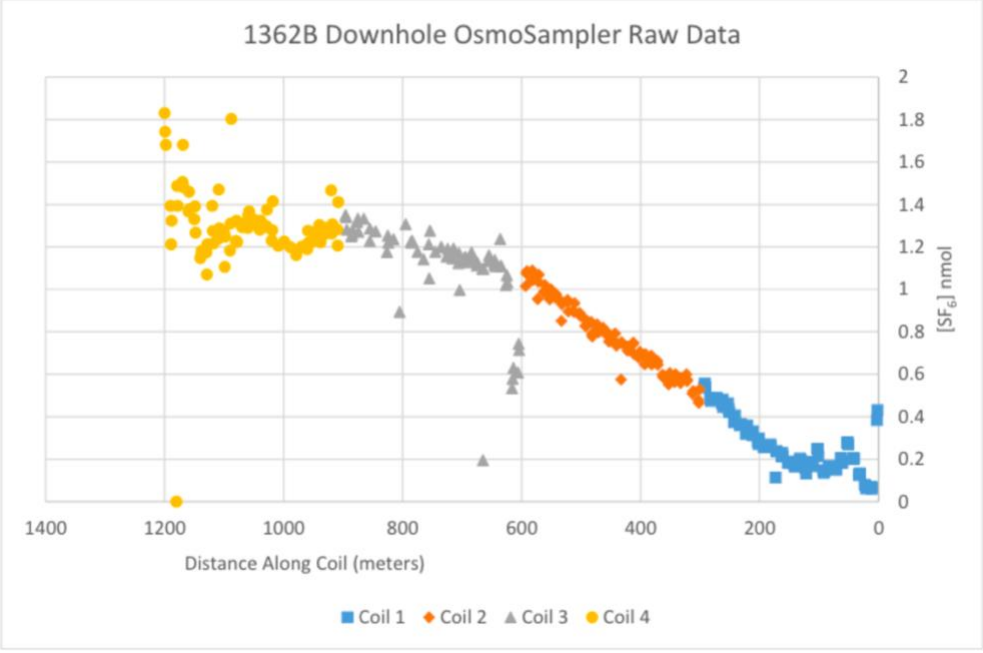

Figure 2.18: *Plot of raw data from downhole Osmosampler in Hole 1362B showing continuity between in-series of sample coils. Sample loss is present (due to faulty connectors or inadequate sealing during storage), but a general pattern of continuity is present (De Jong, 2020).*

2.4.4 Results

Neira et al. (2016) reported the initial SF_6 tracer results from the analysis of wellhead fluid samples collected in 2014. De Jong (2020) reported the results from the tracer experiment that Neira et al. (2016) did not have at the time of their analysis, which includes additional SF_6 data and the downhole tracer breakthrough of Cesium (Cs) in Hole 1362A between summer 2014 until the end of the experiment in 2019. No other tracers were detected above the detection limit outside of SF_6 and Cs throughout the duration of the experiment (De Jong, 2020).

Figure 2.19 shows the wellhead SF_6 tracer concentration data plotted from all four CORKs along the south to north transect illustrated in Figure 2.17. Hole 1301A (Fig. 2.19d) (550 m upgradient of injection hole) had the most complete record of first tracer arrival, with background values present until 258 days post injection where SF_6 concentrations ($[SF_6]$) increased and peaked to ~30 nanomolar (nM) of SF_6 at 305 days post injection, then decreased to background levels (Neira et al., 2016). Fluids in this sampler contained tracer arrival in units of nM, while the tail of the tracer breakthrough curve which extended past 1000 days post injection contained <25 picomolar (pM) of $[SF_6]$. A 2012 servicing cruise to recover and replace Osmosamplers was delayed until 2013 and caused the OS in Hole 1301A to over pump the sample coil, resulting in ~285 days (between 311-606 days post injection) of collected fluid to be expelled before the Osmosamplers could be recovered. As a reminder, Hole 1301A was not well sealed and bottom water flowed into this borehole from 2004-2007 when it reversed flow, discharging fluid at a rate of ~5 l/sec (De Jong, 2020). Hole 1026B (Fig. 2.19a) (532 m downgradient from injection hole) shows initial tracer arrival at 165 days post injection (90 days before arrival at 1301A), and exhibits the same pattern as Hole 1301A, where $[SF_6]$ increased over ~100 days with the highest $[SF_6]$ at ~200 pM, but in the following two years samples were >90% bottom seawater with no $[SF_6]$ (Neira et al., 2016).

The delay in servicing also affected the fluid samples from Holes 1362A and 1362B. Once recovered in 2013, the oldest fluids were from 466 days post injection (1362A) and 363 days post injection (1362B) with elevated $[SF_6]$ recorded for the next two years. Fluid samples from Hole 1362A were found to contain 5-96% formation fluid that varied with bottom seawater with time identified by major ion concentrations which are well constrained for the crustal fluid in the region (Elderfield et al., 1999). $[SF_6]$ were corrected for these samples to account for the fraction of formation fluid (by dividing the raw tracer concentrations injected by 0.05-0.96). There is no record of initial SF_6 arrival in Hole 1362A because the borehole was not instrumented at the wellhead until the front of the tracer plume had already passed the borehole. Injection Hole 1362B contained the highest tracer SF_6 concentrations at ~52 nM, or 1/1000 of $[SF_6]$ in the injected fluid (Neira et al., 2016; Fisher et al., 2011f). The wellhead fluid samples collected from this hole were found to contain a higher proportion of bottom seawater compared to fluid samples collected from Hole 1362A. Samples from Hole 1026B were reported with the uncorrected $[SF_6]$ due to borehole fluid accounting for < 10% of the samples recovered (Neira et al., 2016).

Downhole [Cs] data show decreased concentrations at the injection hole initially, although [Cs] remained an order of magnitude higher than background values (>8 nM) for the rest of the experiment (Figure 2.21c). There was a sudden peak of [Cs] in the data from the injection hole between 310- and 321-days post injection (Figure 2.21c). At Hole 1362A, downhole [Cs] were

detected above background levels as quickly as 9 days post injection, with the data exhibiting a dual breakthrough of Cs at this hole. The initial breakthrough occurred at 24 days post injection with the second breakthrough at 104 days post injection. Between these peaks, [Cs] dropped below background levels (Figure 2.21b) with values similar to surface seawater that the injectate was composed of. [Cs] remained elevated at Hole 1362A until 500 days post injection, then decreased back down close to background levels until the end of the experiment (Figure 2.21b) (De Jong, 2020).

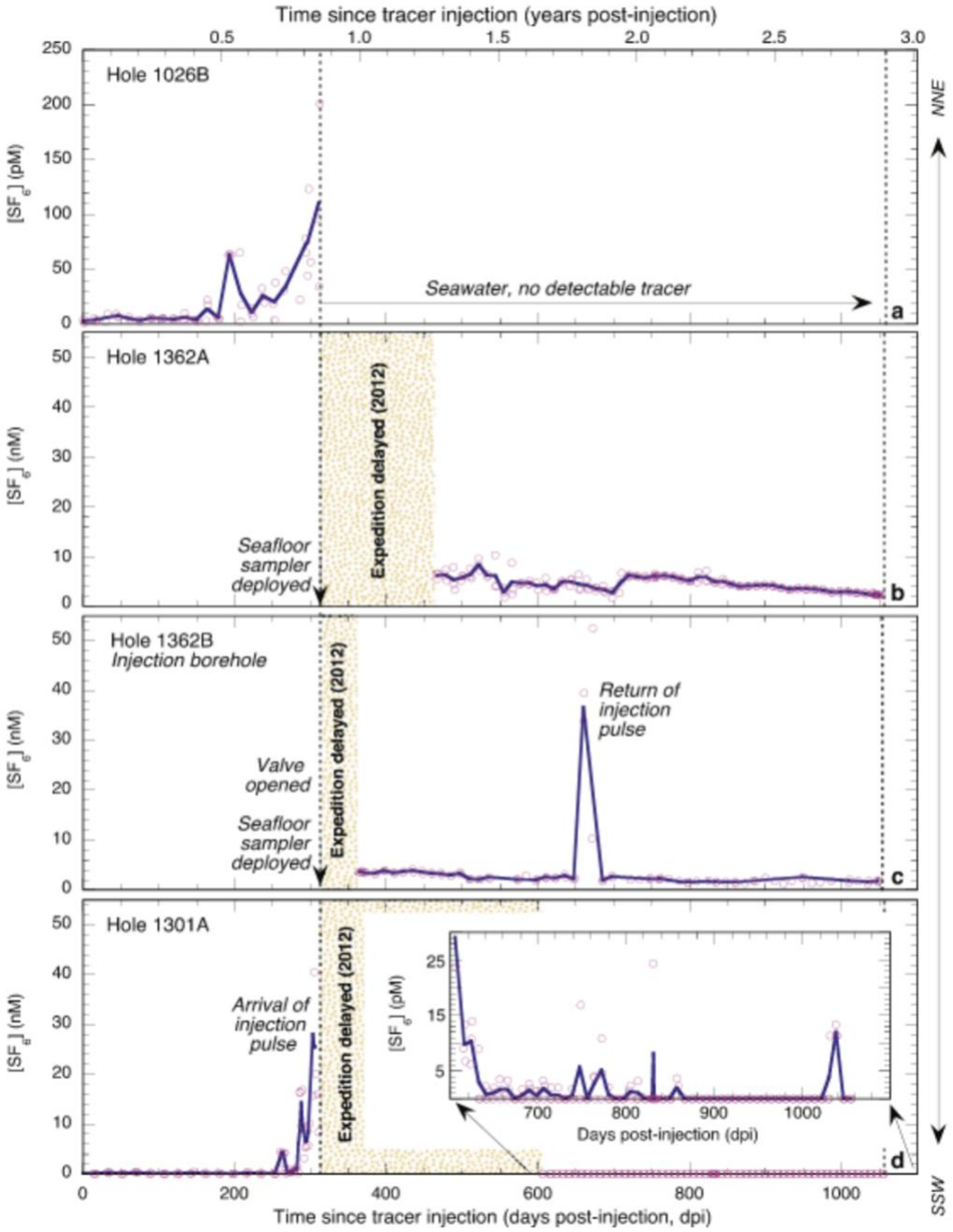

***Figure 2.19**: SF_6 concentration curves from four CORKs along a south to north transect between 2010-2013. Dotted lines are when fluid samplers were replaced or deployed. Open circles are individual measurements. Solid blue line is the mean of three consecutive samples, except for Hole 1362B which shows the mean of two consecutive samples. Standard deviation for all plots is ± 7 nM. Note that [SF_6] from Hole 1026B are in units of pM, and [SF_6] for all other holes reached units of nM. Delay in servicing expeditions is shown in gold dots. Source: Neira et al. (2016).*

2.4.5 Data Interpretations

Interpretation of the wellhead fluid sample results incorporated downhole thermal measurements, physical observations from packer testing, and cores obtained from previous drilling expeditions (Neira et al., 2016). From these data, a conceptual model was built which coupled the results of the fluid samples from the tracer experiment with modeling work previously completed by Winslow et al., (2016) and Hutnak et al., (2006). The fluorescent microspheres, stained bacteria, Erbium, and Holmium tracers were not detected above the detection limit throughout the duration of the experiment, likely to be caused by low signal to noise ratio in the formation fluids (De Jong, 2020).

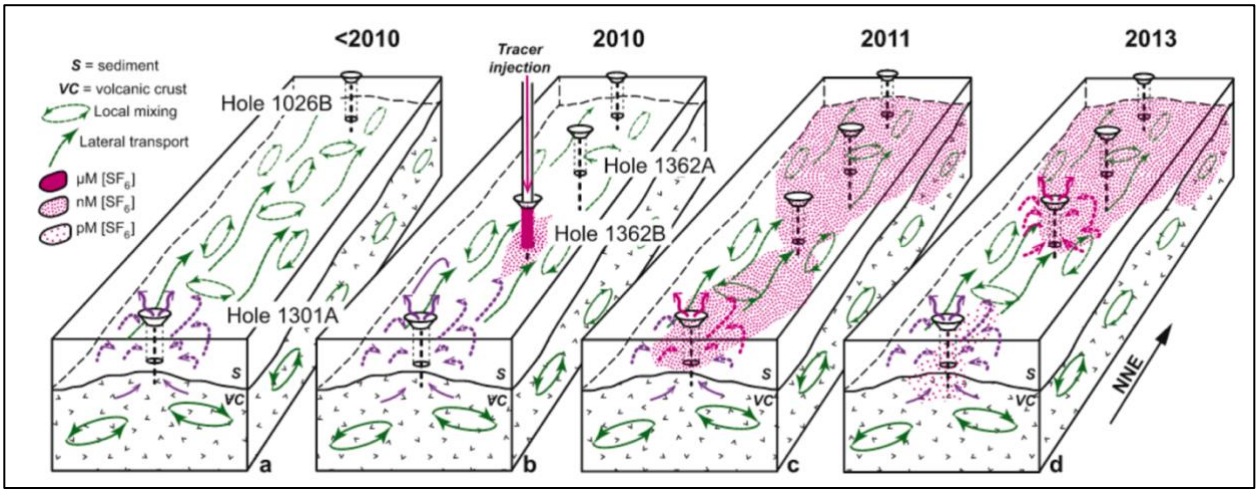

***Figure 2.20:** Schematic showing interpretations of regional fluid flow from 24-hour cross hole experiment during IODP Expedition 327 using SF_6. Purple arrows indicated flow to discharging boreholes containing little to no SF_6. Pink arrows and dots indicate elevated [SF_6]. Before experiment (a) flow is dominantly south to north with local mixing. During experiment (b) SF_6 tracer injected into Hole 1362B prior to CORK installation. One year after experiment (c) tracer arrives at Holes 1301A, 1362A, and 1026B. Two years after experiment (d) and two years after opening valve on the CORK wellhead in Hole 1362B. Formation fluid with tracer discharged from Hole 1362B at 4 ± 1 l/sec. Tracer concentrations remained high (nM) in Holes 1362A and 1362B. Fluids in Hole 1301A had lower concentrations (pM), because the dominant transport direction was inferred from south to north. Not to scale. Source: Neira et al (2016).*

From the injection Hole 1362B, the majority of the SF_6 plume was transported immediately to the north since Hole 1026B saw initial tracer arrival before the other instrumented boreholes (Figure 2.20). Considering the lack of tracer breakthrough seen at Hole 1362A, Hole 1362A

detected higher SF_6 concentrations and a mixture of bottom seawater and formation fluid that varied irregularly with time compared to Hole 1362B for the duration of the experiment, which indicated leakage occurring at the connection near the sampling coil inlet (Neira et al., 2016). Hole 1026B also showed evidence for leakage, due to borehole fluid accounting for <10% of the samples recovered and a higher proportion of bottom seawater compared to Hole 1362A. The initial decline of [Cs] at the injection hole is interpreted to be caused by Cs being transported away from the injection hole by the natural gradient (Cs was injected in two short pulses compared to continuous injection of SF_6 throughout the experiment). Local mixing did not homogenize the Cs into a single pulse as previously hypothesized by Fisher et al. (2011f). The [Cs] differed between Holes 1362A and 1362B, providing evidence of Cs acting not completely conservative and the effects of the pulsed injection are seen in the dual breakthroughs in the data at 24 and 290 days with [Cs] below background levels between these peaks (Figure 2.21a & b).

Once the ball-valve was opened at the injection hole one year after injection, Cs-rich fluid flowed back toward the injection hole as shown by the sudden peak in the data at Hole 1362B between 310-321 days post injection and the elevated [Cs] (> 50 nmol/l) from 321 days post injection onward, compared to [Cs] observed (< 50 nmol/l) before wellhead discharge was initiated (Figure 2.21c). Like the Cs data, the wellhead fluid sample data is consistent with SF_6 remaining higher at Hole 1362A than Hole 1362B for more than two years which confirms some of the SF_6 continued flowing downgradient when the ball-valve was intentionally opened at the wellhead of Hole 1362B (De Jong, 2020; Neira et al., 2016). Furthermore, the timing of SF_6 arrival at 1026B suggests rapid flow to the north more than the south bringing greater mass transport to the north, although there was a lack of early detection of Cs in Holes 1026B and 1301A which provides additional evidence of Cs acting non-conservatively compared to SF_6 (De Jong, 2020; Neira et al., 2016). Moreover, regional flow rates through the aquifer were observed to be greater than the rate of discharge from Hole 1362B (4 ± 1 l/sec), which allowed tracer to keep flowing north towards Hole 1362A after the ball-valve was opened (Neira et al., 2016). Using velocity recorded at Hole 1301A, initial tracer peak occurred at ~310 days post injection indicating velocity of ~2 m/day, which was induced by continuous injection of SF_6 tracer during the first 24 hours and active discharging at Hole 1301A throughout the experiment. Comparing the travel times and distances between Holes 1026B and 1301A (1026B saw tracer 90 days before 1301A), the peak of the tracer plume probably reached Hole 1362A less than 90-120 days post injection, indicating a velocity of more than 3 m/day for tracer transport to the north from the injection hole (Neira et al., 2016). The lack of [SF_6] and > 90% bottom seawater detected at Hole 1026B after the OS was replaced ~300 days after injection indicates a failed connection between the wellhead and OS fitting (Neira et al., 2016).

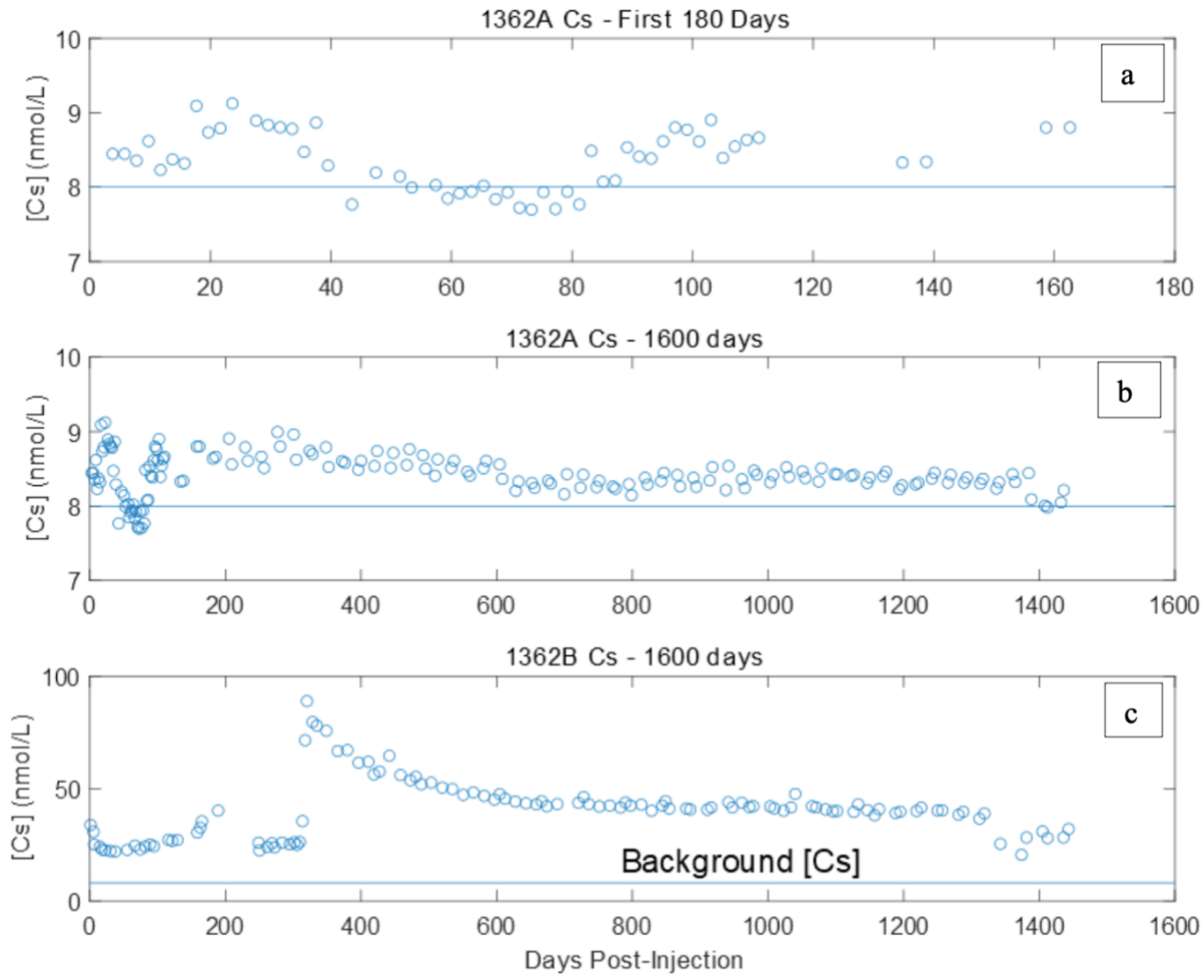

Figure 2.21: *Cesium (Cs) tracer concentration plots for Holes 1362A and 1362B. a) [Cs] recorded in Hole 1362A over first 180 days. b) [Cs] recorded in Hole 1362A over 1600 days. c) [Cs] recorded in Hole 1362B over 1600 days. Blue line represents background concentrations of Cs at each Hole. Source: De Jong (2020).*

One interpretation of the data is that the tracer plume that had originally flowed north of Hole 1362A was pulled back when Hole 1362B was opened for discharge, but this is not consistent with mass balance calculations by Neira et al. (2016) and would indicate a regional flow rate lower than the discharge rate from Hole 1362B. To confirm this was not the case, Neira et al. (2016) used tracer concentrations and borehole flow rates from thermal data to determine rates of tracer mass transport through the crust. For flow to continue south to north even after wellhead discharge was initiated at the injection hole, the regional crustal flow rate must be higher than the combined rates of discharge from Holes 1301A and 1362B (> 9 ± 3 l/sec). The rates of tracer concentration recorded in Hole 1362A show that 15-30 x 10^{-4} mol SF_6 flowed to the north during 460-1050 days post injection, which is two to five times as much SF_6 as flowed to the south towards Hole 1301A. The total mass transported to the north was likely to be much greater but

there is no tracer record from Hole 1362A for the first 460 days post injection when the highest tracer concentrations likely had passed this hole (Neira et al., 2016).

There is a lack of evidence that additional [SF_6] flowed south of Hole 1362B for the duration of the experiment, as tracer concentrations were sustained at much lower concentrations in Hole 1301A (decreased to <25 pM) compared to Holes 1362A and 1362B during the same time interval, where concentrations remained 100x to 1000x greater during the same period (Figure 34) (Neira et al., 2016). This can be explained by a larger amount of tracer remaining close to the injection hole, mixing within a part of the crust that could be poorly connected to the most transmissive flow channels with a fraction of tracer drawn in and transported by rapid flow downgradient to the north towards Hole 1362A (where SF_6 concentrations remained elevated). The Cs data also suggests a larger amount of tracer remaining close to the injection hole, in addition to the lack of detection of Cs above the detection limit in Holes 1026B and 1301A. The peak of [SF_6] in Hole 1362B between 659-672 days post injection (Figure 2.19c) could not have come from the south since the initial SF_6 that arrived at Hole 1301A was discharged into the ocean due to the hole remaining unsealed with continued discharge of formation fluid into the ocean throughout the experiment (cementing the hole during Expedition 301 was unsuccessful). The anomaly of detection of [SF_6] at Hole 1301A could represent a preferred fluid pathway or local convection cell that delivered a small amount of SF_6 upgradient, as suggested by previous transient numerical simulations where an outcrop-to-outcrop hydrothermal siphon can coexist simultaneously with secondary (local) convection, initiating flow in any direction, even opposite to the dominant regional flow direction (Winslow et al., 2016; Stein and Fisher, 2003). Additionally, no more than one-third of the fluid that discharged from Hole 1301A could have originated from the injection hole since overall flow from Hole 1362B to Hole 1301A was 1.7 l/sec, compared to 5 ± 2 l/sec actively discharged from Hole 1301A (Neira et al., 2016).

The rapid detection of Cs at Hole 1362A surpasses linear velocity rates determined by Neira et al.'s (2016) analysis of the initial tracer breakthrough at Hole 1026B. De Jong (2020) applied the same calculation of linear velocity that was applied to SF_6 by Neira et al. (2016) (between the injection hole and Hole 1026B). De Jong's (2020) calculation shows Cs moved at a faster rate than SF_6 (Cs peak arrived at Hole 1362A after 24 days; advection of 311 m and linear velocity of 13 m/day compared to linear velocity of ~3 m/day for SF_6 arrival to Hole 1362A between 90-120 days post injection). De Jong (2020) suggests fracturing is one possibility to have caused Cs to advect 311 m in 24 days at a velocity of 13 m/day and then slowed and advected the remaining 220 m towards Hole 1026B in 326 days at a velocity of 0.7 m/day, although it is difficult to deduce that cesium, a non-conservative tracer, would travel four times faster than SF_6, a conservative tracer, in the formation just based on fracturing alone.

2.4.6 Improvements to Understanding of Hydrothermal System

This cross-hole tracer experiment verified observations previously made regarding ridge-parallel directional flow (section 2.2.3) and made improvements to the understanding of the hydrothermal system. The persistent detection of elevated [SF_6] in Holes 1362A and 1362B support south to north flow direction driven by the hydrothermal siphon formed between outcrops, with the addition of SF_6 detection at the most northern hole, Hole 1026B at 350- and 1343-days post injection (De Jong, 2020).

This experiment was also the first regional scale experiment to attempt to quantify bulk porosity, with only an estimated value of 10% (10^{-1}) from physical pillow basalt cores recovered during drilling (Bartetzko and Fisher, 2008). Previous experiments have used an effective porosity of 10% for other calculations and modeling of a fractured crustal basalt aquifer, but the volume of pores connected and conducting fluid may be much less (Winslow et al., 2016; Wheat et al., 2000). Neira et al., (2016) calculated an effective porosity ranging between 0.01% - 0.1% (10^{-4} to 10^{-3}) in the upper volcanic crust based on travel times between Holes 1362B and 1301A, which is an order of magnitude lower than bulk porosity measured from Bartetzko and Fisher (2008). In addition, lateral transport rates were measured on the order of m/day, while specific discharge rates of flow are in m/year, meaning tracer transport occurred in a small fraction of the upper crust. Because solute transport occurred both south and north of the injection hole, evidence of mixed convection is also supported.

Using the assumption of the width of the tracer plume extending the depth of permeable rocks of at least 320 meters sub-basement (msb) (Winslow et al., 2013; Becker and Fisher, 2000), the cross-sectional area of transport calculated by Neira et al. (2016) is 10^5 m^2. This indicates a specific discharge rate of < 0.5 m/year (Neira et al., 2016) and is accordant with transient numerical simulations of coupled fluid-heat transport, analytical models, and geochemical models depicting fluid evolution (Winslow et al., 2016; Fisher et al., 2003; Wheat et al., 2000).

There is also an agreement between bulk permeability data collected from the cross-hole response during this experiment, single-hole borehole testing in the region, numerical simulations of coupled fluid-heat transport, and values estimated from seafloor heat flux measurements. Bulk permeabilities from the cross-hole response were found to be between 0.7-2 x 10^{-12} m^2 (Neira et al., 2016), while single-hole tests suggest bulk permeabilities between 0.1-15 x 10^{-12} m^2. 3D numerical simulation of coupled fluid-heat transport that correspond with seafloor heat flux data suggest bulk permeability between 0.3-2 x 10^{-12} m^2 (Winslow et al., 2016). This agreement suggests there is strong evidence of the volcanic crust in the vicinity of the boreholes to be connected to channels where fluid and heat are transported through the region, although the transport network is not fully characterized from temperature/pressure data or numerical models that treat crust as a porous medium alone (Neira et al., 2016).

The results of this experiment also highlight the connection between average linear fluid velocities and borehole interconnectivity. An average linear flow of 0.3-30 m/year was calculated by Becker and Fisher (2000) based on geochemical analyses of the transect and modeling. Specific discharge of 10-20 m/year (Hutnak et al., 2006) indicates velocities may come close to 1 m/day if the effective porosity is much lower than bulk porosity. Travel times calculated from Neira et al., (2016) between Holes 1362A and 1362B during the experiment show linear velocity is much faster than expected (≥3 m/day). A second cross-hole tracer experiment conducted west of the Mid-Atlantic Ridge at North Pond, used cesium to trace fluid flow and found similar linear velocity values (2.1 m/day) to SF_6 velocities (2-3 m/day) calculated in this experiment (Wheat et al., 2020; Neira et al., 2016). This finding goes against the linear velocities for Cs in this experiment calculated by De Jong (2020) and the interpretations of the data may need to be revised. Borehole interconnectivity is directly addressed from the results of this experiment due to tracer being detected in all four boreholes and so becomes invaluable data for achieving the monitoring goals for the CO_2 injection demonstration.

Cross-hole observations are consistent with a highly heterogeneous upper crust, where porosity is limited to large scale transport and a larger volume of fluid may exist in stagnant zones or may poorly communicate with a smaller volume of crust that contain isolated flow pathways. Restricted flow paths may create variability on the local scale, and within the larger scale system, few channels experience rapid flow of water, carbon, and nutrients. The restricted flow paths are dependent upon conduction, diffusion, retention, and dispersive transport in the zones that don't communicate well the main pathways and so exchange slowly (Neira et al., 2016).

Table 2.4: *Summary of lessons learned from cross-hole tracer experiment for the Solid Carbon CO_2 injection experiment.*

Summary of Lessons Learned for Solid Carbon
• Using a series of connected Osmosampler sample coils were effective at preserving the natural variability of the data (Figure 2.18). • Osmosampler *in-situ* pumping rates were observed to be higher (~0.8 ml/day) than what was calibrated (~0.5 ml/day), meaning *in-situ* temperatures were higher than expected. • Deploying both wellhead and downhole Osmosamplers would be advantageous to observe differences in the pumping rate (which is heavily dependent on temperature) between Osmosamplers. Temperature at the wellhead is more stable, while downhole may encounter more temperature fluctuations. • Leakage was observed at multiple boreholes (1362A, 1301A, 1026B) in this experiment so Solid Carbon should be aware since existing boreholes are planning to be used for monitoring. • Interpretation of the cesium concentration data needs revisited. • There is strong evidence for borehole interconnectivity as SF_6 tracer was detected at all boreholes north and south of the injection hole. • More fluid was observed to flow north (i.e., hydrothermal siphon flow), but an anomaly of tracer detection occurred in the south (Hole 1301A) and provides evidence for a preferred fluid pathway or local convection cell delivering a small amount of fluid in that direction. • Ball-valves on CORK wellheads at the injection hole (1362B) and monitoring hole 1362A were intentionally opened throughout the experiment to draw tracer fluid back towards the injection hole. This technique may be useful for the CO_2 injection experiment to control CO_2 plume transport. • Tracer transport was observed in a small portion of the upper crust. The data suggests a large amount of fluid remained stagnated close to the injection hole, interpreted to be poorly connected with a small portion of the crust that contains flow pathways such as fractures, as some of the injected fluid rapidly travelled to the most northern borehole (1026B) before being detected in other monitoring holes. • The effective porosity was determined to be much lower (0.01-0.1%) than inferred from previous estimates (10%) made from basalt cores. • Linear velocities were much faster (> 3m/day) than expected from numerical modelling (~1m/day)

Chapter Three: Importance of Monitoring CO_2 Injection

The role of monitoring is essential for demonstrating with confidence that the injected CO_2 remains in the formation, while also tracking what is happening in the subsurface to confirm the sequestration process. Having a comprehensive monitoring plan can reassure the public, regulatory bodies, and policymakers that the operations at the site are safe and risks are managed in a methodical way. The purpose of this chapter is to emphasize why monitoring CO_2 injection is necessary for a carbon sequestration project.

Overall monitoring goals and objectives are initially discussed, followed by Solid Carbon's approach to monitoring which utilizes existing ocean monitoring infrastructure operated by Ocean Networks Canada. Monitoring parameters and sensors to be used for detection in real time are outlined. Tools for monitoring described in this chapter can be used to detect the CO_2 present in the aquifer in addition to added geochemical tracers described in the following chapter.

3.1 Monitoring, Reporting, and Verification

Sequestration site selection, characterization, and engineering plans are some of the most important parameters for long-term security of a storage site (Dean et al., 2020). Even with a highly characterized site, for a carbon storage project to be accepted by the public it must demonstrate the injected CO_2 is safely and securely sequestered in the storage formation (Johnson et al., 2012), with credible and accurate monitoring, reporting, and verification (MRV) of physical and geochemical data collected through experiments, observations, and/or modelling. Development of an MRV plan using a multitude of monitoring parameters is required to substantiate safe and effective storage of CO_2 in the targeted formation and further establish this form of storage as an acceptable method of CO_2 management (NETL, 2009).

Under an MRV lens, the general goals of monitoring CO_2 injection (Shell Canada Limited, 2014; Nimz and Hudson, 2005; Barros et al., 2021; Litynski et al., 2008) are to:

- ensure the integrity of the storage formation;
- ensure the integrity of seals for safety;
- assess ecological and health impacts in the event of leakage;
- document the long-term effectiveness of storage mechanisms; and
- gather information about the physical and chemical changes that occur in the reservoir.

To achieve these goals, monitoring objectives for CO_2 storage in the offshore environment should include (Shell Canada Limited, 2014; Nimz and Hudson, 2005; Winthaegen et al., 2005):

- the flow rates and composition of the injection stream;
- the CO_2 plume development and its transport in the subsurface;
- the integrity of storage mechanisms and seals (both geological and engineered);
- identification of any seafloor and sediment leaks and environmental impacts; and
- for verification the mineralization process is occurring.

Each monitoring plan needs to be tailored specific to each site, taking into consideration the site's geology, hydrogeology, location of nearby boreholes used for monitoring the injection, and

operational considerations (Litynski et al., 2008). Monitoring can be spatial, where monitoring domains have designated monitoring techniques (Ajayi et al., 2019) and/or temporal, where monitoring techniques are outlined for each injection phase (pre-, syn-, post-injection) (Ajayi et al., 2019). Regardless of the type of approach, monitoring should take place pre-injection to gather data for baseline conditions, during injection to ensure it goes according to plan, and after injection to verify the sequestration process is occurring. Remote and direct monitoring methods can be deployed to ensure the goals of monitoring are met throughout each injection phase (Marieni et al., 2013). The MRV plan needs to be flexible to adapt to changes in scope as the project progresses from the pre-injection to post-injection phases (NETL, 2009). In addition to reporting and verification purposes, the data collected can also be used to optimize the MRV plan for future injections after learning what monitoring parameters are the most useful for addressing and mitigating any risks following the initial demonstration (Nimz and Hudson, 2005).

Monitoring, reporting, and verification plans for onshore CCS projects can be much more comprehensive compared to offshore CCS projects, where more challenges exist for monitoring such as site accessibility and water depth. One of the leading industrial scale offshore CCS projects, the Sleipner CO_2 injection project, has injected CO_2 into a saline aquifer in the highly porous (40%) and permeable Utsira sandstone formation since 1996 (Furre et al., 2017). Carbon dioxide produced from the Sleipner natural gas field is injected into the Utsira formation and the plume is monitored using geophysical methods (Furre et al., 2017). Although this project is quintessential for offshore CCS, the MRV plan is less comprehensive compared to other onshore projects. At Sleipner, no monitoring well was drilled prior to or during operations (as it would puncture the caprock seal), and a completely non-invasive geophysical monitoring approach was chosen (Chadwick, 2013). As the conditions for the Solid Carbon project warrant dissolution of the injected CO_2 into existing fluids, a more comprehensive monitoring approach should be considered that includes both the long-standing industry experience and testing of technologies that have not yet proven useful in the offshore environment but may have been used in onshore scenarios (e.g., fluid sampling). The Quest CCS project described below used a combination of new and traditional technologies with a risk management approach and is highly comprehensive (Rock et al., 2017; Bourne et al., 2014). For these reasons the Quest CCS project was chosen as a case study for an MRV approach.

3.1.1 MRV Case Study: Quest CCS Project Approach

In 2015, a commercial scale CCS project was initiated near an oil sands operation in Alberta, Canada (Duong et al., 2019). The Quest CCS Project is a fully integrated project, involving capture, transport, injection, and storage of CO_2 in a supercritical state, guided by a comprehensive MRV program (Rock et al., 2014). The project is operated by Shell (Rock et al., 2014). Between 2015 and 2018, over 3.45 Mt of CO_2 was stored in the targeted formation (Duong et al., 2019). Eighteen different criteria were used to assess the suitability of the site and the identified reservoir met all the criteria (O'Brien, Solid Carbon Annual Workshop, 2021).

The CO_2 is captured at the Shell Scotford Upgrader facility near Edmonton, AB, and transported via pipeline ~65 km and injected into a 44 m thick deep saline aquifer (in the Basal Cambrian Sands; BCS) located 2 km below the ground surface (Duong et al., 2019; Rock et al., 2014).

Three injection wells exist, but only two were used to store > 3 Mt of CO_2 (O'Brien, Solid Carbon Annual Workshop, 2021). Like the Cascadia Basin site, there are geologic seals found above the injection formation, mainly thick layers of shale and salts (Rock et al., 2014). The temperature in the formation is ~60°C, the porosity is ~17%, and permeabilities are on the order of 10^{-13} m^2 (Tawiah et al., 2020). For comparison, porosity in Cascadia Basin basalt is 10-15%, temperatures are ~65°C, and permeabilities in the uppermost 300 m are on the order of 10^{-12} to 10^{-11} m^2 (Fisher et al., 2011a, 2005a; Elderfield et al., 1999; Davis and Becker, 1998).

Since the Quest CCS storage site is made of dominantly sandstone, the capacity for mineral trapping is much lower compared to basalt, and the CO_2 plume may be buoyant in the reservoir for centuries (Tawiah et al., 2020). This increases the risk for injected CO_2 to escape and enter back into the atmosphere. Consequently, post-operational monitoring becomes critical to ensure containment of CO_2 over the long term in these scenarios. The MRV plan for the Quest CCS Project was created to manage risk and demonstrate containment of injected CO_2 in accordance with predictions made around CO_2 plume transport and pressures (Duong et al. 2019; Rock et al., 2014). The plan is reviewed and updated every few years and focuses on monitoring during operational and post-operational phases (Duong et al. 2019). Shell Canada has agreed to monitor the site for up to 10 years post-closure and if the CO_2 remains in accordance with modelled projections, then liability for monitoring is passed onto the Alberta province to ensure containment of the CO_2 for the future centuries.

The monitoring approach was spatially organized where each environmental domain (atmosphere, biosphere, hydrosphere, geosphere, deep monitoring wells, injection wells) is managed using designated technologies which address the monitoring aspects for that domain (Figure 3.1) (Shell Canada Limited, 2014; Bourne et al., 2014). For each domain, monitoring technologies were identified based on monitoring tasks. Geophysical monitoring was heavily relied upon, but fluid sampling and surface monitoring were also included. Any monitoring tools that were found unnecessary were eliminated (O'Brien, Solid Carbon Annual Workshop, 2021).

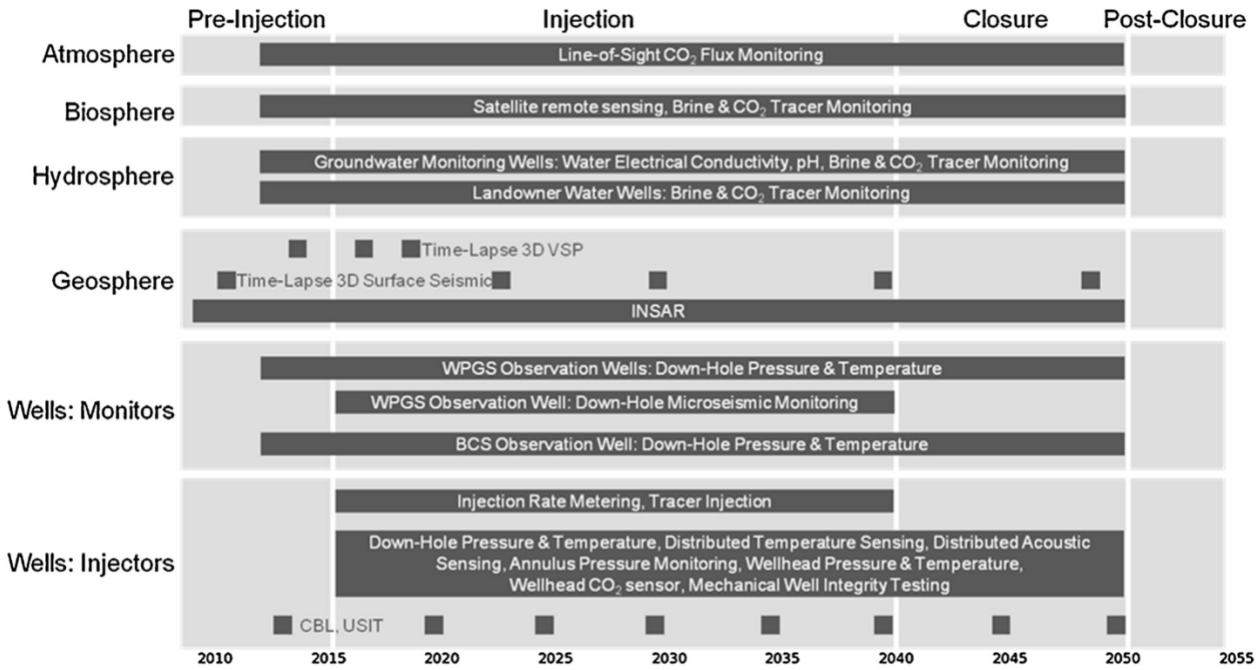

Figure 3.1: *Initial monitoring schedule for Quest CCS project. Table shows environmental domains and the associated monitoring technologies for each throughout the life of the project. Geophysical and geochemical methods were used, as well as both surface and downhole monitoring. Note, this is not a fixed schedule and changes are made in response to changes in the performance of the site. Source: Bourne et al. (2014).*

To outline monitoring tasks and manage risks and uncertainties, a structured, tiered approach was used and was based on a bowtie risk method, which includes development of a bowtie diagram (Figure 3.2) that is a visual of how risks will be managed for the project (Bourne et al., 2014). Each side of the bowtie describes the level of monitoring required for a given hazard (i.e., top event) and preventative or corrective safeguards for determining what action needs to be taken to mitigate any risks. The MRV program also included passive safeguards, which are always present (e.g., geologic/engineered seals), and active safeguards, which represent possible interventions if the monitoring data indicates a hazard is occurring (Bourne et al., 2014). Each active safeguard was made sure to include 1) sensors capable of detecting changes to indicate if an intervention is required, 2) interpretation of the sensor data and decision logic for deciding on a specific intervention, and 3) responses for controlling the outcome of potential loss of site performance. Active safeguards for many potential hazards were outlined in advance for additional precaution (Bourne et al., 2014), although the project has mainly relied on monitoring passive safeguards during its operations.

For each monitoring task, a range of technologies were identified and in case one technology became no longer useful, another technology can take over monitoring which ensures risk is as low as possible. As an example, vertical seismic profiling was used during the first few years of injection to understand the vertical distribution of the CO_2 plume, but once the entire plume

could no longer be captured with vertical seismic profiling, surface seismic was used to take over the identified monitoring task (Bourne et al., 2014).

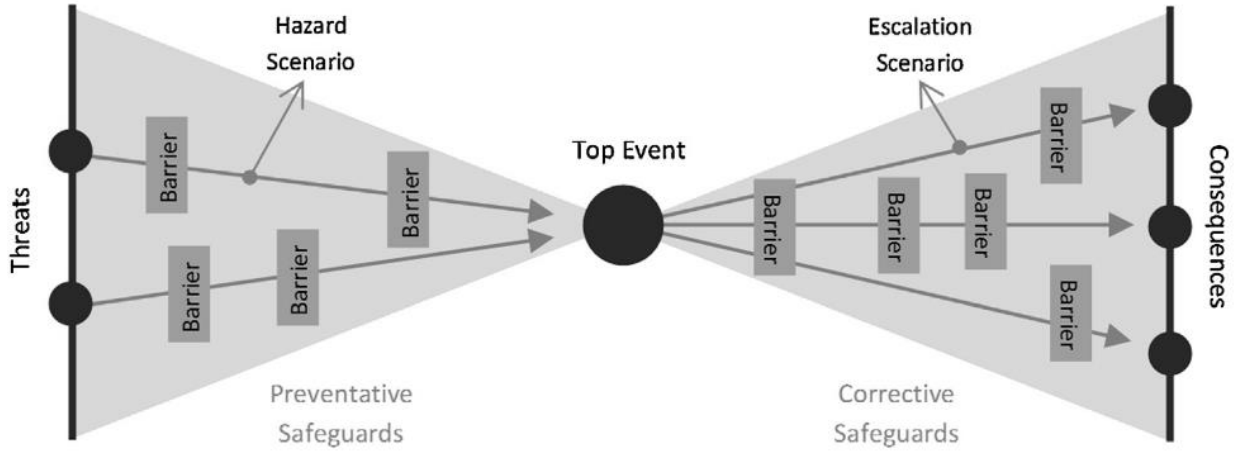

Figure 3.2*: Bowtie diagram template used to monitor risks and uncertainties at the Quest CCS Project. For each hazard (i.e., top event) considered, risks at all levels can be qualitatively assessed through prevention and corrective safeguards. Prevention safeguards (left side of bowtie) are activities that decrease the likelihood of a hazard from occurring, while corrective safeguards (right side of bowtie) are those that decrease consequences related to a hazard. Source: Bourne et al. (2014).*

3.2 Solid Carbon's Approach to Monitoring

The deep-sea basalt in the Cascadia Basin offers a unique monitoring approach compared to other geologic storage reservoirs for many reasons. Compared to terrestrial and depleted oil reservoirs used for CCS, ocean crust is poorly constrained. The Cascadia Basin is one of the most characterized regions of ocean crust, with the first successful cross-hole tracer experiment conducted in ocean crust in the region. Additionally, the proposed site has power and internet capability, large estimated CO_2 storage capacity (~750 Gt CO_2) (Goldberg et al., 2008), and long enough fluid residence times (provided by thick and continuous sediments) for chemical reactions to occur (Goldberg et al., 2008).

The pre-feasibility study preceding the Solid Carbon feasibility study, CarbonSAFE Cascadia, investigated an initial monitoring strategy to address identified risks and verify model predictions for the site planned for CO_2 injection. Existing technologies for direct and remote monitoring were considered in addition to emerging technologies such as an autonomous underwater vehicle (AUV) that can move along the ocean floor, connect to existing ocean monitoring infrastructure, and can enlarge the overall monitoring footprint compared to single monitoring stations (Goldberg et al., 2018a). As part of developing the monitoring strategy, a reactive transport model was built into the existing hydrologic model for the region (Lauer et al., 2018; Winslow et al., 2016) to predict CO_2-fluid-rock reactions and subsurface processes during and after injection into a basaltic aquifer. Additional thermodynamic calculations and basalt dissolution simulations were conducted and used to calibrate the model under site-specific conditions (temperature,

pressure, rock composition) (De Obeso et al., 2023; Tutolo et al., 2021). Data collected during the planned CO_2 injection will be used to test whether these models accurately represent the sub-surface conditions and hydrological and geochemical processes that occur during injection.

3.2.1 Aspects of Monitoring

The main aspects of monitoring for Solid Carbon follow general MRV guidance and will include monitoring of (1) CO_2 transport, (2) the surrounding environment, and (3) the sequestration process whereby the carbon dissolves in the surrounding fluids and precipitates into carbonate minerals in the pore spaces of the basalt. Locations of monitoring are shown in Table 3.1 in relation to each of these aspects. For each location, data is planned to be collected throughout each phase of the project (pre-, syn-, post-injection).

Table 3.1*: Solid Carbon monitoring approach broken down into aspects, the purpose of monitoring each aspect, and the related locations for monitoring each aspect.*

Monitoring Aspect	Purpose	Location
(1) CO_2 transport	• Ensure desired temperature and pressure are maintained	• Ship loading stations • In transit
(2) Sequestration process	• Documenting flow rates and injection rates • Leakage • Documenting chemical changes occurring in the formation • Quantify how much carbon was secured through mineralization	• Injection hole (including injection system) • Monitoring boreholes • Basalt reservoir • Sediments (caprock)
(3) Surrounding environment	• Environmental impact on benthic communities • Leakage through sediments	• Sediments • Seafloor • Lowest part of water column • Borehole seals

Table Footnotes: For each monitoring location, data will be collected pre-, during, and post-injection using instruments connected to an existing sub-sea cabled observatory operated by Ocean Networks Canada. Source: Goldberg et al. (2018a).

The overall monitoring approach will emphasize data collected in real-time from instruments and/or sensors added to existing ocean monitoring infrastructure, with additional data from remote collection of samples analyzed in onshore facilities (Goldberg et al., 2018a). A custom CO_2 injection system for supercritical CO_2 injection will be built and will monitor the flow and composition of the injection stream. The remote location makes any human health impacts negligible but may impact benthic communities on the seafloor if leakage occurs. The most direct observations of the rate and extent of mineralization will come from the geochemical data from collected fluid samples and recovered cores (Goldberg et al., 2018a). To account for the

total amount of carbon removed, carbon accounting will be completed through mass-balance calculations, which is an approach where all carbon inputs and outputs are tracked.

3.2.2 Monitoring Leakage

A big concern for carbon storage projects is the risk of leakage, although leakage is unlikely if a storage site is selected and managed well (Dean et al., 2020; Ajayi et al., 2019). Naturally occurring trapping mechanisms (Section 1.1.3) are used for site selection, but other monitoring approaches are needed to test the integrity of the storage formation regarding leakage. The site being located under almost 2,700 m of water removes concern for risk of CO_2 leaking directly back to the atmosphere, and if some portion of the injected CO_2 does leak through the sediments and onto the seafloor, it will dissolve into the bottom seawater before it could be transported to the surface (Flohr et al., 2021; Taylor et al., 2015). For monitoring early detection of potential leakage, the integrity of both geologic (sediment caprock) and engineered seals (well casing and annulus) are planning to be monitored with sensors (e.g., pH, pCO_2) hung above the seafloor and cameras at the seafloor. Geophysical monitoring systems such as multi-beam sonar (at both injection and monitoring wells) or hydrophones are also options for detection of rising CO_2 gas bubbles at the seafloor and the lowest part (100 m) of water column (Goldberg et al., 2018a; Dean et al., 2020). Remotely operated vehicles (ROV) using video for detecting seafloor changes due to leakage can be combined with passive monitoring with sensors (Dean et al., 2020) but only for short periods of time.

A safe-fail component built into Solid Carbon's MRV plan could be used to demonstrate safety and limited ecologic impacts to the public. A safe-fail is a way of demonstrating the method is fail-safe, by monitoring a failure that is created or pre-existing. This component could be a separate experiment to replicate a controlled CO_2 release experiment (like the ones described below) or to gain insight into the self-sealing trapping mechanism by forming CO_2 hydrate for the planned CO_2 injection in the Cascadia Basin. The safe-fail element could also consist of a control borehole that is known to leak (e.g., IODP Hole 1301A) and could be highly monitored for leakage, or lack thereof, throughout injection phases of the project. Although, using IODP Hole 1301A relies on the CO_2 making it to this borehole if it is injected elsewhere (e.g., IODP Hole 1362B or newly drilled injection hole).

3.2.3 Case Studies of Leakage Scenarios for Monitoring

Two controlled CO_2 release experiments conducted in the offshore environment directly investigated CO_2 leakage in offshore shallow sediments and tested existing technologies to improve understanding of leakage detection and impact assessment for carbon storage projects (Dean et al., 2020). The Strategies for Environmental Monitoring of Marine Carbon Capture and Storage (STEMM-CCS) project injected 0.7 tons of CO_2 gas into the Goldeneye CO_2 storage reservoir (3 m below seabed) in the British sector of the North Sea and monitored its release through the sediments (Flohr et al., 2021). A variety of measurements were made for CO_2 gas and dissolved CO_2 in the sediments and in the water column (Figure 3.3). Technologies tested included geochemical tracers (^{13}C, ^{18}O, SF_6, Kr, and CH_4), hydrophones, chemical lab-on-chip sensors, bubble imaging and sampling, sediment optodes and micro profilers, active acoustics, ROVs, and autonomous underwater vehicles with pH sensors (Flohr et al., 2021). The lab-on-chip sensors are autonomous miniaturized instruments that perform chemical tests *in situ* by drawing in seawater, mixed with chemical reagents, and the reaction products are measured

(Flohr et al., 2021). The sensor suite included total alkalinity (TA), nutrients, pH, pCO_2, dissolved inorganic carbon (DIC), and others (the TA and DIC sensors were custom made for the experiment). The use of tracers in combination with a multitude of direct measurement techniques for monitoring the release CO_2 were successfully demonstrated and quantified (Dean et al., 2020). Additionally, the use of both mobile and single-point sampling methods complemented each other through increased spatial coverage of the data, and any limitations found for a given measurement could be accounted for and reviewed against other measurements for quality control (Flohr et al., 2021). Furthermore, using *in-situ* technology allowed for increased flexibility in decision making and increased responsiveness. Around 50% of the injected CO_2 (0.35 tons) leaked through the sediments into the water column (Flohr et al., 2021), which was below the acceptable rates for leakage listed in the published literature (0.01% reservoir loss per year) (Hepple and Benson, 2005).

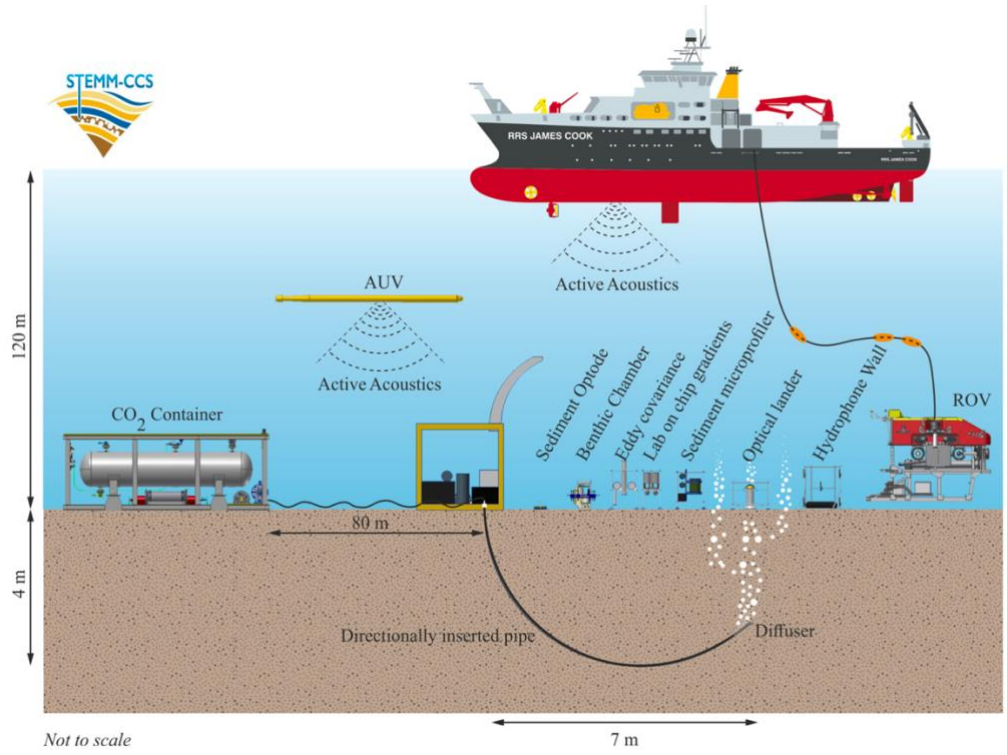

Figure 3.3: *Schematic of STEM-CCS experimental setup. CO_2 gas was intentionally released into sediments and existing technologies were tested in a realistic environment for leakage and assessment of impact. Selected technologies for monitoring shown are remotely operated vehicles, autonomous underwater vehicles, hydrophones, and lab-on-chip sensors for nutrients, pH, total alkalinity. Source: Flohr et al. (2021).*

The Natural Environment Research Council of the U.K. (NERC)-funded Quantifying and Monitoring Potential Ecosystem Impacts for Geological Carbon Storage (QICS) project injected 4.1 tons of CO_2 into sediments 11 m below the seafloor offshore Scotland to understand the shallow sediment and water column dynamics of CO_2 dissolution (Taylor et al., 2015; Blackford et al., 2014). A project goal was to ensure the amount of CO_2 injected was large enough to have detectable signals in the natural system but small enough to avoid pollution (Dean et al., 2020).

Direct and remote monitoring techniques were used such as AUV's, hydrophones, pCO_2 sensor, conductivity temperature depth (CTD) sensor, and an Online pCO_2/pH electrode sensor (Figure 3.4) (Taylor et al., 2015). It was observed only 15% of the injected CO_2 was released as gas at the seafloor, with the remaining dissolved in the sediments (Dean et al., 2020), which is about two times more than what was released in the STEM-CCS experiment, considering different injection depths and volumes. This experiment highlights the challenges in detection and quantification of leakage due to complex dynamics that determine CO_2 flow, even in shallow environments (Dean et al., 2020). This type of experiment should be replicated near an active CCS site (Taylor et al., 2015), such as part of the Solid Carbon demonstration.

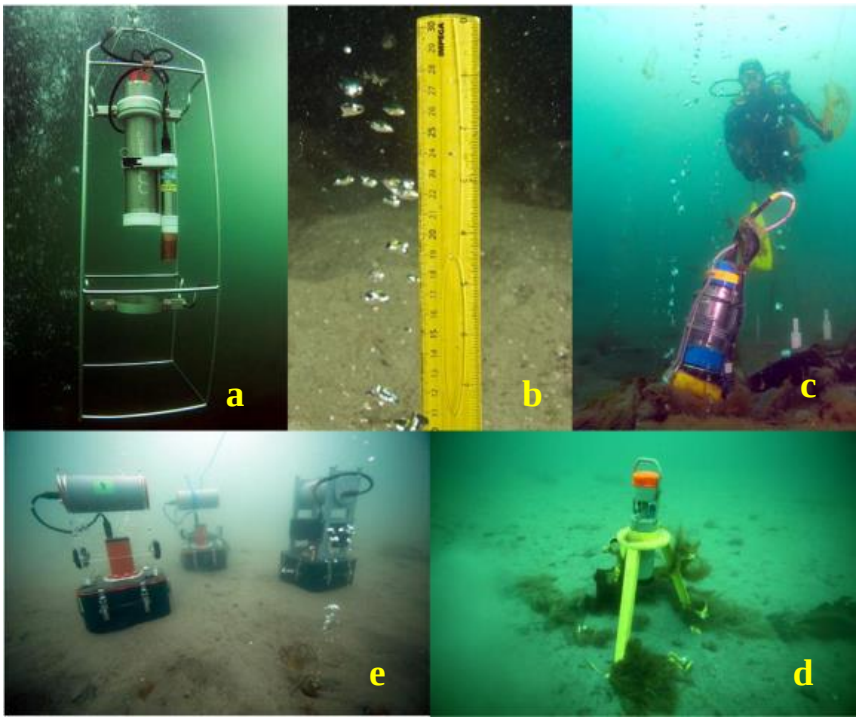

Figure 3.4*: Photo of QICS project release zone, showing CO_2 gas exiting the seabed and various sensors were deployed for monitoring. (a) Contros HydroC_CO_2 sensor for pCO_2 measurements, (b) measurements of bubble size and structure, (c) an Online pCO_2/pH ISFET electrode sensor, (d) Aanderaa recording current meter, (e) benthic chambers for documenting gas exchange within the sediments. Source: Dean et al. (2020).*

3.3 Capabilities of NEPTUNE Cabled Ocean Observatory for Monitoring

The overall concept for monitoring the CO_2 injection demonstration is designed to use the Cascadia Basin node of the Ocean Networks Canada (ONC) NEPTUNE observatory (Figure 3.5) which will connect to CORKs deployed in the existing boreholes chosen for monitoring, likely IODP Holes 1362A and 1362B. Monitoring will also be conducted in the injection borehole, which will be drilled prior to the experiment, but the location of the injection hole and proximity to existing holes is unknown at this time. The Cascadia Basin node sits at 2662 m water depth and will provide active monitoring in real-time for verification of the injection process through to mineralization using both geophysical and geochemical methods. The node is currently

connected to a range of monitoring instruments (Figure 3.5) which collect background information for properties such as pressure, temperature, ground motion, acoustic emissions, conductivity temperature depth (CTD) at and surrounding ODP Holes 1026B and 1027C. The instrumentation connected to these CORKs will be upgraded, and additional monitoring systems for CO_2 injection added to the pre-existing sensor suite operated using ONC's instrument platforms and junction boxes. With a successful funding proposal, ONC can add the monitoring systems for Solid Carbon as early as 2025 expedition to initiate detailed baseline physical and chemical characterizing of the area near the injection site. It is likely an Osmosampler will be deployed in IODP Hole 1362A in Summer 2023 for collecting formation fluids that will contribute to the baseline data (B. Orcutt, pers. comm, 2023). The options for monitoring are many and highly dependent on the budget and logistics for which technologies are chosen. Baseline monitoring is planned for at least two years before injection. The monitoring system would remain in place for longer-term monitoring and any future, possibly larger-scale injections.

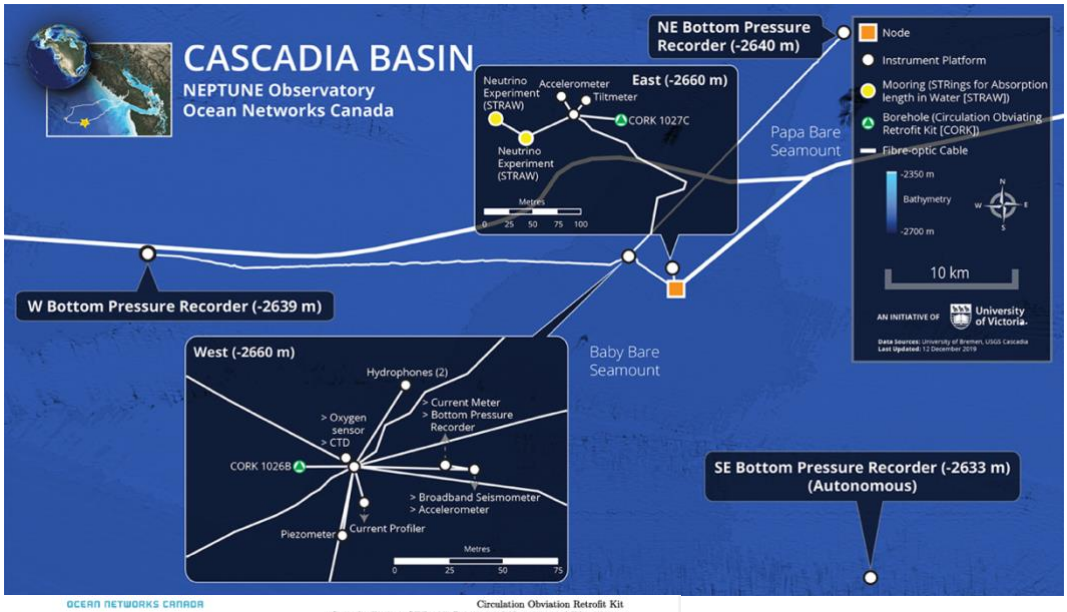

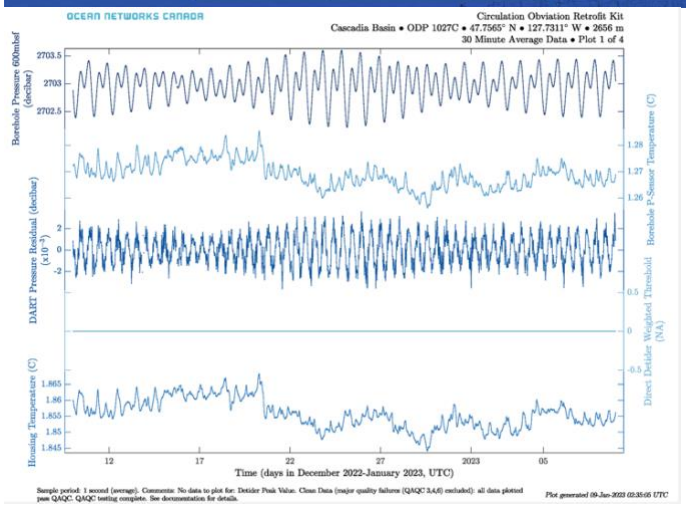

Figure 3.5*: Cascadia Basin node of the NEPTUNE cabled observatory operated by Ocean Networks Canada. (**Top**) Map showing Cascadia Basin node connected to NEPTUNE cabled observatory with regional inset map. Node shown with orange square. Instrument platforms shown with white dots. Boreholes with existing CORKs are shown in green. (**Bottom**) Real time data collected from CORK in ODP Hole 1027C between December 2022-January 2023 showing borehole pressure and temperatures. Source: Ocean Networks Canada.*

Remote geophysical monitoring techniques using the cabled observatory could include controlled source electro-magnetic (CSEM) instruments, distributed acoustic sensing, vertical seismic profiling, and cabled ocean bottom seismometers (Goldberg et al., 2018a). CSEM instruments can track the pure CO_2 plume, distinguish between phases (gas, aqueous, supercritical), and identify if a leakage into sediments is occurring across a 10 km wide plume that migrates slowly overtime (Constable and Stern, 2022). Array systems such as distributed acoustic sensing and vertical seismic profiling can provide time-based sampling of reservoir conditions throughout the experiment (Pevzner et al., 2022). Ocean bottom seismometers can monitor induced seismicity (Johnson et al., 2023) during injection (Tanase et al., 2021).

Direct geochemical monitoring methods will be employed to track geochemical changes that occur as the injected fluids are transported through the reservoir, verifying breakthrough at the monitoring wells, and providing evidence of south to north flow direction from previous studies and modeling efforts (Neira et al., 2016; Fisher et al., 2003). Instruments and interactive live sensors (Section 3.4) hung within and surrounding the selected boreholes will be used for collection of real-time geochemical measurements for a range of parameters. Remote fluid sampling will also be implemented with Osmosamplers that will remain in place over the long-term. The geochemical information gained from remote sampling will build upon the analyses of real-time data collected from the cabled and internet connected instruments and carbon mass balance calculations to determine the extent of mineralization, if successful.

3.4 Real Time Measurements Needed for Geochemical Monitoring

Wellhead and downhole temperature and pressure loggers, conductivity temperature depth (CTD) instruments, and partial pressure of carbon dioxide (pCO_2) and pH sensors could be used to track the injected fluid and can be measured in real time. ONC's existing sensor suite includes temperature and pressure loggers and CTD instruments, and the addition of pH and pCO_2 sensors would help verify the injected CO_2 is dissolving into the formation fluids. Using *in-situ* sensors connected to ONC's cabled observatory will allow data to be collected and interpreted in real time. Sensors can acquire chemical information without the risk of sample compromise and can document the temporal resolution of the data collected from injected geochemical tracers (Myers et al., 2013a). Parameters and *in-situ* sensors considered for monitoring CO_2 sequestration are described below. Most of the parameters are measured in seawater and are reactive, meaning they will change due to CO_2-fluid-rock interactions. Optional optical sensors such as fluorometers are also considered.

3.4.1 Temperature and Pressure

Temperature and pressure changes will need to be continually monitored through the injection hole and monitoring holes for multiple reasons including (i) to document temperature and

pressure changes as CO_2 and injected water (assuming WAG) enters the formation and ensure the pressures are within the threshold of what the formation can withstand; (ii) to monitor temperature changes because the injected CO_2 (and water in WAG) will be much colder than *in-situ* fluids so temperature sensors in the injection hole may record cooling as the injected material reaches the monitoring well. If the temperature of the injected CO_2 is equal to the formation temperature, temperature changes more than 1ºC may be useful for monitoring (Han et al., 2012).

3.4.2 Salinity

Salinity is determined by the total concentration of dissolved salts, or ions, in water and is dominated by sodium chloride (NaCl) in seawater (Figure 3.6) (Emerson and Hamme, 2020). The other major ions account for the remaining salts in seawater and are associated with a positive or negative electrical charge (from gaining or losing electrons) (Webb, 2017). The major ions in seawater with a positive charge, known as cations, are sodium (Na^+), calcium (Ca^{2+}), potassium (K^+), and magnesium (Mg^{2+}). The major ions in seawater with a negative charge, known as anions, are chloride (Cl^-), sulfate (SO_4^{2-}), and bicarbonate (HCO_3^-) (Figure 38; Webb, 2017). Due to having an electrical charge, these dissolved ions act as conductors of electricity (Pilson, 2012).

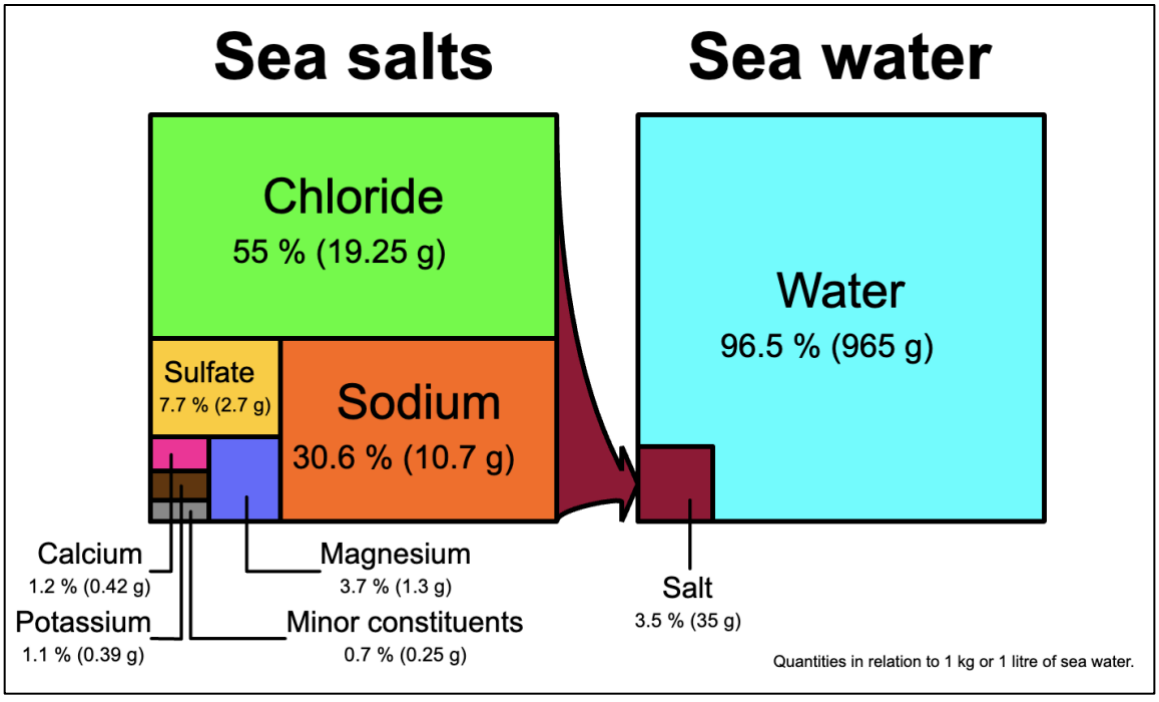

Figure 3.6: *Diagram showing concentrations of various salt ions in 1 kilogram of seawater. Sodium and chloride have the highest abundance followed by sulfate, magnesium, calcium, and potassium. Minor constituents include carbonate and bicarbonate ions. Source: Stefan Majewsky (2008) via Wikimedia Commons.*

Measurements for salinity can be determined by measuring the electrical conductance of seawater which is known as practical salinity and uses the practical salinity scale (PSS-78) (Pilson, 2012; Perkin and Lewis, 1981). Practical salinity measurements depend on conductivity, temperature, and pressure measurements which are simultaneously recorded using an *in-situ* CTD (Lewis and Perkin, 1978). Conductivity is the ability for water to conduct an electrical current and is directly related to the number of ions in solution (i.e., the more ions dissolved, the higher the conductivity) (Pilson, 2012). It is measured using a probe that measures the resistance of the water. Conductivity is the inverse of resistivity, or how water resists electrical flow, and is measured in the amount of conductance over a given distance (micro- or milli-siemens/cm) (Webb, 2017).

A positive correlation exists between temperature and conductivity, as increasing temperature increases mobility of ionic species (Raza et al., 2022; Zhang et al., 2003). For every 1°C increase in temperature, conductivity measurements generally increase by 2-4% (Bradshaw and Schleicher, 1980). Strazisar et al., (2009) observed an increase in conductivity following CO_2 injection in a vertical injection well, suggesting CO_2 dissolution is responsible for the increase, although it may only be a slight increase in conductivity because only a small amount of CO_2 is dissolved in the pore space during its release into the surrounding fluid (Lewicki et al., 2007). In the presence of supercritical CO_2, existing fluids near the injection well are displaced during injection, so there may be a decrease in specific conductivity (i.e., conductivity corrected at a specific temperature) caused by the displacement of surrounding water (Amonette et al., 2014). Increases or decreases in pH, alkalinity, organic compounds, trace metals, nitrate, and carbonate species can impact the conductivity of the *in-situ* fluids, making conductivity a sensitive measurement in relation to other parameters (Zhou et al., 2012; Amonette et al., 2014; Millero, 2000).

Salinity measurements would be useful in a water-alternating-gas (WAG) injection approach (section 4.5.1). If there is a difference in salinity (and temperature) between the *in-situ* formation fluids and the water used for WAG (likely surface seawater), *in-situ* salinity measurements could capture those alternating cycles. Injection of 10,000 tons of CO_2 for the initial demonstration is a small enough quantity to not overwhelm the buffering capacity of the fluids and so WAG may not be necessary (Tutolo et al., 2021). Although, it would be useful to test WAG at the pilot scale if it is planned to be used at large scale injections (i.e., megatons).

3.4.3 pH & Partial Pressure of CO_2

pH and partial pressure of CO_2 (pCO_2) are measures that can be highly diagnostic for monitoring and understanding CO_2-fluid-rock reactions happening in the reservoir (Benson and Cole, 2008). To quantify the carbonate system in real time, at least two of the measurable quantities of the carbonate system (alkalinity, DIC, pH, partial pressure of CO_2) need to be measured using sensors (Esposito et al., 2021; Zeebe and Wolf-Gladrow, 2001). *In-situ* measurement of DIC and alkalinity with sensors does not currently exist, so measurements of pCO_2 and pH are typically used (Atamanchuk, 2013).

Partial pressure of a CO_2 dissolved in water is defined as "the partial pressure of CO_2 in the gas phase that is in equilibrium with that of seawater" (Zeebe and Wolf-Gladrow, 2001). One sensor option is a pCO_2 optode, which allows measurement of pCO_2 in the dissolved phase and can be

deployed in seawater as they have low power requirements and do not include moving parts compared to other sensors (e.g., non-dispersive infrared spectroscopy) (Clarke et al., 2017). These sensors have been deployed at sediment-water interfaces, are frequently used in marine systems, and are mentioned in the published literature as a potential application for CO_2 leak detection at CCS sites (Clarke et al., 2017).

An acronym for the power of hydrogen (pH), the balance of the concentration of protons (H^+) and hydroxide (OH^-) ions determines how acidic ($H^+ > OH^-$) or basic ($OH^- > H^+$) a solution is (Addy et al., 2004). A pH sensor measures H^+ ion activity and is presented as a logarithmic value ($pH = -\log[H^+]$) (Webb, 2017). pH measured in a lab is more accurate than *in-situ* pH probes which are known to be unstable under changing conditions (Zhang et al., 2012; Addy et al., 2004). Blackford et al. (2020) suggests a threshold of 0.01 pH change as the limit of detectability for marine deployable pH sensors.

If observing accurate changes in pH or pCO_2 is difficult, using relative changes could still be useful for understanding changes in the state of the CO_2 within the reservoir over time. For example, if the CO_2 is staying in the formation, it is less important to determine absolute pH for the purpose of monitoring CO_2, only to verify the pH is changing.

pH has been used as a monitoring parameter in other CO_2 storage projects (Matter et al., 2016; Mayer et al., 2013; Jenkins et al., 2012). The data from other projects show a decrease in pH and an increase in CO_2 concentration detected at the injection or monitoring well and have been used to determine the timing of arrival of the CO_2. *In-situ* sensors to measure pCO_2 in seawater have been previously used in controlled CO_2 release experiments in shallow ocean sediments (Dean et al., 2020; Taylor et al., 2015). A pCO_2 optical sensor that was hung in the water column in the QICS field test (See section 3.2.3) successfully detected leakage of CO_2 through seafloor sediments (Atamanchuk, 2013), however it was only calibrated to a maximum temperature of 40°C (Atamanchuk et al., 2014) which is lower than the downhole temperatures (>60ºC) found in the Cascadia Basin. High accuracy measurements remain a challenge for pCO_2 sensors at the seafloor (Atamanchuk, 2013). Newer, possibly miniaturized, technology needs to be developed to test the functionality of pCO_2 sensors at the *in-situ* temperatures of ocean crust, as it is unlikely with the current technology that a pCO_2 sensor could function properly if deployed at depth within a borehole because of the higher temperatures found in the crust.

3.4.4 Fluorescent Dyes

In this research, fluorescent dyes are classified as both a potential real time measurement and added tracer. Therefore, they are included as part of the real time measurements but includes the same information as the other potential added tracers found in Section 4.6. The following section describes several fluorescent dye tracers with a focus on using a fluorometer as the method of analysis for *in-situ* detection.

Advantages of using fluorescent dyes as geochemical tracers include detectability in low concentrations, low toxicity, and easy to analyze in water (Aley et al., 2019; Poulain et al., 2017; Flury and Wai, 2003). Disadvantages include receptivity to sorption and photochemical decay, in addition to pH and temperature dependence, and the effect of salts on fluorescent dye emission

spectra (Flury and Wai, 2003). The use of fluorescent dyes for tracing studies started in the mid-1960's to trace water flow in the subsurface and is a common technique that helps characterize flow direction and velocity in fractured-rock aquifers by measuring travel times of solutes in aquifers (Wilson et al., 1986; Benson and Yuhr, 2016; Kirkendall, 2019). The presence of two phases ($scCO_2$, water) presents an opportunity to use fluorescence to monitor either phase, if feasible.

3.4.4.1 Basic Physical and Chemical Properties of Fluorescent Dyes

Application of fluorescent dye tracers involves the physical phenomenon of fluorescence, a form of luminescence, or emission of light (Wilson et al.,1986). Typically, fluorescence occurs by 1) absorption of energy from an outside light source through 2) excitation of the electrons in the fluorescent compound that produces an excited state where orbiting electrons move to higher energy, followed by 3) emission of energy in the form of light, or photons, as the electrons return to their ground state (Marshall and Johnsen, 2017). Some of the energy is lost through this process, so the emitted energy tends to have longer wavelengths and lower frequencies than the absorbed energy (Wilson et al., 1986). Fluorescent dyes emit light in the visible part of the electromagnetic spectrum and each dye has a specific excitation and emission range (Wilson et al., 1986).

There are many fluorescent dyes commercially available, with most developed for a specific dying purpose (Flury and Wai, 2003). A handful of fluorescent dyes are routinely used as tracers in groundwater or subsurface hydrologic applications, namely Fluorescein, Sodium-Fluorescein (Na-Fluorescein), Rhodamine WT, Rhodamine B, Sulpho rhodamine B, and Acid Yellow 7 (Wilson et al., 1986; Flury and Wai, 2003; Kirkendall, 2019; Smart and Laidlaw, 1977). These dyes are soluble in water, highly detectable in low concentrations (i.e., strongly fluorescent), and generally non-toxic (Klonis and Sawyer, 1996; Smith and Pretorius, 2002; Wilson et al., 1986; Poulain et al., 2017). Table 3.2 summarizes some of the key information described below for each dye considered.

Table 3.2: *Key Factors for Fluorescent Activity of Potential Fluorescent Dye Tracers in this study.*

Fluorescent Dye	**Rhodamine WT**	**Rhodamine B**	**Acid Yellow 7**	**Sulpho rhodamine B**	**Fluorescein**	**Coumarin**	**Na-Fluorescein**
Other Names	Acid red 388[a]	Pontacyl Pink	Lissamine FF	Acid red 52	Uranine	-	Uranine
Detection Limit (µg/l)	0.013 µg/l[c]	0.010 µg/l[c]	0.29 µg/l[c]	0.061 µg/l[c]	0.29 µg/l[c]	n/a*	< 0.02 µg/l[e]
Excitation/Emission (nm)	558/582[a]	555/580[c]	420/515[c]	560/584[a]	492/513[a]	385[f]/410-470[g]	491/513[e]
Sorption Tendency	Moderate[c]	High[c]	Low[c]	Low[c]	Moderate[c]	n/a*	Moderate[c]
pH Range	>5.0[c]	>5.0[c]	4.0-10.0[c]	4.0-10.0[c]	>6.5[c]	n/a*	n/a*
Temperature Sensitivity	Yes[d]	Yes[d]	Relatively insensitive[d]	n/a*	Relatively insensitive[d]	n/a*	Relatively insensitive[d]
Solubility in water	180 g/l[b]	20 g/l[b]	2g/100ml[h]	70 g/l[b]	25 g/l[b]	Low solubility, no data	More soluble than fluorescein
Solubility in supercritical CO_2	n/a*	n/a*	n/a*	n/a*	n/a*	yes, no data value	n/a*
Fluorescence Level	high	high	moderate	high	moderate	low	low

Table Footnotes: It is necessary that the fluorometer is calibrated for the specific dye, and the fluorescent dye chosen functions within the expected pH range in the aquifer. Detection limits are at a pH of 7.5. Sources: (a)Behrens (1986), (b)Gasper (1987), (c)Smart and Laidlaw (1977), (d) Wilson et al. (1986), (e) Khalibadad et al. (2008), (f) Fakhari et al. (2018), (g) Chang et al. (2016), (h) Ford and Thornton, (1983). *=no sources of information found in this study.

Fluorescein was the first fluorescent dye used in water tracing studies (Smart and Laidlaw, 1977). Fluorescein is a prominent groundwater tracer due to its conservative behavior, stability with time, ease of detection at low concentrations, and is readily available (Cascarano, 2018). Sodium-fluorescein has been used successfully in many geothermal fields, including higher temperature systems (Axelsson et al., 1995; Rose et al., 2000). Sodium fluorescein is the Na salt-associated form of fluorescein and is more soluble in water than Fluorescein (Flury and Wai, 2003).

Rhodamine WT was developed to overcome the high adsorption tendency of Rhodamine B (Smart and Laidlaw, 1977) and has been successfully used in marine systems (Skjolding et al., 2021). Rhodamine B and Sulpho rhodamine B are slightly more toxic to marine organisms than Rhodamine WT and Fluorescein (Smart and Laidlaw, 1977; Little and Lamb, 1973). Rhodamine WT and Rhodamine B are three times more fluorescent than Sulpho Rhodamine B (Table 3.2) and can tag a larger volume of water for injection (Smart and Laidlaw, 1977). Rhodamine dyes have the lowest minimum detectability (Table 3.2) (Smart and Laidlaw, 1977). Acid yellow 7 is a highly stable dye that is more resistant to adsorption loss compared to Fluorescein (Smart and Laidlaw, 1977). Acid yellow 7 should be used in water with low organic matter contact since its fluorescence increases with increased total organic carbon (TOC) concentrations (Wilson et al., 1986).

Coumarin fluorescent dyes are blue in color and Coumarin 153 dye is soluble in supercritical CO_2 (Chang et al., 2016; Zhang et al., 2011; Fakhari et al., 2018). Chowdhury et al. (2004) note that Coumarin 153 dye has a very low solubility in water but does not specify the solubility. Chang et al. (2016) also does not specify the solubility of Coumarin 153 dye in supercritical

CO_2. Biswas et al., (1999) presents excitation and emission shifts of Coumarin 153 in a supercritical CO_2 solvent but there is limited information on the behavior of Coumarin-153 dye in subsurface hydrologic studies.

The intensity of each fluorescent dye in a solution is controlled by several factors: 1) solvent type, 2) concentration, 3) temperature, 4) pH, 5) photochemical decay, and 6) chemical decay (Cascarano, 2018; Wilson et al., 1986). If the solvent is water there is no change in intensity, but multi-phase systems (including CO_2-water) may cause a change in the intensity of the fluorescent dye (Wilson et al., 1986). For dilute solutions, the most important factor is temperature (Wilson et al., 1986). Fluorescent activity increases with decreasing temperature (Wilson et al., 1986), and changes to temperature as well as pH affect the efficiency of dye adsorption in water (Behrens, 1986; Kirkendall, 2019; Smart and Laidlaw, 1977; Wilson et al.,1986). Acid yellow 7 and Fluorescein are relatively insensitive to temperature changes, but Rhodamine WT, Rhodamine B, and Sulpho Rhodamine B are affected (Figure 3.7) (Wilson et al., 1986; Smart and Laidlaw, 1977). Rhodamine B has also been determined to experience more chemical decay compared to the other Rhodamine dyes (Watt, 1965).

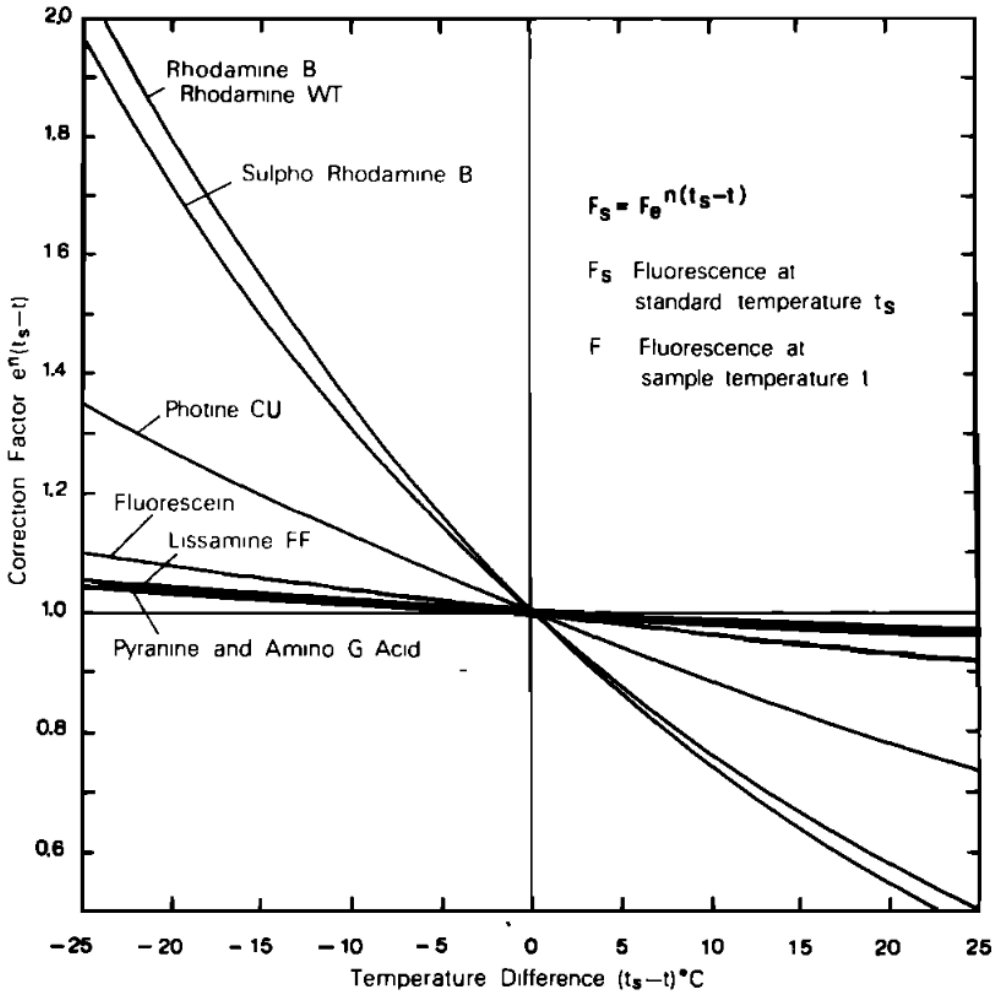

Figure 3.7*: Temperature correction curves for various fluorescent dyes considered in this study. The temperature correction curves were derived from temperature exponents from Feuerstein and Selleck (1963) and Wilson (1968). Temperature is an important factor that affects the fluorescence of dye in dilute solutions as fluorescence activity decreases as sample temperature increases. It is clear from the trends shown that the Rhodamine dyes (Rhodamine WT, Rhodamine B, and Sulpho Rhodamine B) will be affected by changes in temperature more than Lissamine FF (Acid yellow 7) and Fluorescein, which are relatively insensitive to changes in temperature. Source: Smart and Laidlaw (1977).*

3.4.4.1.1 pH sensitivity

Fluorescein is more sensitive to pH compared to Rhodamine dyes (Lindqvist, 1960). Smart and Laidlaw (1977) show that Acid Yellow 7 and Sulpho rhodamine B remain fluorescent at low pH values (Table 3.2). Fluorescein changes its molecular structure when pH decreases (Smart and Laidlaw, 1977). Smith and Pretorius (2002) showed through a series of experiments that it is possible to predict the absorption value of fluorescein at different pH values. It may be possible to measure pH and the fluorescent dye signal simultaneously in the injection well to determine the rate of CO_2 dissolution (Adams, 2013). pH and temperature have a greater effect on dye adsorption than to salinity (Flury and Wai, 2003). Fluorescein shows no change in fluorescence

with increasing salinity, but the Rhodamine dyes (Rhodamine WT, Rhodamine B, and Sulpho Rhodamine B) are affected with increasing salinity (Smart and Laidlaw, 1977).

3.4.4.1.2 Loss through adsorption

A common problem seen in hydrological tracer tests using fluorescent dyes is dye loss (Kirkendall, 2019), which can occur as travel times increase or through tendency for fluorescent dyes to adsorb onto sediments or the rock matrix. Sorption processes (i.e., absorption and adsorption) contribute to retardation of a tracer and adsorption is irreversible (Smart and Laidlaw, 1977) so choosing dyes that are resistant to adsorption is very important for fluorescent tracers. Kasnavia et al. (1999) investigated the sorption behavior of three rhodamine dyes and Fluorescein and found rhodamine dyes are more susceptible to sorption on most mineral surfaces (Table 3.2). Smart and Laidlaw (1977) investigated the characteristics of eight fluorescent dyes used in surface water tracing. Sulpho rhodamine B showed resistance to adsorption (Smart and Laidlaw, 1977). Rhodamine B had the highest rate of sorbing, followed by Rhodamine WT and Fluorescein. Fluorescein has a lower tendency to adsorb compared to Rhodamine dyes (Lindqvist, 1960). Organic phases (sawdust, humus) were observed to result in more adsorption than inorganic phases (clays, limestone) for Rhodamine WT and Fluorescein. The effect of salts leading to loss of fluorescent dye tracers in saline environments is gradual and may be the cause of dye loss in tracer studies that were previously assumed to be caused by adsorption (Smart and Laidlaw, 1977).

3.4.4.2 Logistics of using fluorescent dyes

Fluorescent dyes can be used qualitatively and semi-quantitatively which rely on visual detection, while quantitative methods require frequent sampling to measure changes in dye concentration with time and provide more information (Poulain et a., 2017). Fluorescence can be measured in a laboratory using a fluorometer but is not feasible in this case due to site logistics and the need to analyze samples as soon as possible to minimize deterioration of fluorescence due to interaction with substances found in seawater (Wilson et al., 1986), although these substances are not clearly outlined in the published literature. Since Osmosamplers will be deployed for an extended period, there may be a potential for the collected samples to lose fluorescence overtime before being recovered. *In-situ* detection of fluorescent dyes is possible with a fluorometer and removes the requirement for transportation onshore and analysis of water samples (Poulain et al., 2017) and allows collection of high-resolution temporal data through optical measurements (Kirkendall, 2019; Zarnetske et al., 2017). Measurements are typically recorded as intensity at a given wavelength (Wilson et al., 1986) which is used to determine the concentration of the dye with precision on the order of ~0.1 ppb (Adams, 2013). The sensitivity of the fluorometer determines the limit of detectability of a certain dye, so the optical system needs to match the fluorescent dye chosen for use (Wilson et al., 1986). With specific excitation and emission ranges for each fluorescent dye, this method of analysis is a sensitive and accurate analytical method (Wilson et al., 1986). Excitation and emission spectra for each fluorescent compound is listed in Table 3.2.

Popular oceanographic sensor manufacturers (Turner Designs, WetLabs) provide fluorometers that can detect rhodamine and fluorescein dyes in water (Khalibadad, 2008; WetLabs, 2005). Ocean Networks Canada does have fluorometers (WET Labs) as part of the ocean monitoring

suite but may need to test functionality of the instrument at the *in-situ* temperature where injection will take place, as these are not typically used in ocean crust at elevated temperatures. If portable fluorometers are not functional at the *in-situ* conditions, there is also an option to use a cabled fluorometer and retrieve it when the Osmosamplers are collected after the monitoring period. Flury and Wai (2003) discuss using fiber optic sensors in combination with fluorescence spectroscopy to measure tracer concentrations *in situ*. Fluorescein and Rhodamine WT have been used as fluorescent tracers for fiber optic spectroscopy (Schmid and Barczewski, 1995). Fiber optic sensors can make measurements in real time to detect flow directions, although spatial resolution is poor (Flury and Wai, 2003).

For comparing the cost effectiveness of fluorescent dyes, the published literature appears sparse and outdated. Smart and Laidlaw (1977) discuss cost effectiveness of some of the tracer dyes considered in this study. The prices quoted were for 10 kg of each tracer delivered from suppliers in the UK. The cost of acid yellow 7 dye (£13.50/kg) is twice as expensive than Rhodamine WT (£6.50/kg), for example. Sulpho rhodamine B is more expensive (£8.50/kg) than Rhodamine WT (Smart and Laidlaw, 1977). Fluoresein (£4.00/kg) is close in cost to Rhodamine WT and is recommended for use in tracing experiments where more than one dye is used (Smart and Laidlaw, 1977).

3.4.4.3 Case Studies of the Use of Fluorescent Dyes in Tracer Experiments and Laboratory Studies

The cross-hole tracer experiment conducted in the Cascadia Basin (section 2.4; Neira et al., 2016) did not detect the injected fluorescent microspheres (coumarin and fluorescein dyes inside polymer coating) with sample collection in Osmosamplers (De Jong, 2020; Neira et al., 2016). This is likely due to low signal-to-noise ratio and high amounts of dilution as the microspheres were transported through the extensive aquifer system (De Jong, 2020; Fisher et al., 2011f).

The CarbFix project in Iceland used Na-Fluorescein to characterize the petrophysical properties of the target zone in the basaltic aquifer before the first phase of injection of carbon pre-dissolved into water (Khalibadad, 2008). This short tracer test was conducted to obtain additional information about flow patterns and transport processes for the CO_2 injection strategy (Khalibadad, 2008). Prior to the tracer test, 500 g of Na-Fluorescein was diluted in 100 l of water. The tracer slug was injected into the injection well between November 2007 and May 2008 (Khalibadad, 2008). The results identified conservative behavior of Na-fluorescein in the basaltic host aquifer and at the *in-situ* temperature (95-100°C) of the reservoir (Khalibadad, 2008). It was observed that Na-fluorescein did not interact with minerals in the basaltic rock over a period of several months (Khalibadad, 2008). Based on the observations of the short tracer test, Khalibadad (2008) suggest Na-Fluorescein can be regarded as conservative in the context of thermal decay and sorption effects.

Novakowski et al., (2000) observed Acid Yellow 7 dye to interact with the rock material (dolostone) more than Bromide, another tracer used in a field-scale tracer experiment. Adsorption to the rock matrix was one possibility of for the retardation of acid yellow 7.

Fakhari et al. (2018) used a fluorescent dye (Coumarin-153) to tag the supercritical CO_2 phase in a laboratory pore-scale flow experiment with CO_2 and water in a 2D heterogeneous and porous

micromodel. The purpose of the experiment was to represent liquid CO_2 entering a water-saturated porous medium to understand the phase distribution and CO_2 infiltration at the pore scale (Fakhari et al., 2018). The liquid CO_2 was pressurized to 8 MPa (Fakhari et al., 2018). Prior to injection, the CO_2 was tagged with Coumarin-153 fluorescent dye to image the CO_2 during the experiment using high resolution fluorescent microscopy technique. An LED light source using a wavelength of 385 nm was used to excite the fluorescent dye in the CO_2 phase. The intensity of the CO_2 compared to the water and solid matrix was easily determined which allowed for determination of CO_2 distribution at the pore scale. This technique was originally demonstrated by Zhang et al. (2011) and Chang et al. (2016). The use of Coumarin-153 dye successfully tagging the supercritical CO_2 phase in a laboratory setting may be an opportunity to investigate its potential as a tracer for supercritical CO_2 in multi-phase flow systems.

3.4.5 Limitations with Oceanographic Sensors

Temperatures found within the ocean crust in the region of the Cascadia Basin being considered here (~65°C) are much higher than temperatures commonly found in the ocean (-2°C to 30°C) (Webb, 2017). Oceanographic sensors are not typically manufactured to operate in temperatures outside the ocean range, nor tested in the ocean crustal aquifer setting (Myers et al., 2013a). There is an option to test sensors through simulating how current sensors function in seawater above 65°C. Any chemical changes observed in real time with sensors can be verified with fluid analysis of added geochemical tracers to help quantify the changes observed in real time.

Chapter Four: Tracers for Monitoring

4.1 Overview

Since geophysical monitoring methods are challenged to detect chemical changes occurring once the CO_2 is injected into the subseafloor, the use of geochemical tracers can be useful for quantifying chemical and physical processes (Myers et al., 2013a). A tracer can be any discernible chemical compound with known behavior which is added (or inherent) to a system to improve understanding of dynamics within the system (Cao et al., 2020). Tracers are used in many fields to study geochemical interactions of gases, liquids, and solids, namely environmental chemistry, biochemistry, and marine chemistry (Myers et al., 2013a). Tracers are used in hydrology to study how materials are dispersed and transported through a system to infer environmental processes (Cook and Herczeg, 2012). In oceanographic studies, geochemical tracers have been previously used to verify direction and rates of fluid flow in ocean crust using mostly naturally occurring tracers (e.g., chlorinity, methane, ^{14}C) (Fisher et al., 2011f). More recently, tracers have been used to monitor the state and movement of injected CO_2 in the subsurface in terrestrial-based (sedimentary basins, depleted oil fields, flood basalts) pilot scale experiments, although no pilot project has attempted CO_2 injection into deep sea basalts so application of tracers for monitoring carbon storage in this environment is not fully understood (Roberts et al., 2017).

In a CCS context, tracers are useful for quantifying dissolution and precipitation reactions, evaluating storage behavior (e.g., migration rates), modelling hydrogeologic properties, and determining if leakage is occurring (Kampman et al., 2014; Myers et al., 2012a; Stalker and Myers, 2014). For the Solid Carbon experiment, it is important that tracers help quantify how much CO_2 has dissolved into the formation fluids and how much is trapped in pore spaces or removed through precipitation of carbonate minerals.

Tracers need to meet a list of requirements to be suitable for tracing injected CO_2 in the offshore marine environment (section 4.3). If a tracer is inherent to the formation, background concentrations must be known before injection so changes in the concentrations of that tracer can inform monitoring. It is also important tracers do not biologically or chemically degrade or retard during transport (Leibundgut et al., 2009).

The goal of this research is to determine which tracers are suitable for the *in-situ* conditions at the Cascadia Basin site. This chapter introduces tracers and tracer types, outlines criteria and desired tracer properties, history of tracers used in the region, and different injection strategies. For each potential tracer, a subsection is included describing the tracers physical and chemical properties, followed by the logistics of using it (cost, volume for analysis, methods), and any case studies of its use in laboratory experiments or existing pilot projects. Based on these considerations, several tracers (including any tracer where measurements that can be made in real time) are proposed to be used for targeting various aspects of geochemical monitoring.

4.2 Types of Tracers

Tracers can behave as either reactive or conservative. Each type captures different information, and both are required to quantify CO_2 transport and reaction (Matter et al., 2014). Changes in

tracer concentrations or the ratio of the concentration of two different tracers with different properties can help characterize the physical and geochemical processes occurring at the formation scale (Matter et al., 2014). Tracers can also be classified as inherent to the injection CO_2 stream, the storage reservoir, or added separately with the CO_2 stream during injection. Tracers can also be added with water if the injection strategy includes a WAG approach.

4.2.1 Conservative Tracers

Conservative tracers do not interact with reservoir rocks and flow passively with the velocity of their host fluid. These can be used to track a parcel of fluid to understand the hydrology of the system and characterize physical properties (Cao et al., 2020; Khalilabad, 2008), which include flow pathways (if more than one monitoring well is used), velocities, and dispersivity of the system (Cao et al., 2020). Dispersivity describes how solutes may spread from a highly concentrated area to a lower concentrated area and helps determine mixing fractions between the injected tracer and aquifer fluids (i.e., dilution of the tracer into aquifer fluids) (Matter et al., 2011). These tracers should be unaffected by chemical or biological processes, but it is important to note that, no tracer will behave completely conservatively under all conditions (e.g., some conservative tracers may absorb onto organic matter). Conservative tracers should be present in the reservoir prior to injection at concentrations much lower than the added tracer concentration or not present at all in the reservoir pre-injection (Khalilabad, 2008). Fluorescent dyes (Basava-Reddi, 2011), sulfur hexafluoride (Matter et al., 2014), trifluoromethyl sulfur pentafluoride (Matter et al., 2014), other perfluorocarbons (Myers et al., 2013a; Kharaka et al., 2006), and noble gases (Kharaka et al., 2006) have been used as conservative tracers for monitoring geologic CO_2 storage in both basaltic and saline formations.

4.2.2 Reactive Tracers

Reactive tracers undergo reactions within the system and changes in their concentration provide information about these reactions. For using tracers to trace CO_2, reactive tracers should react and partition in response to chemical changes that occur as CO_2 reacts with the formation fluids and surrounding rock (Cao et al., 2020). For accurate analysis of the reactive tracer results, background conditions need to be characterized before CO_2 injection, which allows for tracking any changes in the formation fluids after injection. It is vital changes in concentrations of the reactive tracer can be used to determine how much of the CO_2 dissolved or was removed from the pore fluids by forming carbonate minerals. Comparison of carbon and oxygen isotopic signatures between pre- and post-injection waters, and in carbonate minerals has been used to verify carbonate mineral formation from injection of CO_2 (McGrail et al., 2017; Matter et al., 2011). Changes in pH, major and minor ions, DIC, and alkalinity can also serve as reactive tracers to confirm chemical changes pre- and post-injection (Stalker et al., 2009; Emberley et al., 2005).

4.2.3 Added versus Inherent Tracers

Depending on the goals of the monitoring program and logistics such as cost and legal constraints, tracers can be added or already inherent to the storage reservoir and/or inherent to the CO_2 sourced for injection (Roberts et al., 2017). Tracers can be purposefully added to the CO_2 injection stream if the behavior of the tracer is well understood. Legal constraints only allow a small portion (< 5%) of the total CO_2 stream to consist of tracers, dependent on the tracer compound chosen (R. Webb, pers. comm. 2021). One advantage for using added tracers includes

being able to inject the tracer in known quantities making sure the tracer is at concentrations above the detection limit, even after dilution within the reservoir.

Inherent tracers are constituents which are already present in the formation, or a natural component of the injected CO_2. If the CO_2 used for injection is derived from industrial processes, there may be an inherent signature from impurities (N_2, H_2, CH_4, H_2S, NO_x) (Boot-Handford et al., 2014) or stable carbon and oxygen isotope signatures already present in the CO_2 so any changes in the original signature can inform monitoring (Flude et al., 2016). The impurities can be used as tracers which can greatly reduce the cost of the tracer program (Roberts et al., 2017). Solid Carbon's CO_2 injection experiment is planning to use a purified source of CO_2 so impurities within the CO_2 may not be at high enough concentrations to use as tracers.

4.2.4 Interpreting Tracer Data

Tracer data is analyzed and interpreted from fluid samples collected over the monitoring period and provides direct evidence for tracer transport, as well as indirect evidence of CO_2 transport (Stalker and Myers, 2014). Information regarding the system being investigated is derived based on how the tracer concentration varies over time, depicted as a breakthrough curve (Figure 4.1) which help in determining velocities and hydraulic properties (Cao et al., 2020; Benson and Yuhr, 2016). By comparing the breakthrough curves of the reactive tracers and conservative tracers, the extent to which reactions retard the reactive tracers can be quantified (Cao et al., 2020; Leibundgut et al., 2009). Conservative tracers can act as a reference tracer to account for hydrodynamic transport processes which affect both types of tracers (Cao et al., 2020). In its simplest form, tracer data can identify whether a tracer behaves more conservatively, or reactive. The shape of the breakthrough curve can be used to determine if a tracer has degraded, retarded, or both (Figure 4.1). For example, if a tracer has degraded during transport, there will be a reduction in the peak area of the curve relative to that of a conservative tracer, signifying there is less than what was originally injected. Retardation implies some process is slowing tracer travel down (e.g., partitioning between phases, sorption) and should only affect reactive tracers (Cao et al., 2020).

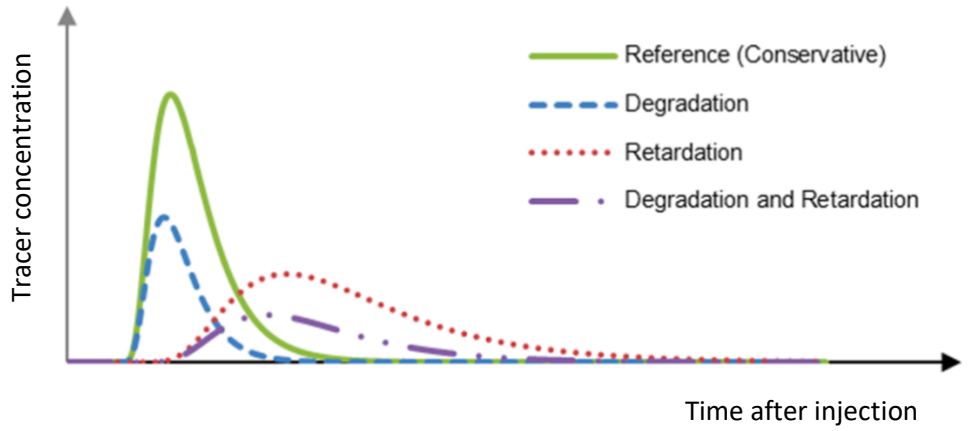

Figure 4.1*: Visual representation of conservative and reactive tracer breakthrough curves from a simulated pulsed tracer test. Conservative tracers act as reference tracers to account transport processes affecting both tracer types and show zero excess concentration for some time after injection starts and then a rapid increase in concentration when the fluid injected first reaches the monitoring well. A time shift in the curve indicates retardation of the tracer (red dotted line) for example due to adsorption to the rock matrix or partitioning. A reduction in the area under the peak of the curve indicates degradation of a tracer (blue dashed line) for example due to chemical reactions. Retardation and degradation can simultaneously affect tracer transport as well (purple dashed-dotted line). Source: Cao et al. (2020).*

For heterogeneous formations, only a portion of the injected fluids will be recovered as residual tracer concentrations follow different pathways (Khalilabad et al., 2008), which is likely the case for the Cascadia site (Fisher et al., 2003). A single peak in a breakthrough curve may not rule out heterogeneity if other pathways do not reach the monitoring site. Multiple peaks in the breakthrough curve indicates different pathways through which the tracers reach the monitoring well, as was observed in the CarbFix short duration tracer test (section 1.1.3.4.1). Conservative tracer breakthrough curves can be used to calculate how much tracers were diluted (Leibundgut et al., 2009).

4.3 Criteria and Desired Tracer Properties for Carbon Storage in Basalts

Chemical tracers chosen for monitoring carbon sequestration in offshore deep-sea basalts need to meet a list of requirements to be suitable for CO_2 injection. The requirements historically have been adopted from experience in the hydrocarbon and geothermal industries (Roberts et al., 2017). Carbon capture and storage presents new challenges for finding suitable tracers, in particular the use of tracers in the offshore environment. The published literature contains a handful of comprehensive reviews of the developments in using tracers for CCS purposes (Roberts et al., 2017; Stalker and Myers, 2014; Myers et al., 2013a; Stalker et al., 2009). As summarized in detail in those reviews, the choice of tracer should be unique to the site characteristics and background conditions but overall they should be: (i) chemically stable (i.e., no degradation or chemical breakdown in the subsurface), (ii) low in cost (for both the tracer and laboratory analysis), (iii) available in the necessary volume, (iv) reliably detected (i.e., sufficient quantities added to allow for dilution), (v) easily transported offshore, (vi) have well understood behavior at the *in-situ* conditions including during injection into the reservoir with changing temperature and pressure conditions, (vii) meet ship regulations for transporting offshore through to injection, and (viii) be safe and non-toxic (Roberts et al., 2017; Stalker et al., 2009). Ideally, a suite of tracers should be used, each with different properties that can provide more information compared to using a single added tracer (Roberts et al., 2017).

Choosing tracers that are unsafe, toxic, or polluting could negate the overall purpose of carbon storage so tracer choices should reflect stewardship of the environment. Tracers that are known to degrade or adsorb onto organic matter should be avoided (Shell Canada Limited, 2014), especially for detection in a complex fractured rock aquifer system.

4.3.1 Detectability and Dilution

For reliable detection, the concentration of the injected tracer must be high enough that the small volume collected by the Osmosampler tubing has detectable amounts of the tracer for analysis, even after being diluted in the formation fluids (Fisher et al., 2011f). To determine how much dilution will occur during transport through the aquifer, a conceptual dilution model was created (Figure 4.2). The assumptions of model are that the formation is homogeneous and the concentration of tracer does not change with transport (i.e., conservative transport). The mass of the aquifer (M_{aq}) was determined as the volume of a cylinder with known porosity based on the assumption of radial dispersal of the tracer around the injection site in a constant thickness aquifer:

$$\mathrm{M_{aq}(kg)} = 2(\pi)(\mathrm{r}^2)(H_{aq})(\emptyset)\left(1000\,\frac{\mathrm{kg}}{\mathrm{m}^3}\right)$$

Where r^2 represents the distance between wells and is variable, H_{aq} is the height of the aquifer (300 m), ø is the porosity of the formation (0.1), and 1000 kg/m^3 is the density (ρ) of seawater. Values for porosity and the height of the aquifer have uncertainties associated with them as it is difficult to constrain these values in ocean crustal aquifers. The values used here have been used in reactive transport models for the Cascadia basin (Winslow and Fisher, 2015; Hutnak et al., 2006). The density of seawater is known to be 1026 kg/m^3, but 1000 kg/m^3 was used for simplicity. The concentration of tracer in the aquifer (C_{aq}) was determined through:

$$\mathrm{C_{aq}(mol/l)} = \left(\frac{\text{mass of solution (kg) x concentration of tracer } \left(\frac{\mathrm{mol}}{\mathrm{kg}}\right)}{\text{mass of the aquifer } \left(M_{aq}\right) \text{ (kg)}}\right)$$

Where the concentration of tracer is 1 mol/kg, and the mass of solution it is dissolved in is 1000 kg in this example. Tracer concentrations need to be at least seven orders of magnitude above the detection limit of the tracer if the closest monitoring well is 300 m away from the injection well (Figure 4.2). For other well separations, tracer concentrations need to be at least six orders of magnitude above the detection limit of the tracer if the closest monitoring well is less than 100 m away from the injection hole, and eight orders of magnitude above the detection limit of the tracer for 700 m distance. If the height of the aquifer is <300 m, there would be less dilution with distance away from the injection hole but if the porosity is more than 10%, there would more dilution with distance. To change the amount of dilution affecting tracers in this system, increasing or decreasing the well distance, or adding more concentration or mass of tracer would be required.

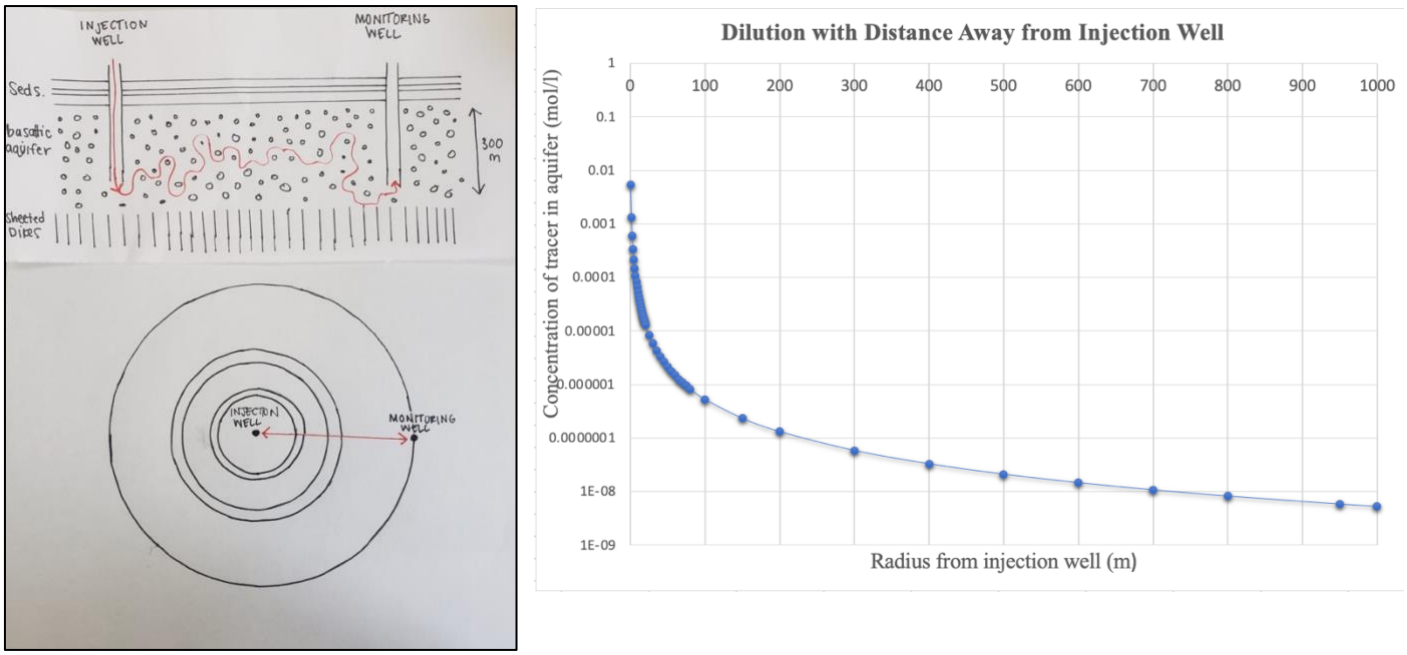

Figure 4.2*: Conceptual model for dilution. (left) drawing of conceptual model showing basaltic aquifer and injection and monitoring well. The uppermost 300 m of the basaltic crust is inferred to be the most permeable portion of the aquifer and this value was used as the height of the aquifer. The red arrow represents tracer being injected and transported through the porous (0.1) formation, arriving at the monitoring well after some period. (right) Graph showing calculated dilution with distance away from the injection well with a tracer concentration of 1 mol/kg. Assumptions of the model include radial dispersal of the tracer around the injection hole, the formation being homogenous, and tracer concentration does not change during transport.*

4.3.2 Partitioning Behavior

Tracer concentration data and how it varies with time is modelling to predict tracer behavior and make more accurate interpretations of tracer transport (Leibundgut et al., 2009). Partition coefficients describe the relative concentration of a tracer at equilibrium in two phases (e.g., oil/water, air/water, supercritical CO_2/water) (Myers et al., 2012a). It is crucial to choose tracers where their behavior is known since interactions with the surrounding basalt and partitioning of tracers between formation fluids and supercritical CO_2 phases significantly influence the interpretation of the information gained from tracers used (Myers et al., 2013b). The dearth of experimentally derived partition coefficients for tracers used for CCS is one of the current gaps in the published literature.

For solutions that are highly diluted, the partition coefficient can be defined as the ratio of the chemical concentrations in each of the two phases (Srebrenik and Cohen, 1976). Since tracers will be in low concentrations, this simple form of a partition coefficient is adequate (i.e.,

assuming Henry's law) (Myers et al., 2012a). Partition coefficients generally vary with temperature and pressure and with fluid composition such as pH (Misra, 2012).

Current models of tracer behavior in CCS systems use either Henry's law coefficients, or octanol/water coefficients, which have been used to understand the environmental fate of organic species (Cronin et al., 2003; Myers et al., 2013a &b). For many tracer compounds, supercritical CO_2/water partition coefficients have not been experimentally determined (Stalker and Myers, 2014; Burant et al., 2012; Timko et al., 2004), apart from some organic compounds (Myers et al., 2012a), a few ester compounds (Myers et al., 2013b) and noble gases (Warr et al., 2015). The dearth of experimental data on the partitioning behavior of many tracers between supercritical CO_2 and water and/or brine makes assessing and modelling tracer behavior difficult (Kampman et al., 2014). Timko et al. (2004) determined that octanol/water partition coefficients do not correlate well with CO_2/water partition coefficients for organic compounds, such as benzene, toluene, ethylbenzene, acetic acid. Burant et al. (2012) reviewed the solubility of organic compounds in supercritical CO_2 and the partitioning between brine (>10 g/l total dissolved solids) and CO_2, suggesting that volatile compounds with low solubility in water will partition preferentially into the CO_2 phase. Since partition coefficients partially determine the suitability of a tracer, to accurately interpret the tracer data and/or models, partitioning behavior of considered tracers should be determined at the temperature and pressure conditions of each site (Myers et al., 2012a). This would require laboratory testing of certain tracer compounds under high pressure/high temperature conditions and requires a more complicated laboratory testing set up which includes a vessel that can withstand high pressures.

4.4 Brief History of Tracers used in the Cascadia Basin Region

In the past, tracers have been used in the Cascadia Basin region to understand properties of ocean crust such as porosity and dispersivity through conducting tracer tests. These tests have included natural (inherent) tracers, pumping tests (i.e., surface seawater tracer) as part of IODP standard operating procedures, and injection followed by sampling of specific compounds as part of scientific experiments (Fisher et al., 2005a). Historical use of tracers in this region is important for baseline geochemical conditions and some of the tracers previously used are considered for the CO_2 injection experiment. Additionally, baseline geochemical conditions cannot be assumed, so historical use of tracers in the region becomes important for pre-injection monitoring strategies.

IODP Expedition 301 used surface seawater and a perfluorocarbon tracer for assessing core contamination (Fisher et al., 2005a). The tracer injection experiment conducted during IODP Expedition 327 (section 2.2.2.3) used the following tracers: SF_6, Rhodamine WT fluorescent dye, rare earth element salts (CsCl, ErCl, HoCl), and fluorescent microspheres (Fisher et al., 2011f; Fisher et al., 2005a). Other candidate tracers considered in the IODP Expedition 327 drilling proposal but were not selected were potassium bromide (KBr), sodium bromide (NaBr), and a stable isotope of Helium (^{3}He) (Fisher et al., 2003b).

4.5 Injection Strategies for Tracers

4.5.1 Pulsed vs Continuous Injection

The injection strategy for a given tracer is partly determined by the volume of tracer introduced and the chemical (e.g., solubility) and physical (e.g., density) properties of the tracer (Myers et al., 2013a). For CCS projects, the injection of both CO_2 and tracers allows for different injection approaches. Possible tracer injection strategies include 1) adding small amounts of tracer to the main CO_2 stream, or as a concentrated slug during brief pauses in CO_2 injection, known as pulsed injection, 2) a continuous injection followed by water or CO_2, or 3) simply adding the tracer to water during injection (Myers et al., 2013a).

A pulsed tracer injection strategy lowers the total amount of tracer required and hence cost (Roberts et al., 2017; Myers et al., 2013a). Injecting slugs of tracers during brief pauses in CO_2 injection is logistically simpler (Myers et al. 2013a), especially if continuous injection involves development of a specialized tracer injection system. Additionally, pulsed tracer injections are typically used to determine partitioning behavior, which describes how a tracer is distributed between two immiscible phases (e.g., supercritical CO_2/water), and migration mechanisms (Stalker and Myers, 2014) which are advantageous for using tracers to trace subsurface CO_2.

A continuous tracer injection strategy increases cost due to needing larger volumes and increases the background concentrations in the reservoir and may require specialized infrastructure for continuous co-injection of CO_2 and tracers (Roberts et al., 2017; Stalker and Myers, 2014). Increasing tracer volumes to tag the entire injection stream may cause issues for regulatory bodies when using artificial tracers (e.g., perfluorocarbons, chlorofluorocarbons) but regulatory issues may be avoided if using natural tracers (e.g., noble gases, isotopic composition of carbon or oxygen) (Roberts et al., 2017).

The scale of the injection is important when determining if tracers should be pulsed or continuously injected. The cross-hole tracer experiment conducted during IODP Expedition 327 continuously injected SF_6 for a 24-hour period into the deep-sea basalt. If CO_2 is injected (either continuously or pulsed) over a period of ~35 days, this substantially increases the amount of tracer required compared to a 24-hour period. At pilot scales, it is unlikely a large amount of a single tracer would be necessary, especially if small quantities of one or more tracers are used in combination with real-time measurements.

4.5.1 Water-Alternating-Gas Method

The water-alternating-gas CO_2 injection strategy is more focused on optimizing mineralization rates in the aquifer but does affect a tracer injection strategy. As suggested by Tutolo et al. (2021), CO_2 transport becomes the limiting factor for the progress of reactions towards mineralization since once the portion of water that is in contact with the CO_2 becomes in equilibrium (or saturated) with the CO_2, it can't dissolve anymore CO_2 and so needs a new parcel of aquifer water that is unsaturated with CO_2 (Tutolo et al., 2021).

Water-alternating-gas (WAG) cycling, a method routinely used for enhanced oil recovery, has been modelled to try to understand the processes involved in using this approach to enhance rates

of CO_2 mineralization compared to CO_2 injection only (Figure 4.3). This is due to increasing the amount of CO_2 dissolving into solution, which exposes more basalt to the dissolved CO_2 (Tutolo et al., 2021; Goldberg et al., 2018a). This injection strategy would also hold advantages by maximizing CO_2 injection volumes (Goldberg et al., 2018a). At the pilot scale, a 10,000-ton CO_2 injection is not a large enough volume for WAG cycling to make a difference in mineralization rates but will make a difference at larger scale injections (megatons) (Tutolo et al., 2021).

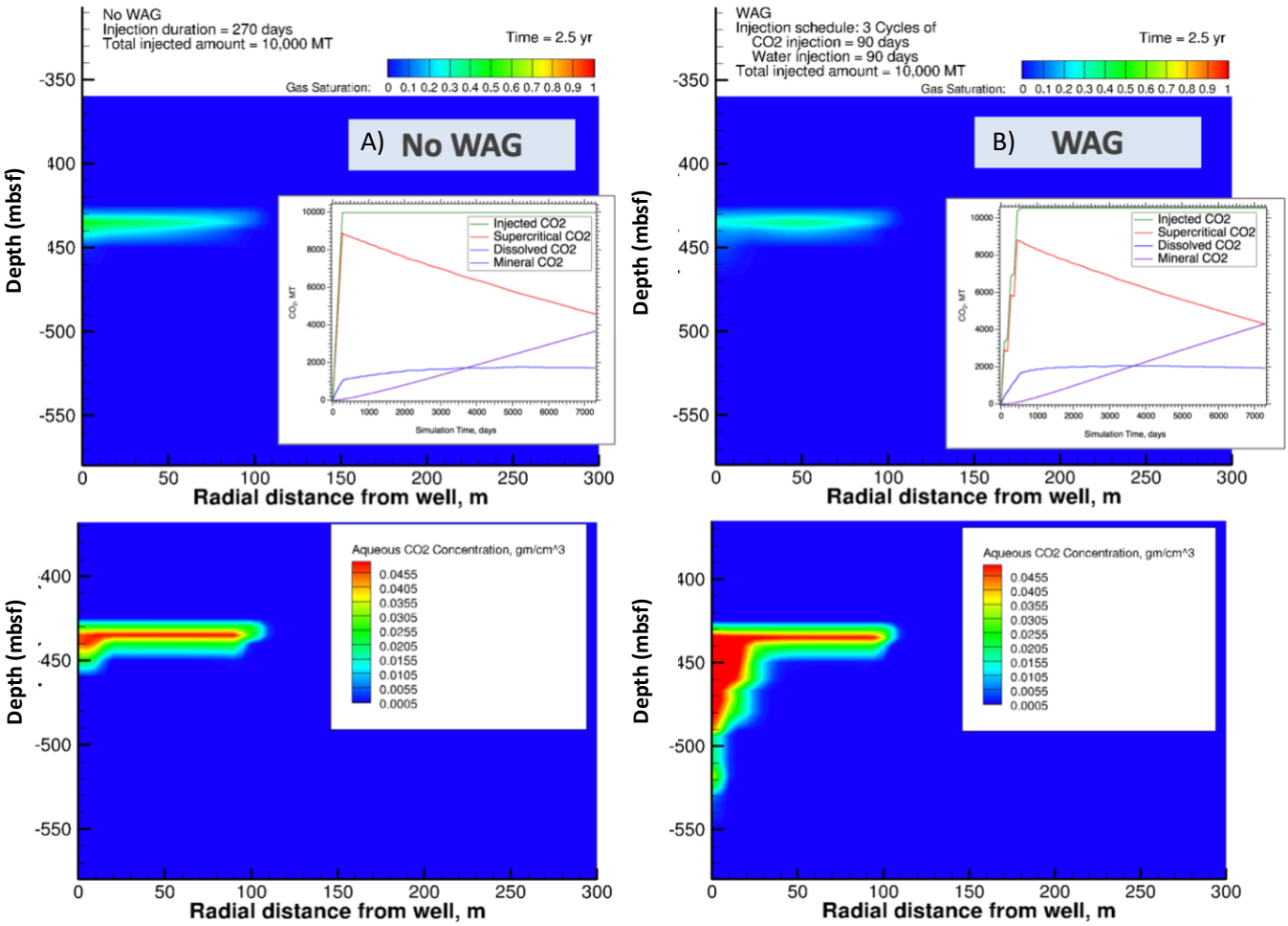

Figure 4.3*: Numerical simulation results for injection of CO_2 into a deep-sea basalt formation using CO_2 injection only and the addition of water-alternating-gas cycling. The ECKChem software and STOMP-EOR and STOMP-CO_2 modeling code was used (Goldberg et al., 2018a). Depth is listed in meters below the seafloor (mbsf), and the radial distance from the injection well is in meters. Aqueous CO_2 concentrations are listed in gm/cm^3. (A) Simulation without WAG cycling, with injection of 10,000 metric tons of supercritical CO_2 over 2.5 years. (b) Simulation including three cycles of WAG where supercritical CO_2 was injected for 90 days, then followed with injection of water for 90 days, totaling 10,000 metric tons of injected fluids over the same 2.5-year period as A. The amount of dissolved CO_2 in the simulation without WAG (~1,000 metric tons) is less than the amount of dissolved CO_2 in the simulation including WAG (~1900 metric tons). WAG cycling could increase rates of mineralization by increasing the amount of dissolved CO_2 in contact with the minerals in the basalt, although flow rates in*

the simulation were not included in the source publication. Sources: Demirkanli et al. (2017) & Goldberg et al. (2018a).

4.6 Potential Tracers

The information in this section is the focus of this research with a goal of investigating which tracers would be most suitable for use during the Solid Carbon CO_2 injection experiment where 10,000 tons is planning to be injected into the Cascadia Basin basalt using CO_2 in a supercritical phase. Six of the potential tracers considered in this research are recognized greenhouse gases and each of the compound's global warming potential is included for thoroughness. Even if leakage into the bottom ocean does occur, it is unlikely they would be released back into the atmosphere since they are detectable in very low concentrations. Injection of CO_2 into basaltic crust and using geochemical tracers for monitoring the injected CO_2 is a relatively new field so many of the tracers considered have not yet been used in ocean crust. Additionally, the solubilities in water for most of the potential tracers found in the published literature were determined at 1 atm and lower temperatures (25-40ºC) than the *in-situ* conditions (65ºC, ~30 MPa) in the Cascadia Basin and have not been determined at higher temperatures or pressures (Table 4.1).

Table 4.1: *Comparison of detection limits and solubility of tracers in water and supercritical CO_2.*

Tracer	**Detection Limit (mol/l)**	**Solubility in water (mol/l)**	**Soluble in supercritical CO_2**
Perfluorocarbons (PFC)*	1×10^{-15} to 3.5×10^{-16}	5.7×10^{-6} **	Yes (n/a)
Sulfur Hexafluoride (SF_6)*	3×10^{-17}	2.0×10^{-4} (35ºC)	
Trimethyl sulfur pentafluoride (SF_5CF_3)*	5×10^{-14}	7.7×10^{-5} (35ºC)	
Chlorofluorocarbons (CFC)*	1×10^{-14}	0.0021 (40ºC)	
Hydrofluorocarbons (HFC-134a)*	7.48×10^{-15}	0.01 (40ºC)	
Hydrochlorofluorocarbons (HCFC-22)*	1.41×10^{-14}	0.02 (40 ºC)	
Cesium chloride	1.23×10^{-10}	12.5 (40 ºC)	
Esters (propylene glycol diacetate)	6.0×10^{-6}	0.624 (25 ºC)	
Fluorescent Dyes	8.7×10^{-10}	0.075 **	Yes (coumarin dyes; n/a)

Table Footnotes: All measurements converted to mol/l for comparison. All solubilities were measured at 1 atm. Three CFC compounds are considered in this research, the average of all three solubilities in water are shown here. Fluorescein is used as an example for fluorescent dyes. The detection limit for fluorescein was measured at a pH of 7.5. Data from the other fluorescent dyes considered can be found in Table 3.2. Data for other esters can be found in Table 4.4, and for PFCs in Table 4.2. * = greenhouse gas; ** = the original source publication did not include temperature along with the value; n/a = no data value provided. Sources can be found in each individual section.

4.6.1 Conservative Tracers

4.6.1.1 Perfluorocarbons

4.6.1.1.1 Introduction

Perfluorocarbons are commonly used tracers due to their inertness and wide range of available compounds (Stalker and Myers, 2014). In this research, perfluorocarbons are considered as potential conservative tracers of CO_2 while it remains in a supercritical phase. Five perfluorocarbon compounds are suitable candidates as tracers in CCS scenarios (Stalker and Myers, 2014; Myers and White, 2018; Myers et al., 2013a). Basic physical and chemical properties, logistics, and a case study of their use in a pilot CO_2 sequestration project are described below.

4.6.1.1.2 Basic Physical and Chemical Properties

From the chemical compound class perfluoroalkanes, perfluorocarbon (PFC) compounds are synthetic compounds solely consisting of a carbon and fluorine chemical structure which makes them exceptionally stable (chemically, thermally) in the environment (Galdiga and Greibrook, 1997; Simmonds et al., 2002). PFCs demonstrate high compressibility (Smart, 2001; Dunitz, 2003), have unusual physiochemical properties (Oliveira et al., 2007), are non-flammable (Ljosland et al., 1993), non-toxic, and stable to 1200°C (Li and Tanhua, 2021). PFCs are generally considered to be conservative tracers due to the compounds exhibiting strong intramolecular bonding (Oliveira et al., 2007; Freire et al., 2005; Myers and White, 2018). Perfluorocarbons listed in the published literature as tracers for CCS are listed in Table 4.2.

PFCs have very low solubilities in water (Myers and White, 2018; Roberts et al., 2017), although solubility values are difficult to measure since these compounds are highly volatile (Rauh et al., 2014). There is limited published data on the solubility of PFCs in water (Rauh et al., 2014) except for Perfluoromethylcyclohexane (PMCH), which has a solubility in water of ~2 mg/l (House et al., 2003). PFCs are known to be highly soluble in supercritical CO_2 (Oliveira et al., 2007; Berven et al., 2009; Wai et al., 1998) but factors that contribute to increased solubility of PFCs in the presence of supercritical CO_2 (compared to other solvents) are currently undefined (Raveendran et al., 2005). One study hypothesized the reason for this could be unique interactions between CO_2 and fluorine (Dardin et al., 1998), while other studies (Yee et al., 1992; Diep et al., 1998; Yonker and Palmer, 2001; Kanakubo et al., 2002) have disputed this hypothesis. Berven et al. (2009) suggests that PFCs with increased molecular weight will have a decreased solubility in supercritical CO_2.

Table 4.2: *Commonly used Perfluorocarbon tracers.*

Acronym	Chemical Name (perfluoro-)	Formula	Molecular Weight	Detection limits (nM)
PDCB	dimethylcyclobutane	C_6F_{12}	300.04	2×10^{-7}
PMCP	methylcyclopentane	C_6F_{12}	300.05	2×10^{-7}
PMCH	methylcyclohexane	C_7F_{14}	350.05	2×10^{-7}
PDCH	dimethylcyclohexane	C_8F_{16}	400.06	1×10^{-6}
PTCH	trimethylcyclohexane	C_9F_{18}	450.07	3.5×10^{-6}

Table Footnotes: Molecular weights from Dugstad et al. (1993) and Myers and White (2018). Chemical names and formulas are from Watson and Sullivan (2013). Detection limits of perfluorocarbons analyzed using a GC-ECD from Draxler et al. (1991).

4.5.1.1.3 Logistics

Since the 1980s, perfluorocarbons have been used in the manufacturing industry, and as cleaning solvents and fire suppression agents among other uses (Tsai et al., 2002). As they are anthropogenically produced, they have low and stable background concentrations in the atmosphere (parts per quadrillion by volume, ppqv) (Li and Tanhua, 2021; Myers and White, 2018; Watson et al., 2007). They also have long residence times in the atmosphere ranging between 3,000-50,000 years (Harnisch et al., 1996; Simmonds et al., 2002). Their stability in the environment limits their contribution to air pollution or ozone depletion (Simmonds et al., 2002) but they are potent greenhouse gases with a global warming potential ~9 orders of magnitude higher than compared to CO_2 (Stalker and Myers, 2014; Watson and Sullivan, 2013; Simmonds et al., 2002). Since they have low atmospheric concentrations and release rates (Watson et al., 2007), they have a minor contribution to global warming compared to rapidly increasing atmospheric CO_2 concentrations (Watson et al., 2007).

There is uncertainty surrounding the partitioning behavior of PFCs between aqueous and non-aqueous fluids (e.g., supercritical CO_2) at various temperatures, pressures, and salinities (Rauh et al., 2014). Octanol/water partition coefficients have been previously used but there is no existing published data that defines partition coefficients for PFCs between $scCO_2$/water phases (Shell Canada Limited, 2014). Additionally, there are no known biological processes that effect the behavior of PFCs in the subsurface (Li and Tanhua, 2021; Watson et al., 2007). The larger PFC molecules may interact with sediment surfaces in comparison to the smaller PFC molecules (Zhong et al. 2014; Myers and White, 2018), but they are documented as not being retained during migration by adsorption of organic compounds such as clays (Shell Canada Limited, 2014). If tagged to the supercritical CO_2, PFC concentrations will likely increase relative to the amount of CO_2 (i.e., DIC) in the reservoir since PFCs are unable to tag CO_2 once it dissolves into water (Myers and White, 2018).

The highly sensitive measurements and high volatility of PFCs require special precautions to prevent sampling contamination (Wells et al., 2007, 2013). The procedure for analysis requires volatilizing the compounds (i.e., heating them up), which can cause cross-contamination in the instrument if running other samples (Orcutt et al., 2017). The low solubility of PFCs in water facilitates gas partitioning within the collected sample, allowing a quantitative headspace analysis with gas chromatography with an electron capture detector (GC-ECD) (Sauvage et al., 2017; Dugstad, 1992, 1993). A GC-ECD can detect PFC compounds with different molecular weights (Draxler et al., 1991; Myers et al., 2013; Nazzari et al., 2013) so multiple PFCs can be analyzed in a single analysis (McCallum et al., 2005). PFCs are detectable at femtogram levels (10^{-15}) with a GC-ECD or negative ionization chemical ionization mass spectrometry (NICI-MS) (Watson et al., 2007; Cooke et al., 2001; Begley et al., 1988; Lovelock and Ferber, 1982; Roberts et al., 2017; Smith et al., 2000; Draxler et al., 1991). Detection limits vary with variations in instrument calibration, and limits of detection for each PFC compound in this research range between 2×10^{-7} to 3.5×10^{-6} nanomolar (Draxler et al., 1991) and are listed in Table 4.2.

Costs for PFCs are too expensive for industrial scales (Gyore et al., 2017). A 250 ml sample can be more than $100 USD (Beth Orcutt, pers. communication, 2023) and general cost estimates from the UK are ~£100 per metric ton of CO_2 (Roberts et al., 2017).

4.6.1.1.4 Case Studies of the use of Perfluorocarbons in Experiments and CCS Pilot Projects
Perfluorocarbons have been used as tracers in near surface monitoring studies (Lagomarsino, 1996; Strazisar et al., 2009; Wells et al., 2013) and oil and gas well tracing (Ljosland et al., 1993; Dugstad et al., 1992). Perfluorocarbon tracers have also been routinely used to trace drilling fluid in terrestrial and offshore subsurface microbiological studies to assess seabed drilling contamination to core samples (Orcutt et al., 2017; Smith et al., 2000; McKinley and Colwell, 1996; Russell et al., 1992; Senum and Dietz, 1990).

Perfluoromethylcyclohexane (PMCH) was used during IODP Expedition 357 for contamination testing with seabed drills and was chosen because a large range of concentrations are detectable (across 6 orders of magnitude) using a GC-ECD (Orcutt et al., 2017). Drilling fluid samples (10ml) were collected from the seabed drills after drilling completed and analyzed using a GC-ECD. A total mass of 2 picograms needs to be concentrated from a sample to be detectable during analysis for PMCH (Orcutt et al., 2017).

Experimental data produced by Shell Canada in collaboration with the Commonwealth Scientific and Industrial Research Organization (CSIRO) has shown that PFCs could be suitable as conservative tracers for injected CO_2 (Shell Canada Limited, 2014). A slim tube experiment was performed to test how various PFC compounds interact with different rock types (sandstone, coal, carbonates) at different temperatures and pressures (65°C and 12MPa, 80°C and 20.7 MPa). The results indicated that in general, PFCs are not retained during migration by matrices that could retard PFC transport such as clays (Shell Canada Limited, 2014). A batch reactor experiment was also conducted to observe if PFCs partition into the water phase. The results were inconclusive due to the PFCs forming a separate phase compared to the supercritical CO_2 and not dispersing back into the supercritical CO_2 once separated. This was assumed to be caused by the differences in density of PFCs and supercritical CO_2, and the injection approach used (i.e., PFCs were not dispersed into the supercritical CO_2 prior to injection into the vessel).

There have been a handful of CCS pilot projects which have used PFCs as part of their monitoring strategies (Strazisar et al., 2009; Wells et al., 2013; Vandeweijer et al., 2011) but none are applicable to this study due to very different temperature/pressure conditions (e.g., CO_2 in a gas phase) and/or rock type (e.g., coal seams). One CO_2 pilot project that used PFCs to trace supercritical CO_2 is described below although it was conducted in a terrestrial sandstone formation between closely spaced wells.

Frio Brine Pilot Project
The Frio Brine pilot project in Texas, U.S.A continuously injected 1600 tons of food grade CO_2 in a supercritical state at a rate of 3 kg/s over 10 days into an ~6 m thick brine-filled highly permeable sandstone interval within the Oligocene Frio formation (Figure 4.4) (Hovorka et al., 2006; Freifeld et al., 2005). The CO_2 was injected at a depth of ~1540 m in the injection well (McCallum et al., 2005). The porosity was very high in the CO_2 injection interval at upwards of 35% (Hovorka et al., 2006). A monitoring well (30 m away from injection well) was used to

collect formation fluid samples at depth (Figure 4.4) (McCallum et al., 2005). The temperature and pressure in the formation was 63°C and 143 bars, respectively (Freifeld et al., 2005).

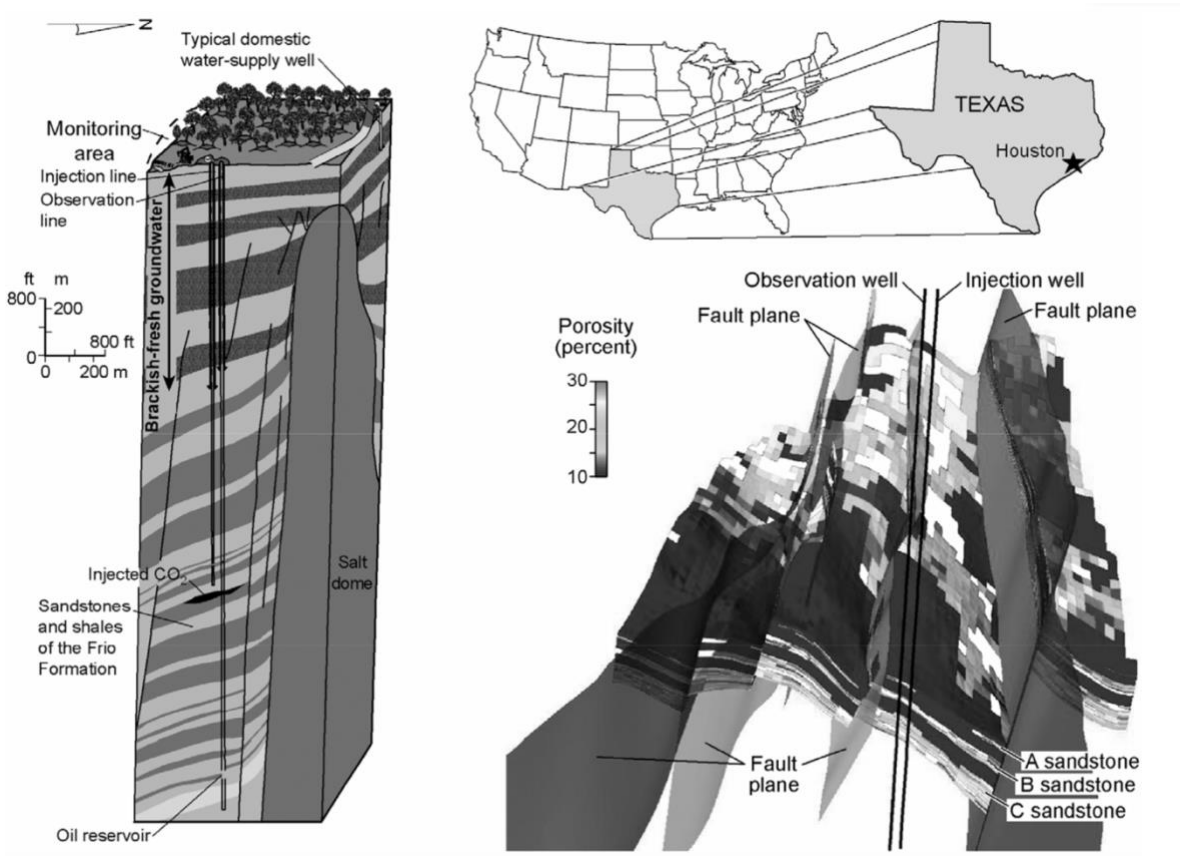

Figure 4.4: *Frio Brine pilot CO_2 sequestration site location (top right), geologic setting (left), and locations of wells used for injection and monitoring from a reservoir model (bottom right). The site is in Houston, Texas, U.S.A. The Frio Formation was the targeted formation for CO_2 injection at ~1540 m below the surface and composed of highly permeable and porosity sandstones (dark grey, left). Caprock seals above the injection zone are composed of shales and siltstones (light grey, left). The site is within a fault-bounded zone, part of a bigger system of faults above the salt dome. The injection well was drilled close to a deep existing well that was used as the monitoring well in this experiment. The locations of wells used for injection and monitoring are shown within a reservoir model created using 3-D seismic data and logs. Source: Hovorka et al. (2006).*

The goals of this experiment included determining arrival time of the CO_2 plume, observe geochemical changes as the plume moved past the monitoring well, and estimate residual saturation of the brine (Freifeld et al., 2005). To accomplish these goals, chemical tracers (PMCH, PTCH, PMCP, PDCH, in addition to Kr, and SF_6) were added to the continuous CO_2 stream for a total of three tracer injection tests (McCallum et al., 2005). The first tracer injection consisted of 1.55 kg PMCH and 1.55 kg of PTCH, which initiated 2 hours after CO_2 injection started. A second tracer injection consisted of 150 g of PMCB and 150 g of PDCH. The third tracer injection consisted of 83.80 g of Krypton and < 200 g of SF_6 (this was undetermined

because there was a problem with the pump during injection of SF_6), 150 g PMCH, and 150 g PTCH (McCallum et al., 2005).

Subsurface sampling was conducted using a novel U-tube system which collected samples on an hourly basis at *in-situ* reservoir conditions during the 10-day period (Freifeld et al., 2005; McCallum et al., 2005). Gas chromatography with an electron capture detector (McCallum et al., 2005) and mass spectrometry (Kharaka et al. 2006) were used to analyze the samples in a laboratory. Since each tracer injection included different PFC volumes and compounds, the data were standardized for comparison (McCallum et al., 2005).

With each tracer injection, there were associated breakthroughs at 54, 157, and 173 hours after CO_2 injection started (McCallum et al., 2005). The average tracer travel time was ~51 hours for each injection (well spacing was 30 m) (McCallum et al., 2005). The first tracer breakthrough was observed to be fast, with similar travel times between CO_2 and PFCs, due to complete solubility of PFCs in the supercritical CO_2 and limited interaction with the surrounding rock matrix (Figure 4.5a). The second and third tracer breakthroughs had slightly slower travel times (~1 hour) compared to the CO_2 (Figure 4.5b) which may indicate PFCs moving as a single phase rather than be dispersed into the injected CO_2 (McCallum et al. 2005).

The travel times between all PFC tracers being generally constant (standard deviation of 1.6 hours between all injections) indicates a rapidly formed preferential flow path (McCallum et al., 2005). The travel times of the PFCs were used to estimate residual saturation of the CO_2 plume (~17%) using a radial flow model, although the model did not consider permeability, buoyancy, or capillary pressure (McCallum et al., 2005). Each subsequent breakthrough of PFCs showed a broadening of the data (i.e., dilution of PFCs) (Figure 4.5b), which could be interpreted to mean 1) PFCs dispersed themselves in the CO_2 as the experiment progressed, and/or 2) smaller flow paths started to develop with subsequent injections which would cause more dispersion especially as more CO_2 became available and PFCs are more soluble in CO_2 than brine (McCallum et al., 2005). Compared to other CCS pilot projects, the quick breakthrough of tracers observed was likely due to a short distance between the two wells (Myers et al., 2013a). This experiment shows that using PFCs to tag supercritical CO_2 is possible and that the PFCs disperse in supercritical CO_2 during injection and stayed dispersed while the supercritical phase is present. The conditions of this experiment are different than the deep-sea basalt in the Cascadia Basin and processes such as dilution and dispersion of PFCs need to be considered.

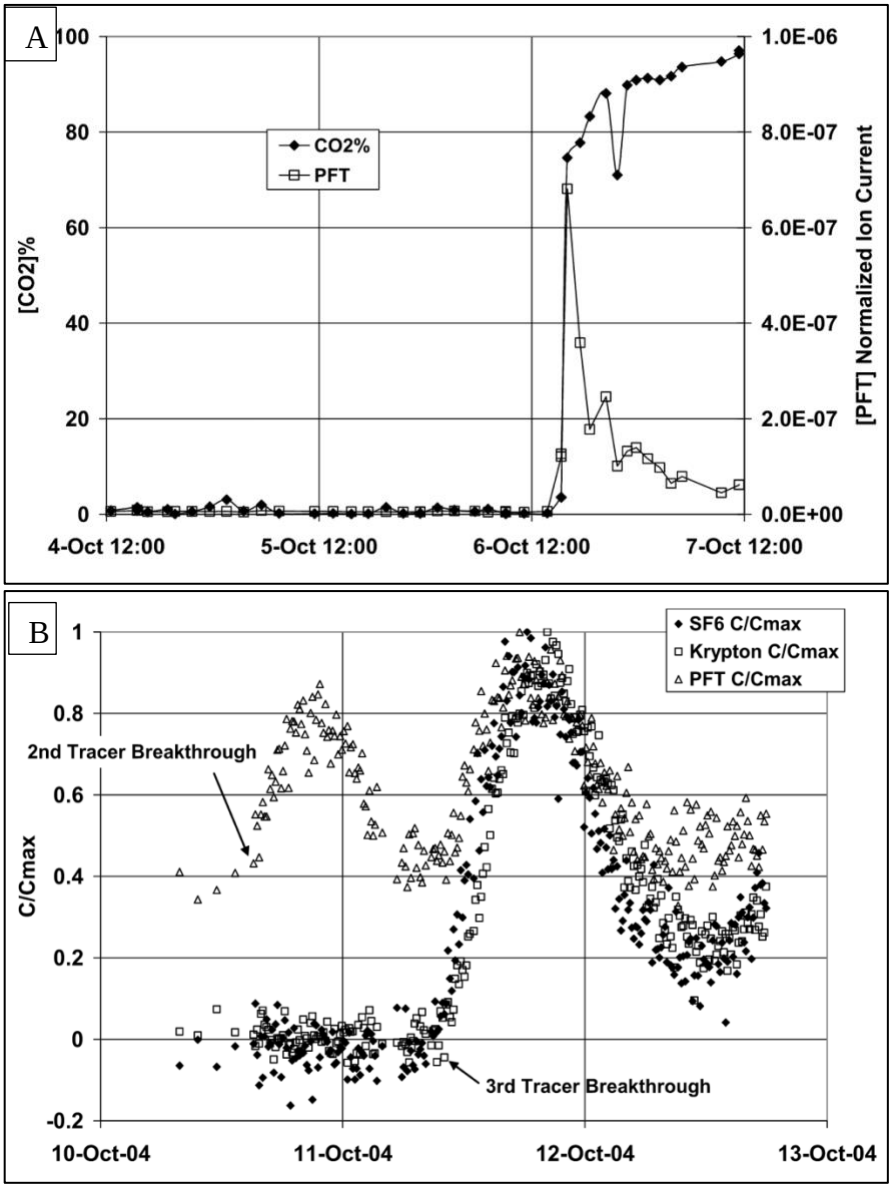

Figure 4.5*: Tracer breakthrough curves for all three tracer injections. A) Initial breakthrough of CO_2 plotted along with initial breakthrough of PFC tracers (PMCH, PTCH). CO_2 was measured as percent of total gas recovered in the sample. PFC concentration is mass spectrometer ion current normalized to total mass current. B) PFCs (PMCB, PDCH), and Kr and SF_6 breakthrough curves from the second and third tracer injections, respectively. Concentrations were determined by quadrupole mass spectrometry and are shown as the concentration divided by the maximum concentration (C/Cmax) for each tracer injection. PFC has a starting concentration above zero because of PFCs were used in the first tracer injection. PFCs are denoted as PFT in the sourced publication as "perfluorocarbon tracer". Source: Freifeld et al. (2005).*

4.6.1.2 Sulfur Hexafluoride and Trifluoromethyl Sulfur Pentafluoride

4.5.1.2.1 Introduction

Two perfluorinated compounds are discussed below as conservative tracers for their inexpensive nature, low detection limits, and previous use in CCS projects. The compounds are discussed together because they possess similar physical and chemical properties.

4.6.1.2.2 Basic Physical and Chemical Properties

Sulfur Hexafluoride (SF_6) is an inert perfluorine compound that has been commercially produced since 1953 (Stalker et al., 2009) and used for its electrical and thermal insulation properties in industry (Watson et al., 2001). SF_6 is a widely used tracer gas, analyzed by inexpensive methods at high sensitivity, and can be easily sourced at a reasonable cost due to being commercially available (Kim et al., 2020; Busenberg and Plummer, 2010; Stalker et al., 2009). It is minimally affected by degradation over a wide range of conditions (International Atomic Energy Agency, 2006; Mroczek and Glover, 1996). At sea surface temperatures and pressures, SF_6 is a gas, but liquefies at low pressures (> 2 MPa) (Fisher et al., 2011f; Watson et al., 2001). Furthermore, SF_6 is chemically stable up to 500°C (Busenberg and Plummer, 2010). At 35ºC and 1 atm, the solubility of SF_6 in seawater is 2×10^{-4} mol kg^{-1} (Figure 4.6) (Busenberg and Plummer, 2008; Ashton et al., 1968; Cosgrove and Walkley, 1981).

Trifluoromethyl sulfur pentafluoride (SF_5CF_3) is a perfluorocarbon and has no known industrial uses but is of anthropogenic origin, either as a breakdown of atmospheric SF_6 or released as a byproduct of manufacturing fluorochemicals (Ho et al., 2008; Erboy and Smethie, 2012). It was first recorded by Kisliuk and Silvey (1952). SF_5CF_3 is considered a perturbed SF_6 molecule in which one fluorine atom is replaced by a CF_3 group (Tuckett, 2006). Like SF_6, SF_5CF_3 is a highly stable compound that doesn't degrade under aerobic or anaerobic conditions (Erboy and Smethie, 2012). The solubility of SF_5CF_3 in water at 1 atm and 35ºC is 7.48×10^{-5} mol kg^{-1}, about two times less than SF_6 (Figure 4.6) (Busenberg and Plummer, 2008).

Both SF_6 and SF_5CF_3 molecules behave like other perfluorocarbon tracers (PFC) since they all have low solubility in water, although SF_6 and SF_5CF_3 have a smaller molecular size than conventional PFC molecules (Amonette et al., 2014). There is limited information on partitioning behavior of both SF_6 and SF_5CF_3 between supercritical CO_2 and water (Busenberg and Plummer, 2000). Additionally, there is a lack of information in the published literature on the solubilities of SF_6 and CF_3SF_5 in supercritical phase CO_2 at any temperature or pressure.

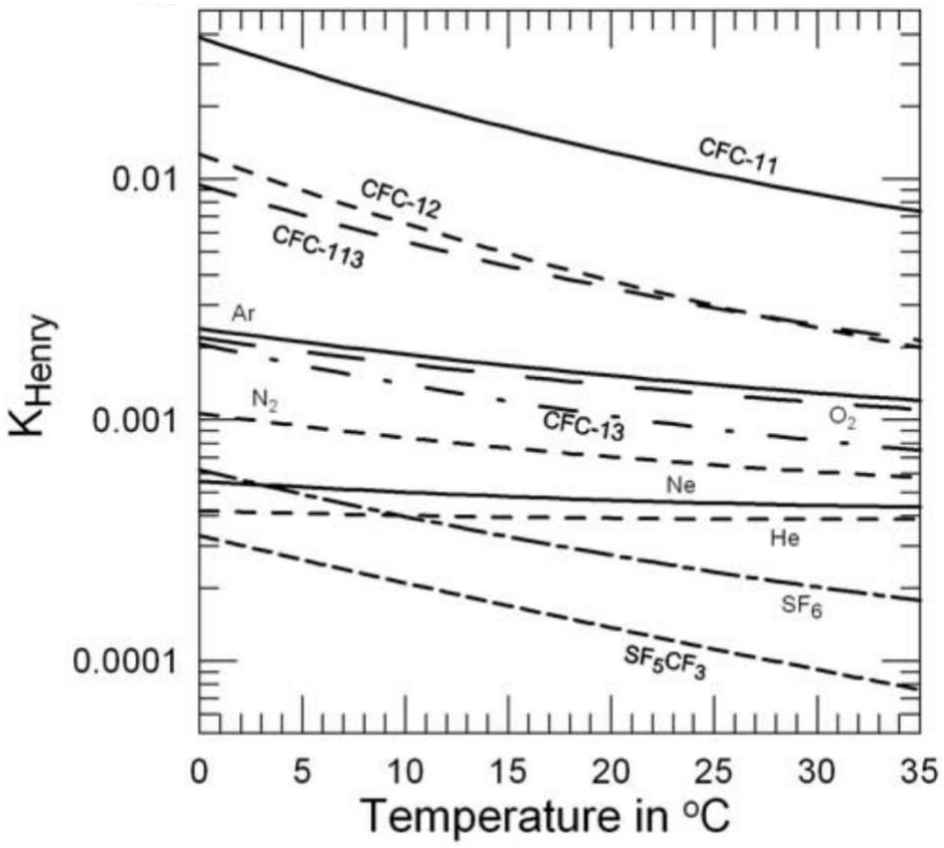

Figure 4.6: *Temperature dependence of Henry's Law solubility constants for SF_5CF_3 and SF_6, along with CFC-11, CFC-12, CFC-113, CFC-13, Ne, He, O_2, and N_2. CFC-11, CFC-12, CFC-113, Ne, and He are also tracers considered in this research. At 35°C and 1 atm, SF_5CF_3 has a solubility of 7.48 x 10^{-5} mol kg^{-1} and is two times less soluble than SF_6 (2 x 10^{-4} mol kg^{-1}) in water at the same temperature and pressure. The solubility of SF_6 and SF_5CF_3 is much less than CFC's and only slightly less than He. Source: Busenberg and Plummer (2008).*

4.6.1.2.3 Logistics

The Kyoto Protocol in 1997 deemed SF_6 as one of the six main greenhouse gases, with SF_6 having a per molecule global warming potential ~23,900 times that of CO_2 and an atmospheric residence time of ~3,200 years (Ravishankara et al., 1993). SF_5CF_3 was not clearly outlined in the Kyoto Protocol but is a strong greenhouse gas with a per molecule global warming potential ~18,000 times higher than CO_2 (Tuckett, 2006). CO_2 has a concentration in the atmosphere more than nine orders of magnitude greater than current SF_5CF_3 concentrations (Tuckett, 2006). SF_5CF_3 has a relatively shorter atmospheric residence time than SF_6 (~800 years), so its global warming potential is less prolonged than that of SF_6 (Ho et al., 2008). Observed changes in atmospheric concentrations are similar for SF_6 and SF_5CF_3 over the past 40 years (Tuckett, 2006).

As a synthetic, non-toxic, commercially produced compounds, there are essentially no background SF_6 concentrations in subsurface formations, as has been shown using SF_6 as a

conservative tracer in multiple terrestrial geologic carbon storage pilot projects in recent years (Boreham et al., 2011, Jenkins et al., 2012, Matter et al., 2016, Soltanian et al., 2018). There has been limited use of SF_5CF_3 in geologic carbon storage projects to date (Snæbjörnsdóttir et al., 2017), but with such small atmospheric concentrations (Tuckett, 2006), it is likely there are no background SF_5CF_3 concentration in subsurface formations. The Cascadia Basin site is even more removed from the atmosphere than the terrestrial subsurface, so reduces concern over SF_6 or SF_5CF_3 escaping back to the atmosphere if either is chosen as a tracer for monitoring the Solid Carbon CO_2 injection experiment. Additionally, both compounds require no special handling precautions (Mroczek and Glover, 1996), and would likely be permitted for use in the offshore environment under a research exemption (R. Webb, pers. comm., 2021). Both compounds are known to have a low likelihood of retarding as they are transported through an aquifer (Snæbjörnsdóttir et al., 2017; Busenberg and Plummer, 2010).

The detection limit for SF_6 in water is 3×10^{-17} mol/l (Gooddy et al., 2006; Mroczek and Glover, 1996) while SF_5CF_3 has a detection limit in water of 5×10^{-14} mol/l (Busenberg and Plummer, 2010). Both SF_6 and SF_5CF_3 can be analyzed using a gas chromatograph-electron capture detector (GC-ECD) with a precision of ± 2% (Mroczek and Glover, 1996; Matter et al., 2016; Matter et al., 2014; Wakkinkhof et al., 1991). SF_5CF_3 can be injected using the same technology used for SF_6 (Ho et al., 2008).

Estimated costs for SF_6 are less than $100 USD per metric ton of CO_2 (Roberts et al., 2017) while costs for SF_5CF_3 have not be outlined in the published literature.

4.6.1.2.4 Case studies of the use of SF_6 and SF_5CF_3 in field trials

SF_6 was previously used as a conservative tracer at the Cascadia Basin site as part of the cross-hole tracer experiment (section 2.4), where SF_6 was detected in the same crustal aquifer more than 1000 m from the injection borehole as well as in a borehole 311 m from the injection hole up to nine years after injection based on fluids collected during the experiment (Neira et al., 2016; De Jong, 2020). Furthermore, SF_6 remained stable within the temperature range in the ocean basement at the Cascadia Basin site which is observed to be ~62-64°C (Mottl et al., 1998; Fisher et al., 2005a). The previous use of this tracer at the planned CO_2 injection site means there will be background concentrations. If background concentrations fluctuate over time, it would be difficult to differentiate any new SF_6 concentrations injected into the formation. Pre-injection monitoring would need to demonstrate background concentrations are low and steady for SF_6 to be chosen as a tracer for the CO_2 injection experiment. The Osmosampler that will be installed in summer 2023 will collect samples of formation fluids for at least one year and those samples can determine if SF_6 is at steady and low enough concentrations to be chosen as a tracer again.

The CarbFix pilot project (section 1.1.3.4.1) used SF_6 and SF_5CF_3 as conservative tracers to assess plume migration and observe breakthrough of CO_2-rich fluid and CO_2+H_2S-fluid at the monitoring well. The SF_6 was mixed into the CO_2 fluid (during phase I) while the SF_5CF_3 was mixed into the CO_2+H_2S flue gas stream (during phase II), then each stream dissolved into water, and injected into the formation (Matter et al., 2014). The similar transport of SF_6 and SF_5CF_3 in the basaltic formation validates that the compounds are stable within a temperature range of 20-50°C (Snæbjörnsdóttir et al., 2017).

Introduced in section 4.6.1.1.4, the Frio Brine CO_2 storage project observed similar travel times between injected SF_6 and PFC's (PMCH, PTCH, PMCP, PDCH) (Figure 4.4) (Kampman et al., 2014), and SF_6 had slightly faster transport compared to Krypton, likely because Krypton is more soluble in water than SF_6 at the *in-situ* conditions of the site (Busenberg and Plummer, 2008; Lu et al., 2012; Preuss et al., 2005).

A tracer test using SF_6 and Na-Fluorescein was conducted in the Hot Dry Rock artificial geothermal reservoir in a fractured granite formation 2 km below the ground surface at the Rosemanowes Quarry in south-west England (Upstill-Goddard and Wilkins, 1995). The *in-situ* temperature was 20-35ºC and pressure in the injection stream was 9 MPa. For injection, 50 cm^3 of SF_6 gas was added to 20 cm^3 of water until it was saturated in the aqueous phase, while 1 kg of Na-Fluorescein was dissolved into 10 kg water. Both tracers were injected simultaneously into the injection well and samples were collected at a monitoring well after ~ 52 hours of injection. SF_6 was analyzed with a GC-ECD (± 1% analytical precision) and fluorescent samples were analyzed using a fluorometer (± 5% analytical precision). The tracer concentrations were plotted against each other, and the breakthrough curves showed identical transport of both tracers in the reservoir for the first 25 hours, indicating conservative behavior of SF_6 compared to Na-Fluorescein at the *in-situ* conditions. After 25 hours, SF_6 concentrations showed more tailing (i.e., slower transport), and it was concluded that SF_6 diffused into more stagnant zones of fracture fluid or into the bulk rock (Upstill-Goddard and Wilkins, 1995).

4.6.1.3 Chlorofluorocarbons

4.6.1.3.1 Introduction

Chlorofluorocarbons are included in the published literature as potential conservative tracers for carbon storage projects. Basic physical and chemical properties, logistics for using them, and case studies of their use are described below.

4.6.1.3.2 Basic Physical and Chemical Properties

Chlorofluorocarbons (CFCs) are highly stable, non-toxic, anthropogenic compounds with a chemical structure made up of carbon, fluorine, and chlorine atoms (Blasing and Jones, 2012; Bauer et al., 2001). CFCs were originally produced in the 1940s and 1950s (Stalker et al., 2009). They are manufactured under the trade name Freon (Busenberg and Plummer, 1992) and are mainly used in dry cleaning, refrigeration, air-conditioning, and as propellants in aerosols (Stalker et al., 2009). They are low in toxicity, nonflammable, and noncorrosive (International Atomic Energy Agency, 2006).

CFC compounds have been used in groundwater and hydrological studies (International Atomic Energy Agency, 2006 and references therein) for over 50 years to determine groundwater recharge and movement, to trace contaminant sources, groundwater age, and chemical reactions in groundwater (Chambers et al., 2019; Stalker et al., 2009; International Atomic Energy Agency, 2006). CFCs have been used in oceanographic studies as transient tracers of ocean circulation and mixing processes (Bullister, 1989, Smethie, 1993). Commonly used CFCs in groundwater studies include Trichlorofluoromethane (CFC-11; CCl_3F), Dichlorodifluoromethane (CFC-12; CCl_2F_2), and Trichlorotrifluoroethane (CFC-113; CCl_2FCClF_2) (Chambers et al., 2019;

Han et al., 2014) and will be the only CFC compounds considered due to the focus of this research in a purely aqueous environment.

CFCs exist in very low concentrations in seawater (< 2 picomol CFC/kg H_2O) (Tokieda et al., 2005). At 40°C and 1 bar, CFC-11 has a solubility in seawater of 0.004 mol l^{-1} and CFC-12 has a solubility in seawater of 0.001 mol l^{-1} (Warner and Weiss, 1985) and CFC-113 has a solubility in seawater of 0.0013 mol l^{-1} (Bu and Warner, 1995). There is a lack of published data for solubility of these CFC compounds in seawater above 40°C, or in supercritical CO_2. The solvency of supercritical CO_2 may mobilize CFCs compared to aqueous CO_2 injection (Kampman et al., 2014, Myers et al., 2013) but has not yet been tested.

There is no known natural source for CFCs but there are known sinks, mainly microbial degradation in the subsurface due to their organic nature (Roberts et al., 2017; Stalker et al., 2009). CFCs degrade on the order of years in groundwater (Horneman et al., 2008). They are generally stable in aerobic environments but are subject to degrading in anaerobic conditions (Han et al., 2014). CFC-12 is more resistant to degradation compared to CFC-11 and CFC-113 (Han et al., 2014; International Atomic Energy Agency, 2006; Lovley and Woodward, 1992). Other processes that lower dissolved CFC concentrations in subsurface environments are adsorption onto organic matter and hydrodynamic dispersion (Han et al., 2014).

4.6.1.3.3 Logistics

From industrial use, these compounds increased in concentration in the atmosphere until 1987 when the Montreal Protocol restricted the use of CFCs in order to protect the ozone layer (Stalker et al., 2009; Chambers et al., 2019). These compounds are broken down in the stratosphere, where strong UV radiation degrades the CFCs, freeing the chlorine atom, which acts as a free radical catalyst to deplete the ozone layer (Newman et al., 2009). The subseafloor is removed enough from the atmosphere that any potential leakage would go into the ocean. Although mixing in the ocean could lead to loss to the atmosphere and could be a regulation problem but is unlikely if injected concentrations are low.

The detection limit for CFCs in water is 1×10^{-14} mol/l (Gooddy et al., 2006), 1000 times larger than the detection limit for SF_6 (1×10^{-17} mol/l) (Stalker et al., 2009). Analytical procedures were developed for these compounds by Bullister and Weiss (1988) using a gas chromatography with an electron capture detector (GC-ECD), which is highly sensitive to halogenated compounds (CFCs are fully halogenated) (Bullister, 1989; Busenberg and Plummer, 1992; Tokieda et al., 2005). A minimum of 10 ml of sample is required for analysis (Tokieda et al., 2005) and can be analyzed easily within minutes (Tokieda et al., 2005; Han et al., 2014).

Contamination during sampling is a concern for these compounds as even a small amount of air (0.01 cm^3) exposed to the sample would cause contamination (Busenberg and Plummer, 1992). For preservation of collected samples, CFCs should be preserved in stainless steel, Teflon, Nylon, or glass, and should not encounter plastics, rubber, or polymers (Busenberg and Plummer, 1992).

Approximate costs for CFCs are hard to find, although, Cook and Solomon (1997) briefly mention a range of $50-100 USD with no designation for CFC concentrations or different CFC compounds.

4.6.1.3.4 Case Studies of Their Use

Field and laboratory studies have shown CFC-11 is the most vulnerable to degradation among the three CFCs considered (Han et al., 2014, Cook et al., 1995). CFCs are no longer used in the hydrocarbon industry and PFC are used instead (Roberts et al., 2017). CFCs have been suggested as tracers in CO_2 injection projects, but they have not been reportedly used to date.

4.6.1.3.5 Conclusion

The potential for certain CFCs to be removed from solution at varying extents by processes such as microbial degradation or adsorption (Chambers et al., 2019; Cook et al., 1995), lowers the reliability of using these compounds as conservative tracers to monitor CO_2 movement in oceanic crust. Out of the three CFCs considered here, CFC-12 seems the most suitable due to being the most resistant to degradation, although the lack of information for its use as a conservative tracer in recent carbon storage projects presents uncertainties. Furthermore, the question of the conservative nature of CFCs introduces disadvantages that may outweigh the advantages such as relative ease of analysis and low cost compared to other tracers and limits the application of CFCs as conservative tracers until their behavior as tracers in deep subsurface formations is understood, particularly in basaltic ocean crust.

4.6.1.4 Hydrofluorocarbons and Hydrochlorofluorocarbons

4.6.1.4.1 Introduction

Hydrofluorocarbons and hydrofluorochlorocarbons are considered as potential conservative tracers that could be used in carbon storage projects. Their basic chemical and physical properties and the logistics of their use are described below.

4.6.1.4.2 Basic Physical and Chemical Properties

Hydrofluorocarbons (HFCs) and hydrofluorochlorocarbons (HCFCs) together are referred as hydrohalocarbons, which contain carbon-hydrogen bonds (Simmonds et al., 1995). These compounds are stable fluorinated organic compounds from anthropogenic origin. Like CFCs, they have low toxicity, low surface tension, and are non-flammable (Sekiya and Misaki, 2000). HFCs are made of hydrogen, fluorine, and carbon, while HCFCs are made of carbon, fluorine, chlorine, and hydrogen (Blasing and Jones, 2012).

A few compounds listed frequently in the literature regarding tracers for hydrology and hydrogeology are HCFC-22, HFC-134a, HCFC-141b, and HCFC-142b (Li et al., 2019; Haase et al., 2014; Roberts et al., 2017). HCFC-22 was first commercially produced in 1936 (Calm and Domanski, 2004) and has been used as an ozone safe refrigerant and foam blowing agent (Haase et al., 2014; Manzer, 1990). HFC-134a has also been used as an ozone safe refrigerant and foam blowing agent since phasing out CFCs in the 1990s (Haase et al., 2014). HCFC-141b and HCFC-142b have been considered as potential tracers for ocean ventilation (Li and Tanhua, 2021) and have been used in atmospheric tracer programs (Kloss et al., 2014; Schmidt et al., 1995) but there is not enough data in the published literature to consider these compounds as potential tracers in this research. Their behavior in geologic formations has not yet been tested. There is

also a lack of published safety data, costs, and solubility values for those compounds in seawater at the temperature and pressure conditions for Cascadia Basin.

HFCs and HCFCs have similar ways of degrading in subsurface waters and have shown to be less stable than CFCs, PFCs, and SF_6, degrading over years to decades (Roberts et al., 2017). HFC-134a and HCFC-22 become oxidized when in contact with methanotrophic bacteria (Haase et al., 2014). Additionally, HCFC-22 is a product of anoxic degradation of CFC-12 and is not stable in reducing waters (Haase et al., 2014; Lesage et al., 1992). Sorption of HFC-134a and HCFC-22 is low apart from in carbon-rich sediments (Plummer and Busenberg, 2000).

HCFC-22 and HFC-134a are more soluble in seawater than CFC-11, CFC-12, CFC-113 and SF_6 at low pressures (1 bar) and temperatures (0°C-40°C) (Figure 4.7) (Haase et al., 2014). The absence of chlorine in HFC-134a leads to a lower solubility in water compared to HCFC-22 (Manzer, 1990). There is no current published literature citing solubility of these compounds in seawater at high pressures and temperatures. Furthermore, solubilities of these compounds in supercritical CO_2 have not yet been experimentally determined.

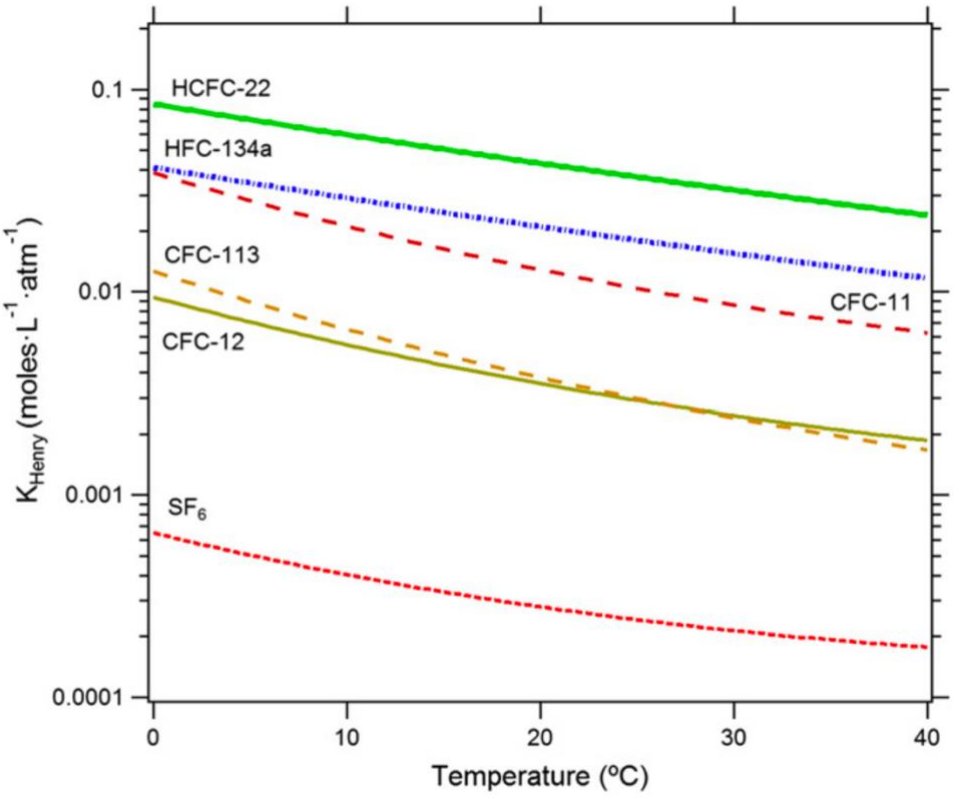

Figure 4.7: *Henry's Law solubility constants of HFC-134a and HCFC-22 compared to CFC-11, CFC-12, CFC-113, and SF_6 as a function of temperature (0℃-40℃). All solubilities were determined at a pressure of 1 bar. Both HCFC-22 and HFC-134a have a higher solubility in seawater compared to other tracers considered in this research. Solubility data for HFC-134a and HCFC-22 are from Zheng et al. (1997); solubilities of CFC-11 and CFC-12 are from Warner and Weiss, (1985) and Bullister and Weiss,*

(1988); solubility of CFC-113 is from Bu and Warner (1995); solubility of SF_6 is from Bullister et al. (2002). Source: Haase et al. (2014).

4.6.1.4.3 Logistics

Once restrictions were put in place limiting the use of CFCs, HFCs and HCFCs were developed as an alternative to CFCs to perform the same function in industry (Manzer, 1990), although both are extremely potent greenhouse gases with uncertainty around their long-term effects in the atmosphere (Simmonds et al., 1995; Solomon et al., 2007; Roberts et al., 2017; Yvon-Lewis and Butler, 2002). Although they are included in the Montreal Protocol as substances that deplete the ozone layer (Montzka et al., 2014) the atmospheric residence times are shorter compared to CFCs (HFCs have an even shorter residence time than HCFCs) and they break down before reaching the ozone (Blasing and Jones, 2012; Stalker et al., 2009; Manzer, 1990). This means HFCs have a lower global warming potential, but in the context of CCS this may be a negative factor regarding stability of these compounds in the subsurface (Stalker et al., 2009). The two most abundant HCFC and HFC compounds in the atmosphere are HCFC-22 and HFC-134a (Li et al., 2019; Haase et al., 2014).

As these compounds are commercially produced, acquisition would be relatively easy (Stalker et al., 2009). HCFC-22 has a detection limit in seawater of 1.38×10^{-14} mol/kg, while HFC-134a has a lower detection limit of 7.3×10^{-15} mol/kg in seawater (Li and Tanhua, 2021) HCFC-22 and HFC-134a can be measured using gas chromatography with an electron capture detector (GC-ECD) from less than 100 ml sample (Lobert et al., 1996), or from a larger volume (~ 1l) by gas chromatography with a mass spectrometer (GC-MS) (Ooki and Yokouchi, 2011; Simmonds et al., 1995; Montzka et al., 1993). The extremely low detection limit suggests this analytical method is very sensitive (Li and Tanhua, 2021). Using a GC-MS instrument allows for identification of multiple compounds (HFC-134a, HCFC-22) simultaneously. Cost estimates for these compounds as geochemical tracers are limited in the published literature but are approximately two to five times more than the cost of CFCs (Manzer, 1990).

There are no case studies which have used HFCs or HCFCs as tracers for CCS projects, but they are mentioned in review articles as potential tracers in the context of CCS (Roberts et al., 2017; Stalker et al., 2009). HFC and HCFC literature mainly consists of their use in age-dating groundwaters (Haase et al., 2014).

Haase et al. (2014) investigated HCFC-22 and HFC-134a as potential tracers for age-dating groundwater by determining the atmospheric mixing ratio of each compound from measured concentrations in groundwater, which were then compared to historic mixing curves for age-dating the water sample (assuming the water moves at the same velocity and there is minimal mixing). Groundwater samples were collected throughout Virginia, Tennessee, and North Carolina, U.S. Sampling methods used were identical to a sampling method used for SF_6 (Busenberg and Plummer, 2000) and the samples were preserved in stainless steel cylinders for several weeks with no change to HFC-134a and HCFC-22 concentrations (Haase et al., 2014). The analytical method used a GC with an atomic emission detector (GC-AED), which allows for detection of specific trace gases at pico- and femto-mole levels compared to other GC instruments. The study concluded that both compounds are not conservative as groundwater age-

dating tracers, due to many samples analyzed showing an absence or complete depletion of the compounds, likely due to being consumed by methanotrophic bacteria in aerobic conditions.

4.6.1.5 Noble Gases and Isotopes

4.6.1.5.1 Introduction

Noble gases are a group of inert tracers that may be useful in understanding processes controlling the behavior of CO_2 injected into the subsurface (Gilfillan et al., 2008; Zhou et al., 2012; Nimz and Hudson, 2005). Advantages include their ability to trace physical processes due to their unique physical properties, being nontoxic and stable, and are routinely measured with high precision (Preuss et al., 2005; Weber et al., 2021). Each noble gas (and their associated isotopes) uniquely responds to changes affecting a system because they each have unique physiochemical properties and possess different solubilities and partition coefficients in fluids (Gyore et al., 2017; Warr, 2013). Noble gases are one of few tracers which have experimentally defined partition coefficients for supercritical CO_2-water systems at high pressures and temperatures (Warr et al., 2015). Basic physical and chemical properties, logistics, and case studies of their use are described below for five of the noble gases.

4.6.1.5.2 Basic Physical and Chemical Properties

Noble gases are stable, environmentally safe, and inert due to having complete electron shells and so are unreactive (Weber et al., 2021; Warr et al., 2013; Nimz and Hudson, 2005; Kampman et al., 2014). The six noble gases that exist in nature include Helium (He), Neon (Ne), Argon (Ar), Krypton (Kr), Xenon (Xe), and Radon (Rn). Radon is radioactive, has a short half-life (~3.8 days) (Amonette et al., 2014), and has no associated stable isotopes (Warr, 2013), so will not be considered as a potential tracer in this research. The five remaining noble gases have a total of 22 stable isotopes between them, derived from either accretion into the planet when it first formed or by radioactive decay of another element (Holland and Gilfillan, 2013; Warr, 2013). The noble gas signature of a fluid consists of the concentrations of each noble gas and their isotopic ratios (Warr, 2013). Holland and Gilfillan (2013) suggest noble gas isotope tracers such as ^{3}He, ^{4}He, ^{40}Ar, and ^{21}Ne which have potential to be used to detect migration of CO_2 once injected into a reservoir. Roberts et al. (2017) identified helium (^{3}He) and xenon isotopes (^{124}Xe, ^{129}Xe) as the most suitable added noble gas tracers for CCS projects. Nimz and Hudson (2005) suggest ^{3}He, ^{22}Ne, ^{36}Ar, and $^{124,129,136}Xe$ for subsurface CO_2 monitoring.

The solubility of noble gases in seawater relates to their molar mass (Roberts et al., 2017) and depends on temperature, pressure, and salinity (Stanley and Jenkins, 2013). At 30°C and 0.1 MPa, Xe has the highest solubility in seawater and is followed by Kr and Ar, and Ne and He are relatively unaffected by changes in temperature (Figure 4.8) (Stanley and Jenkins, 2013; Hamme and Emerson, 2004). They all have a strong non-linear temperature dependence of solubility, with solubility decreasing with increasing temperature (Stanley and Jenkins, 2013). At 50°C, noble gas isotope ^{136}Xe has the highest solubility in water, followed by ^{84}Kr, and ^{36}Ar (Flude et al., 2016). Diffusivities of noble gases in seawater increases with increasing temperature (Figure 4.8). Diffusivities range by a factor of seven across the five noble gases at a given temperature (Figure 4.8), with helium having the highest diffusion coefficient (due to its small molecular size) (Stanley and Jenkins, 2013).

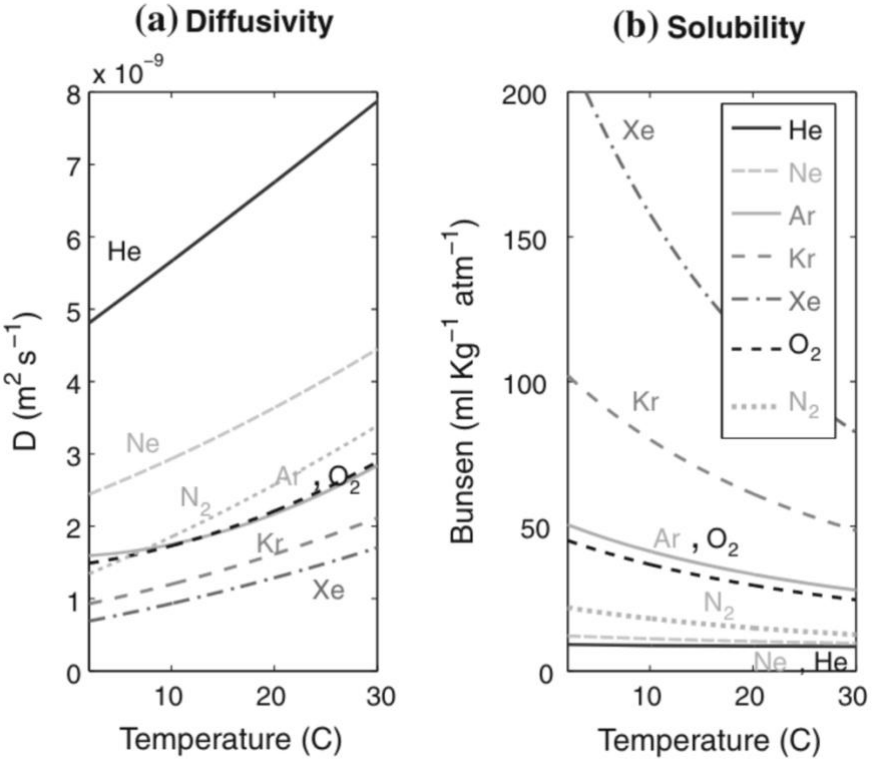

***Figure 4.8**: **(a)** Diffusion coefficients for the five stable noble gases, nitrogen, and oxygen in seawater as a function of temperature (0-30℃). Diffusivity values originally from Jahne et al. (1987) and Wise and Houghton (1966). Helium has the largest diffusion coefficient in seawater in this temperature range due to its molecular size. **(b)** Bunsen solubility coefficients (ml/kg atm^{-1}) for the five stable noble gases, nitrogen, and oxygen in seawater as a function of temperature. The Bunsen coefficient is described as the volume of a pure gas at standard temperature and pressure that dissolves in a volume of water at equilibrium with a partial pressure of 1 atm (Hamme and Emerson, 2004). Henry's law coefficients compare partial pressure of a gas to solubility, while Bunsen coefficients express solubility at a partial pressure of 1 atm. Nitrogen and oxygen were included for biogeochemical processes. Xe, Kr, and Ar have a strong temperature dependence, with solubility decreasing as temperature increases. He and Ne have a low solubility in water and are relatively insensitive to temperature changes. Solubility values for He are from Weiss (1971), Ne, Ar, and N_2 solubilities from Hamme and Emerson (2004), Kr solubility is from Weiss and Kyser (1978), and Xe solubility is from Wood and Caputi (1966). Source: Stanley and Jenkins (2013).*

With the presence of multi-phase flow, noble gas isotopes are expected to fractionate due to partitioning between CO_2 and water (Warr, 2013; Holland Gilfillan, 2013). This means that a fraction of the noble gas content will enter both phases (Warr, 2013). Supercritical CO_2 acts as a solvent and its solvent power increases as a function of how dense the supercritical CO_2 is (Warr et al., 2015). Dispersion of noble gases is related to atomic size and solvent density, so higher density CO_2 will enhance the solubility of noble gases in order of molecular size (Xe, Kr, Ar, Ne, He) (Warr et al., 2013, 2015). It is therefore necessary that partition coefficients are known for each noble gas between supercritical CO_2 and water for the relevant conditions. The partitioning behavior of Xe, Kr, and Ar for these multi-phase systems show an increasing affinity (positive

deviation from a near-ideal gas) for the supercritical CO_2 phase with increasing CO_2 density compared to pure noble gas-water systems (Figure 4.9) (Warr et al., 2015). This is from enhanced molecular interactions of dense-phase CO_2 with the more polarizable and larger noble gases. Helium was shown to be the opposite, having decreasing affinity (negative deviation from ideality) for a dense-phase CO_2 as a function of density (i.e., as CO_2 density increases, the solubility of He decreases) (Warr et al., 2015). Radon was not included in the experiment, and neon was measured but the analytical instruments were unable to correct for substantial interference peaks and so conclusions were unable to be reached regarding neon's behavior in dense CO_2-water systems.

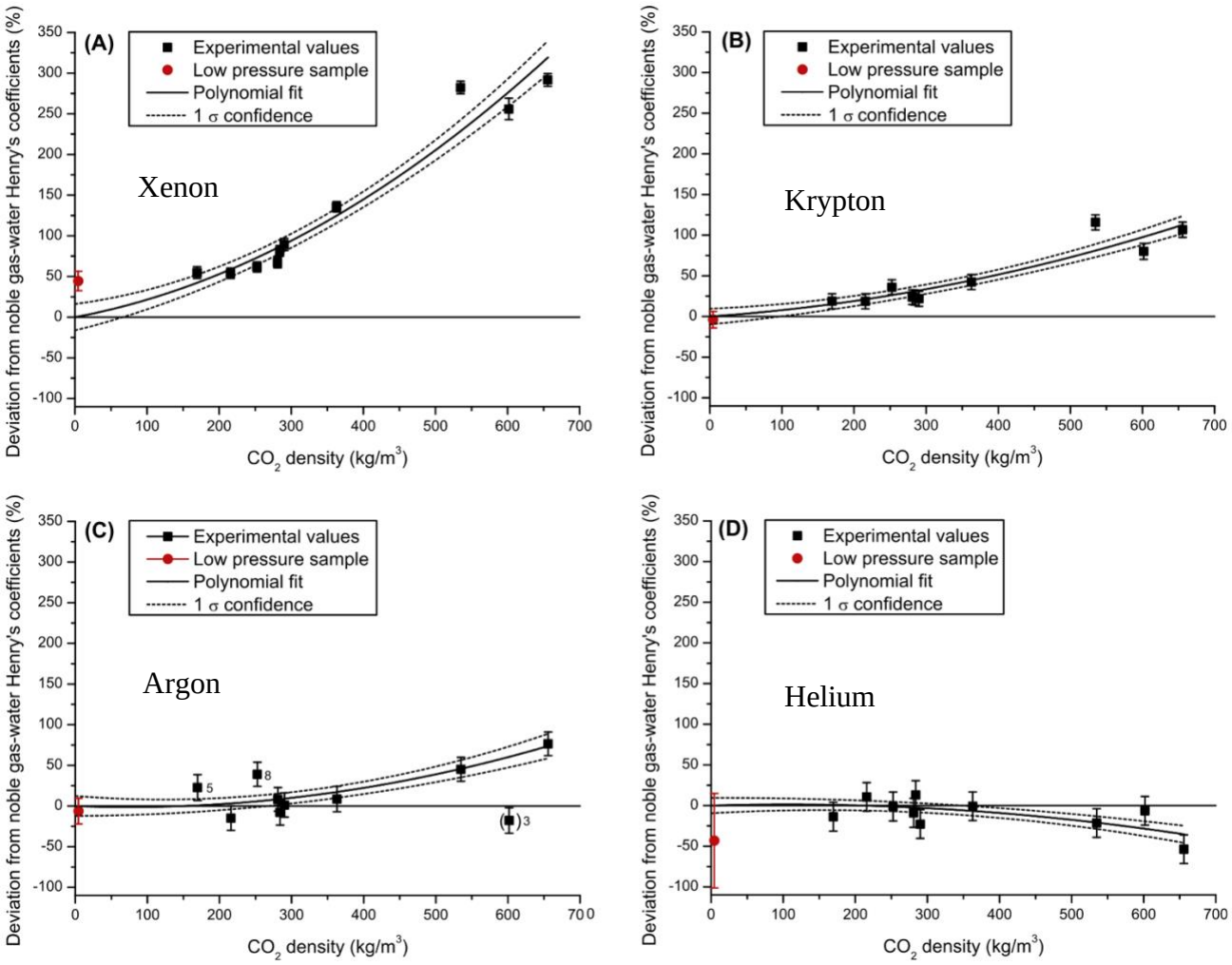

***Figure 4.9**: Experimental data of the partitioning behavior of noble gases for two-phase CO_2-water systems at a range of CO_2 densities (169-656 kg/m^3) and corresponding temperature and pressure conditions (49-103 ℃, 8.9-13.4 MPa) where CO_2 exists in a supercritical phase. Deviations of experimental Henry's Law partition coefficients for (A) xenon, (B) krypton, (C) argon, and (D) helium from near-ideal gas-water behavior (Smith, 1985) as a function of CO_2 density. Xenon, argon, and krypton all show positive deviations, or increasing affinity to partition into the CO_2 phase. Helium shows*

a negative deviation or decreasing affinity to partition into the CO_2 phase at experimental temperature (49-103°C) and pressure (8.9-13.4 MPa) conditions. Modified from: Warr et al. (2015).

4.6.1.5.3 Logistics

The offshore environment is logistically simpler than terrestrial environments for detecting noble gas tracers since noble gases exist in low concentrations in seawater (Nimz and Hudson, 2005). Noble gases have been previously collected using Osmosamplers (Tryon et al., 2012) and require copper tubing for sampling to prevent atmospheric contamination or leakage from sample bottles due to their small atomic size (Roberts et al., 2017). If surface seawater is injected in a WAG scenario, the seawater will introduce the noble gas signature imprinted on the seawater (Roberts et al., 2017).

Noble gases and their isotopes can be measured at high precision in a lab (Weber et al., 2021) using gas chromatography (Roberts et al., 2017), or mass spectrometry (Stanley and Jenkins, 2013; Stalker et al., 2009; Nimz and Hudson, 2005). Cost for noble gas analysis is typically two times the price per sample compared to SF_6 (IEAGHG, 2015). The required sampling volume to be able to detect noble gases in seawater depends on their atomic sizes, for example, ^{3}He measurements require ~1l of sample (Beyerle et al., 2000), the heavier noble gases (Ar, Kr, Xe) require ~45 ml (Beyerle et al., 2000), and isotope ratios of Ar, Kr, and Xe require ~100ml of sample volume (Seltzer et al., 2019). Bieri et al. (1964) used an omegatron mass spectrometer which can detect all five noble gases in 5.5 ml of seawater. Some methods such as (Emerson et al., 1999) only analyze one or two noble gases, while other methods can analyze for all five noble gases from a single sample (Beyerle et al., 2000; Stanley et al., 2009). Samples should be preserved in copper tubes, or coils, until the time of analysis (Stanley and Jenkins, 2013).

The cost to obtain noble gases are high (Nimz and Hudson, 2005), but the small amounts required for injection lowers the cost for each noble gas (Weber et al., 2021). Weber et al. (2021) provide costs for noble gas isotopes in US$ per ton of CO_2 with the necessary noble gas concentration required for tracer addition to the CO_2 injection stream (Table 4.3). The necessary concentrations required are lowest for ^{3}He and ^{124}Xe (Weber et al., 2021). Helium-3 and $^{124,129,136}Xe$ have low abundance in the atmosphere and are low in cost, at < $7 US/ton CO_2 (Table 4.3) (Weber et al., 2021). Costs for ^{3}He have increased in the past few decades due to a supply shortage (Cho, 2009), which limits the feasibility for using this tracer (Weber et al., 2021). The cost for ^{36}Ar is extremely high per ton of CO_2, and the reason for this is unclear in the published literature on tracer costs. Costs are expected to decrease with increased tracer demand apart from ^{3}He (Roberts et al., 2017).

***Table 4.3**: Costs for noble gas tracers per ton of CO_2 and necessary concentrations for labelling injected CO_2.*

Tracer	Necessary concentration for labelling injected CO_2 (cm^3_{STP}/cm^3_{STP})	Cost per ton of CO_2 in $USD
^{3}He	2.72×10^{-10}	$0.69
^{124}Xe	9.70×10^{-11}	$1.84
^{129}Xe	1.58×10^{-8}	$2.66
^{136}Xe	5.43×10^{-9}	$6.09
^{22}Ne	1.68×10^{-7}*	$4.27*
^{36}Ar	2.09×10^{-6}	$1066
^{84}Kr	1.08×10^{-8}	$10.67

Table Footnotes: Necessary concentrations (cm^3_{STP}/cm^3_{STP}) and cost per ton of CO_2 is from Weber et al. (2021). Cost estimates assume no loss or adsorption of tracer. Costs for ^{36}Ar and $^{129,136}Xe$ were obtained from Shell, all other noble gas costs are from Roberts et al. (2017). *Necessary volume and cost per ton for ^{22}Ne are from Nimz and Hudson (2005). Calculations from Weber et al (2021) are based on the minimum concentration of tracer (per ton of injected CO_2) needed to show a detectable shift in isotopic ratio or concentration using present analytical techniques.

Neon-22 is commercially available and could be used in scenarios where CO_2 is injected in a supercritical phase, or in environments where background concentrations are extremely low, so the total volume of tracer required would be lower (Nimz and Hudson, 2005). An advantage to using xenon compared to other noble gases is the commercial availability of multiple isotopes of xenon routinely used in the medical and aircraft industries (Nimz and Hudson, 2005). Injecting multiple isotopes of xenon may be useful for tagging different CO_2 batches, or a series of different CO_2 pulses (Stalker et al., 2009). Additionally, if using multiple isotopes of xenon, only one analysis would be required, compared to using a suite of different noble gases where separate analyses may be required depending on the laboratory used (Nimz and Hudson, 2005). There is the possibility of utilizing commercial isotope separation to create a distinctive tracer that consists of non-naturally occurring isotopic ratios (Nimz and Hudson, 2005). For example, ^{136}Xe constitutes ~8.9% of all naturally occurring xenon. Pure xenon gas is commercially available for purchase that consists of 60% of ^{136}Xe, which would cause the injected ^{136}Xe to have a fractional abundance in the subsurface different to what is found in nature and would be easily identified (Nimz and Hudson, 2005).

4.5.1.5.4 Case Studies of Their Use

The Frio Brine project (section 4.6.1.1.4) located in Texas, USA, used added tracers' krypton, SF_6, and PFCs to determine arrival time of the CO_2 plume at the monitoring well, observe geochemical changes as the plume moved past the monitoring well, and estimate residual saturation of the brine (Kampman et al., 2014; Freifeld et al., 2005). Tracers were injected in pulses with continuous injection of 1,600 tons of supercritical CO_2 into a saline formation (Stalker et al., 2009). Krypton had a longer travel time compared to SF_6 and PFCs, likely due to Kr having a higher solubility in water than SF_6 or PFCs (Freifeld et al., 2005). The breakthrough curves for the final tracer injection exhibit only a small difference in observed travel times for CO_2, SF_6, PFCs, and krypton in the reservoir (Figure 4.5), but this could be due to both a short

distance between injection and monitoring wells (30 m) and samples being collected only a few days after injection with not much time to react with the surrounding rock (Myers et al., 2013a).

Many terrestrially based carbon storage projects have used the composition of noble gases (^{20}Ne, ^{36}Ar, ^{84}Kr, ^{132}Xe) that are intrinsic to the injected CO_2 stream at temperature and pressure conditions where CO_2 exists as a gas phase (Gyore et al., 2017; Kampman et al., 2014; Nimz and Hudson, 2005). Since there are no existing pilot projects that have used noble gases to trace CO_2 in offshore basaltic crust, and it will be a multi-phase environment, more experiments are needed to understand the behavior of CO_2 and noble gases in a water-saturated environment with the presence of supercritical CO_2 (Roberts et al., 2017).

4.6.2 Reactive Tracers

4.6.2.1 Isotopic Composition of Carbon and Oxygen

4.6.2.1.1 Introduction

Stable carbon and oxygen isotopes can be highly useful for tracking the geochemical changes occurring to the CO_2 injected into a geologic formation. Basic physical and chemical properties, logistics, and a case study of their use in a commercial scale CO_2 sequestration project are described below.

4.6.2.1.2 Basic Chemical and Physical Properties

The isotopic composition of carbon is commonly used as a tracer for water sources and geochemical reactions (Cook, 2020). Carbon has two stable isotopes (^{12}C, ^{13}C) and one radioactive isotope (^{14}C) (Cook, 2020; Shanks et al., 1995). Carbon-12 is the dominant stable isotope of carbon with an average natural abundance of 98.93%, and ^{13}C and ^{14}C have minor abundances of 1.07% and 1 x 10^{-10} %, respectively (Shanks et al., 1995; Berglund and Wieser, 2011; Mayer et al., 2015). The $^{13}C/^{12}C$ ratio is 0.01 (Clark and Fritz, 1997). Radiocarbon (^{14}C) has traditionally been used for dating groundwater and late Quaternary chronology (Clark and Fritz, 1997).

The stable isotopic composition of oxygen has been used as a tracer in climatological, groundwater, and hydrological studies (Terzer-Wassmuth et al., 2023). Oxygen has three stable isotopes (^{16}O, ^{17}O, ^{18}O) (Berglund and Wieser, 2011). Oxygen-16 is the dominant stable isotope of oxygen with a natural abundance of 99.796%, while ^{18}O has a minor natural abundance of 0.204% (Clark and Fritz, 1997). Oxygen-17 has a natural abundance of 0.0375% and the natural variability of the $^{17}O/^{16}O$ ratio is considered insignificant and challenging to measure (Terzer-Wassmuth et al., 2023), and is not mentioned in the published literature as a tracer for CCS. The $^{18}O/^{16}O$ ratio is 0.00204 (Clark and Fritz, 1997). The difference in abundance of stable carbon and oxygen isotopes means isotopic ratios are either very large or very small (Shanks et al., 1995).

Due to differences in mass between the stable carbon or oxygen isotopes, each isotope will have different reaction rates leading to isotope fractionation, which is when the isotopic ratio is slightly altered by different amounts through interaction with other carbon or oxygen compounds in fluid or solid phases (Clark and Fritz, 1997; Shanks et al., 1995; Urey, 1974). Processes that affect stable carbon isotope fractionation include carbonate mineral dissolution, precipitation of

carbonate minerals, diffusion and mixing, changes to pressure and temperature, and sorption (Mayer et al., 2015; Clark and Fritz, 1997). Isotope fractionation between supercritical CO_2 and DIC has been experimentally determined to be no different than isotope fractionation observed between subcritical CO_2 and DIC ($\delta^{18}O_{CO2}$ is +22.7‰ at 70ºC and pressures up to 9.0 MPa) (Barth et al., 2015; Becker et al., 2015). Radiocarbon is also affected by isotope fractionation during phase changes (Clark and Fritz, 1997).

Mid-ocean ridge basalt, marine sediments, and seawater are all carbon isotopic reservoirs that show little variation within each reservoir, but much variation in carbon isotope values between reservoirs (Shanks et al., 1995). Carbon-13 isotopic values in basaltic crust range between -4 to -11‰, while $\delta^{18}O$ range from +5.5-6.5‰ (Shanks et al., 1995). Calcite vein samples from a core recovered from ODP Site 1026 (at 229.3 mbsf) had a $\delta^{13}C$ value of -2.16‰ and a $\delta^{18}O$ value of +24.43‰ (Coggon et al., 2004). Formations fluids collected from ODP Hole 1026B have an average $\delta^{13}C$ value of -6.5‰ (Walker et al., 2008). Bottom seawater has a $\delta^{13}C$ of ~ -1.4‰ (Walker et al., 2008).

During physical and chemical reactions such as carbonate mineral formation, the lighter carbon isotope (^{12}C) will diffuse and react faster than the heavier isotope (^{13}C), leading to the heavier isotope being preferentially incorporated into the solid phase more than the lighter isotope (Cook, 2020; Matter et al., 2014). In this regard, variations in the ratios of stable carbon isotopes can be used as reactive tracers to infer geochemical processes affecting CO_2 along flow paths in the subsurface (Cook, 2020; Mayer et al., 2015). For CO_2 sequestration projects, it is essential the $\delta^{13}C$ value of the injected CO_2 remains constant and distinct from $\delta^{13}C$ values of carbon compounds found in the reservoir fluids (i.e., DIC) and rock (Mayer et al., 2013; Johnson et al., 2009, 2011; Kharaka et al., 2006; Stalker et al., 2009; Myers et al., 2013a; Becker et al., 2015). Therefore, it is important for baseline geochemical monitoring to determine 1) the isotopic composition of the CO_2 (and DIC) in the reservoir and 2) the isotopic composition of the CO_2 used for injection, prior to injection (Johnson et al., 2011). DIC measurements are important because once the injected CO_2 dissolves, it will produce a DIC value in the formation fluids with a $\delta^{13}C_{DIC}$ that is different from baseline DIC, and this change can be used to detect migration of CO_2 in the reservoir and breakthrough of the injected CO_2 at a monitoring well (Flude et al., 2016).

Changes in the $\delta^{18}O$ values in formation fluids have been used to calculate pore saturation of supercritical CO_2 in laboratory studies (Johnson and Mayer, 2011; Johnson et al., 2011; Li and Pang, 2015; Serno et al., 2016), and is dependent on the $\delta^{18}O$ value of the injected CO_2 being different from the $\delta^{18}O$ value of the native oxygen in the formation fluids (Barth et al., 2015; Johnson and Mayer, 2011). Additionally, $\delta^{18}O$ values of the DIC in the formation fluids is controlled by the $^{18}O/^{16}O$ isotopic ratio in water and may be able to complement stable carbon isotopic ratios for differentiating increases in DIC caused by CO_2 dissolution (Serno et al., 2017).

4.6.2.1.3 Logistics

Detection of stable carbon isotopic ratios is less sensitive compared to other tracers from background $^{13}CO_2$ present in geologic formations (Amonette et al., 2014), and can be analyzed using a GC coupled with isotope-ratio mass spectrometry (IRMS) with a precision of ± 0.1‰ or

better (Adams, 2013; Coggon et al., 2004; Shanks et al., 1995). The analytical technique needs to be very precise to measure the minor isotope in relation to the major isotope (Shanks et al., 1995). Stable isotopic ratios of oxygen are analytically determined used IRMS with an analytical uncertainty of $< \pm 0.2‰$ and ~0.3 ml of fluid is required for analysis (Johnson et al., 2012).

For measurement, variations of stable isotope ratios of carbon ($^{13}C/^{12}C$) and oxygen ($^{18}O/^{16}O$) are expressed in delta notation (δ) in per mil (‰) deviation from the international standard (Vienna Pee Dee Belemnite, V-PDB for carbon, Vienna Standard Mean Ocean Water, VSMOW for oxygen) (Clark and Fritz, 1997):

$$\delta_{\text{sample}}\,(‰) = \left[\left(\frac{R_{\text{sample}}}{R_{\text{standard}}}\right) - 1\right] \text{x } 1000$$

Where R is the $^{13}C/^{12}C$ or $^{18}O/^{16}O$ ratio of the sample and the standard. Positive delta values mean the sample is isotopically heavier (i.e., higher heavy/light ratio) compared to the standard, while negative delta values mean the sample is isotopically lighter (i.e., lower heavy/light ratio) compared to the standard (Shanks et al., 1995).

Radiocarbon values are referenced to an international standard known as "modern carbon", which is defined as 95% of the ^{14}C activity in 1950 of the National Bureau of Standards oxalic acid standard. ^{14}C activities are expressed as percent of the modern carbon standard (Clark and Fritz, 1997).

Solid Carbon may use a purified food-grade CO_2 source for the initial injection experiment, and if the CO_2 has a distinct isotopic signature compared to the carbon found in the formation fluids and basalt, monitoring changes in the isotopic composition of formation fluids is possible if baseline concentrations of ^{13}C are determined prior to injection. For collection of fluid samples using Osmosamplers, copper coils are required. Mobile pumping systems may be used as well.

Radiocarbon is problematic for drill ships such as the *JOIDES* Resolution as it will contaminate the entire ship and negatively impact paleoclimate research (L. LeVay, IODP, pers. comm. 2022) and it is likely not permitted for use in the ocean system at Cascadia making it unsuitable as tracer for the CO_2 injection experiment. Costs for added stable carbon isotope ratios ($^{13}C/^{12}C$) can be high (>$100,000 per Mt/$CO_2$) (Roberts et al., 2017), although for a 10,000-ton CO_2 injection this would translate to $1000, showing how cost of an added tracer is dependent on how much tracer is required given the scale of injection. There is no additional cost for using the inherent isotopic signature of purified CO_2 as opposed to adding stable carbon isotopes (Flude et al., 2016; Mayer et al., 2013).

4.6.2.1.4 Case studies of using stable isotopic ratios in CO_2 monitoring and storage projects
The CarbFix pilot project (section 1.1.3.4.1) used radiocarbon and the Wallula pilot project (section 1.1.3.4.2) used stable carbon and oxygen isotopes for monitoring carbonate mineral formation. Radiocarbon was added to the groundwater during injection at CarbFix, and the ratio of $^{14}C/^{12}C$ in reservoir fluids and precipitated carbonate minerals were used to quantify the amount of CO_2 removed from formation fluids to form carbonate minerals (Matter et al., 2011). At Wallula, the isotopic composition of carbon and oxygen in pre-, syn-, and post-injection fluid

and rock samples were analyzed. Important to note is that Wallula successfully used food grade purified CO_2 with a distinct isotope signature compared to the native CO_2 in the injected formation. Stable isotopic ratios of carbon and oxygen have been used in a handful of other pilot projects (Kharaka et al., 2006; Myrttinen et al., 2010; Serno et al., 2016, Johnson and Mayer, 2011) in addition to the case study discussed below.

The use of stable carbon and oxygen isotopes has been proven as useful tracers and cost-effective measurements at a long-term CO_2 storage project, the Weyburn-Midale CO_2 monitoring and storage project, where more than 1 Mt of captured CO_2 has been injected per year since 2000 (Mayer et al., 2013). This project conducts CO_2-EOR at a commercial scale, with pilot and demonstration tests completed starting in 1984 (Wildgust et al., 2013). The CO_2 used for injection (~96% purity) is purchased from the Great Plains synfuel (i.e., coal gasification) plant in Beulah, North Dakota (Mayer et al., 2013). The CO_2 is transported by pipeline ~323 km to the Weyburn and Midale oilfields in Saskatchewan, Canada. The Weyburn oilfield produces crude oil (~28,000 barrels/day) from the carbonate deposits in the Midale beds of the Mississippian Charles Formation (Mayer et al., 2013). The deposits are ~30 m thick and located ~1.4 km below the ground surface (Wildgust et al., 2013). The *in-situ* temperature and pressure in the calcite-dominated injection zone is 60°C and 15.5 MPa, respectively (Hutcheon et al., 2016; Mayer et al., 2013). Since 2000, ~18 million tons (Mt) of anthropogenic CO_2 has been injected along with water into the reservoir (i.e., WAG injection strategy) (Wildgust et al., 2013). After the initial CO_2 breakthrough at the monitoring wells, CO_2 was also collected from producing wells and re-injected, partially supplementing the CO_2 obtained from the synfuel plant (Mayer et al., 2013). Injection of CO_2 is planned to continue until 2033 at a rate of ~5,000 tons/day (Serno et al., 2017).

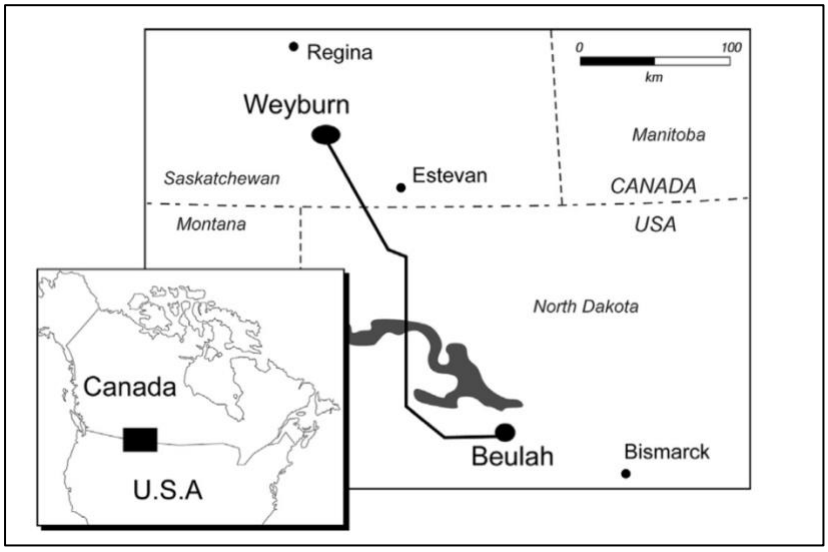

Figure 4.10: *Location of Weyburn-Midale CO_2 monitoring, and storage project. Anthropogenic CO_2 gas is provided from the Great Plains synfuel plant in Beulah, North Dakota and is transported across the US-Canada border where it is injected into the Weyburn reservoir in Saskatchewan, Canada. Source: Mayer et al. (2013).*

Baseline geochemical surveys were conducted prior to injection in addition to multiple monitoring surveys throughout injection periods, about three times per year during phase I (2000-2004), and two times per year during phase II (2008-2010). No monitoring was conducted between 2005-2007, but CO_2 was still continuously injected during this time (Mayer et al., 2013). Between 40 and 55 monitoring wells were sampled to collect fluid and gas samples, and no fluid samples were collected *in-situ*. The collected fluid/gas samples, injected CO_2, and carbonate minerals recovered prior to injection were analyzed for carbon and oxygen isotopic compositions. The results of the gas samples collected from monitoring wells are not discussed here for simplicity but can be found in Mayer et al. (2013).

Oxygen isotopic measurements of water samples was completed by equilibrating CO_2 gas with water at 25°C (Mayer et al., 2013), following Epstein and Mayeda (1953). The $^{18}O/^{16}O$ ratio of the CO_2 gas was analyzed with IRMS and the $\delta^{18}O$ values were reported in ‰ relative to the VSMOW standard with an analytical uncertainty of <0.2‰ (Mayer et al., 2013). The carbon isotopic composition of DIC was measured through reaction of strontium carbonate ($SrCO_3$) with ortho-phosphoric acid and the evolved CO_2 gas. The $\delta^{13}C$ value of the evolved CO_2 gas was analyzed using IRMS. (Mayer et al., 2013). The $\delta^{13}C$ values of both the evolved CO_2 gas and rock samples were reported in per mil relative to the PDB standard with an analytical uncertainty of <0.3‰ (Mayer et al., 2013).

The injected CO_2 was repeatedly measured (n = 8) and contained an average $\delta^{13}C$ value of -20.5 ± 0.3‰. After addition of the recycled CO_2, the average $\delta^{13}C$ value of the injected CO_2 did not change and was interpreted to be constant (Mayer et al., 2013). The carbonate minerals (calcite, dolomite) recovered prior to injection had $\delta^{13}C$ values that are typical for marine carbonates (+3‰ and +5‰) (Mayer et al., 2013; Veizer et al., 1999). The average $\delta^{13}C$ values of DIC from fluids sampled prior to injection were –1.8‰. Importantly, the injected CO_2 contained a ^{13}C isotopic signature >18‰ lower than the $\delta^{13}C$ of the DIC in the reservoir brine (-1.8 ‰) and the reservoir rock (+4 ‰) (Mayer et al., 2013).

Throughout the beginning of the monitoring period, the $\delta^{13}C$ values for DIC in the fluid samples increased to -9.2‰, and eventually decreased to -13‰ as monitoring continued (Figure 4.12a) (Mayer et al., 2013). Decreases in $\delta^{13}C_{DIC}$ coincided with increases in total alkalinity of the fluids due to the elevated HCO_3^- produced from CO_2 dissolution into reservoir fluids (Figure 4.12b). The observed decrease $\delta^{13}C_{DIC}$ implies the reservoir fluids are becoming isotopically light with time as more of ^{13}C is incorporated into the newly formed carbonate minerals.

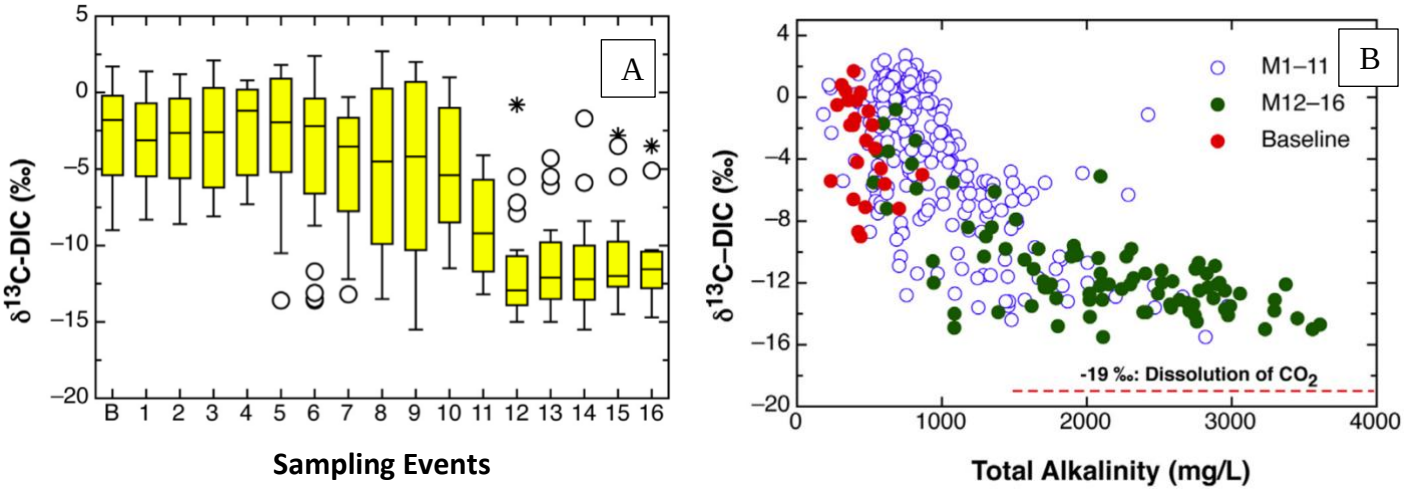

Figure 4.11: *Results of $\delta^{13}C_{DIC}$ from collected fluid samples compared with total alkalinity measurements for all fluid sampling events.* ***A)*** *Box plot of $\delta^{13}C_{DIC}$ values relative to PDB from reservoir fluid samples (y-axis) collected during all sampling events (1-16 shown on x-axis). The sampling event labeled "B" represents the baseline values measured in the reservoir fluids prior to injection, which was -1.8‰. During sampling events 6 and 11, $\delta^{13}C_{DIC}$ decreased from -2‰ to -9.2‰, while sampling events 12-16 observed $\delta^{13}C_{DIC}$ values decrease even more to -13.0‰.* ***B)*** *Plot comparing $\delta^{13}C_{DIC}$ values and total alkalinity measurements from collected water samples from all sampling events. Alkalinity increased from 500 mg/l to >3000 mg/l due to elevated [HCO_3^-] produced from CO_2 dissolution into reservoir fluids. Simultaneous decreases in $\delta^{13}C_{DIC}$ values were observed in the fluids, most prominently during sampling events M12-16. Dissolution of existing carbonate minerals from injection of CO_2 resulted in increased alkalinity and decreases in $\delta^{13}C_{DIC}$, meaning the reservoir fluids were increasingly becoming isotopically lighter compared to baseline values. Source: Mayer et al. (2013).*

Baseline $\delta^{18}O$ values for the reservoir brine varied between -9.8‰ and -1.2‰ with an average of -6.0‰ (1σ) (Serno et al., 2017). The injected CO_2 had a $\delta^{18}O$ value of +3.8 ± 0.2‰ which remained constant (Serno et al., 2017). Most of the monitoring wells did not detect $\delta^{18}O$ shifts compared to observed baseline values, but five of the wells showed repeated shifts to lower oxygen isotope values in the reservoir brine compared to the baseline values. The shifts were observed to be highly variable (Figure 4.13). The use of WAG injection and re-injection of produced CO_2 complicated interpretation of the $\delta^{18}O$ shifts in the reservoir since different water sources were used (with different $^{18}O/^{16}O$ ratios) (Serno et al., 2017). The $\delta^{18}O$ isotope data from this project could not be used to quantify CO_2 pore-saturations as attempted by Serno et al. (2017).

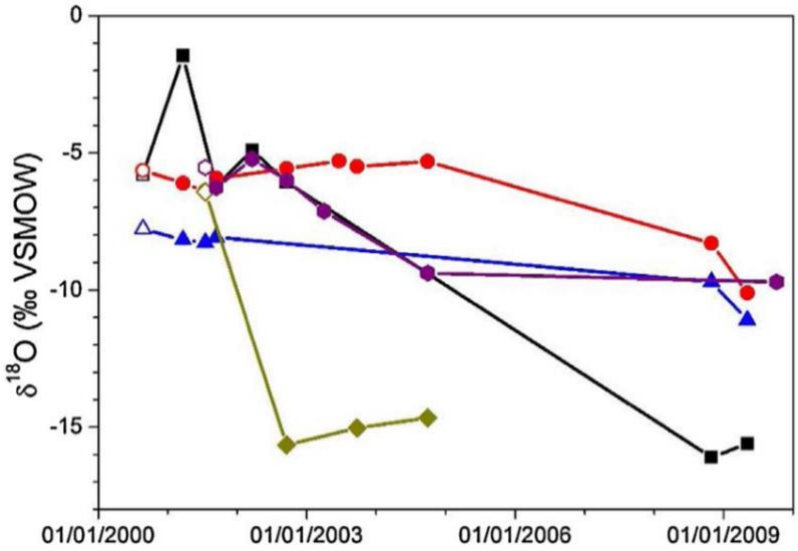

***Figure 4.12**: Isotopic composition of oxygen data relative to VSMOW from reservoir fluid samples collected from five wells at Weyburn between 2000-2009. Each well is represented by a different color. Only 5 monitoring wells (out of 55 wells) detected isotopic shifts to lower $\delta^{18}O$ values in the brine as compared to baseline values. Open symbols represent baseline values for reservoir fluids (average of -6.2‰). Filled symbols represent values obtained during the monitoring period, which are highly variable between monitoring wells where isotopic shifts were detected (ranging between -9.7 and -16.7‰). The maximum analytical uncertainty was ± 0.2‰. The $\delta^{18}O$ value of the injected CO_2 remained constant at +3.8 ± 0.2‰. The variability of the isotopic shifts was assumed to be caused by WAG injection whereby new sources of water were added which had different $^{18}O/^{16}O$ ratios. The re-injection of produced CO_2 may have also contributed to the variability of the data. Source: Serno et al. (2017).*

4.6.2.2 Dissolved Inorganic Carbon

Total dissolved inorganic carbon is the sum of dissolved forms of CO_2, HCO_3^-, and CO_3^{2-} (Zeebe and Wolf-Gladrow, 2001). Dissolved inorganic carbon concentrations are informative for monitoring dissolution and precipitation reactions. As dissolved inorganic carbon has been described in other sections (1.1.4 and 3.4.3), this section will be limited to discussing existing concentrations of DIC in the basaltic aquifer and logistics for fluid sampling and analysis for DIC.

The DIC of seawater is ~2.6 mmol kg^{-1}, while DIC concentrations in formation fluids collected from ODP Hole 1026B are 0.55 mmol kg^{-1} (Walker et al., 2008). DIC is removed from the crust in low temperature (<100°C) ridge flank environments from precipitation of calcite and aragonite within flow pathways and this mechanism is understood to be the source of removal of DIC in the crustal aquifer along the eastern flank of the Juan de Fuca ridge (Walker et al., 2008; Alt and Teagle, 1999; Brady and Gislason, 1997; Mottl and Wheat, 1994).

4.6.2.2.1 Logistics

Aside from using pH and pCO_2 sensors to derive DIC measurements in real time (section 3.4.3), total DIC in seawater can be measured by acidifying a collected fluid sample (0.5-1 ml) and extracting CO_2 gas from the sample and measuring its amount (Dickson et al., 2007). The result is typically expressed as mol kg^{-1} of solution, independent of temperature and pressure of the sample (Dickson et al., 2010). If fluid collected in Osmosamplers is used for DIC analysis, copper coils are required. Mobile pumping systems can also serve to collect fluids for DIC analysis. Dissolved inorganic carbon concentrations in the formation fluids will be changed by the addition of CO_2 into the aqueous environment and if elevated compared to baseline concentrations, this means the CO_2 has dissolved into formation fluids. The concentration of the carbon injected versus the DIC concentrations observed at the monitoring well could be used to determine how much carbon was removed from formations fluids and assumed to be precipitated.

4.6.2.3 Esters

4.6.2.3.1 Introduction

Esters are organic compounds that react with water to produce alcohols, organic, and inorganic acids. Although the use of esters as tracers of fluid flow and fluid-rock reaction is limited to only one carbon storage project where they were used to determine residual trapping of CO_2 in a sandstone formation, ester compounds are discussed here due to being one of two tracer groups where supercritical CO_2/water partition coefficients (at 62ºC and 15 MPa) have been determined (Table 9) (Myers et al., 2012b). These tracers are mentioned in published reviews on tracers for CCS (Roberts et al., 2017; Kampman et al., 2014; Cao et al., 2020) although they have only been considered for saline formations (Myers et al., 2012b, 2015) and depleted oilfields (Deans, 1971; Tomich et al., 1973; Tang and Harker, 1990) and for determining residual trapping of CO_2 (or hydrocarbons for oilfields).

Using reactive ester tracers involves a partial hydrolysis reaction where the injected parent compounds break-down (i.e., chemical reaction splitting the molecule) to daughter tracers *in-situ* (Figure 48). In the original patent (Deans, 1971), a reactive ester (ethyl acetate) was injected into a depleted oilfield followed by an injection of water. The ester partially hydrolyzed to produce daughter compounds (ethanol and acetic acid for ethyl acetate) (Myers et al., 2012b). The kinetics of the hydrolysis reaction determines the time between injection and collection of samples and the concentrations of both parent and daughter compounds are quantified (Cao et al., 2020). In this example, the ethyl acetate partitions into the oil phase, while the ethanol and acetic acid partition into the water phase (Myers et al., 2012b) and the difference in the arrival times for the two tracers determines the amount of residual oil saturation (Cao et al., 2020). For CCS projects, the same approach is applied but the formation needs to establish saturation of CO_2 prior to injection and the injected esters should partition into the supercritical CO_2 and their daughter products should partition into water (Myers et al., 2012b). Additionally, to maintain saturation during injection, the injection of water that follows injection of esters should be saturated with CO_2 (to prevent changes in saturation due to CO_2 dissolution) (Myers et al., 2015b).

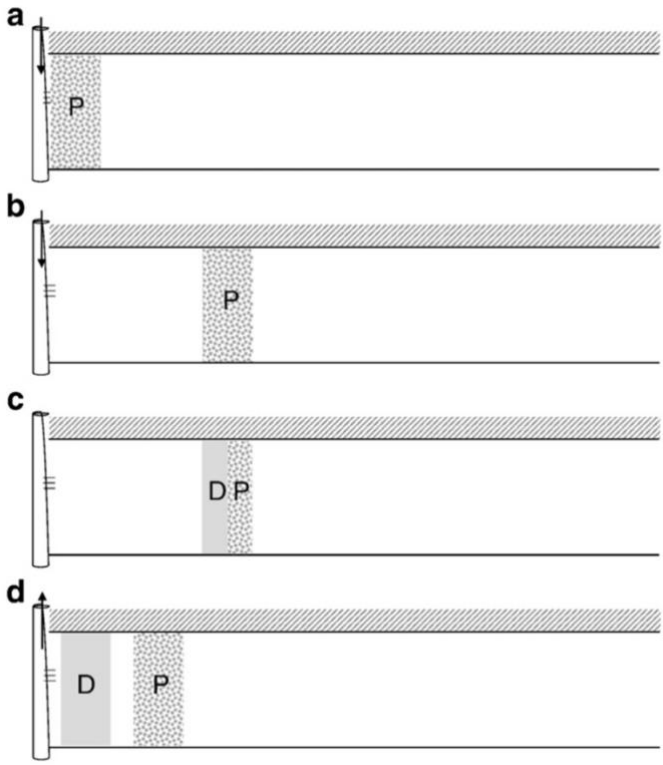

Figure 4.13: *Illustration of a single well push-pull test using reactive tracers. a) Parent tracer (P) is injected into the formation, b) injection of CO_2-saturated water to push the parent tracer further into the formation, c) waiting period where the P partially hydrolyses into daughter products (D), d) water from the formation is collected from the same well, where D arrives earlier than P, due to P partitioning more strongly into the supercritical CO_2 than D. Source: Myers et al. (2015b).*

Even though geophysical methods exist for determining residual CO_2 saturation (Furre et al., 2017; Hovorka et al., 2006), these tracers are included for thoroughness, even if the method does not align with solid carbon's current field-testing approach (no plans to inject CO_2-saturated water) but could be a possibility in the future. Three esters have been investigated in both laboratory experiments and a field trial and are described in this section.

4.6.2.3.2 Basic Chemical and Physical Properties

Reactive esters triacetin, tripropionin, and propylene glycol diacetate are all organic compounds (Myers et al., 2012b). Triacetin is used as a food additive and tripropionin and propylene glycol diacetate are used as solvents for flavor and fragrances (Myers et al., 2015a). These tracers all dissolve in water (Myers et al., 2015b). Propylene glycol diacetate is low in toxicity and biodegradable (Myers et al. 2012). Partition coefficients between supercritical CO_2 and water were determined at 62°C and 15 MPa (Table 4.4) (Myers et al., 2012b, 2013b). Since the hydrolysis reaction is determined in water, solubility in supercritical CO_2 were not experimentally determined.

Table 4.4: *Partition coefficients of propylene glycol diacetate, triacetin, and tripropionin between supercritical CO_2 and water, and their daughter products determined at 62°C and 15 MPa.*

Parent Ester	Daughter Product	Partition coefficient (62°C and 15 MPa)	Solubility in water (25°C and 0.1 MPa)
Propylene Glycol Diacetate		8.77 ± 0.86	100 g/l
	Propylene glycol monoacetate 1 (PGMA1)	0.167 ± 0.019	n.d.
	Propylene glycol monoacetate 2 (PGMA2)	1.57 ± 0.36	n.d.
Triacetin		4.46 ± 0.90	72 g/l
	Diacetin 1	0.135 ± 0.034	n.d.
	Diacetin 2	0.124 ± 0.017	n.d.
	Monoacetin 1	0.141 ± .044	n.d.
	Monoacetin 2	0.0263 ± 0.0093	n.d.
Tripropionin		50.3 ± 9.3	2.6 g/l
	Dipropionin 1	0.820 ± 0.137	n.d.
	Dipropionin 2	0.778 ± 0.170	n.d.
	Monopropionin 1	1.40 ± 0.26	n.d.
	Monopropionin 2	0.0562 ± 0.0143	n.d.

Table Footnotes: Solubilities of parent tracers in water were determined at 25°C and 1 atm. N.d. = no data. Source: Myers et al. (2012).

4.6.2.3.3 Logistics

Esters can be injected using the same equipment for injection of water (Myers et al., 2015b). Since these tracers are liquids, sampling does not require special equipment that is required for gas sampling (Myers et al., 2015b). Collected fluid samples need to be frozen to reduce the hydrolysis rate prior to analysis (Myers et al., 2015a) and would be a problem for using Osmosamplers in this context. Costs are limited in the published literature, but one source quoted £100-1,000 for esters per Mt/CO_2 (Roberts et al., 2017). Samples can be analyzed by GC-MS and initial concentrations of 1000 ppm for parent tracers has been sufficient for detection of both parent and daughter compounds (Myers et al., 2012b). There is a short time frame between injection and collection of fluids where the parent and daughter tracers are still detectable (6-20 days) (Myers et al., 2012b), which could increase flexibility of using these tracers in a field trial.

4.6.2.3.4 Case studies of their use in laboratory experiments and a field trial

Three esters (triacetin, tripropionin, and propylene glycol diacetate) were injected into to the Otway CO_2 storage site in Victoria, Australia as part of the Otway residual gas saturation test. Since there was no previous experimental data for these esters, laboratory experiments were conducted to determine the partition coefficients between supercritical CO_2 and water for each compound and to investigate the temperature sensitivity of these tracers under commonly found conditions for CCS projects (Myers et al., 2012b; Myers et al. 2015a).

The high-pressure vessel used in the lab experiments was set up to replicate the *in-situ* reservoir conditions at Otway (62ºC and 14-17 MPa, 28% porosity, 2.1 x 10^{-12} m^2) (Myers et al., 2012b).

Distilled water and pure food grade CO_2 were used for the experiments. To determine partitioning, the vessel was pressurized with CO_2 to 5 MPa and 1.9 l of water and 2g of each parent tracer was added. Once the CO_2 diffused into the water portion, the vessel was sealed, and temperature increased to 62ºC. The fluids were given 6-20 days to partially hydrolyze, and then fluid samples were collected from the supercritical phase (from the top of the vessel) and from the water phase (bottom of vessel). The samples were analyzed with GC-MS to determine concentrations of both parent and daughter compounds. Partition coefficients were determined by measuring the equilibrium concentration of each species in the supercritical CO_2 phase and water phase (Myers et al., 2012b, 2013) and followed the method used by Timko et al. (2004). A decrease in the concentration of parent tracers and increase in the concentration of the daughter products was observed. The hydrolysis reaction for tripropionin was observed to be much slower compared to triacetin and propylene glycol diacetate (Myers et al., 2012b, 2013).

Temperature sensitivity of these compounds was also investigated in the lab (at 14 MPa and 60ºC, and 24 MPa and 120ºC), to understand the effect of temperature on the partitioning behavior of the esters in geologic formations. The experiment concluded that larger ester compounds (e.g., tripropionin) are more sensitive to changes in temperature relative to the smaller ester compounds (e.g., propylene glycol diacetate). Additionally, the partition coefficients were observed to decrease with increasing temperature (Myers et al., 2015a), meaning as temperature increases, a higher proportion of the tracer will remain in the water phase.

These compounds were also used in a field trial at the Otway CO_2 storage site conducted by the Cooperative Research Centre for Greenhouse Gas Technologies (CO2CRC) (Myers et al., 2015b). A single well push-pull field test was conducted using the three esters described above. After establishing the CO_2/water ratio near saturation in the target injection interval, 12 kg of triacetin, 10 kg of propylene glycol diacetate, and 8 kg of tripropionin were dissolved in 5.1 tons of water and 0.3 tons of CO_2 and injected into the formation. After waiting 10 days (based on laboratory experiments), 23.7 tons of water was produced from the formation and hundreds of 50-100 ml fluid samples were collected. Triacetin and propylene glycol diacetate and their hydrolysis products had high percent recoveries, 77% and 87%, respectively. Tripropionin and hydrolysis products had a much lower percent recovery of 21%. There was uncertainty around the reason for this and was inferred to be partially attributed to its lower solubility in water and higher partition coefficient compared to the other tracers (Myers et al., 2015b). Propylene glycol diacetate (and daughter product PGMA 1) was determined to be the most suitable tracer for predicting residual saturation of CO_2 in CCS projects with similar conditions. This field trial found that when using esters for determining residual saturation of CO_2 for CCS projects, it is important to make sure the CO_2/water ratio is maintained at near saturation to prevent the supercritical CO_2 dissolving into the formation water (Zhang et al., 2011). This is the inverse of Solid Carbon's planned field-testing approach (i.e., dissolution of supercritical CO_2 into formation fluids) but could be useful to determine residual saturation of supercritical CO_2 at the end of the injection period, or after injection.

4.6.2.4 Major ions and Trace Elements in Seawater

4.6.2.4.1 Introduction

Major ions and trace elements found in seawater are expected to change in concentration due to CO_2-fluid-rock reactions in the aquifer and the extent to which their concentrations change can inform the progress of reactions in the subsurface. Description of elemental concentrations in formation fluids in the Cascadia Basin and why they are useful for monitoring CO_2 sequestration, logistics for using them, and case studies are provided below.

4.6.2.4.2 Basic Physical and Chemical Properties

Major ions in seawater make up the background ionic medium of seawater (Dickson, 2010). The major cations and anions in seawater are introduced in Section 3.4.2. Major ions are those with concentrations in seawater above 10 µmol/kg (Emerson and Hamme, 2020). Trace elements are elements that are present at very low concentrations (pmol kg^{-1}) and do not contribute to salinity (Chester, 1990) but do play a role in carbonate mineral formation (Veizer, 1983). These elements include Mo, U, Cd, Ni, Cu, Zn, Co, and U (Emerson and Hamme, 2020; Smrzka et al., 2019). Rare earth elements (REEs) are present in formation fluids at low concentrations (Smrzka et al., 2019). Concentrations of major ions, trace elements, and REEs found in formation fluids along the eastern flank of the Juan de Fuca Ridge and bottom seawater are given in Table 4.5. The concentrations differ compared to seawater as elements are partitioned between sediment pore waters, formation fluids, and the basaltic crust (Hulme and Wheat, 2019).

The concentrations of Ca and Mg drastically change between seawater and the warm formation fluids, with concentrations of Ca ~5 times higher in formation fluids compared to seawater (Hulme and Wheat, 2019). Iron also has increased concentrations in formation fluids compared to bottom seawater. Magnesium is depleted from formation fluids by reactions with the basaltic crust where it participates in forming secondary minerals (Hulme and Wheat, 2019). The overlying sediments provide a source of silicon to basement fluids through diffusive exchange (Wheat and McManus, 2005). Silicon is known to be removed in the crust through formation of secondary minerals and clays (Alt, 2004) and its presence plays a key role in the dissolution rates of the basalt (Oelkers, 2001).

Table 4.5: *Elemental concentrations in formation fluids along the eastern flank of the Juan de Fuca Ridge.*

Element	Unit	Bottom Seawater	Baby Bare	IODP Site 1301	ODP Site 1026
Temperature	°C	1.8°C	25	63.5	64
K	mmol/kg	10.1	7.1	6.9	7.1
Ca	mmol/kg	10.3	55.2	55.8	56.8
Mg	mmol/kg	52.5	1.0	1.9	1.8
Na	mmol/kg	467	473	463	469
Cl	mmol/kg	542	554	553	552
SO_4	mmol/kg	28.1	17.8	17.6	17.5
NH_4	µmol/kg	0.3	76.0	n/d	90.0
Ba	µmol/kg	0.15	0.43	0.83	1.0
Sr	µmol/kg	86	110	110	113
Li	µmol/kg	26.6	9.0	13.7	14.4
Rb	µmol/kg	1.37	1.12	1.11	1.10
Cs	nmol/kg	2.2	5.3	7.8	8.0
Mn	µmol/kg	0.001	2.9	3.8	4.4
Fe	µmol/kg	0.001	0.1	0.7	1.1
Mo	nmol/kg	110	297	374	389
Co	nmol/kg	0.03	0.3	0.3	0.6
Zn	nmol/kg	10	15	20	20
Cd	nmol/kg	1.2	2.2	0.01	0.04
U	nmol/kg	14.0	0.6	0.03	0.02
Y	nmol/kg	0.33	0.03	0.01	0.01
La	pmol/kg	55	8	8	11
Ce	pmol/kg	7	15	11	13
Gd	pmol/kg	9	4	1	1
Yb	pmol/kg	11	1.5	0.5	0.4

Table footnotes: Bottom seawater concentrations are from samples taken at IODP Site 1301 (Hulme et al., 2008). Baby Bare concentrations are from Wheat and Mottl (2000) and Wheat et al. (2003). IODP Site 1301 concentrations are from Wheat et al. (2010) and Hulme and Wheat (2019). ODP Site 1026 concentrations are from Wheat et al. (2004) and Hulme and Wheat (2019). Temperature values (included for reference) for bottom seawater, Baby Bare springs, and Site 1026 are taken from Wheat et al. (2000) and Site 1301 taken from Fisher et al. (2011d). n/d = no data.

The extent to which mineralization of the injected CO_2 can occur in basaltic crust is dependent on the concentration of available divalent cations, mainly Ca^{2+}, Mg^{2+}, and Fe^{2+} (Raza et al. 2022; Marieni et al., 2020; Gunter et al., 1997). These divalent cations promote precipitation of CO_3^{2-} into carbonate minerals (Marieni and Oelkers, 2018). Concentrations of these divalent cations are expected to increase during dissolution of the basalt and decrease during precipitation of carbonate minerals formed from the injected CO_2. The formation of carbonate minerals also acts as either a sink or source for trace elements and REEs in solution (Smrzka et al., 2019; Veizer, 1983; Lorens, 1981). Factors which affect how trace elements are incorporated into carbonate minerals as they form include precipitation rate and element concentration in solution (Smrzka et al., 2019). Silicon (Si) has been noted to be important in the rates of dissolution of the basalt because of its importance in the silicate mineral framework (Oelkers, 2001).

4.6.2.4.3 Logistics

Major and trace elements in seawater are inherent to the aquifer fluids so only need to be sampled and analyzed throughout the monitoring period to record geochemical changes with time. This means cost is lowered to only the analysis of the samples, and logistics only concern sampling and analysis. Major elements can be analyzed using inductively coupled plasma-atomic

emission spectroscopy (ICP-AES) which requires only 0.05 mL to measure Ca, Mg, Na, K, Sr, and S (Marieni et al., 2020; Fisher et al., 2011f). Fe, Mn, Si can be analyzed using ICP-OES (McCarthy et al., 2005). Concentrations of SO_4 and Cl can be analyzed using ion chromatography (Marieni et al., 2020). The small amount of fluid required for analysis means the fluid collected by Osmosamplers can be used for major and minor ions with remaining fluid for other analyses. Major ions and trace elements can be collected using Teflon or PTFE tubing (Wheat et al., 2003). Volumes for analysis can also be collected using mobile pumping systems.

4.6.2.4.4 Case Studies of their use in pilot projects and laboratory experiments

A few case studies already discussed in this thesis are examples of where the concentrations of major ions were used to inform CO_2-fluid-rock reactions (i.e., Wallula and Carbfix in section 1.1.3.4, and Frio Brine introduced in section 4.6.1.1.4). Calcium was observed to be important for indicating carbonate mineralization at the CarbFix pilot project at temperatures between 35-50ºC (Marieni and Oelkers, 2018). During CO_2 injection at the Frio Brine pilot project, increases in dissolved Mg (0.02-0.022M), Mn (0.00005-0.0003M), and Ca (0.07-0.08M), and Fe (0.0005-0.02M) were observed (Ilgen and Cygan, 2016; Hovorka et al, 2006). Additional increases in the concentration of trace elements Zn, Pb, and Mo were also observed (Kharaka et al. 2006). Keeping in mind the monitoring well was 30 m away from the injection site at Frio Brine, these observations show that major element concentrations are quickly affected by injection of CO_2.

Marieni et al. (2020) conducted batch dissolution experiments with basalt recovered from the Juan de Fuca ridge to determine how quickly elements are released from the basalt samples during dissolution. The experiment was conducted at 40°C with an initial pH of ~4.8 and 1 bar pCO_2. The experimental setup included a three-phase system (basalt, artificial seawater, and CO_2 in a gas phase), where 500 ml of seawater was added to a 1000 ml bottle and warmed to 40°C. The seawater was then saturated with CO_2 gas using a stainless-steel bubbler, controlled by a gas flowmeter. The CO_2 injection rate was 0.3 l/min. Iron was excluded from the analysis, due to potential iron contamination from observed oxidation of the bubbler. Measurements of pH were taken throughout the process where seawater was saturated with CO_2. Once the seawater was saturated with CO_2, ground basalt rock was added to the bottle and was not stirred to limit formation of fine particles. Fluid samples (1 ml) were collected regularly over a 10-day period with 0.5 ml used for major cation analysis with ICP-OES. These samples were preserved by adding HNO_3. This study found that Si and Ca may be the key elements for determining basalt dissolution and observed consistent increases in their concentrations with time. The absence of silicon in the artificial seawater used for the experiment allowed easier observation of chemical changes for silicon. Aluminum was observed to be dissolved into solution in very small quantities, and Na, K, and Mg showed inconsistent variations in the solution with time. Silicon and calcium released from the basalt during dissolution were similar or higher in the Juan de Fuca ridge basalt compared to what was observed during the CarbFix project, suggesting deep-sea basalts are capable of dissolving just as quickly as what was observed in the CarbFix pilot project (Marieni et al., 2020). Other experimental studies (Marieni and Oelkers, 2018; Gysi and Stefansson, 2012) have reached similar conclusions, where at temperatures <100ºC, the mobility of major cations (Ca, Mg, Fe) and Si are shown to play a key role for CO_2 mineralization in basalts.

4.6.2.5 Alkalinity

The alkalinity of seawater is a measure of the ability of the seawater solution to react with H^+ added to a system (Emerson and Hamme, 2020), or the capacity of seawater to neutralize acid (Esposito et al., 2021). Alkalinity plays a major role in the oceans ability to be a sink for CO_2 from the atmosphere (Middelburg et al., 2020). Carbonate alkalinity is the dominant kind of alkalinity in the ocean and can be thought of as describing a simplified seawater solution in which the only source of alkalinity is from the carbonate species. This accounts for ~96% of the total alkalinity in natural seawater due to these ions being present at much higher concentrations compared to other proton acceptors such as boron, phosphate, silicate, and ammonia (Emerson and Hamme, 2020; Zeebe and Wolf-Gladrow, 2001). Carbonate alkalinity (A_C) measures the charge concentration of the bicarbonate and carbonate anions in a solution (Zeebe and Wolf-Gladrow, 2001):

$$A_C = [HCO_3^-] + 2[CO_3^{2-}]$$

Alkalinity has units of equivalents per kg (meq/kg) because it measures the charge balance of the solution (Stumm and Morgan, 1996). The unit meq/kg is equal to mmol alkalinity kg^{-1} if the measurement implies mmol HCO_3^- kg^{-1} (Zeebe and Wolf-Gladrow, 2001). Carbonic acid (H_2CO_3) and CO_2(aq) do not contribute to carbonate alkalinity since both are uncharged (Emerson and Hamme, 2020; Zeebe and Wolf-Gladrow, 2001). Alkalinity is a conservative measure and is unaffected by changes in temperature and pressure (Dickson, 2010) but is affected by acid-base additions, redox reactions, carbonate mineral dissolution and precipitation reactions (Middelburg et al., 2020) which will occur from CO_2 injection into the basaltic aquifer.

Bottom ocean seawater has a high alkalinity (~2.5 mmol HCO_3^-/kg) (Wheat and Mottl, 2000). The aquifer fluids along the eastern flank of the Juan de Fuca ridge have a much lower alkalinity (~0.3 mmol HCO_3^-/kg) compared to seawater partly due to alkalinity being consumed from aquifer fluids by reactions in the basement that produce acidity (i.e., Mg, K, Li, U, and H_2O are used to form alteration minerals in exchange for Ca, Fe, and Mn from the basalt) (Elderfield et al., 1999; Mottl and Wheat, 1998). Alkalinity is also depleted from precipitation of calcite and aragonite (Wheat et al., 2022). Injecting CO_2 into this environment will increase the reactivity of the system and, depending on the rate and volume of CO_2 injected, may impact the aquifers' ability to generate alkalinity (Tutolo et al., 2021).

How quickly the injected CO_2 dissociates into HCO_3^- and CO_3^{2-} is dictated by the alkalinity of the solution (Dickson, 2010). Alkalinity will increase as the carbonate minerals in the basalt dissolve from reaction with the protons supplied by the injection of CO_2 (Gunter et al., 1997). As alkalinity increases, it allows more carbon (in the form of HCO_3^-) to be held in solution (Dickson, 2010). This was observed in formation water samples collected post-injection at the Wallula pilot project (Section 1.1.3.4.2, Figure 10). Alkalinity will decrease as more of the injected CO_2 is precipitated into carbonate minerals (Kempe and Kazmierczak, 1994).

Tutolo et al. (2021) conducted simulations where aquifer fluids collected from IODP Site 1301 in the Cascadia Basin were reacted with a typical basaltic core (containing olivine, plagioclase, clinopyroxene) to show how much alkalinity will increase at a water-to-rock mass ratio of 100 (assuming a constant fugacity of CO_2 at 100 bar). The experiments were performed at 25°C and

60°C. When 1 kg of basalt is dissolved in 100 kg of aquifer fluid, the alkalinity is expected to increase to above 40 meq/kg (Figure 49) (Tutolo et al., 2021).

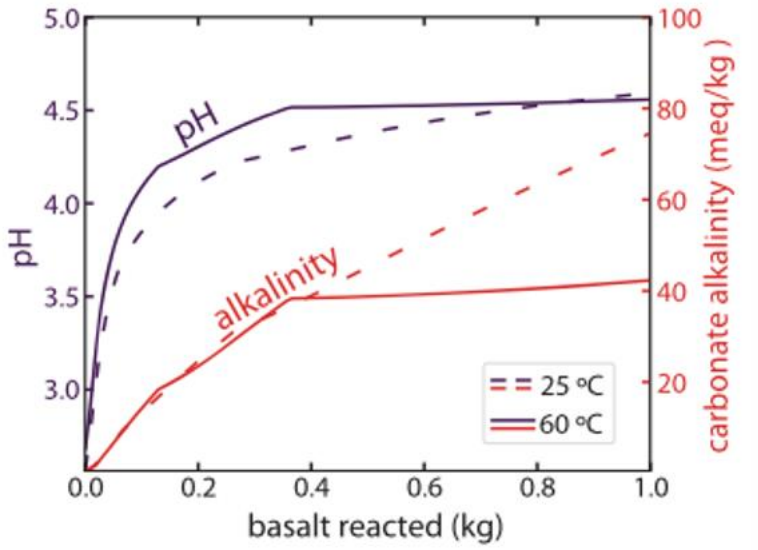

***Figure 4.14**: The effect on pH and alkalinity as a function of basalt dissolution from CO_2 injection using aquifer fluids collected from IODP Site 1301 in the Cascadia Basin. Simulations were conducted at 60°C (solid lines) to represent the conditions in the Cascadia Basin, and 25°C (dashed lines) to represent conditions found in other locations of deep-sea basaltic crust. The fugacity of CO_2 is constant (100 bar). The water-to-rock mass ratio is 100 (1 kg of basalt to 100 kg of aquifer fluids). When 1 kg of basalt is dissolved in 100 kg of aquifer fluids, at 60°C, alkalinity (red) is expected to increase to ~40 meq/kg of solution. The effect on the pH of the system is also shown (purple). Source: Tutolo et al. (2021).*

4.6.2.5.3 Logistics

Using alkalinity measurements as a way of informing CO_2-fluid-rock reactions is logistically very simple and all that is required is analysis of collected fluid samples to record geochemical changes, with a lower price tag compared to injection of added tracers. The method used to determine alkalinity is through titration, where a strong acid (e.g., HCl) is added to the sample and the solution is stirred continuously until a consistent pH is obtained (Pilson, 2012). The alkalinity is calculated from the final pH, the amount of acid added, and a salinity-dependent correction factor (Pilson, 2012). This is a simple analysis to complete, compared to other tracers considered in this research. The volume required for analysis (15-100 ml) is higher than Osmosamplers can collect (0.5-1 ml) (Dickson, 2010), so mobile pumping systems should be utilized to collect enough fluid for analysis.

4.6.2.6 Cesium Chloride

4.6.2.6.1 Introduction

Cesium chloride has been used as a tracer in basaltic crust in two previous experiments to assess the nature of hydrothermal fluid transport in each region. In this research, cesium chloride is considered as a reactive tracer. Basic physical and chemical properties, logistics, and the two previous case studies are described in this section.

4.6.2.6.2 Basic chemical and physical properties

Cesium is an alkali element and is highly reactive in hydrothermal fluids (Palmer and Edmonds, 1989; Berger et al., 1988). Cesium is a minor constituent of seawater and ocean crust (Berger et al., 1988). Cesium exists in low concentrations in seawater, ~2.2 nmol/kg (Hulme and Wheat, 2019; Pilson, 2012; Hulme et al., 2008). Cesium concentrations are ~8.0 nmol/kg in the crustal fluids along the eastern flank of the Juan de Fuca ridge (Table 4.4) (Hulme and Wheat, 2019). Cesium concentrations are higher in the crustal fluids than seawater due to sediments providing a source for cesium in the basaltic aquifer (Hulme and Wheat, 2019). Cesium is known to be removed from basalt in the presence of hydrothermal fluids and can be absorbed by secondary minerals more easily compared to other alkali elements (Palmer and Edmonds, 1989).

Cesium easily reacts with nonmetals to form ionic compounds, such as cesium chloride (CsCl). Cesium chloride is an inorganic compound (Pilson, 2012; Hulme and Wheat, 2019). The solubility of CsCl in water increases with increasing temperature at all pressures and decreases with increasing pressure at all temperatures (Matsuo et al., 2001). At 40°C and atmospheric pressure (0.10 MPa), the solubility of CsCl in water is 12.20 mol/kg, and at 40°C and 50 MPa, CsCl has a solubility of 11.84 mol/kg (Matsuo et al., 2001).

Table 4.6*: Cesium concentrations from collected fluid samples at ODP Site 1026, IODP Sites 1301 and 1362, and bottom seawater along the eastern flank of the Juan de Fuca Ridge.*

	Seawater	IODP Site 1301	ODP Site 1026	IODP Site 1362
Cs concentration (nmol/kg)	2.2	7.8	8.0	20

Table Footnotes: As of 2019, the Cs concentration in formation fluids at IODP Site 1362 was higher than in ODP Site 1026 and IODP Site 1301 along the same basement ridge because Cs was used as a tracer in the cross-hole experiment conducted in 2010 at that site. Cs concentrations in seawater were sampled from bottom seawater near IODP Site 1301 from Hulme et al. (2008). Cs concentrations from IODP Site 1301 formation fluids are from Wheat et al. (2010 and Hulme and Wheat (2019). Cs concentrations from ODP Site 1026 formation fluids are from Wheat et al. (2004) and Hulme and Wheat (2019). Cs concentrations from IODP Site 1362 formation fluids are from Wheat et al. (2022).

4.6.2.6.3 Logistics

Using CsCl as a tracer is logistically simple to inject into the crust (Wheat et al., 2020), is relatively low in cost, and Cs can be measured precisely in samples collected by Osmosamplers or mobile pumping systems.

For collection in Osmosamplers, an acid-addition package is required (Wheat et al., 2020; Jannasch et al., 2004). Cesium concentrations can be detected in seawater down to 0.1 nM (0.12 nmol/kg) (Fisher et al., 2011f; Hulme et al., 2008). The volume requirement for analysis is ~0.1 mL for cesium and other trace elements (V, Mo, Ba, Cs, U) using an inductively coupled plasma mass spectrometer (ICP-MS) (Wheat et al., 2011) which can provide measurements with a

precision 5% better than for seawater (Wheat et al., 2020). Collection of fluids containing cesium using a mobile pumping system is briefly described in the case study below and in section 2.3.3.

Cost for CsCl is not specifically outlined in published literature where cesium has been used as a tracer. A chemical manufacturer, Sigma Aldrich can provide 1 kg of cesium chloride for $686.00 CAD (UVic Science Store, 2023).

4.6.2.6.4 Case Study of the use of Cesium as a tracer in basaltic crust

Cesium chloride has not yet been used as a tracer for monitoring CO_2 sequestration projects but has been successfully injected into basaltic crust and sampled using Osmosamplers and mobile pumping systems (Wheat et al., 2020; De Jong, 2020; Fisher et al., 2011f). Cesium chloride was chosen as a conservative tracer in these experiments because: (i) of the difference in injected tracer concentration of Cs and that of seawater was at least 6 orders of magnitude, (ii) simple to analyze and low detection limits for analysis (Fisher et al., 2011f), and (iii) the tracer solution had a higher density than seawater and would easily be delivered into the borehole (Wheat et al., 2020). Cesium chloride has a higher density (3.99 g/cm^3) than seawater (1.03 g/cm^3) so a saturated cesium chloride salt solution that is denser than the surrounding seawater means it will descend into the borehole easier than if it was less dense than the surrounding fluids.

A second cross-hole tracer experiment conducted in basaltic crust at North Pond also used CsCl as a tracer to determine variations in fluid composition because of drilling and to constrain permeabilities of the upper volcanic crust in this area (Wheat et al., 2020). Existing IODP borehole observatories (Hole U1383B and U1383C) at North Pond installed in 2011 during IODP Expedition 336 were used as injection and monitoring wells for the tracer experiment. The distance between the holes was approximately 25 m and Hole 1383B was the injection hole. Downhole Osmosamplers (with standard and *in-situ* acidification packages) were installed in 2012. In 2017, expedition AT39-01 used an ROV to inject the CsCl tracer into the injection hole. Injection consisted of using the ROV to attach a 21-l plastic bag in a large milk crate to tubing connected to the sampling port on the CORK wellhead (Figure 4.15). A plastic cover was placed over the bag so the human operating the ROV could instruct the ROV to push down and force the tracer through the tubing and into the borehole (Wheat et al., 2020, supplementary information pp 4-5). A total of 15.6 l of 1.6 mol Cs/kg tracer solution was injected in the formation (Wheat et al., 2020). The Cs concentration in the borehole was expected to be 2.3 mmol Cs/kg, given mixing in the borehole of a total volume of 11,400 l (Wheat et al., 2020). The experiment kept the monitoring borehole (U1383C) open for the first twelve days of the experiment to promote fluid delivery to the borehole, and then closed for the remaining time. On day 11, bottom seawater, with a Cs concentration of ~2.1 nmol/kg, was allowed to enter the formation through injection Hole 1383B (Wheat et al., 2020). This was done to increase the rate of fluid flow towards the monitoring hole.

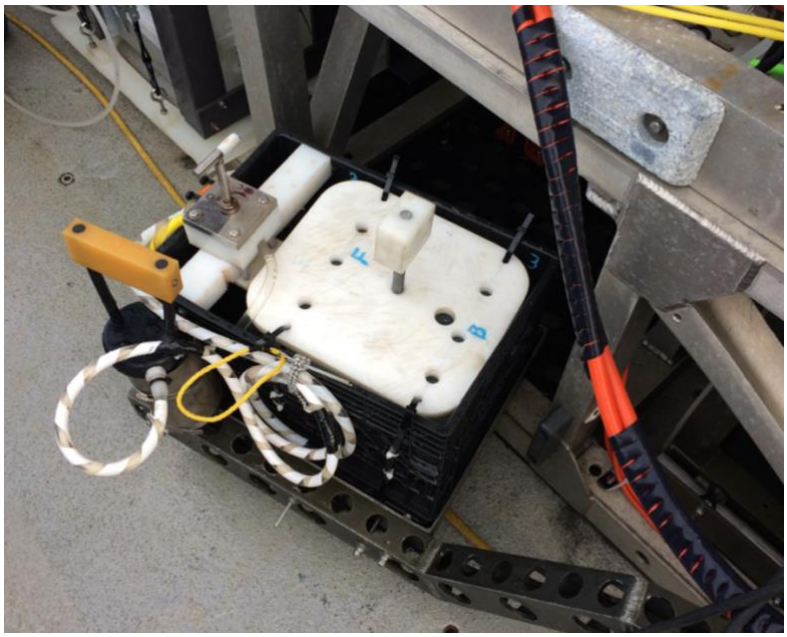

Figure 4.15*: Tracer injection system used for cesium chloride injection at North Pond. The injection system was positioned on the ROV (Jason II) and includes the Cs solution in a 21-l plastic bag (under the white plastic cover), a ball valve, and Jannasch-style handle (Wheat et al., 2011). The bag of tracer solution was connected to Tygon tubing which was connected to a ball valve. Three metres of additional tubing connects the ball valve to the Jannasch-style handle that is connected to the sampling port on the CORK wellhead (not shown). The tracer solution was delivered to the borehole by the manipulator of the ROV pushing down on the white plastic cover to push the fluid into the tubing and into the borehole. The entire 15.6 l of cesium chloride tracer solution was injected into the borehole within 15 minutes. Source: Wheat et al. (2020, supplementary information pp 4-5).*

The downhole Osmosamplers were collected 6 days after the tracer was injected from the monitoring hole, and after 11.3 days from the injection hole (Wheat et al., 2020). Sampling was completed in three ways: 1) shallow subseafloor Osmosamplers in both the injection hole (at 52.8 mbsf) and monitoring hole (at 100 mbsf), 2) collection through pumping formation fluids from the CORK umbilicals (i.e., mobile pumping system), and 3) a reverse osmosis (RO) Osmosampler that was deployed at the CORK wellhead when the borehole seal at Hole 1383C was temporarily open. During recovery of the Osmosamplers deployed in Hole 1383B they were brought to the sea surface and accidentally dropped to the seafloor where they remained for a full day before being recovered (Wheat et al., 2020, supplementary information pp 6-7). The temperature changes subjected to the OS during this incident made determining the timing within the sampling coil difficult. Once recovered, the sample coils were cut into 1.2 m lengths and the fluid was transferred to microcentrifuge tubes for analyses (Wheat et al., 2020).

Collection of formation fluids using the mobile pumping system followed the protocol outlined in Cowen et al. (2012) and discussed in Section 2.3.3. Using the mobile pumping system, one 50-l fluid sample and six 15-l samples were collected in acid-washed plastic bags. Samples were distributed for different analyses once recovered on the ship. For cesium analysis, aliquots of

sample were filtered into acid-washed (10% HCl) high-density polyethylene bottles for ICP-MS analysis (Wheat et al., 2020 supplementary information pp. 5-6).

The RO sampler is another type of continuous fluid sampler that have faster pump rates (ml/hr) with much larger diameter tubing (47 mm) compared to traditional Osmosamplers (ml/day). These samplers can provide hourly resolution for short term tracer experiments where Osmosamplers are deployed (Wheat et al., 2011, 2020). The faster pump rates can potentially increase dispersion within the larger diameter sample tubing, but this experiment retrieved the Osmosamplers within days after injection, so dispersion was not an issue compared to long-term Osmosampler deployments.

Seven to ten days after the cesium tracer was injected, the data from the injection hole showed a peak concentration of 410 μmol Cs/kg, which is almost six times less than the 2.3 mmol Cs/kg concentration that was expected if the entire volume of borehole fluid was thoroughly mixed with tracer (Wheat et al., 2020). Only seawater Cs concentrations were detected within 6 days at the monitoring hole before the samplers were recovered (Wheat et al., 2020). Although, after sealing the monitoring borehole, Cs concentrations increased to between 38-50 nmol Cs/kg, which confirmed transport of the injected Cs to the monitoring well which took longer than 6 days (even when ~300 l of formation fluids were removed during collection of the samples) (Wheat et al., 2020). Even with uncertainties in determining timing, the changes in Cs associated with the tracer experiment were captured by the Osmosamplers.

4.7 Discussion of Suitable Tracers

Finding suitable tracers for monitoring CO_2 sequestration in the offshore environment is challenging as geochemical tracers have not yet been used in deep-sea basalt to trace artificially injected CO_2. Many tracers meet some but not all the criteria to be suitable, particularly for the *in-situ* conditions for Cascadia Basin, and evidence for this is discussed below.

4.7.1 Conservative tracers

From this research, the most suitable conservative tracer for the water phase is SF_6. The behavior of SF_6 is understood at the *in-situ* conditions in Cascadia, and the use of it during the cross-hole tracer experiment provides evidence for its ability to track fluid transport and velocities in the aquifer and meeting ship regulations for offshore transport through to injection. It also has successfully been detected in the small fluid volumes produced from Osmosamplers in multiple boreholes throughout the region. A prerequisite for using SF_6 again at this site are low and constant background concentrations for an extended period prior to the CO_2 injection experiment, which can be constrained through baseline fluid monitoring for a few years before CO_2 injection. SF_6 has also been successful at determining CO_2-rich fluid breakthrough at the CarbFix pilot project.

If SF_6 does not have low and constant background concentrations, SF_5CF_3 is the next most suitable conservative tracer that meets most of the criteria, apart from it not being used previously in the Cascadia Basin nor collected using Osmosamplers. This compound has been used as a conservative tracer in basalt and observed breakthrough of CO_2-rich fluid at the same temperature and pressure as SF_6. Since it is physically and chemically like SF_6, and can be

injected in the same way, it is plausible that using SF_5CF_3 would be successful without additional testing. SF_5CF_3 does have a slightly higher detection limit compared to SF_6 but is still detectable at very low concentrations and will likely maintain those concentrations above the detection limit with dilution and mixing during transport. Since it is slightly less soluble than SF_6 in water at the same temperature and pressure, it is important that copper sampling coils are used, and precautions are taken to avoid sample loss. SF_5CF_3 could be used in place of SF_6 to monitor CO_2 movement and fluid breakthrough at the monitoring well but with some uncertainties.

Other potentially suitable tracers based on experimental laboratory data are xenon isotopes and fluorescent dyes. Fluorescent dyes can potentially be detected *in-situ* in real time with a fluorometer, or through collection of fluid samples and analysis of fluorescent dye concentrations in a lab onshore. Neither xenon isotopes nor fluorescent dyes have been used during field trials in the presence of supercritical CO_2, but more testing would be helpful in determining if these tracers could be used at the *in-situ* conditions in the Cascadia Basin.

PFCs have low detection limits and low solubilities in water but the factors contributing to increased solubility of PFCs in supercritical CO_2 are currently undefined. Additionally, partitioning behavior of PFCs between supercritical CO_2 and water is undefined. The inability of being able to tag the CO_2 with PFCs once it dissolves, the sampling precautions, and potential contamination during analysis presents challenges for using these compounds as conservative tracers. HFCs, HCFCs, and CFCs do not have enough data nor field testing to be considered as tracers for this project at this stage.

4.7.2 Reactive tracers

Stable carbon isotopic ratios are likely the most suitable tracer for confirming precipitation of carbonate minerals by informing how much carbon has been removed from the formation fluids with time. The Wallula pilot project and Weyburn-Midale CO_2 Monitoring and Storage project have shown evidence this is possible, where the change in stable carbon isotopic values were compared between pre- and post-injection fluid samples. If the stable carbon isotope values of the injected CO_2, formation fluids, and basaltic rock are distinct from one another, these tracers can be very useful in tracing the carbon in the reservoir without adding cost to the monitoring program. Another way of quantifying how much carbon has been removed from formation fluids to form minerals would be to measure the concentration of the carbon injected versus the amount of DIC measured at the monitoring well. Even if stable isotopes of carbon are not chosen to be used, DIC measurements along with a conservative tracer can indicate changes to baseline DIC, confirming CO_2-fluid-rock reactions, which can be measured using sensors (pH, pCO_2) or through collection and analysis of fluid samples.

Major ions and trace elements can aid in verifying dissolution of basalt, while changes in pH can help determine CO_2 dissolution as the fluids become more acidic as more CO_2 dissolves. Fluid samples should be analyzed for alkalinity as well using mobile pumping systems for collection. Pressure, temperature, and conductivity measurements are essential for monitoring and are currently used in ONC's existing sensor suite at the Cascadia Basin node. Changes to DIC, pH, major ions, trace elements, and alkalinity are controlled by the introduction of CO_2 to the system, so fluids only need to be collected and analyzed, which lowers cost while also complementing

the data obtained from any injected tracers. This research shows that changes observed between different geochemical measurements can aid in interpreting the overall picture of what is happening to the injected CO_2 in the crustal aquifer.

Chapter Five: Conclusions and Future Work

5.1 Conclusions

Monitoring CO_2 injection and sequestration in deep-sea basalt is vital for determining whether the carbon remains in the aquifer and to test if it is being sequestered as predicted through carbonate mineral formation. The remote nature of the proposed site of interest in the Cascadia Basin in the northeast Pacific Ocean, introduces monitoring challenges not commonly found in terrestrial settings, where most CCS projects have been conducted to date. Direct geochemical methods considered in this research include tracers and sensors to make measurements in real time to interpret geochemical changes in the aquifer, verify breakthrough of injected fluid, confirm carbon has been removed from aquifer fluids, and provide evidence of south to north flow observed in previous studies.

This study evaluated seven potential conservative tracers to trace fluid residence times and rates of transport for verifying CO_2 breakthrough at monitoring wells. I conclude SF_5CF_3 to be the most suitable conservative tracer due to its low detection limits, low solubility in seawater, chemical stability in the subsurface, and having similar chemical and physical properties to SF_6, a conservative tracer used previously in the Cascadia Basin region and at the CarbFix pilot project in a basaltic formation in southwest Iceland. A pulsed tracer injection is recommended for SF_5CF_3 to lower cost and amount of tracer required in addition to being logistically simpler than a continuous injection for injection of ~10,000 tons of CO_2 over ~35 days. Furthermore, three potential reactive tracers were investigated. Based on their ability to inform how much carbon has been removed from the *in-situ* fluids in carbon sequestration field trials, I conclude stable carbon isotopes to be the most suitable reactive tracer. Collection of fluid samples for analysis of major ion and trace element concentrations, pH, DIC concentrations, and alkalinity are also recommended for confirming CO_2-fluid-rock reactions. Measurements made from sensors in real time, connected to the NEPTUNE cabled ocean observatory that already exists at the site will complement the interpretations of transport observed from the tracer data. Among the various measurements that can be made in real time, I conclude temperature, pressure, conductivity, pH, and pCO_2 should be used, although it is currently unknown if pH and pCO_2 sensors will be reliable for *in-situ* measurements at higher temperatures than what these sensors are usually designed for, such as found in the basaltic aquifer in the Cascadia Basin. The recommended monitoring parameters (including tracers) for three CO_2 injection approaches (i.e., supercritical CO_2, WAG, aqueous CO_2) are outlined in Table 5.1.

Table 5.1: *Pros and cons of geochemical monitoring parameters for three different injection approaches.*

Monitoring Parameters	**Aqueous CO_2 Injection**	**Supercritical CO_2 Injection**	**WAG Injection (surface seawater/supercritical CO_2)**	**Detection**
Measurements from sensors				
Temperature & Pressure$^+$	Fluid will be colder than *in-situ* fluids (1)	Sensors may record cooling as the injected CO_2 will be colder than *in-*	Sensors may record cooling as surface seawater and $scCO_2$ will be colder than *in-situ* fluids; Injection	Injected CO_2 plume

		situ fluids; pressure changes as CO_2 enters formation (1)	pressure will denote WAG cycles (1)	
pH^+	Will decrease as CO_2-rich fluid enters formation (2)	will decrease as $scCO_2$ dissolves and acidifies formation fluids	May document relative pH changes between alternating cycles (3)	CO_2 dissolution & mineralization
pCO_2^+	Will increase as CO_2-rich fluid enters formation	Will increase when as $scCO_2$ dissolves & decrease as more is mineralized		CO_2 dissolution & mineralization
Salinity $(conductivity)^+$		$scCO_2$ may displace formation fluids and may detect a decrease in conductivity around the injection hole (2)	Capture alternating cycles of differing salinity from surface seawater and the salinity of the *in-situ* formation fluids (2)	Injected CO_2 plume
Geochemical tracers				
DIC			Concentrations in surface seawater and supercritical CO_2 needs to be known so signals can be identified	CO_2 dissolution & mineralization
Coumarin fluorescent dyes		Soluble in $scCO_2$ but unable to tag CO_2 once it dissolves into water – no published data on $scCO_2$/water partition coefficients		Injected CO_2 plume (more testing of fluorescent dye is needed determine if this is possible)
PFCs		Soluble in scCO2 but		Injected CO_2 plume

		problematic overall; not useful once supercritical CO_2 dissolves		
SF_6	Used at Carbfix to document CO_2-rich fluid breakthrough	Used previously in Cascadia Basin – requires low and constant background concentrations		Fluid velocities and breakthrough of injected fluid at monitoring well
SF_5CF_3	Used at Carbfix to document breakthrough of CO_2-rich fluid (3)	(3)		Fluid velocities and breakthrough of injected fluid at monitoring well
Noble gases and their isotopes	Will introduce noble gas signature of water	Larger noble gases (Xe, Kr, Ar) show positive deviation for supercritical CO_2 compared to pure noble gas-water systems (Warr et al., 2015)	Will introduce noble gas signature of water	Fluid velocities and breakthrough of injected fluid at monitoring well
Stable carbon isotopes		Used at Wallula; $\delta^{13}C$ should differ between injected CO_2, basalt, and formation fluids prior to injection		Mineralization
Stable oxygen isotopes		Used at Wallula;	Decrease ability to monitor fluid with O-isotopes as alternating water with CO_2 injection would complicate	Mineralization

			interpretation of $\delta^{18}O$ data	
Alkalinity		Alkalinity will increase during basalt dissolution	Alkalinity will differ between surface seawater and formation fluids	Dissolution, mineralization
Major ions and trace element concentrations	Concentrations expected to increase after injection and decrease during mineralization	Concentrations expected to increase once CO_2 dissolves into fluids and decrease during mineralization	Surface seawater will have different concentrations compared to formation fluids so changes in concentrations can be identified	CO_2 dissolution, mineralization

Table Footnotes: For each monitoring approach, monitoring parameters are ranked by denoting parameters as (1), (2), or (3). $^{+}$ = data collected via sensor. Testing of pH and pCO_2 sensor functionality above 65ºC is required prior to using them for monitoring the experiment. For stable carbon isotopes, before injection $\delta^{13}C$ isotopic values of the sourced CO_2 and formation fluids need to be determined. During injection, fluid samples should be collected for $\delta^{13}C$ analysis, and after injection $\delta^{13}C$ values need to be determined from post-injection fluid samples and from a recovered core to quantify how much carbon has been removed from the aquifer fluids.

Formation fluids will be collected in long term autonomous fluid sampling systems known as Osmosamplers during *in-situ* baseline sampling, during injection, and after injection. More fluid may need to be collected to meet volume requirements for the analyses using mobile pumping systems. Existing sensors (temperature, pressure, conductivity) connected to the NEPTUNE cabled observatory should make measurements in real time before, during, and after injection as well. Temperature measurements can record cooling once the injected fluids reach the monitoring well. Conductivity measurements are useful for observing any changes in salinity. It would be ideal to use pH and pCO_2 sensors to monitor changes to DIC in real time, but analyzing fluids onshore for DIC concentrations is also possible. Stable carbon isotopic values of the formation fluids, sourced CO_2, and a recovered basalt core should be constrained prior to and after CO_2 injection.

Seafloor and downhole Osmosamplers should be deployed in multiple monitoring boreholes for collection of fluid samples in areas fluid is expected to be transported (e.g., both south and north of the site) based on the observations made during a cross-hole tracer experiment conducted in 2010 using these boreholes. For monitoring leakage in real time, pH and pCO_2 sensors should be hung above the water column near the seafloor. Cameras connected to NEPTUNE will also detect any bubbles rising above the sediments. Conducting a controlled CO_2 release experiment like the QICS experiment offshore in the North Sea in the area prior to the CO_2 injection experiment will help to assess overall risk of leakage and what to expect if leakage through the sediments does occur without formation of a CO_2 hydrate that would trap CO_2 in the sediments. During the experiment, the injection hole will be one of the existing boreholes or a newly drilled hole. Existing nearby boreholes IODP Hole 1301A or ODP Hole 1026B could be used as a safe-fail, whereby induced failure could reveal fail-safe conditions, as both holes are known to leak,

and injected fluid was observed to flow quickly to both holes during the cross-hole tracer experiment.

5.2 Future Work

The lack of tracers used to monitor carbon sequestration in deep-sea ocean crust, presents an opportunity to test tracers at the *in-situ* conditions found in the crustal aquifer environment and in the presence of supercritical CO_2. Furthermore, assessing tracer behavior at the *in-situ* conditions would be useful for future offshore deep-sea basalt scenarios and future MRV plans for offshore projects. I propose that future work should include small-scale experiments prior to CO_2 injection to understand potentially suitable tracer behavior with better confidence.

A key piece of future work is finding fluorescent dyes that are strongly fractionated between supercritical CO_2 and seawater to be able to trace the differential transport of these in the basaltic aquifer. This could look like a fluorescent dye that is highly soluble in supercritical CO_2 but breaks down over time into a substance that partitions into seawater. Coumarin fluorescent dyes could serve this purpose, but the solubility in supercritical CO_2 and seawater at the temperature and pressure conditions in the Cascadia Basin would need to be experimentally determined. A model could then be used to test if it is feasible to use a fluorescent dye in this way to verify breakthrough of CO_2-rich fluid at the monitoring well. The intensity of fluorescence may also be affected by changes in temperature, salinity, or pH (Cascarano, 2018; Wilson et al., 1986) so this would need to be confirmed for coumarin dyes through modeling. Although only briefly mentioned in this research, the potential for using fiber optic sensors in combination with fluorescence spectroscopy in real time could be explored as a few fluorescent dyes (e.g., Rhodamine WT, Fluorescein) are easily detected with a fiber optic system (Flury and Wai, 2003).

One experiment that would be very useful would be to observe how long it would take for pH to change in the monitoring well, and how big of a change to be measurable. This could be investigated using the reactive transport model, as a laboratory experiment would not be comparable to the field-scale. Keeping in mind the large uncertainties that are inherent to using models, conducting the CO_2 injection experiment will inform if model predictions are correct regarding how quickly pH will change, and if it is a measurable change, at the closest monitoring well. Ocean Networks Canada should test pH and pCO_2 sensors through simulating their functionality in seawater above 65ºC.

The experimental evidence presented by Warr et al. (2015) showing that a fraction of the heavier noble gases (Xe, Kr, Ar) will preferentially enter the supercritical CO_2 phase presents an opportunity to further test how noble gas tracers can be used in deep-sea ocean crust in supercritical CO_2/water systems. It is likely that the remaining noble gas concentration that enters the water phase would determine how much of the noble gas is left behind in the supercritical CO_2 phase. The experimental pressure conditions (8.9-13.4 MPa) are not representative of the pressures found in the Cascadia Basin (~30 MPa), but it is likely the heavier noble gases will still show positive deviations towards supercritical CO_2 at increased pressures. Noble gas behavior could be modeled prior to the CO_2 injection experiment to determine if these compounds could be used as conservative tracers for injection. Noble gases are more soluble in

water than other conservative tracers considered in this research (SF_6, SF_5CF_3, PFCs), but are not classified greenhouse gases as the other conservative tracers are, so more understanding of their behavior in multi-phase systems through modeling could determine that noble gases may then be recommended instead.

Another experiment should be conducted in a lab with a permeable and porous rock core and a high-pressure vessel to test the behavior of PFC compounds (PMCH, PMCP, PDCB) dispersed in supercritical CO_2 in a CO_2/water system at the temperature and pressure conditions relevant to the basaltic aquifer in the Cascadia Basin. Since PFCs are highly soluble in supercritical CO_2, it would be useful to disperse PFCs in supercritical CO_2 prior to injection to test whether the PFCs form a separate phase in the presence of water and supercritical CO_2 or remain dispersed in the supercritical CO_2 until it dissolves. The PFCs would then be transported along with the formation fluids since a gas phase does not exist at the *in-situ* conditions in the Cascadia basin.

References

Adams, E. E. Evaluation of Tracers for Use in the International Field Experiment on CO_2 Ocean Sequestration. (2013).

Addy, K. *et al.* pH and Alkalinity. University of Rhode Island Watershed Watch. (2004).

Ajayi, T., Gomes, J. S. & Bera, A. A review of CO_2 storage in geological formations emphasizing modeling, monitoring, and capacity estimation approaches. *Pet. Sci.* **16**, 1028–1063 (2019).

Aley, T. Groundwater Tracing Handbook. 44 (2019).

Alt, J. C. Alteration of the upper oceanic crust: mineralogy, chemistry, and processes. (2004).

Alt, J. C. & Teagle, D. A. H. The uptake of carbon during alteration of ocean crust. *Geochimica et Cosmochimica Acta* **63**, 1527–1535 (1999).

Amonette, J. E. *et al.* Geochemical Monitoring Considerations for the FutureGen 2.0 Project. *Energy Procedia* **63**, 4095–4111 (2014).

Andreani, M. *et al.* Experimental Study of Carbon Sequestration Reactions Controlled by the Percolation of CO_2 -Rich Brine through Peridotites. *Environ. Sci. Technol.* **43**, 1226–1231 (2009).

Aradóttir, E. S. P., Sigurdardóttir, H., Sigfússon, B. & Gunnlaugsson, E. CarbFix: a CCS pilot project imitating and accelerating natural CO2 sequestration. *Greenhouse Gases: Science and Technology* **1**, 105–118 (2011).

Aradóttir, E. S. P., Sonnenthal, E. L., Björnsson, G. & Jónsson, H. Multidimensional reactive transport modeling of CO2 mineral sequestration in basalts at the Hellisheidi geothermal field, Iceland. *International Journal of Greenhouse Gas Control* **9**, 24–40 (2012).

Arts, R., Chadwick, A., Eiken, O., Thibeau, S. & Nooner, S. Ten years' experience of monitoring CO2 injection in the Utsira Sand at Sleipner, offshore Norway. **26**, 8 (2008).

Ashton, J. T., Dawe, R. A., Miller, K. W., Smith, E. B. & Stickings, B. J. The solubility of certain gaseous fluorine compounds in water. *J. Chem. Soc., A* 1793 (1968) doi:10.1039/j19680001793.

Atamanchuk, D. Development and use of an optical pCO_2 sensor in marine studies. University of Gothenburg (2013).

Atamanchuk, D. *et al.* Performance of a lifetime-based optode for measuring partial pressure of carbon dioxide in natural waters. *Limnology and Oceanography: Methods* **12**, 63–73 (2014).

Awolayo, A. N. *et al.* Mineral surface area accessibility and sensitivity constraints on carbon mineralization in basaltic aquifers. *Geochimica et Cosmochimica Acta* **334**, 293–315 (2022).

Barros, E. G. D., Leeuwenburgh, O. & Szklarz, S. P. Quantitative assessment of monitoring strategies for conformance verification of CO2 storage projects. *International Journal of Greenhouse Gas Control* **110**, 103403 (2021).

Barry, T. L. *et al.* Eruption chronology of the Columbia River Basalt Group. in *The Columbia River Flood Basalt Province* (Geological Society of America, 2013). doi:10.1130/2013.2497(02).

Bartetzko, A. & Fisher, A. T. Physical properties of young (3.5 Ma) oceanic crust from the eastern flank of the Juan de Fuca Ridge: Comparison of wireline and core measurements with global data. *Journal of Geophysical Research: Solid Earth* **113**, (2008).

Barth, J. A. C. *Geological Storage of CO2 – Long Term Security Aspects: GEOTECHNOLOGIEN Science Report No. 22*. (Springer International Publishing, 2015). doi:10.1007/978-3-319-13930-2.

Basava-Reddi, L. *Geological Storage of CO2 in Basalts*. (2011).

Bauer, S., Fulda, C. & Schaefer, W. A multi-tracer study in a shallow aquifer using age dating tracers 3H, 85Kr, CFC-113 and SF6 indication for retarded transport of CFC-113. *Journal of Hydrology* 21 (2001).

Becker, K. & Fisher, A. T. Permeability of upper oceanic basement on the eastern flank of the Juan de Fuca Ridge determined with drill-string packer experiments. *Journal of Geophysical Research: Solid Earth* **105**, 897–912 (2000).

Becker, K. & Fisher, A. T. Borehole packer tests at multiple depths resolve distinct hydrologic intervals in 3.5-Ma upper oceanic crust on the eastern flank of Juan de Fuca Ridge. *Journal of Geophysical Research: Solid Earth* **113**, (2008).

Becker, V. *et al.* Stable carbon and oxygen equilibrium isotope fractionation of supercritical and subcritical CO2 with DIC and H2O in saline reservoir fluids. *International Journal of Greenhouse Gas Control* **39**, 215–224 (2015).

Begley, P., Foulger, B., Simmonds, P. Femtogram detection of perfluorocarbon tracers using capillary gas chromatography-electron-capture negative ion chemical ionization mass spectrometry. *Journal of Chromatography* 445, 119-128. (1988).

Benson, R. C. & Yuhr, L. B. Dye Tracing. in *Site Characterization in Karst and Pseudokarst Terraines* 295–306 (Springer Netherlands, 2016). doi:10.1007/978-94-017-9924-9_22.

Benson, S. M. & Cole, D. R. CO2 Sequestration in Deep Sedimentary Formations. *Elements* **4**, 325–331 (2008).

Benson, S. *et al.* Underground geological storage. *IPCC Special Report on Carbon Dioxide Capture and Storage* (2005).

Berger, G., Schott, J. & Guy, C. Behavior of Li, Rb and Cs during basalt glass and olivine dissolution and chlorite, smectite and zeolite precipitation from seawater: Experimental investigations and modelization between 50° and 300°C. *Chemical Geology* **71**, 297–312 (1988).

Berglund, M. & Wieser, M. E. Isotopic compositions of the elements 2009 (IUPAC Technical Report). *Pure and Applied Chemistry* **83**, 397–410 (2011).

Berven, B. M. *et al.* Highly Fluorous Complexes of Ruthenium and Osmium and Their Solubility in Supercritical Carbon Dioxide. *Inorg. Chem.* **48**, 11832–11842 (2009).

Beyerle, U. *et al.* A Mass Spectrometric System for the Analysis of Noble Gases and Tritium from Water Samples. *Environ. Sci. Technol.* **34**, 2042–2050 (2000).

Bieri, R., Koide, M. & Goldberg, E. D. Noble Gases in Sea Water. *Science* **146**, 1035–1037 (1964).

Biswas, R., Lewis, J. E. & Maroncelli, M. Electronic spectral shifts, reorganization energies, and local density augmentation of Coumarin 153 in supercritical solvents. *Elsevier* **310**, 485–494 (1999).

Blackford, J. *et al.* Impact and detectability of hypothetical CCS offshore seep scenarios as an aid to storage assurance and risk assessment. *International Journal of Greenhouse Gas Control* **95**, 102949 (2020).

Blackford, J. *et al.* Detection and impacts of leakage from sub-seafloor deep geological carbon dioxide storage. *Nature Clim Change* **4**, 1011–1016 (2014).

Boot-Handford, M. E. *et al.* Carbon capture and storage update. *Energy Environ. Sci.* **7**, 130–189 (2014).

Boreham, C. *et al.* Monitoring of CO2 storage in a depleted natural gas reservoir: Gas geochemistry from the CO2CRC Otway Project, Australia. *International Journal of Greenhouse Gas Control* **5**, 1039–1054 (2011).

Bourne, S., Crouch, S. & Smith, M. A risk-based framework for measurement, monitoring and verification of the Quest CCS Project, Alberta, Canada. *International Journal of Greenhouse Gas Control* **26**, 109–126 (2014).

Bradshaw, A. & Schleicher, K. Electrical conductivity of seawater. *IEEE Journal of Oceanic Engineering* **5**, 50–62 (1980).

Brady, P. V. & Gislason, S. Seafloor weathering controls on atmospheric C02 and global climate. *Geochimica et Cosmochimica Acta* **61**, 965–977 (1997).

Bu, X., and Warner, M.J. Solubility of Chlorofluorocarbon 113 in water and seawater. *Deep-Sea Research* **42**, 1151-1161 (1995).

Budisa, N. & Schulze-Makuch, D. Supercritical Carbon Dioxide and Its Potential as a Life-Sustaining Solvent in a Planetary Environment. *Life (Basel)* **4**, 331–340 (2014).

Bullister, J. L. and Weiss, R.F. Determination of CCl_3F and CCl_3F_2 in seawater and air. Deep-Sea Research **35**, 839-853 (1988).

Bullister, J. L. Chlorofluorocarbons as Time Dependent Tracers in the Ocean. *oceanog* **2**, 12–17 (1989).

Bullister, J. L., Wisegarver, D. P. & Menzia, F. A. The solubility of sulfur hexafluoride in water and seawater. *Deep Sea Research Part I: Oceanographic Research Papers* **49**, 175–187 (2002).

Burant, A., Lowry, G. V. & Karamalidis, A. K. Partitioning Behavior of Organic Contaminants in Carbon Storage Environments: A Critical Review. *Environ. Sci. Technol.* **47**, 37–54 (2012).

Burton, M. & Bryant, S. L. Surface dissolution: Minimizing groundwater impact and leakage risk simultaneously. *Energy Procedia* **1**, 3707–3714 (2009).

Busenberg, E. & Plummer, L. N. Use of chlorofluorocarbons (CCl3F and CCl2F2) as hydrologic tracers and age-dating tools: The alluvium and terrace system of central Oklahoma. *Water Resources Research* **28**, 2257–2283 (1992).

Busenberg, E. & Plummer, L. N. Dating young groundwater with sulfur hexafluoride: Natural and anthropogenic sources of sulfur hexafluoride. *Water Resources Research* **36**, 3011–3030 (2000).

Busenberg, E. & Plummer, L. N. Dating groundwater with trifluoromethyl sulfurpentafluoride (SF5CF3), sulfur hexafluoride (SF6), CF3Cl (CFC-13), and CF2Cl2 (CFC-12). *Water Resources Research* **44**, (2008).

Busenberg, E. & Plummer, L. N. A rapid method for the measurement of sulfur hexafluoride (SF6), trifluoromethyl sulfur pentafluoride (SF5CF3), and Halon 1211 (CF2ClBr) in hydrologic tracer studies. *Geochemistry, Geophysics, Geosystems* **11**, (2010).

Callow, B., Falcon-Suarez, I., Ahmed, S. & Matter, J. Assessing the carbon sequestration potential of basalt using X-ray micro-CT and rock mechanics. *International Journal of Greenhouse Gas Control* **70**, 146–156 (2018).

Calm, J. M. & Domanski, P. A. R-22 Replacement Status. *ASHRAE Journal* (2004).

Campbell, J. S. *et al.* Geochemical Negative Emissions Technologies: Part I. Review. *Front. Clim.* **4**, 879133 (2022).

Cao, V. *et al.* Solute Reactive Tracers for Hydrogeological Applications: A Short Review and Future Prospects. *Water* **12**, 653 (2020).

Carlson, P. R. & Nelson, C. H. Marine Geology and Resources Potential of Cascadia Basin. (1987).

Cascarano, R. N. Use of Fluorescein Dye for Characterizing Water and Solute Flux Across the Groundwater – Surface Water Interface. (2018).

Chadwick, A. Offshore CO2 Storage: Sleipner natural gas field beneath the North Sea. (2013).

Chambers, L. A., Gooddy, D. C. & Binley, A. M. Use and application of CFC-11, CFC-12, CFC-113 and SF_6 as environmental tracers of groundwater residence time: A review. *Geoscience Frontiers* **10**, 1643–1652 (2019).

Chang, C. *et al.* Pore-scale supercritical CO2 dissolution and mass transfer under imbibition conditions. *Advances in Water Resources* **92**, 142–158 (2016).

Cho, A. Helium-3 Shortage Could Put Freeze On Low-Temperature Research. *Science* **326**, 778–779 (2009).

Clark, D. E. *et al.* CarbFix2: CO2 and H2S mineralization during 3.5 years of continuous injection into basaltic rocks at more than 250 °C. *Geochimica et Cosmochimica Acta* **279**, 45–66 (2020).

Clark, I. D. & Fritz, P. *Environmental Isotopes in Hydrogeology*. (CRC Press, 1997).

Clark, J. F., Hudson, G. B. & Avisar, D. Gas Transport below Artificial Recharge Ponds: Insights from Dissolved Noble Gases and a Dual Gas (SF_6 and ^{3}He) Tracer Experiment. *Environ. Sci. Technol.* **39**, 3939–3945 (2005).

Clarke, J. S. *et al.* Developments in marine pCO2 measurement technology; towards sustained in situ observations. *TrAC Trends in Analytical Chemistry* **88**, 53–61 (2017).

Coggon, R. M. *et al.* Linking basement carbonate vein compositions to porewater geochemistry across the eastern flank of the Juan de Fuca Ridge, ODP Leg 168. *Earth and Planetary Science Letters* **219**, 111–128 (2004).

Constable, S. & Stern, L. A. Monitoring Offshore CO2 Sequestration Using Marine CSEM Methods; Constraints Inferred from Field- and Laboratory-Based Gas Hydrate Studies. *Energies* **15**, 7411 (2022).

Cook, P. G. & Solomon, D. K. Recent advances in dating young groundwater: chlorofluorocarbons, 3H/3He and 85Kr. *Journal of Hydrology* **191**, 245–265 (1997).

Cook, P. G., Solomon, D. K., Plummer, L. N., Busenberg, E. & Schiff, S. L. Chlorofluorocarbons as Tracers of Groundwater Transport Processes in a Shallow, Silty Sand Aquifer. *Water Resources Research* **31**, 425–434 (1995).

Cook, P. *Introduction to Isotopes and Environmental Tracers as Indicators of Groundwater Flow*. (The Groundwater Project, 2020). doi:10.21083/978-1-7770541-8-2.

Cook, P. G. & Herczeg, A. L. *Environmental Tracers in Subsurface Hydrology*. (Springer Science & Business Media, 2012).

Cooke, K. M., Simmonds, P. G., Nickless, G. & Makepeace, A. P. W. Use of Capillary Gas Chromatography with Negative Ion-Chemical Ionization Mass Spectrometry for the Determination of Perfluorocarbon Tracers in the Atmosphere. *Anal. Chem.* **73**, 4295–4300 (2001).

Cosgrove, B. A. & Walkley, J. Solubilities of gases in H2O and 2H2O. *Journal of Chromatography A* **216**, 161–167 (1981).

Cowen, J. P. *et al.* Advanced instrument system for real-time and time-series microbial geochemical sampling of the deep (basaltic) crustal biosphere. *Deep Sea Research Part I: Oceanographic Research Papers* **61**, 43–56 (2012).

Crank, J. The Mathematics of Diffusion. (1975).

Cronin, M. T. D. *et al.* Use of QSARs in international decision-making frameworks to predict health effects of chemical substances. *Environ Health Perspect* **111**, 1391–1401 (2003).

Dalit, M. Sampling fluids from Earth's crust. *MBARI* https://www.mbari.org/sampling-fluids-from-earths-crust/ (2004).

Dardin, A., DeSimone, J. M. & Samulski, E. T. Fluorocarbons Dissolved in Supercritical Carbon Dioxide. NMR Evidence for Specific Solute−Solvent Interactions. *J. Phys. Chem. B* **102**, 1775–1780 (1998).

Davis, E., Fisher, A. & Firth, J. Ocean Drilling Program Leg 168 Scientific Prospectus: Hydrothermal Circulation in the Oceanic Crust: Eastern Flank of the Juan de Fuca Ridge. (1996a).

Davis, E. E. *et al.* Ocean Drilling Program Leg 168 Preliminary Report: Hydrothermal Circulation in the Oceanic Crust: Eastern flank of the Juan de Fuca Ridge. (1996b).

Davis, E. E. *et al.* FlankFlux: an experiment to study the nature of hydrothermal circulation in young oceanic crust. *Can. J. Earth Sci.* **29**, 925–952 (1992).

Davis, E. E. *et al.* Regional heat flow variations across the sedimented Juan de Fuca Ridge eastern flank: Constraints on lithospheric cooling and lateral hydrothermal heat transport. *J. Geophys. Res.* **104**, 17675–17688 (1999).

Davis, E. E. & Hyndman, R. D. Accretion and recent deformation of sediments along the northern Cascadia subduction zone. *Geological Society of America Bulletin* **101**, 1465–1480 (1989).

Davis, E. E. *et al.* Seafloor Heat Flow on the Eastern Flank of Juan de Fuca Ridge: Data from "Flankflux" studies through 1995. in *Proceedings of the Ocean Drilling Program, Initial Reports, Vol. 168* (1997).

Davis, E. & Becker, K. Borehole observatories record driving forces for hydrothermal circulation in young oceanic crust. *Eos, Transactions American Geophysical Union* **79**, 369–370 (1998).

Davis, E. E., Chapman, D. S., Forster, C. B. & Villinger, H. Heat-flow variations correlated with buried basement topography on the Juan de Fuca Ridge flank. *Nature* **342**, 533–537 (1989).

De Jong, Menso Thomas. Constraining hydraulic properties in oceanic crust near the Juan de Fuca Spreading Center. PhD. Dissertation. (2020).

De Obeso, J. C. *et al.* Experimental study on plagioclase dissolution rates at conditions relevant to mineral carbonation of seafloor basalts. *Chemical Geology* **620**, 121348 (2023).

Dean, M., Blackford, J., Connelly, D. & Hines, R. Insights and guidance for offshore CO_2 storage monitoring based on the QICS, ETI MMV, and STEMM-CCS projects. *International Journal of Greenhouse Gas Control* **100**, 103120 (2020).

Deans, H. A. Method of determining fluid saturations in reservoirs. (1971).

Delaney, P. & Higgins, S. 'Core on deck!' The End of SODV and the Return of the JOIDES Resolution as the IODP Riserless Vessel. *Scientific Drilling* **8**, 38–40 (2009).

Delbeke, J., Runge-Metzger, A., Slingenberg, Y. & Werksman, J. THE PARIS AGREEMENT.

Demirkanli, I., White, S., White, M., Bonneville, A. & Goldberg, D. Water Alternating Gas Cycling to Optimize CO2 Mineralization for Geological Carbon Storage: Cascadia Project. 1.

DePaolo, D. J. *et al.* Opportunities for large-scale CO2 disposal in coastal marine volcanic basins based on the geology of northeast Hawaii. *International Journal of Greenhouse Gas Control* **110**, 103396 (2021).

Dickson, A.G. The carbon dioxide system in seawater: Equilibrium chemistry and measurements (2010).

Dickson, A.G. *et al.* Guide to best practices for ocean CO_2 measurements. North Pacific Marine Science Organization Special Publication 3, 191 pp (2007).

Diep, P., Jordan, K. D., Johnson, J. K. & Beckman, E. J. CO_2 −Fluorocarbon and CO_2 −Hydrocarbon Interactions from First-Principles Calculations. *J. Phys. Chem. A* **102**, 2231–2236 (1998).

Draxler, R. R., Dietz, R., Lagomarsino, R. J. & Start, G. Across North America tracer experiment (ANATEX): Sampling and analysis. *Atmospheric Environment. Part A. General Topics* **25**, 2815–2836 (1991).

Dugstad, O., Bjornstad, T. & Hundere, I. Measurements and Application of Partition Coefficients of Compounds Suitable for Tracing Gas Injected Into Oil Reservoirs. *Rev. Inst. Fr. Pét.* **47**, 205–215 (1992).

Dugstad, Ø., Bjørnstad, T. & Hundere, I. A. Measurements of gas tracer retention under simulated reservoir conditions. *Journal of Petroleum Science and Engineering* **10**, 17–25 (1993).

Dunitz, J. D., Gavezzotti, A. & Schweizer, W. B. Molecular Shape and Intermolecular Liaison: Hydrocarbons and Fluorocarbons. *Helvetica Chimica Acta* **86**, 4073–4092 (2003).

Duong, C., Bower, C., Hume, K., Rock, L. & Tessarolo, S. Quest carbon capture and storage offset project: Findings and learnings from 1st reporting period. *International Journal of Greenhouse Gas Control* **89**, 65–75 (2019).

Earle, S. Physical Geology - 2nd Edition. (2019).

Elderfield, H., Wheat, C. G., Mottl, M. J., Monnin, C. & Spiro, B. Fluid and geochemical transport through oceanic crust: a transect across the eastern flank of the Juan de Fuca Ridge. *Earth and Planetary Science Letters* **172**, 151–165 (1999).

Emberley, S. *et al.* Monitoring of fluid–rock interaction and CO2 storage through produced fluid sampling at the Weyburn CO2-injection enhanced oil recovery site, Saskatchewan, Canada. *Applied Geochemistry* **20**, 1131–1157 (2005).

Emerson, S. R. & Hamme, R. C. *Chemical Oceanography*. Cambridge University Press. (2020).

Emerson, S., Stump, C., Wilbur, D. & Quay, P. Accurate measurement of O2, N2, and Ar gases in water and the solubility of N2. (1999).

Emerson and Hedges. Chemical Oceanography. (2008).

Energy Futures Initiative. CO_2-Secure: A national program to deploy carbon removal at gigaton scale. (2022).

Epstein, S., and Mayada, T. Variation of O18 content of waters from natural sources. *Geochimica et Cosmochimica Acta* 4, 213-224. (1953).

Erboy, Y. & Smethie, W. M. Trifluoromethyl sulfur pentafluoride and its relationship to sulfur hexafluoride and chlorofluorocarbon-12 in the atmosphere near the New York City metropolitan area. *Atmospheric Environment* **55**, 135–138 (2012).

Esposito, M. *et al.* Water column baseline assessment for offshore Carbon Dioxide Capture and Storage (CCS) sites: Analysis of field data from the Goldeneye storage complex area. *International Journal of Greenhouse Gas Control* **109**, 103344 (2021).

Exon, N. F. & Malone, M. J. Scientific Ocean drilling and the capabilities of the IODP drillship *JOIDES Resolution*. *ASEG Extended Abstracts* **2015**, 1–2 (2015).

Expedition 327 Scientists. Integrated Ocean Drilling Program Expedition 327 Preliminary Report: Juan de Fuca Ridge-Flank Hydrogeology. *Integrated Ocean Drilling Program.* (2010). doi:10.2204/iodp.pr.327.2010.

Fakhari, A., Li, Y., Bolster, D. & Christensen, K. T. A phase-field lattice Boltzmann model for simulating multiphase flows in porous media: Application and comparison to experiments of CO2 sequestration at pore scale. *Advances in Water Resources* **114**, 119–134 (2018).

Fawzy, S., Osman, A. I., Doran, J. & Rooney, D. W. Strategies for mitigation of climate change: a review. *Environ Chem Lett* **18**, 2069–2094 (2020).

Fisher, A. T., Becker, K. & Davis, E. E. The permeability of young oceanic crust east of Juan de Fuca Ridge Determined using borehole thermal measurements. *Geophysical Research Letters* **24**, 1311–1314 (1997).

Fisher, A. T. *et al.* Hydrothermal recharge and discharge across 50 km guided by seamounts on a young ridge flank. *Nature* **421**, 618–621 (2003).

Fisher, A. T. *et al.* IODP Expedition 327 and *Atlantis* Expedition AT 18-07: Observatories and Experiments on the Eastern Flank of the Juan de Fuca Ridge. *Sci. Dril.* **13**, 4–11 (2012).

Fisher, A. T., Urabe, T., Klaus, A., & and the Expedition 301 Scientists. Expedition 301 summary. in *Proceedings of the Integrated Ocean Drilling Program, Volume 301* (2005a).

Fisher, A.T. et al. Scientific and technical design and deployment of long-term subseafloor observatories for hydrogeologic and related experiments. *Proceedings of the Integrated Ocean Drilling Program, Volume 301.* (2005b).
Fisher, A. T., Urabe, T., Klaus, A., & the IODP Expedition 301 Scientists. IODP Expedition 301 Installs Three Borehole Crustal Observatories, Prepares for Three-Dimensional, Cross-Hole Experiments in the Northeastern Pacific Ocean. *Sci. Dril.* **1**, 6–11 (2005c).

Fisher, A. T. Marine hydrogeology: recent accomplishments and future opportunities. *Hydrogeol J* **13**, 69–97 (2005d).

Fisher, A. T., Tsuji, T., Petronotis, K., & Expedition 327 Scientists. Expedition 327 Summary. in *Proceedings of the Integrated Ocean Drilling Program, Volume 327* (Integrated Ocean Drilling Program, (2011a). doi:10.2204/iodp.proc.327.2011.

Fisher, A. T. & Expedition 327 Scientists. Site U1362. in *Proceedings of the Integrated Ocean Drilling Program, Volume 327* (2011b). doi:10.2204/iodp.proc.327.2011.

Fisher, A. T., Tsuji, T. & Petronotis, K. Site 1027. in *Proceedings of the Integrated Ocean Drilling Program, Volume 327* (2011c). doi:10.2204/iodp.proc.327.2011.

Fisher, A. T. & Expedition 327 Scientists. Site U1301. in *Proceedings of the Integrated Ocean Drilling Program, Volume 327* (2011d). doi:10.2204/iodp.proc.327.2011.

Fisher, A. T., Wheat, C. G. & Becker, K. Design, deployment, and status of borehole observatory systems used for single-hole and cross-hole experiments, IODP Expedition 327, eastern flank of Juan de Fuca Ridge. in *Proceedings of the Integrated Ocean Drilling Program, Volume 327* (2011e). doi:10.2204/iodp.proc.327.2011.

Fisher, A. T., Cowen, T., Wheat, C. G. & Clark, J. F. Preparation and injection of fluid tracers during IODP Expedition 327, eastern flank of Juan de Fuca Ridge. in *Proceedings of the Integrated Ocean Drilling Program, Volume 327* (2011f). doi:10.2204/iodp.proc.327.2011.

Fisher, A.T., *et al.* Preliminary Cruise Report for R/V *Atlantis*/ROV *Jason-II* Expedition AT18-07: Hydrogeologic, Geochemical, and Microbiological Experiments in Young Ocean Crust of the Northeastern Pacific Ocean using Subseafloor Observatories. (2011g).

Fisher, A. T., Tsuji, T. & Gamage, K. *Integrated Ocean Drilling Program Expedition 327 Scientific Prospectus Juan de Fuca Ridge-Flank Hydrogeology*. (2010). doi:10.2204/iodp.sp.327.2010.

Fisher, A.T. et al. Scientific Prospectus for R/V *Atlantis*/Alvin Expedition AT26-18: Completing single and cross-hole hydrogeologic and microbial experiments: Juan de Fuca Flank. (2014).

Fisher, A. T. Permeability within basaltic oceanic crust. *Reviews of Geophysics* **36**, 143–182 (1998).

Flohr, A. *et al.* Towards improved monitoring of offshore carbon storage: A real-world field experiment detecting a controlled sub-seafloor CO2 release. *International Journal of Greenhouse Gas Control* **106**, 103237 (2021).

Flude, S., Johnson, G., Gilfillan, S. M. V. & Haszeldine, R. S. Inherent Tracers for Carbon Capture and Storage in Sedimentary Formations: Composition and Applications. *Environ. Sci. Technol.* **50**, 7939–7955 (2016).

Flury, M. & Wai, N. N. Dyes as tracers for vadose zone hydrology. *Reviews of Geophysics* **41**, (2003).

Ford, D. E. & Thornton, K. W. Lissamine FF Fluorescent Dye. *J. Environ. Eng.* **109**, 952–955 (1983).

Freifeld, B. M. *et al.* The U-tube: A novel system for acquiring borehole fluid samples from a deep geologic CO2 sequestration experiment. *Journal of Geophysical Research: Solid Earth* **110**, (2005).

Freire, M. G. *et al.* Solubility of Hexafluorobenzene in Aqueous Salt Solutions from (280 to 340) K. *J. Chem. Eng. Data* **50**, 237–242 (2005).

Furre, A.-K., Eiken, O., Alnes, H., Vevatne, J. N. & Kiær, A. F. 20 Years of Monitoring CO2-injection at Sleipner. *Energy Procedia* **114**, 3916–3926 (2017).

Fuss, S. *et al.* Negative emissions—Part 2: Costs, potentials and side effects. *Environ. Res. Lett.* **13**, 063002 (2018).

Galdiga, C. U. & Greibrokk, T. Simultaneous determination of trace amounts of sulphur hexafluoride and cyclic perfluorocarbons in reservoir samples by gas chromatography. *Chromatographia* **46**, 440–443 (1997).

Gasper, E. Natural and artificial tracers in the study of the hydrodynamics of karst. *Theoretical and Applied Karstology.* 3, 31-107 (1987).

Giacomel, P. *et al.* Frictional Instabilities and Carbonation of Basalts Triggered by Injection of Pressurized H2O- and CO2- Rich Fluids. *Geophysical Research Letters* **45**, 6032–6041 (2018).

Gilfillan, S. M. V. *et al.* The noble gas geochemistry of natural CO2 gas reservoirs from the Colorado Plateau and Rocky Mountain provinces, USA. *Geochimica et Cosmochimica Acta* **72**, 1174–1198 (2008).

Gislason, S. R. *et al.* Rapid solubility and mineral storage of CO2 in basalt. *Energy Procedia* **63**, 4561–4574 (2014).

Gislason, S. R. & Oelkers, E. H. Carbon Storage in Basalt. *Science* **344**, 373–374 (2014).

Gislason, S. R., Sigurdardottir, H., Aradottir, E. S. & Oelkers, E. H. A brief history of CarbFix: Challenges and victories of the project's pilot phase. *Energy Procedia* **146**, 103–114 (2018).

Gislason, S. R. *et al.* Mineral sequestration of carbon dioxide in basalt: A pre-injection overview of the CarbFix project. *International Journal of Greenhouse Gas Control* **4**, 537–545 (2010).

Goldberg, D. S., Takahashi, T. & Slagle, A. L. Carbon dioxide sequestration in deep-sea basalt. *Proceedings of the National Academy of Sciences* **105**, 9920–9925 (2008).

Goldberg, D. Integrated Pre-Feasibility Study for CO2 Sequestration in the Cascadia Basin, Offshore of Washington State and British Columbia (Phase 1). https://www.osti.gov/servlets/purl/1488562 (2018a).

Goldberg, D. *et al.* Geological storage of CO_2 in sub-seafloor basalt: the CarbonSAFE pre-feasibility study offshore Washington State and British Columbia. *Energy Procedia* **146**, 158–165 (2018b).

Goldberg, D. & Slagle, A. L. A global assessment of deep-sea basalt sites for carbon sequestration. *Energy Procedia* **1**, 3675–3682 (2009).

Gooddy, D. C., Darling, W. G., Abesser, C. & Lapworth, D. J. Using chlorofluorocarbons (CFCs) and sulphur hexafluoride (SF6) to characterise groundwater movement and residence time in a lowland Chalk catchment. *Journal of Hydrology* **330**, 44–52 (2006).

Guillot, S., Hattori, K., Agard, P., Schwartz, S. & Vidal, O. Exhumation Processes in Oceanic and Continental Subduction Contexts: A Review. in *Subduction Zone Geodynamics* (eds. Lallemand, S. & Funiciello, F.) 175–205 (Springer Berlin Heidelberg, 2009). doi:10.1007/978-3-540-87974-9_10.

Gunnarsson, I. *et al.* The rapid and cost-effective capture and subsurface mineral storage of carbon and sulfur at the CarbFix2 site. *International Journal of Greenhouse Gas Control* **79**, 117–126 (2018).

Gunter, W. D., Wiwehar, B. & Perkins, E. H. Aquifer disposal of CO2-rich greenhouse gases: Extension of the time scale of experiment for CO2-sequestering reactions by geochemical modelling. *Mineralogy and Petrology* **59**, 121–140 (1997).

Gunter, W. D., Perkins, E. H. & McCann, T. J. Aquifer disposal of CO2-rich gases: Reaction design for added capacity. *Energy Conversion and Management* **34**, 941–948 (1993).

Györe, D., Gilfillan, S. M. V. & Stuart, F. M. Tracking the interaction between injected CO2 and reservoir fluids using noble gas isotopes in an analogue of large-scale carbon capture and storage. *Applied Geochemistry* **78**, 116–128 (2017).

Györe, D., Stuart, F. M., Gilfillan, S. M. V. & Waldron, S. Tracing injected CO 2 in the Cranfield enhanced oil recovery field (MS, USA) using He, Ne and Ar isotopes. *International Journal of Greenhouse Gas Control* **42**, 554–561 (2015).

Gysi, A. P. & Stefánsson, A. CO2-water–basalt interaction. Low temperature experiments and implications for CO2 sequestration into basalts. *Geochimica et Cosmochimica Acta* **81**, 129–152 (2012).

Haase, K. B., Busenberg, E., Plummer, L. N., Casile, G. & Sanford, W. E. Measurements of HFC-134a and HCFC-22 in groundwater and unsaturated-zone air: Implications for HFCs and HCFCs as dating tracers. *Chemical Geology* **385**, 117–128 (2014).

Hamme, R. C. & Emerson, S. R. The solubility of neon, nitrogen and argon in distilled water and seawater. *Deep Sea Research Part I: Oceanographic Research Papers* **51**, 1517–1528 (2004).

Han, W. S. *et al.* Modeling of Spatiotemporal Thermal Response to CO2 Injection in Saline Formations: Interpretation for Monitoring. *Transp Porous Med* **93**, 381–399 (2012).

Han, Z. *et al.* Application of chlorofluorocarbons (CFCs) to estimate the groundwater age at a headwater wetland in Ichikawa City, Chiba Prefecture, Japan. *Appl Water Sci* **4**, 291–302 (2014).

Harnisch, J., Borchers, R., Fabian, P. & Maiss, M. Tropospheric trends for CF4 and C2F6 since 1982 derived from SF6 dated stratospheric air. *Geophysical Research Letters* **23**, 1099–1102 (1996).

Hepple, R. P. & Benson, S. M. Geologic storage of carbon dioxide as a climate change mitigation strategy: performance requirements and the implications of surface seepage. *Environ Geol* **47**, 576–585 (2005).

Ho, D. T., Ledwell, J. R. & Smethie, W. M. Use of SF5CF3 for ocean tracer release experiments. *Geophys. Res. Lett.* **35**, L04602 (2008).

Holford, S., Schofield, N., Bunch, M., Bischoff, A. & Swierczek, E. Storing CO2 in buried volcanoes. *The APPEA Journal* **61**, 626 (2021).

Holland, G. & Gilfillan, S. Application of Noble Gases to the Viability of CO2 Storage. in *The Noble Gases as Geochemical Tracers* 177–223 (2013). doi:10.1007/978-3-642-28836-4_8.

Horneman, A. *et al.* Degradation rates of CFC-11, CFC-12 and CFC-113 in anoxic shallow aquifers of Araihazar, Bangladesh. *Journal of Contaminant Hydrology* **97**, 27–41 (2008).

House, C. H., Cragg, B. A., Teske, A. & Leg 201 Scientific Party. *Proceedings of the Ocean Drilling Program, 201 Initial Reports.* (2003).

House, K. Z., Schrag, D. P., Harvey, C. F. & Lackner, K. S. Permanent carbon dioxide storage in deep-sea sediments. *Proceedings of the National Academy of Sciences* **103**, 12291–12295 (2006).

Hovorka, S. D. *et al.* Monitoring CO_2 storage in brine formations: lessons learned from the Frio field test one year post injection. (2006).

Huey, D. & Storms, M. The Ocean Drilling Program IV: Deep water coring technology-Past, present, and future. in *OCEANS '85 - Ocean Engineering and the Environment* 146–159 (1985). doi:10.1109/OCEANS.1985.1160102.

Hulme, S. M., Wheat, C. G., Coggon, R. & McManus, J. Data report: trace element, Sr isotope, and Ge/Si composition of fluids and sediments in ridge-flank low-temperature hydrothermal environments. in *Proceedings of the IODP, 301* (2008).

Hulme, S. M. & Wheat, C. G. Subseafloor Fluid and Chemical Fluxes Along a Buried-Basement Ridge on the Eastern Flank of the Juan de Fuca Ridge. *Geochemistry, Geophysics, Geosystems* **20**, 4922–4938 (2019).

Hutnak, M. *et al.* Hydrothermal recharge and discharge guided by basement outcrops on 0.7–3.6 Ma seafloor east of the Juan de Fuca Ridge: Observations and numerical models. *Geochemistry, Geophysics, Geosystems* **7**, (2006).

IEAGHG. Review of Offshore Monitoring for CCS Projects. Report: 2015/02. (2015).

IEAGHG. Review of CO_2 Storage in Basalts. 2017 Technical Review. (2017).

Ilgen, A. G. & Cygan, R. T. Mineral dissolution and precipitation during CO2 injection at the Frio-I Brine Pilot: Geochemical modeling and uncertainty analysis. *International Journal of Greenhouse Gas Control* **44**, 166–174 (2016).

International Atomic Energy Agency. Use of Chlorofluorocarbons in Hydrology: A Guidebook. (2006).

International Energy Agency. CO_2 Emissions in 2022. (2022).

IPCC. Climate Change 2021: The Physical Science Basis. Contribution of Working Group I to the Sixth Assessment Report of the Intergovernmental Panel on Climate Change. Cambridge University Press. (2021).

IPCC. Climate Change 2023: Synthesis Report: A report of the Intergovernmental Panel on Climate Change. Contribution of Working Groups I, II, and III to the Sixth Assessment Report of the Intergovernmental Panel on Climate Change. (2023).

Jannasch, H. W., Wheat, C. G., Plant, J. N., Kastner, M. & Stakes, D. S. Continuous chemical monitoring with osmotically pumped water samplers: OsmoSampler design and applications. *Limnology and Oceanography: Methods* **2**, 102–113 (2004).

Jarrard, R. D. Subduction fluxes of water, carbon dioxide, chlorine, and potassium: SUBDUCTION FLUXES OF WATER. *Geochem. Geophys. Geosyst.* **4**, n/a-n/a (2003).

Jayne, R. S., Zhang, Y. & Pollyea, R. M. Using Heat as a Predictor of CO2 Breakthrough in Highly Heterogeneous Reservoirs. *Geophysical Research Letters* **46**, 5879–5888 (2019).

Jenkins, C. R. *et al.* Safe storage and effective monitoring of CO2 in depleted gas fields. *Proceedings of the National Academy of Sciences* **109**, E35–E41 (2012).

Johnson, E. E. *et al.* Fault Slip Tendency Analysis for a Deep-Sea Basalt CO2 Injection in the Cascadia Basin. *GeoHazards* **4**, 121–135 (2023).

Johnson, G. & Mayer, B. Oxygen isotope exchange between H2O and CO2 at elevated CO2 pressures: Implications for monitoring of geological CO2 storage. *Applied Geochemistry* **26**, 1184–1191 (2011).

Johnson, G. *et al.* Tracing the movement of CO2 injected into a mature oilfield using carbon isotope abundance ratios: The example of the Pembina Cardium CO2 Monitoring project. *International Journal of Greenhouse Gas Control* **5**, 933–941 (2011).

Johnson, G. *et al.* The use of stable isotope measurements for monitoring and verification of CO2 storage. *Energy Procedia* **1**, 2315–2322 (2009).

Johnson, H. P., Hautala, S. L. & Bjorklund, T. A. The thermal environment of Cascadia Basin. *Geochemistry, Geophysics, Geosystems* **13**, (2012).

Kampman, N., Bickle, M., Wigley, M. & Dubacq, B. Fluid flow and CO2-fluid-mineral interactions during CO2-storage in sedimentary basins. *Chemical Geology* **369**, 22–50 (2014).

Kanakubo, M. *et al.* High-pressure NMR studies on solvation structure in supercritical carbon dioxide. *Fluid Phase Equilibria* **194–197**, 859–868 (2002).

Kasnavia, T., Vu, D. & Sabatini, D. A. Fluorescent Dye and Media Properties Affecting Sorption and Tracer Selection. *Groundwater* **37**, 376–381 (1999).

Kastner, M. *et al.* New Insights into the Hydrogeology of the Oceanic Crust through Long-Term Monitoring. *Oceanog.* **19**, 46–57 (2006).

Kelemen, P., Benson, S. M., Pilorgé, H., Psarras, P. & Wilcox, J. An Overview of the Status and Challenges of CO2 Storage in Minerals and Geological Formations. *Front. Clim.* **1**, (2019).

Kelley, D. S. *et al.* Endeavour Segment of the Juan de Fuca Ridge: ONE OF THE MOST REMARKABLE PLACES ON EARTH. *Oceanography* **25**, 44–61 (2012).

Kempe, S., Kazmierczak, J. The Role of Alkalinity in the Evolution of Ocean Chemistry, Organization of Living Systems, and Biocalcification Processes. *Bulletin de l'Institut oceanographique.* (1994).

Kerr, A. C. Oceanic Plateaus. in *Encyclopedia of Marine Geosciences* (eds. Harff, J., Meschede, M., Petersen, S. & Thiede, J.) 1–15 (Springer Netherlands, 2015). doi:10.1007/978-94-007-6644-0_21-1.

Khalilabad, M. R., Axelsson, G. & Gislason, S. R. Aquifer characterization with tracer test technique; permanent CO2 sequestration into basalt, SW Iceland. *Mineralogical Magazine* **72**, 121–125 (2008).

Khalilabad, M. R. *Characterization of the Hellisheidi-Threngsli CO2 sequestration target aquifer by tracer testing*. (United Nations University, Geothermal Training Programme, 2008).

Kharaka, Y. K. *et al.* Gas-water-rock interactions in Frio Formation following CO2 injection: Implications for the storage of greenhouse gases in sedimentary basins. *Geology* **34**, 577–580 (2006).

Kim, M. *et al.* Characterizing Tracer Transport Behavior in Two-Phase Flow System: Implications for CO2 Geosequestration. *Geophysical Research Letters* **47**, e2020GL089262 (2020).

Kirkendall, A. B., Schindel, G. M. & Gao, Y. Investigation of Methods in Fluorescent Dye Extraction from Activated charcoal for use in dye tracing. (2019). doi:10.1130/abs/2019AM-337014.

Kisliuk, P. & Silvey, G. A. The Microwave Spectrum of CF_3SF_5. *The Journal of Chemical Physics* **20**, 517–517 (1952).

Kloss, C. *et al.* Atmospheric Abundances, Trends and Emissions of CFC-216ba, CFC-216ca and HCFC-225ca. *Atmosphere* **5**, 420–434 (2014).

Koppers, A. *et al.* Introduction to the Special Issue on Scientific Ocean Drilling: Looking to the Future. *Oceanog* **32**, 14–15 (2019).

Krevor, S. *et al.* Capillary trapping for geologic carbon dioxide storage – From pore scale physics to field scale implications. *International Journal of Greenhouse Gas Control* **40**, 221–237 (2015).

Lackner, K. S., Wendt, C., Butts, D. P., Joyce, E. L. & Sharps, D. H. CARBON DIOXIDE DISPOSAL IN CARBONATE MINERALS. *Energy* **20**, 1153–1170 (1995).

Lagomarsino, R. J. An Improved Gas Chromatographic Method for the Determination of Perfluorocarbon Tracers in the Atmosphere. *Journal of Chromatographic Science* **34**, 405–412 (1996).

Lauer, R. M., Fisher, A. T. & Winslow, D. M. Three-dimensional models of hydrothermal circulation through a seamount network on fast-spreading crust. *Earth and Planetary Science Letters* **501**, 138–151 (2018).

Lee, J.M. *et al.* Observed stratospheric profiles and stratospheric lifetimes of HCFC-141b and HCFC-142b. Geophysical Research Letters 22, 1369-1372. (1995).

Leibundgut. *Tracers in Hydrology*. (John Wiley & Sons, Ltd, 2009). doi:10.1002/9780470747148.

Lesage, S., Brown, S. & Hosler, K. R. Degradation of chlorofluorocarbon-113 under anaerobic conditions. *Chemosphere* **24**, 1225–1243 (1992).

Levine, J. S., Matter, J. M., Goldberg, D. & Lackner, K. S. Gravitational trapping of carbon dioxide in deep ocean sediments: hydraulic fracturing and mechanical stability. *Energy Procedia* **1**, 3647–3654 (2009).

Lewicki, J. L., Birkholzer, J. & Tsang, C.-F. Natural and industrial analogues for leakage of CO2 from storage reservoirs: identification of features, events, and processes and lessons learned. *Environ Geol* **52**, 457–467 (2007).

Lewis, E. L. & Perkin, R. G. Salinity: Its definition and calculation. *Journal of Geophysical Research: Oceans* **83**, 466–478 (1978).

Lewis, E. L. & Perkin, R. G. The practical salinity scale 1978: conversion of existing data. *Deep Sea Research Part A. Oceanographic Research Papers* **28**, 307–328 (1981).

Li, J. & Pang, Z. Environmental isotopes in CO2 geological sequestration. *Greenhouse Gases: Science and Technology* **5**, 374–388 (2015).

Li, P. *et al.* Atmospheric histories, growth rates and solubilities in seawater and other natural waters of the potential transient tracers HCFC-22, HCFC-141b, HCFC-142b, HFC-134a, HFC-125, HFC-23, PFC-14 and PFC-116. *Ocean Science* **15**, 33–60 (2019).

Li, P. & Tanhua, T. Medusa–Aqua system: simultaneous measurement and evaluation of novel potential halogenated transient tracers HCFCs, HFCs, and PFCs in the ocean. *Ocean Sci.* **17**, 509–525 (2021).

Lin, H.-T., Cowen, J. P., Olson, E. J., Amend, J. P. & Lilley, M. D. Inorganic chemistry, gas compositions and dissolved organic carbon in fluids from sedimented young basaltic crust on the Juan de Fuca Ridge flanks. *Geochimica et Cosmochimica Acta* **85**, 213–227 (2012).

Litynski, J. T., Plasynski, S., McIlvried, H. G., Mahoney, C. & Srivastava, R. D. The United States Department of Energy's Regional Carbon Sequestration Partnerships Program Validation Phase. *Environment International* **34**, 127–138 (2008).

Liu, Z., Dreybrodt, W. & Liu, H. Atmospheric CO2 sink: Silicate weathering or carbonate weathering? *Applied Geochemistry* **26**, S292–S294 (2011).

Ljosland, E., Bjørnstad, T., Dugstad, Ø. & Hundere, I. Perfluorocarbon tracer studies at the Gullfaks field in the North Sea. *Journal of Petroleum Science and Engineering* **10**, 27–38 (1993).

Lobert, J. M. *et al.* BLAST94: BROMINE LATITUDINAL AIR/SEA TRANSECT 1994. (1996).

Lovelock, J. E. & Ferber, G. J. Exotic tracers for atmospheric studies. *Atmospheric Environment (1967)* **16**, 1467–1471 (1982).

Lovley, D. R. & Woodward, J. C. Consumption of Freons CFC-11 and CFC-12 by anaerobic sediments and soils. *Environ. Sci. Technol.* **26**, 925–929 (1992).

Lu, J. *et al.* Complex fluid flow revealed by monitoring CO2 injection in a fluvial formation. *Journal of Geophysical Research: Solid Earth* **117**, (2012).

Luhmann, A. J. *et al.* Permeability, porosity, and mineral surface area changes in basalt cores induced by reactive transport of CO2-rich brine. *Water Resources Research* **53**, 1908–1927 (2017).

Manley, J. *et al.* Innovations in Ocean Research Infrastructure to Advance High Priority Science. *Marine Technology Society Journal* **38**, (2004).

Manzer, L. E. The CEC-Ozone Issue: Progress on the Development of Alternatives to CFCs. *Science* **249**, (1990).

Marieni, C., Henstock, T. J. & Teagle, D. A. H. Geological storage of CO2 within the oceanic crust by gravitational trapping. *Geophysical Research Letters* **40**, 6219–6224 (2013).

Marieni, C., Matter, J. M. & Teagle, D. A. H. Experimental study on mafic rock dissolution rates within CO2-seawater-rock systems. *Geochimica et Cosmochimica Acta* **272**, 259–275 (2020).

Marieni, C. & Oelkers, E. Carbon sequestration potential of altered mafic reservoirs. *Energy Procedia* **146**, 68–73 (2018).

Marshall, J. & Johnsen, S. Fluorescence as a means of colour signal enhancement. *Phil. Trans. R. Soc. B* **372**, 20160335 (2017).

Matsuo, H., Koga, Y. & Sawamura, S. Solubility of cesium chloride in water under high pressures. *Fluid Phase Equilibria* **189**, 1–11 (2001).

Matter, J. M. *et al.* Rapid carbon mineralization for permanent disposal of anthropogenic carbon dioxide emissions. *Science* **352**, 1312–1314 (2016).

Matter, J. M. *et al.* The CarbFix Pilot Project–Storing carbon dioxide in basalt. *Energy Procedia* **4**, 5579–5585 (2011).

Matter, J. M. *et al.* Permanent Carbon Dioxide Storage into Basalt: The CarbFix Pilot Project, Iceland. *Energy Procedia* **1**, 3641–3646 (2009).

Matter, J. M. *et al.* Monitoring permanent CO2 storage by in situ mineral carbonation using a reactive tracer technique. *Energy Procedia* **63**, 4180–4185 (2014).

Matter, J. M. *et al.* Rapid carbon mineralization for permanent disposal of anthropogenic carbon dioxide emissions. *Science* **352**, 1312–1314 (2016).

Matter, J. *et al.* Radiocarbon as a Reactive Tracer for Tracking Permanent CO_2 Storage in Basaltic Rocks. (2015) doi:10.2172/1238341.

Matter, J. M. & Kelemen, P. B. Permanent storage of carbon dioxide in geological reservoirs by mineral carbonation. *Nature Geosci* **2**, 837–841 (2009).

Mayer, B. *et al.* Assessing the usefulness of the isotopic composition of CO_2 for leakage monitoring at CO2 storage sites: A review. *International Journal of Greenhouse Gas Control* **37**, 46–60 (2015).

Mayer, B. *et al.* Tracing the movement and the fate of injected CO_2 at the IEAGHG Weyburn-Midale CO2 Monitoring and Storage project (Saskatchewan, Canada) using carbon isotope ratios. *International Journal of Greenhouse Gas Control* **16**, S177–S184 (2013).

McCallum, S.D. *et al.* Monitoring Geologically Sequestered CO_2 during the Frio Brine Pilot Test using Perfluorocarbon Tracers. Gulf Coast Carbon Center Digital Publication Series #05-04n, 1-9 (2005).

McGrail, B., Ho, A., Reidel, S. & Schaef, H. Use and Features of Basalt Formations for Geologic Sequestration. in *Greenhouse Gas Control Technologies - 6th International Conference* vol. II 1637–1640 (2003).

McGrail, B. P. *et al.* Potential for carbon dioxide sequestration in flood basalts. *Journal of Geophysical Research: Solid Earth* **111**, (2006).

McGrail, B. P. *et al.* Preliminary Hydrogeologic Characterization Results from the Wallula Basalt Pilot Study. (2009).

McGrail, B. P. *et al.* Field Validation of Supercritical CO_2 Reactivity with Basalts. *Environ. Sci. Technol. Lett.* **4**, 6–10 (2017a).

McGrail, B. P. *et al.* Wallula Basalt Pilot Demonstration Project: Post-injection Results and Conclusions. *Energy Procedia* **114**, 5783–5790 (2017b).

McGrail, B. P. *et al.* Injection and Monitoring at the Wallula Basalt Pilot Project. *Energy Procedia* **63**, 2939–2948 (2014).

McGrail, B. P. *et al.* The Wallula basalt sequestration pilot project. *Energy Procedia* **4**, 5653–5660 (2011).

McKinley, J. P. & Colwell, F. S. Application of perfluorocarbon tracers to microbial sampling in subsurface environments using mud-rotary and air-rotary drilling techniques. *Journal of Microbiological Methods* **26**, 1–9 (1996).

McLaren, D. A comparative global assessment of potential negative emissions technologies. *Process Safety and Environmental Protection* **90**, 489–500 (2012).

Middelburg, J. J., Soetaert, K. & Hagens, M. Ocean Alkalinity, Buffering and Biogeochemical Processes. *Rev Geophys* **58**, e2019RG000681 (2020).

Misra, K. C. Introduction to Geochemistry. (2012).

Montzka, S. A. *et al.* Recent Trends in Global Emissions of Hydrochlorofluorocarbons and Hydrofluorocarbons: Reflecting on the 2007 Adjustments to the Montreal Protocol. *J. Phys. Chem. A* **119**, 4439–4449 (2014).

Montzka, S. A. *et al.* Global tropospheric distribution and calibration scale of HCFC-22. *Geophysical Research Letters* **20**, 703–706 (1993).

Mottl, M. J., Wheat, G. & Baker, E. Warm springs discovered on 3.5 Ma oceanic crust, eastern flank of the Juan de Fuca Ridge. 4 (1998).

Mottl, M. J. & Wheat, C. G. Hydrothermal circulation through mid-ocean ridge flanks: Fluxes of heat and magnesium. *Geochimica et Cosmochimica Acta* **58**, 2225–2237 (1994).

Mroczek, E. K. & Glover, R. B. Behaviour of sulphur hexafluoride in water above 210ºC: Implications for its use as a geothermal tracer. *Proceedings 18th NZ Geothermal Workshop* (1996).

Myers, M. *et al.* Literature Review of Tracer Partition Coefficients. 16 (2012a).

Myers, M. *et al.* Method for the determination of residual carbon dioxide saturation using reactive ester tracers. *Applied Geochemistry* **27**, 2148–2156 (2012b).

Myers, M. *et al.* Tracers – Past, present, and future applications in CO_2 geosequestration. *Applied Geochemistry* **30**, 125–135 (2013a).

Myers, M. *et al.* Chemical Tracer Partition Coefficients for CCS. 83 (2013b).

Myers, M., White, C., Stalker, L. & Pejcic, B. Temperature sensitivity of reactive ester tracers for measuring CO2 residual trapping capacity. *Chemical Geology* **399**, 30–35 (2015a).

Myers, M. *et al.* Field measurement of residual carbon dioxide saturation using reactive ester tracers. *Chemical Geology* **399**, 20–29 (2015b).

Myers, M. & White, C. Evaluation of Perfluorocarbons (PFCs) as Tracers for CO_2 Containment and Migration Monitoring. in *Geophysical Monograph Series* 271–281 (2018). doi:10.1002/9781119118657.ch13.

Myrttinen, A. *et al.* Carbon and oxygen isotope indications for CO_2 behaviour after injection: First results from the Ketzin site (Germany). *International Journal of Greenhouse Gas Control* **4**, 1000–1006 (2010).

National Academies of Science, Engineering, and Medicine. *Negative Emissions Technologies and Reliable Sequestration: A Research Agenda*. 25259. National Academies Press (2019). doi:10.17226/25259.

National Academies of Sciences, Engineering, and Medicine. *A Research Strategy for Ocean-based Carbon Dioxide Removal and Sequestration*. 26278. National Academies Press. (2021). doi:10.17226/26278.

National Energy Technology Laboratory. *Best practices for: Monitoring, Verification, and Accounting of CO2 Stored in Deep Geologic Formations*. (2009).

Nazzari, M., Sciarra, A. & Quattrocchi, F. A simple and sensitive gas chromatography–electron capture detection method for analyzing perfluorocarbon tracers in soil gas samples for storage of carbon dioxide. *International Journal of Greenhouse Gas Control* **14**, 60–64 (2013).

Neira, N. M. *et al.* Cross-hole tracer experiment reveals rapid fluid flow and low effective porosity in the upper oceanic crust. *Earth and Planetary Science Letters* **450**, 355–365 (2016).

Newman, P. A. *et al.* What would have happened to the ozone layer if chlorofluorocarbons (CFCs) had not been regulated? *Atmospheric Chemistry and Physics* **9**, 2113–2128 (2009).

Nimz, G. J. & Hudson, G. B. The Use of Noble Gas Isotopes for Monitoring Leakage of Geologically Stored CO2. in *Carbon Dioxide Capture for Storage in Deep Geologic Formations* 1113–1128 (Elsevier, 2005). doi:10.1016/B978-008044570-0/50152-5.

Novakowski, K. *et al.* The development of a conceptual model for contaminant transport in dolostone underlying Smithville, Ontario. (2000).

Oelkers, E. H. General kinetic description of multioxide silicate mineral and glass dissolution. *Geochimica et Cosmochimica Acta* **65**, 3703–3719 (2001).

Oliveira, M. B. *et al.* Modeling the Liquid−Liquid Equilibria of Water + Fluorocarbons with the Cubic-Plus-Association Equation of State. *Ind. Eng. Chem. Res.* **46**, 1415–1420 (2007).

Ooki, A. & Yokouchi, Y. Dichloromethane in the Indian Ocean: Evidence for in-situ production in seawater. *Marine Chemistry* **124**, 119–124 (2011).

Orcutt, B. N. *et al.* Colonization of subsurface microbial observatories deployed in young ocean crust. *ISME J* **5**, 692–703 (2011).

Orcutt, B. N. *et al.* Contamination tracer testing with seabed drills: IODP Expedition 357. *Scientific Drilling* **23**, 39–46 (2017).

Owari, S., Tomaru, H. & Matsumoto, R. Long-term, continuous OsmoSampler results for interstitial waters from an active gas venting site at a shallow gas hydrate field, Umitaka Spur, eastern margin of the Japan Sea. *Applied Geochemistry* **104**, 25–32 (2019).

Owens, D. *et al.* The Oceans 2.0/3.0 Data Management and Archival System. *Frontiers in Marine Science* **9**, (2022).

Palmer, M. R. & Edmond, J. M. Cesium and rubidium in submarine hydrothermal fluids: Evidence for recycling of alkali elements. *Earth and Planetary Science Letters* **95**, 8–14 (1989).

Park, K., Weyl, P. K. & Bradshaw, A. Effect of Carbon Dioxide on the Electrical Conductance of Seawater. *Nature* **201**, 1283–1284 (1964).

Pearce, J. K. *et al.* Geological storage of CO2 and acid gases dissolved at surface in production water. *Journal of Petroleum Science and Engineering* **210**, 110052 (2022).

Penman, D. E. *et al.* Silicate weathering as feedback and forcing in Earth's climate and carbon cycle. *Earth-Science Reviews* **209**, 103298 (2020).

Pevzner, R. *et al.* Monitoring subsurface changes by tracking direct-wave amplitudes and traveltimes in continuous distributed acoustic sensor VSP data. *GEOPHYSICS* **87**, A1–A6 (2022).

Pilson, M. E. Q. *An Introduction to the Chemistry of the Sea*. Cambridge University Press. (2012). doi:10.1017/CBO9781139047203.

Pollyea, R. M. *et al.* Physical constraints on geologic CO2 sequestration in low-volume basalt formations. *Geological Society of America Bulletin* **126**, 344–351 (2014).

Postma, T. J. W., Bandilla, K. W. & Celia, M. A. Implications of CO 2 mass transport dynamics for large-scale CCS in basalt formations. *International Journal of Greenhouse Gas Control* **121**, 103779 (2022).

Poulain, A. *et al.* A compact field fluorometer and its application to dye tracing in karst environments. *Hydrogeol J* **25**, 1517–1524 (2017).

Preuss, K. *et al.* Use of Gas Phase Tracers for Monitoring CO_2 Injection at the Frio Test Site. Gulf Coast Carbon Center Digital Publication Series #05-04r. (2005).

Ratouis, T. M. P. *et al.* Carbfix 2: A transport model of long-term CO2 and H2S injection into basaltic rocks at Hellisheidi, SW-Iceland. *International Journal of Greenhouse Gas Control* **114**, 103586 (2022).

Rauh, F. *et al.* A mid-infrared sensor for the determination of perfluorocarbon-based compounds in aquatic systems for geosequestration purposes. *Talanta* **130**, 527–535 (2014).

Raveendran, P., Ikushima, Y. & Wallen, S. L. Polar Attributes of Supercritical Carbon Dioxide. *Acc. Chem. Res.* **38**, 478–485 (2005).

Ravishankara, A. R., Solomon, S., Turnipseed, A. A. & Warren, R. F. Atmospheric Lifetimes of Long-Lived Halogenated Species. *Science* **259**, 194–199 (1993).

Raza, A., Glatz, G., Gholami, R., Mahmoud, M. & Alafnan, S. Carbon mineralization and geological storage of CO2 in basalt: Mechanisms and technical challenges. *Earth-Science Reviews* **229**, 104036 (2022).

Reidel, S. P. *et al.* The Columbia River flood basalt province: Stratigraphy, areal extent, volume, and physical volcanology. in *The Columbia River Flood Basalt Province* (Geological Society of America, 2013). doi:10.1130/2013.2497(01).

Reidel, S. P. *et al.* The Grande Ronde Basalt, Columbia River Basalt Group; Stratigraphic descriptions and correlations in Washington, Oregon, and Idaho. in *Geological Society of America Special Papers* vol. 239 21–54 (Geological Society of America, 1989).

Reidel, S. P., Spane, F. A. & Johnson, V. G. *Natural Gas Storage in Basalt Aquifers of the Columbia Basin, Pacific Northwest USA: A Guide to Site Characterization*. PNNL-13962, 15020781 http://www.osti.gov/servlets/purl/15020781-61JNNk/ (2002) doi:10.2172/15020781.

Reilly, J., Mayer, M. & Harnisch, J. The Kyoto Protocol and non-CO2 greenhouse gases and carbon sinks. *Environmental Modeling and Assessment* 217–229 (2002).

Rezvani Khalilabad, M., Axelsson, G. & Gislason, S. R. Aquifer characterization with tracer test technique; permanent CO_2 sequestration into basalt, SW Iceland. *Mineral. mag.* **72**, 121–125 (2008).

Roberts, J. J., Gilfillan, S. M. V., Stalker, L. & Naylor, M. Geochemical tracers for monitoring offshore CO2 stores. *International Journal of Greenhouse Gas Control* **65**, 218–234 (2017).

Rock, L. *et al.* Investigation of Natural Tracers for MMV at the Quest Carbon Capture and Storage Project, Alberta, Canada. *Energy Procedia* **63**, 4191–4198 (2014).

Rock, L. *et al.* The Quest CCS Project: 1st Year Review Post Start of Injection. *Energy Procedia* **114**, 5320–5328 (2017).

Rohr, K. M. M. Increase of seismic velocities in upper oceanic crust and hydrothermal circulation in the Juan de Fuca plate. *Geophysical Research Letters* **21**, 2163–2166 (1994).

Russell, B. F., Phelps, T. J., Griffin, W. T. & Sargent, K. A. Procedures for Sampling Deep Subsurface Microbial Communities in Unconsolidated Sediments. *Groundwater Monitoring & Remediation* **12**, 96–104 (1992).

Sæmundsson, K., Sigurgeirsson, M. Á. & Friðleifsson, G. Ó. Geology and structure of the Reykjanes volcanic system, Iceland. *Journal of Volcanology and Geothermal Research* **391**, 106501 (2020).

Saffer, D. M., Wallace, L. M., Petronotis, K., & Expedition 375 Scientists. Hikurangi Subduction Margin Coring and Observatories- Unlocking the secrets of slow slip through drilling to sample and monitor the forearc and subducting plate. International Ocean Discovery Program. (2018). doi:10.14379/iodp.pr.375.2018.

Sandalow, D., *et al.* Carbon mineralization roadmap. ICEF Innovation Roadmap Project. (2021).

Sauvage, J. *et al.* Data report: quantification of potential drilling contamination using perfluorocarbon tracer at IODP Expedition 329 sites. *Proceedings of the Integrated Ocean Drilling Program* **329**, (2017).

Schaef, H. T., McGrail, B. P. & Owen, A. T. Basalt Reactivity Variability with Reservoir Depth in Supercritical CO2 and Aqueous Phases. *Energy Procedia* **4**, 4977–4984 (2011).

Schaffer, M. *et al.* A new generation of tracers for the characterization of interfacial areas during supercritical carbon dioxide injections into deep saline aquifers: Kinetic interface-sensitive tracers (KIS tracer). *International Journal of Greenhouse Gas Control* **14**, 200–208 (2013).

Seifritz, W. CO_2 disposal by means of silicates. *Nature* **345**, 486 (1990).

Sekiya, A. & Misaki, S. The potential of hydrofluoroethers to replace CFCs, HCFCs and PFCs. *Journal of Fluorine Chemistry* (2000).

Seltzer, A. M. *et al.* Heavy Noble Gas Isotopes as New Constraints on the Ventilation of the Deep Ocean. *Geophysical Research Letters* **46**, 8926–8932 (2019).

Senum, G.I., and Dietz, R.N. Perfluorocarbon tracer tagging of drilling muds for the assessment of sample contamination. U.S. Department of Energy. (1990).

Serno, S. *et al.* Using oxygen isotopes to quantitatively assess residual CO2 saturation during the CO2CRC Otway Stage 2B Extension residual saturation test. *International Journal of Greenhouse Gas Control* **52**, 73–83 (2016).

Serno, S. *et al.* Oxygen isotopes as a tool to quantify reservoir-scale CO2 pore-space saturation. *International Journal of Greenhouse Gas Control* **63**, 370–385 (2017).

Shanks, W. C., Böhlke, J. K. & Seal, R. R. Stable Isotopes in Mid-Ocean Ridge Hydrothermal Systems: Interactions Between Fluids, Minerals, and Organisms. in *Geophysical Monograph Series* 194–221 (1995). doi:10.1029/GM091p0194.

Shell Canada Limited. Quest Carbon Capture and Storage Project: Second Annual Status Report. (2014).

Shipboard Scientific Party. Rough Basement Transect (Sites 1026 and 1027). in *Proceedings of the Ocean Drilling Program, Initial Reports, Vol. 168* 101–160 (1997a).

Shipboard Scientific Party. Introduction and Summary: hydrothermal circulation in the oceanic crust and its consequences on the eastern flank of the Juan de Fuca Ridge. in *Proceedings of the Ocean Drilling Program, 168 Initial Reports* (1997b).

Sigfússon, B. *et al.* Reducing emissions of carbon dioxide and hydrogen sulphide at Hellisheidi power plant in 2014-2017 and the role of CarbFix in achieving the 2040 Iceland climate goals. *Energy Procedia* **146**, 135–145 (2018).

Sigfusson, B. *et al.* Solving the carbon-dioxide buoyancy challenge: The design and field testing of a dissolved CO2 injection system. *International Journal of Greenhouse Gas Control* **37**, 213–219 (2015).

Simmonds, P. G. *et al.* The background atmospheric concentrations of cyclic perfluorocarbon tracers determined by negative ion-chemical ionization mass spectrometry. *Atmospheric Environment* **36**, 2147–2156 (2002).

Smart, B. E. Fluorine substituent effects (on bioactivity). *Journal of Fluorine Chemistry* **109**, 3–11 (2001).

Smart, P. L. & Laidlaw, I. M. An evaluation of some fluorescent dyes for water tracing. *Water Resources Research* **13**, 15–33 (1977).

Smethie, W. M. Tracing the thermohaline circulation in the western North Atlantic using chlorofluorocarbons. *Progress in Oceanography* **31**, 51–99 (1993).

Smith, D. C. *et al. Methods for Quantifying Potential Microbial Contamination during Deep Ocean Coring*. vol. // (Ocean Drilling Program, 2000).

Smith, S. & Pretorius, W. The conservative behaviour of fluorescein. *WSA* **28**, 403–406 (2002).

Smrzka, D. *et al.* The behavior of trace elements in seawater, sedimentary pore water, and their incorporation into carbonate minerals: a review. *Facies* **65**, 41 (2019).

Snæbjörnsdóttir, S. Ó., Gislason, S. R. & Oelkers, E. H. Carbon dioxide storage through mineral carbonation. 13 (2020).

Snæbjörnsdóttir, S. Ó. & Gislason, S. R. CO2 Storage Potential of Basaltic Rocks Offshore Iceland. *Energy Procedia* **86**, 371–380 (2016).

Snæbjörnsdóttir, S. Ó. *et al.* The chemistry and saturation states of subsurface fluids during the in situ mineralisation of CO_2 and H_2S at the CarbFix site in SW-Iceland. *International Journal of Greenhouse Gas Control* **58**, 87–102 (2017).

Solomon, E. A. *et al.* Long-term hydrogeochemical records in the oceanic basement and forearc prism at the Costa Rica subduction zone. *Earth and Planetary Science Letters* **282**, 240–251 (2009).

Soltanian, M. R. *et al.* Transport of perfluorocarbon tracers in the Cranfield Geological Carbon Sequestration Project. *Greenhouse Gas Sci Technol* **8**, 650–671 (2018).

Spane, F., McGrail, B., Bonneville, A. & Thorne, P. Hydrologic Characterization Results and Recommendations for the Wallula Basalt Pilot Well. 110 (2012).

Spinelli, G. A. & Fisher, A. T. Hydrothermal circulation within topographically rough basaltic basement on the Juan de Fuca Ridge flank. *Geochemistry, Geophysics, Geosystems* **5**, (2004).

Srebrenik, S. & Cohen, S. Theoretical derivation of partition coefficient from solubility parameters. *J. Phys. Chem.* **80**, 996–999 (1976).

Stalker, L., Boreham, C. & Perkins, E. A Review of Tracers in Monitoring CO2 Breakthrough: Properties, Uses, Case Studies, and Novel Tracers. *Carbon dioxide sequestration in geological media—State of the science: AAPG Studies in Geology* **59**, 595–608 (2009).

Stalker, L. & Myers, M. Tracers – Pilot versus Commercial Scale Deployment for Carbon Storage. *Energy Procedia* **63**, 4199–4208 (2014).

Stanislowski, K., Roesner, A. & Ikari, M. J. Implications for megathrust slip behavior and pore pressure at the shallow northern Cascadia subduction zone from laboratory friction experiments. *Earth and Planetary Science Letters* **578**, 117297 (2022).

Stanley, R. H. *et al.* A new automated method for measuring noble gases and their isotopic ratios in water samples. *Geochemistry, Geophysics, Geosystems* **10**, (2009).

Stanley, R. H. R. & Jenkins, W. J. Noble Gases in Seawater as Tracers for Physical and Biogeochemical Ocean Processes. in *The Noble Gases as Geochemical Tracers* (ed. Burnard, P.) 55–79 (2013). doi:10.1007/978-3-642-28836-4_4.

Stein, C. A. & Stein, S. A model for the global variation in oceanic depth and heat flow with lithospheric age. *Nature* **359**, 123–129 (1992).

Stein, C. A., Stein, S. & Pelayo, A. M. Heat Flow and Hydrothermal Circulation. in *Seafloor Hydrothermal Systems: Physical, Chemical, Biological, and Geological Interactions* 425–445 (American Geophysical Union) (1995). doi:10.1029/GM091p0425.

Stein, J. S. & Fisher, A. T. Observations and models of lateral hydrothermal circulation on a young ridge flank: Numerical evaluation of thermal and chemical constraints. *Geochemistry, Geophysics, Geosystems* **4**, (2003).

Strazisar, B. R. *et al.* Near-surface monitoring for the ZERT shallow CO_2 injection project. *International Journal of Greenhouse Gas Control* **3**, 736–744 (2009).

Tanase, D. *et al.* Progress of CO_2 injection and monitoring of the Tomakomai CCS Demonstration Project. (2021).

Tang, J. S. & Harker, B. Mass Balance Method to Determine Residual Oil Saturation From Single Well Tracer Test Data. *Journal of Canadian Petroleum Technology* **29**, (1990).

Tawiah, P. *et al.* CO_2 injectivity behaviour under non-isothermal conditions – Field observations and assessments from the Quest CCS operation. *International Journal of Greenhouse Gas Control* **92**, 102843 (2020).

Taylor, P. *et al.* A novel sub-seabed CO_2 release experiment informing monitoring and impact assessment for geological carbon storage. *International Journal of Greenhouse Gas Control* **38**, 3–17 (2015).

Terzer-Wassmuth, S. *et al.* Balancing precision and throughput of δ17O and Δ'17O analysis of natural waters by Cavity Ringdown Spectroscopy. *MethodsX* **10**, 102150 (2023).

Timko, M. T. *et al.* Partition Coefficients of Organic Solutes between Supercritical Carbon Dioxide and Water: Experimental Measurements and Empirical Correlations. *J. Chem. Eng. Data* **49**, 768–778 (2004).

Tokieda, T., Ishii, M., Enyo, K. & Hirota, M. A comparison of dissolved chlorofluorocarbons in seawater measured by MRI and JMA CFCs Systems. Papers in Meteorology and Geophysics. **55** 1-11 (2005).

Tomich, J. F. *et al.* Single-Well Tracer Method to Measure Residual Oil Saturation. *Journal of Petroleum Technology* **25**, 211–218 (1973).

Tryon, M. D., Henry, P. & Hilton, D. R. Quantifying submarine fluid seep activity along the North Anatolian Fault Zone in the Sea of Marmara. *Marine Geology* **315–318**, 15–28 (2012).

Tsai, W.T., Chen, H.P. & Hsien, W.Y. A review of uses environmental hazards and recovery/recycle technologies of perfluorocarbons (PFCs) emissions from the semiconductor manufacturing processes. *Journal of Loss Prevention in the Process Industries* **15**, 65–75 (2002).

Tuckett, R. P. Trifluoromethyl Sulphur Pentafluoride, SF_5CF_3: Atmospheric Chemistry and Its Environmental Importance via the Greenhouse Effect. in *Advances in Fluorine Science* vol. 1 89–129 (2006).

Tutolo, B. M., Awolayo, A. & Brown, C. Alkalinity Generation Constraints on Basalt Carbonation for Carbon Dioxide Removal at the Gigaton-per-Year Scale. *Environ. Sci. Technol.* (2021) doi:10.1021/acs.est.1c02733.

Underschultz, J. *et al.* CO_2 storage in a depleted gas field: An overview of the CO2CRC Otway Project and initial results. *International Journal of Greenhouse Gas Control* **5**, 922–932 (2011).

Underwood, M. & Hoke, K. Composition and Provenance of Turbidite Sand and Hemipelagic Mud in Northwestern Cascadia Basin. in *Proceedings of the Ocean Drilling Program, Scientific Results, Vol. 168* (2000).

United Nations Environmental Programme (UNEP). Emissions Gap Report 2019. (2019).

Upstill-Goddard, R. C. & Wilkins, C. S. The Potential of SF_6 as a Geothermal Tracer. *Water Resources* 29, 1065-1068 (1995).

Urey, H. C. Regarding the Early History of the Earth's Atmosphere. Bulletin of the Geological Society of America 67, 1125-1128. (1956).

Uwineza, P. A. & Waśkiewicz, A. Recent Advances in Supercritical Fluid Extraction of Natural Bioactive Compounds from Natural Plant Materials. *Molecules* **25**, 3847 (2020).

Van Pham, T. H., Aagaard, P. & Hellevang, H. On the potential for CO2 mineral storage in continental flood basalts – PHREEQC batch- and 1D diffusion–reaction simulations. (2012).

Vandeweijer, V. *et al.* Monitoring the CO_2 injection site: K12-B. *Energy Procedia* **4**, 5471–5478 (2011).

Veizer, J. Chemical Diagenesis of Carbonates: Theory and Application of Trace Element Technique. in *Stable Isotopes in Sedimentary Geology* (1983).

Veizer, J. *et al.* 87Sr/86Sr, δ13C and δ18O evolution of Phanerozoic seawater. *Chemical Geology* **161**, 59–88 (1999).

Wai, C. M. *et al.* Chemical Reactions in Supercritical Carbon Dioxide. *J. Chem. Educ.* **75**, 1641 (1998).

Walker, B. D. *et al.* Dissolved inorganic carbon isotopic composition of low-temperature axial and ridge-flank hydrothermal fluids of the Juan de Fuca Ridge. *Marine Chemistry* **108**, 123–136 (2008).

Walker, J. C. G., Hays, P. B. & Kasting, J. F. A negative feedback mechanism for the long-term stabilization of Earth's surface temperature. *J. Geophys. Res.* **86**, 9776 (1981).

Wanninkhof, R., Ledwell, J. R. & Watson, A. J. Analysis of sulfur hexafluoride in seawater. *Journal of Geophysical Research: Oceans* **96**, 8733–8740 (1991).

Warner, M. J. & Weiss, R. F. Solubilities of chlorofluorocarbons I I and 12 in water and seawater. 13 (1985).

Warr, O. Understanding phase behavior in the geological storage of carbon dioxide. PhD Dissertation. The University of Manchester (2013).

Warr, O. *et al.* Determining noble gas partitioning within a CO_2–H_2O system at elevated temperatures and pressures. *Geochimica et Cosmochimica Acta* **159**, 112–125 (2015).

Watson, A. J., Ledwell, J. R. & Hole, W. Tracer Release Experiments. (2001).

Watson, T. & Sullivan, T. Design of a perfluorocarbon tracer based monitoring network to support monitoring verification and accounting of sequestered CO_2. *EPJ Web of Conferences* **50**, 04003 (2013).

Watson, T. B. *et al.* The Atmospheric Background of Perfluorocarbon Compounds Used as Tracers. *Environ. Sci. Technol.* **41**, 6909–6913 (2007).

Webb, P. Introduction to Oceanography. (2017).

Weber, U. W., Kampman, N. & Sundal, A. Techno-Economic Aspects of Noble Gases as Monitoring Tracers. *Energies* **14**, 3433 (2021).

Weiss, R. F. Solubility of helium and neon in water and seawater. *J. Chem. Eng. Data* **16**, 235–241 (1971).

Weiss, R. F. & Kyser, T. K. Solubility of krypton in water and sea water. *J. Chem. Eng. Data* **23**, 69–72 (1978).

Wells, A. W. *et al.* The use of tracers to assess leakage from the sequestration of CO2 in a depleted oil reservoir, New Mexico, USA. *Applied Geochemistry* **22**, 996–1016 (2007).

Wells, A. W. *et al.* Atmospheric and soil-gas monitoring for surface leakage at the San Juan Basin CO2 pilot test site at Pump Canyon New Mexico, using perfluorocarbon tracers, CO2 soil-gas flux and soil-gas hydrocarbons. *International Journal of Greenhouse Gas Control* **14**, 227–238 (2013).

Wheat, C. G. *et al.* Subseafloor Cross-Hole Tracer Experiment Reveals Hydrologic Properties, Heterogeneities, and Reactions in Slow-Spreading Oceanic Crust. *Geochem. Geophys. Geosyst.* **21**, (2020).

Wheat, C. G. *et al.* Chemical composition of basement fluids within an oceanic ridge flank: Implications for along-strike and across-strike hydrothermal circulation. *Journal of Geophysical Research: Solid Earth* **105**, 13437–13447 (2000).

Wheat, C. G. *et al.* Subseafloor seawater-basalt-microbe reactions: Continuous sampling of borehole fluids in a ridge flank environment. *Geochemistry, Geophysics, Geosystems* **11**, (2010).

Wheat, C. G. & McManus, J. The potential role of ridge-flank hydrothermal systems on oceanic germanium and silicon balances. *Geochimica et Cosmochimica Acta* **69**, 2021–2029 (2005).

Wheat, C. G. & Mottl, M. J. Hydrothermal circulation, Juan de Fuca Ridge eastern flank: Factors controlling basement water composition. *Journal of Geophysical Research: Solid Earth* **99**, 3067–3080 (1994).

Wheat, C. G. *et al.* Heat flow through a basaltic outcrop on a sedimented young ridge flank: HEAT FLOW THROUGH A BASALTIC OUTCROP. *Geochem. Geophys. Geosyst.* **5**, n/a-n/a (2004).

Wheat, C. G., Jannasch, H. W. & Kastner, M. Fluid sampling from oceanic borehole observatories: design and methods for CORK activities (1990–2010). in *Proceedings of the Integrated Ocean Drilling Program, Volume 327* (2011). doi:10.2204/iodp.proc.327.2011.

Wheat, C. G. *et al.* Seawater transport and reaction in upper oceanic basaltic basement: chemical data from continuous monitoring of sealed boreholes in a ridge flank environment. *Earth and Planetary Science Letters* **216**, 549–564 (2003).

Wheat, C. G. & Mottl, M. J. Composition of pore and spring waters from Baby Bare: global implications of geochemical fluxes from a ridge flank hydrothermal system. *Geochimica et Cosmochimica Acta* **64**, 629–642 (2000).

Wheat, C. G. *et al.* Formation Waters Delineate Diverse Hydrogeologic Conditions at a Plate Scale: Eastern Flank of the Juan de Fuca Ridge. *Geochemistry, Geophysics, Geosystems* **23** (2022).

White, C. M. *et al.* Separation and Capture of CO_2 from Large Stationary Sources and Sequestration in Geological Formations—Coalbeds and Deep Saline Aquifers. *Journal of Air & Waste Management Association* 645–715 (2003).

White, S. K. *et al.* Quantification of CO_2 Mineralization at the Wallula Basalt Pilot Project. *Environ. Sci. Technol.* acs.est.0c05142 (2020) doi:10.1021/acs.est.0c05142.

Wildgust, N., Gilboy, C. & Tontiwachwuthikul, P. Introduction to a decade of research by the IEAGHG Weyburn–Midale CO_2 Monitoring and Storage Project. *International Journal of Greenhouse Gas Control* **16**, S1–S4 (2013).

Wilson, J. F., Cobb, E. D. & Kilpatrick, F. A. Fluorometric procedures for dye tracing. *U.S. Geological Survey* 69 (1986).

Winslow, D. *et al.* Three-dimensional modeling of outcrop-to-outcrop hydrothermal circulation on the eastern flank of the Juan de Fuca Ridge. *Journal of Geophysical Research: Solid Earth* **121**, 1365–1382 (2016).

Winslow, D. M. & Fisher, A. T. Sustainability and dynamics of outcrop-to-outcrop hydrothermal circulation. *Nat Commun* **6**, 7567 (2015).

Winthaegen, P., Arts, R. & Schroot, B. Monitoring Subsurface CO_2 Storage. *Oil & Gas Science and Technology - Rev. IFP* **60**, 573–582 (2005).

Witkowski, A., Majkut, M. & Rulik, S. Analysis of pipeline transportation systems for carbon dioxide sequestration. *Archives of Thermodynamics* **35**, 117–140 (2014).

Wood, D. & Caputi, R. Solubilities of Kr and Xe in Fresh and Seawater: http://www.dtic.mil/docs/citations/AD0631557 (1966) doi:10.21236/AD0631557.

Wright, J. *et al.* The ocean basins: Their structure and evolution. 2nd Edition. Oxford. (1998).

Wu, H. *et al.* Simulation of CO2 mineral trapping and permeability alteration in fractured basalt: Implications for geologic carbon sequestration in mafic reservoirs. *International Journal of Greenhouse Gas Control* **109**, 103383 (2021).

Yee, G. G., Fulton, J. L. & Smith, R. D. Fourier transform infrared spectroscopy of molecular interactions of heptafluoro-1-butanol or 1-butanol in supercritical carbon dioxide and supercritical ethane. *J. Phys. Chem.* **96**, 6172–6181 (1992).

Yonker, C. R. & Palmer, B. J. Investigation of CO_2 /Fluorine Interactions through the Intermolecular Effects on the ^{1}H and ^{19}F Shielding of CH_3F and CHF_3 at Various Temperatures and Pressures. *J. Phys. Chem. A* **105**, 308–314 (2001).

Yuan-Hui, L. & Gregory, S. Diffusion of ions in sea water and in deep-sea sediments. *Geochimica et Cosmochimica Acta* **38**, 703–714 (1974).

Yvon-Lewis, S. A. & Butler, J. H. Effect of oceanic uptake on atmospheric lifetimes of selected trace gases. *Journal of Geophysical Research: Atmospheres* **107**, ACH 1-1-ACH 1-9 (2002).

Zeebe, R.E. and Wolf-Gladrow, D. CO_2 in seawater: equilibrium, kinetics, isotopes. *Elsevier Oceanography Series.* (2001).

Zhang, C. *et al.* Liquid CO_2 Displacement of Water in a Dual-Permeability Pore Network Micromodel. *Environ. Sci. Technol.* **45**, 7581–7588 (2011).

Zhang, J. *et al.* Effect of dissolved CO_2 on the conductivity of the ionic liquid [bmim][PF6]. *New J. Chem.* **27**, 333–336 (2003).

Zhao, X. *et al.* The CO_2 storage capacity evaluation: Methodology and determination of key factors. *Journal of the Energy Institute* **87**, 297–305 (2014).

Zheng, D. *et al.* Experimental and modeling studies on the solubility of CO_2, CHC1F2, CHF3, CzH2F4 and C2HnF2 in water and aqueous NaC1 solutions under low pressures. *Fluid Phase Equilibria* (1997).

Zhong, L. *et al.* Transport of perfluorocarbon tracers and carbon dioxide in sediment columns – Evaluating the application of PFC tracers for CO_2 leakage detection. *Applied Geochemistry* **45**, 25–32 (2014).

Zhou, Z., *et al.* Identifying and quantifying natural CO_2 sequestration processes over geological timescales: The Jackson Dome CO_2 Deposit, USA. *Geochimica et Cosmochimica Acta* **86**, 257–275 (2012).

Zühlsdorff, L. *et al.* Site surveys related to IODP Expedition 301: ImageFlux (SO149) and RetroFlux (TN116) expeditions and earlier studies. in *Proceedings of the Integrated Ocean Drilling Program, Volume 301* (2005).